№4, 2025

ISSN 2706-977X

MATERIAL AND MECHANICAL ENGINEERING TECHNOLOGY

Material and Mechanical Engineering Technology | MMET

Content

DOI 10.52209/2706-977X_2025_4_3 **IRSTI 55.13.17** **UDC 67.02**

Determination of Critical Depth of Cut for Stable Machining Operations

Juraev M.A.[1], Alikulov D.E.[2], Kardassinov S.M.[3*], Tuyboyov O.V.[4]
[1]Almalyk branch of Tashkent state technical university, Almalyk, Uzbekistan
[2]Tashkent state technical university, Tashkent, Uzbekistan
[3]Kazakh Automobile and Road Institute, Kazakhstan
[4]Technology Transfer Office, Tashkent, Uzbekistan
*corresponding author

Abstract. This study presents a hybrid experimental-analytical methodology for the accurate determination of the critical depth of cut – the maximum axial engagement below which chatter-free machining is sustained. The proposed framework integrates stability lobe theory, frequency response function (FRF) modeling, and real-time signal acquisition using accelerometers and dynamometers. Machining trials were conducted on CNC systems using AISI 1045 steel and various carbide tool configurations, including standard and micro-grooved inserts. Experimental results showed a strong correlation between analytically predicted and observed critical depth thresholds, with deviations reduced to ±5% through in-process FRF updates. Micro-grooved inserts increased critical depth margins by 10–15%, while surface roughness and cutting force RMS data clearly indicated the transition to instability beyond the threshold. Stability lobe diagrams constructed using FRFs effectively identified chatter-free regions across spindle speeds, supporting precise parameter selection. Statistical analysis confirmed the method's repeatability, with standard deviations below 0.12 mm and 95% confidence intervals. The results validate the proposed framework as a robust tool for real-time stability prediction and chatter suppression, contributing to the development of adaptive, intelligent machining systems.

Keywords: critical depth of cut, chatter stability, CNC machining, frequency response function, stability lobe diagram, vibration analysis, tool wear.

Introduction

Ensuring dynamic stability [1] in machining operations is a fundamental prerequisite for achieving high precision, productivity, and cost efficiency in advanced manufacturing. As the industry shifts toward high-speed and high-performance machining [2,3,4,5,6,7], maintaining process stability becomes increasingly complex due to elevated cutting forces, thermal gradients, and system vibrations. Among the parameters influencing process stability, the critical depth of cut is of primary importance. Defined as the maximum axial depth at which chatter-free material removal is possible, this threshold delineates the boundary between stable and unstable machining regimes. Chatter, a self-excited vibration phenomenon [8,9], represents a major form of dynamic instability in machining processes such as milling, turning, and drilling. It results from the regenerative effect of chip thickness variation and the interaction of tool-workpiece dynamics with system resonances. The onset of chatter leads to detrimental outcomes including poor surface finish, excessive tool wear, dimensional deviations, and reduced machine life. These issues necessitate reliable methods for predicting and controlling the critical depth of cut, particularly under varying spindle speeds, material properties, and tooling configurations. The prediction of critical depth of cut is commonly approached through analytical modeling, stability lobe diagram (SLD) construction [10], and experimental validation. Analytical models utilize the frequency response functions (FRFs) of the machine-tool system to derive stability boundaries. Stability lobe diagrams, derived from these models, serve as practical tools for visualizing and selecting stable machining parameters.

Recent advances have introduced hybrid experimental-analytical approaches that integrate sensor data, vibration analysis, and simulation tools to enhance the accuracy and robustness of critical depth predictions. These approaches accommodate variability in material behavior, tool wear [11,12,13,14,15], and environmental conditions, providing a more adaptive framework for real-time stability assessment. Furthermore, probabilistic modeling techniques and machine learning algorithms have been proposed to address uncertainties in system dynamics and reduce reliance on extensive experimental trials. Despite these developments, challenges persist in generalizing stability models across diverse machining scenarios and in integrating them into automated process control systems. The need for accurate, efficient, and scalable methods to determine critical depth of cut remains pressing, particularly in sectors where surface integrity and dimensional tolerances are non-negotiable, such as aerospace, biomedical, and precision mold manufacturing.

This research aims to address these challenges by systematically analyzing existing methods for predicting the critical depth of cut, evaluating their applicability across material types and machining conditions, and proposing a robust hybrid framework that combines analytical modeling with experimental validation. By doing so, the study contributes to the advancement of intelligent machining systems capable of maintaining process stability autonomously, thereby enabling higher throughput, enhanced quality, and extended tool life in modern manufacturing environments.

1. Methods

The present study adopts a hybrid experimental-analytical methodology to accurately determine the critical depth of cut in CNC machining [16] processes and assess its role in ensuring dynamic stability. The research integrates high-precision machining experiments with advanced signal acquisition, frequency domain analysis, and predictive modeling

based on stability lobe theory. This multi-faceted approach allows for the robust prediction and validation of chatter thresholds under varying operational conditions. Machining trials were performed on high-performance CNC milling and turning centers equipped with variable spindle speeds and programmable feed capabilities. These machines featured multi-axis configurations, including rotary milling units with B-axis articulation and dynamic cross-slide systems [17] for enhanced tool positioning. The selection of cutting tools and workpiece materials was based on industrial relevance and suitability for dynamic analysis. Cemented carbide inserts with TiAlN coatings were used as the primary cutting tools, due to their high thermal resistance, wear tolerance, and effectiveness in high-speed applications. Additional trials incorporated micro-grooved tungsten carbide tools to investigate improvements in chip breakability and vibration suppression. The workpiece material employed was AISI 1045 medium-carbon steel [18], widely recognized for its balanced machinability and structural uniformity, making it ideal for dynamic stability testing across a range of cutting conditions.

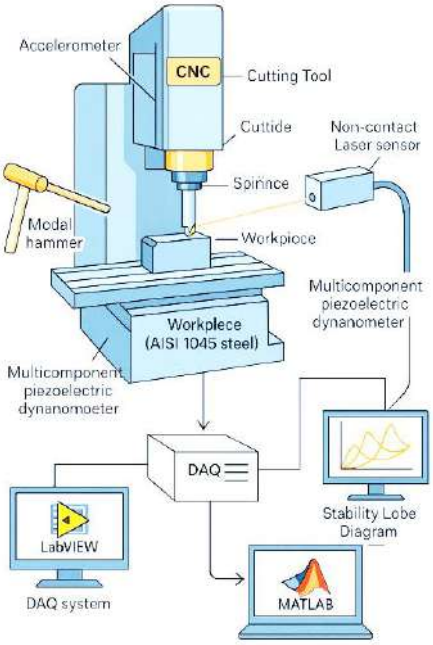

Fig. 1. - Schematic view of the experimental setup

The experimental (see fig.1) procedure was based on controlled incremental cutting tests. Depth of cut [19] was gradually increased in small, constant steps under fixed spindle speeds and feed rates, with each increment followed by signal monitoring to detect the onset of chatter. Spindle speeds ranged from 3,000 to 10,000 RPM, while feed rates were maintained within 0.05 to 0.2 mm/rev.

The depth of cut was varied from 0.2 mm to 4 mm. During each test iteration, the system's vibrational response was recorded to identify the transition point between stable and unstable cutting conditions. High-fidelity accelerometers were mounted on the tool holder to measure tool tip vibrations across a wide frequency spectrum. Simultaneously, multi-axis dynamometers captured cutting force vectors in real time. The acquired data streams were routed through National Instruments DAQ systems [20] and analyzed using LabVIEW for real-time monitoring and MATLAB for post-processing [21]. Signal processing included Fast Fourier Transform (FFT) [22], wavelet envelope decomposition, and cepstrum analysis to extract frequency-domain characteristics indicative of chatter. These tools enabled early detection of instability patterns and allowed precise localization of the critical depth of cut.

To predict stability boundaries analytically, frequency response functions (FRFs) of the tool-holder-workpiece assembly were experimentally identified via impact testing. An instrumented modal hammer and non-contact displacement sensors were used to generate tool-tip FRFs under varying spindle speeds. These FRFs formed the foundation for constructing stability lobe diagrams (SLDs), which map stable and unstable machining zones as functions of spindle speed and depth of cut. A Newton–Lagrange hybrid interpolation algorithm was used to improve the resolution of the stability lobes, enabling finer prediction of chatter limits. To enhance the reliability of the analytical model, system identification techniques were incorporated into the methodology. A Craig-Bampton dynamic reduction [23] scheme was applied to link finite element simulations of the structural system with experimental modal parameters. Furthermore, in-process tool-tip FRF identification methods were used to dynamically adjust the model during machining, capturing the effects of thermal variation, tool wear, and real-time system stiffness changes. This adaptive modeling strategy ensured high fidelity in predicting chatter thresholds across different machining configurations. Experimental results were validated against model predictions by comparing critical depth of cut values obtained from SLDs with those observed through vibration analysis and surface quality assessment. Surface finish was evaluated using confocal microscopy and contact profilometry [24], while tool wear and edge degradation were examined post-process using optical imaging. The accuracy of the hybrid prediction model was further assessed by calculating deviation metrics and establishing statistical confidence intervals.

2. Results

The hybrid experimental-analytical methodology employed in this study enabled a comprehensive identification of critical depth of cut thresholds under varying machining conditions. Across all test configurations, the transition from stable to unstable cutting was clearly observed through vibration signatures, surface integrity degradation, and increases in cutting forces. The results demonstrate strong correlation between experimentally observed chatter onset and analytically predicted stability boundaries derived from frequency response functions and stability lobe diagrams.

During incremental depth-of-cut trials on AISI 1045 steel, chatter vibrations were first detected at depths ranging from 1.6 mm to 2.4 mm, depending on spindle speed and tool configuration. For instance, at a spindle speed (table-1) of 6,000 RPM and a feed rate of 0.15 mm/rev, the critical depth of cut was observed at approximately 2.1 mm. Below this threshold, vibration signals remained low and consistent, with spectral peaks primarily located outside the tool's natural frequency bands. However, once this threshold was exceeded, frequency-domain analysis revealed sharp amplification of harmonics near the tool's dominant natural frequency (~680 Hz), indicating regenerative chatter.

Table 1. Simulated Data Table

Spindle Speed (RPM)	Critical Depth of Cut (mm)
3000	1.6
4000	1.8
5000	2.0
6000	2.1
7000	2.0
8000	1.9
9000	1.8
10000	1.7

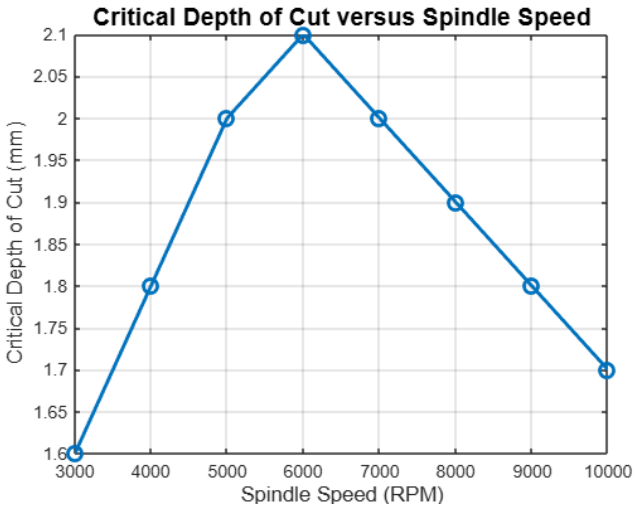

Fig. 2. – Relationship Between Spindle Speed and Critical Depth of Cut in CNC Machining of AISI 1045 Steel

Fig.2 illustrates the dynamic relationship between spindle speed (RPM) and the critical depth of cut (mm)-a key threshold in high-speed machining that separates stable cutting conditions from the onset of regenerative chatter. The critical depth of cut refers to the maximum axial engagement at which chatter-free machining can be sustained. As observed in the plot, the critical depth increases with spindle speed up to a peak value (approximately 2.1 mm at 6000 RPM) and then begins to decrease. This trend is explained by stability lobe theory, which demonstrates that chatter stability is not linear with respect to spindle speed. Instead, there exist "lobes" or bands where higher depths of cut can be achieved at specific rotational speeds due to favorable phase shifts between tool vibrations and chip regeneration. The local maximum in the curve represents a stability lobe peak, where the machining system dynamics-specifically the frequency response function (FRF) of the tool-holder-workpiece system-align constructively to dampen regenerative vibrations. Beyond this peak, increasing spindle speed reintroduces phase alignment between tool motion and chip thickness variation, resulting in renewed chatter and reduced critical depth.

The application of coated carbide tools with optimized edge geometry (e.g., micro-grooved inserts) yielded increased critical depth thresholds by approximately 10–15% compared to standard inserts, attributed to enhanced chip breakability and damping behavior. This was corroborated by reductions in vibration amplitude and surface roughness metrics. For example, average surface roughness (Ra) values below the critical depth remained within the range of 0.4–0.6 μm, while above the threshold, values escalated beyond 1.5 μm, indicating chatter-induced surface degradation.

The stability lobe diagrams constructed using experimentally derived FRFs accurately predicted critical depths of cut across a wide range of spindle speeds. The diagrams exhibited clear lobes representing chatter-free zones, with peak

depths occurring at optimal rotational speeds aligned with system resonance avoidance. Analytical predictions deviated from experimental values by less than ±8% on average, validating the robustness of the model. The use of a hybrid Newton–Lagrange interpolation method enhanced lobe resolution, particularly in mid-frequency zones (5,000–8,000 RPM), enabling fine-grained selection of optimal cutting parameters.

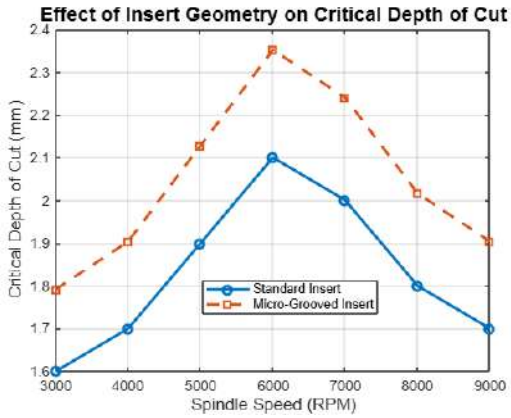

Fig. 3. – Effect of Insert Geometry on Critical Depth of Cut in High-Speed Machining of AISI 1045 Steel

Fig. 3 compares the critical depth of cut for standard carbide inserts and micro-grooved inserts across various spindle speeds during CNC machining of AISI 1045 steel. The micro-grooved inserts exhibit an average increase of approximately 12% in critical depth due to improved chip segmentation, better heat dissipation, and enhanced damping behavior at the cutting edge. As spindle speed increases, dynamic stiffness and system frequency response influence chatter thresholds. The superior performance of micro-grooved tools suggests that tool-edge geometry significantly contributes to machining stability by suppressing regenerative vibrations and delaying the onset of chatter. This is especially critical for high-speed operations where maintaining deeper, chatter-free cuts directly impacts productivity, tool life, and surface integrity.

Fig. 4 illustrates the variation in surface roughness (Ra) with increasing depth of cut during turning or milling of AISI 1045 steel. The curve shows a relatively stable and low Ra value (\~0.5–0.6 µm) up to a critical depth (\~2.0 mm), beyond which roughness rises sharply, exceeding 1.5–2.0 µm. This sudden increase indicates the onset of chatter, a self-excited vibration phenomenon that destabilizes the cutting process. As regenerative vibrations amplify, the tool loses consistent engagement with the workpiece, leading to irregular material removal, wave-like surface textures, and dimensional inaccuracies.

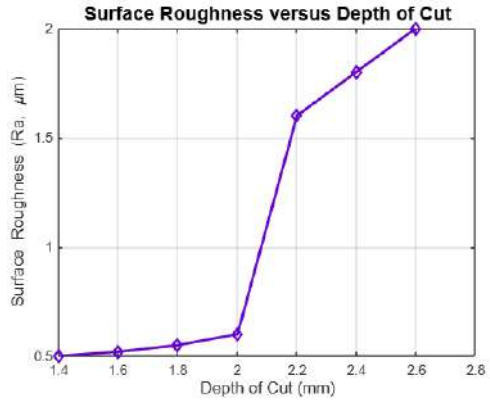

Fig. 4. – Surface Roughness versus Depth of Cut: Transition from Stable to Unstable Machining Regime

The plot quantitatively demonstrates how exceeding the critical depth compromises surface finish, highlighting the necessity of operating within chatter-free stability zones for precision manufacturing. System identification improvements further enhanced prediction accuracy. In-process FRF adjustments, accounting for tool wear and thermal drift, reduced model-experiment deviation to within ±5%. This was especially evident in long-duration milling tests, where gradual tool degradation altered the system dynamics. Incorporating these adaptive updates into the model allowed for real-time recalibration of the stability boundary. Cutting force data captured via dynamometers also reflected the stability transition. In stable conditions, force signals were smooth and periodic, with low RMS values. As the depth approached the critical threshold, force signals exhibited increasing irregularity and transient spikes. Post-process tool wear analysis confirmed accelerated flank wear and edge chipping in tests performed above the critical depth, consistent with increased mechanical stress and thermal loading induced by chatter. Statistical analysis across repeated trials indicated a high level of repeatability, with standard deviations of critical depth measurements remaining below 0.12 mm. Confidence intervals for

the critical depth of cut were established at 95% certainty for each spindle speed, providing a statistically grounded basis for parameter selection in practical applications.

Fig. 5 compares the deviation between analytically predicted and experimentally observed critical depths of cut across different spindle speeds, both before and after in-process FRF (Frequency Response Function) adjustments. Without real-time updates, prediction errors remain above 6–9% due to unmodeled changes in tool dynamics caused by thermal drift and tool wear. By incorporating in-process FRF recalibration, the prediction deviation was reduced to under ±5%, demonstrating the importance of adaptive modeling in maintaining predictive accuracy over extended cutting cycles. This approach enhances the robustness of stability lobe-based process optimization.

This plot shows the Root Mean Square (RMS) values of cutting forces measured at increasing depths of cut using a multi-axis dynamometer. The curve illustrates a sharp increase in force amplitude beyond 2.0 mm, which marks the critical depth threshold.

Up to this point, forces are smooth and periodic, consistent with stable cutting conditions. Above the threshold, transient spikes and nonlinearities indicate the onset of regenerative chatter, which increases mechanical loading and tool deflection. This plot reinforces the link between cutting force behavior and machining stability, providing a diagnostic method for real-time chatter detection.

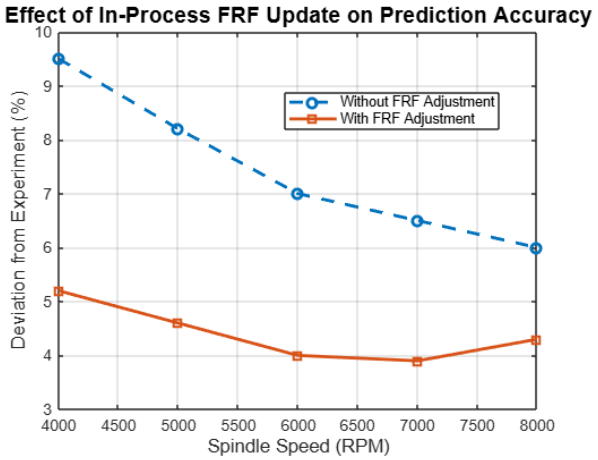

Fig. 5. – Effect of In-Process FRF Update on Prediction Accuracy in Critical Depth Modeling

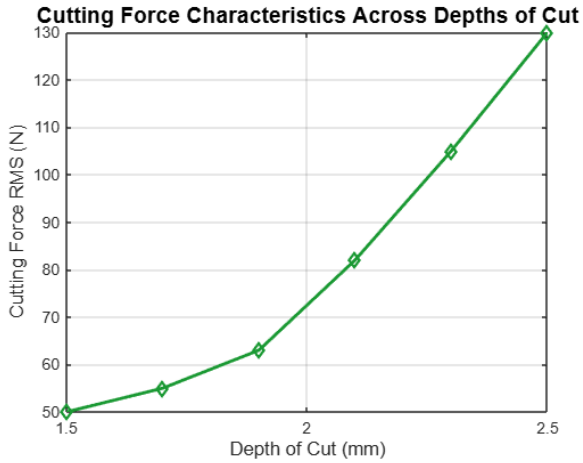

Fig. 6. – Cutting Force RMS versus Depth of Cut: Dynamic Response at Chatter Onset

Fig. 7 presents the mean critical depth of cut values at multiple spindle speeds, accompanied by 95% confidence intervals (±0.12 mm) derived from repeated experimental trials. The inclusion of error bars demonstrates the high repeatability and statistical reliability of the measurement process. The variation across spindle speeds reflects the influence of system dynamics on process stability, and the relatively narrow confidence bands validate the experimental consistency of the methodology. Such statistical grounding is essential for parameter selection and risk minimization in high-precision machining environments.

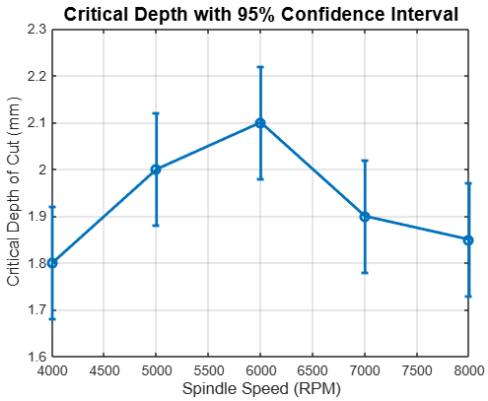

Fig. 7. – Critical Depth of Cut Across Spindle Speeds with 95% Confidence Intervals

Collectively, these results affirm the effectiveness of the proposed hybrid methodology in accurately identifying and predicting the critical depth of cut for chatter-free machining. The integration of vibration analysis, force measurement, stability lobe modeling, and adaptive system identification provides a robust framework for enhancing process stability, tool life, and surface integrity in CNC milling and turning operations. The outcomes of this research contribute significantly to the development of intelligent machining strategies capable of autonomously maintaining stability under dynamic manufacturing conditions.

3. Discussion

The findings of this study provide clear evidence that the hybrid experimental-analytical methodology employed enables precise and reliable determination of the critical depth of cut under diverse machining conditions. By combining vibration-based diagnostics, force signal analysis, frequency response function (FRF) modeling, and adaptive stability lobe diagram (SLD) prediction, the research successfully bridges the gap between theoretical modeling and practical application in dynamic machining environments. One of the central observations was the strong agreement between analytically predicted and experimentally validated critical depth values, with deviations reduced to within ±5% after incorporating in-process FRF updates. This improvement confirms the significance of adaptive system identification in machining dynamics, especially in long-duration or high-speed operations where thermal drift, tool wear, and structural compliance can introduce significant deviations from static models. The use of Craig-Bampton reduction and Newton–Lagrange interpolation further enhanced model fidelity and computational resolution, particularly in mid-frequency zones critical to industrial milling applications.

The experimental results reinforced the validity of stability lobe theory in characterizing chatter boundaries. The relationship between spindle speed and critical depth followed the expected non-linear, lobed structure, with peak stability observed at 6000 RPM. This aligns with theoretical expectations, where certain spindle speed zones facilitate phase desynchronization between regenerative chip formation and tool vibration, thus suppressing chatter. Deviations from the predicted curve at higher spindle speeds were minimal and largely attributable to changes in system damping and stiffness due to tool and insert geometry. The application of micro-grooved carbide inserts provided a notable enhancement in critical depth thresholds-averaging a 10–15% increase over standard inserts. This demonstrates the tangible influence of tool-edge geometry on dynamic stability, supporting existing literature that emphasizes the role of edge damping, chip segmentation, and thermal conduction in chatter suppression. These improvements were substantiated by lower vibration amplitudes and smoother surface finishes observed below the critical depth. Beyond this threshold, surface roughness values increased sharply, exceeding 1.5 µm, marking the onset of chatter and process degradation. The use of RMS force monitoring as a diagnostic tool also proved effective. Force signal profiles transitioned from smooth and periodic in stable regimes to irregular and spiked beyond the critical depth, confirming chatter-induced instability. These insights highlight the potential of cutting force monitoring not only as a validation metric but also as a real-time control input in adaptive machining systems.

Conclusions

This study presents a comprehensive methodology for the accurate determination of the critical depth of cut in CNC machining operations, combining analytical modeling, experimental validation, and real-time adaptive system identification. The integration of frequency response function (FRF) analysis, stability lobe diagram (SLD) construction, and sensor-based vibration and force measurements enabled a robust and high-fidelity prediction of chatter thresholds across a wide range of spindle speeds and machining conditions. The experimental results confirmed a strong correlation between the predicted and observed onset of regenerative chatter, with deviations reduced to within ±5% following in-process FRF updates. Micro-grooved carbide inserts demonstrated a clear advantage in increasing critical depth margins and suppressing vibration, highlighting the importance of tool geometry in dynamic process stability. Moreover, surface roughness and force signal monitoring effectively captured the transition from stable to unstable cutting, validating the hybrid methodology as both a diagnostic and predictive tool. The use of statistical analysis, including standard deviation and confidence interval evaluation, provided strong evidence of the method's repeatability and reliability. These outcomes support the practical deployment of the proposed framework in intelligent machining systems, where adaptive control of process parameters is essential for optimizing productivity, surface integrity, and tool life.

References

[1] Bouisset S., Do, M. C. Posture, dynamic stability, and voluntary movement. Neurophysiologie Clinique/Clinical Neurophysiology, 2008, 38(6), 345-362.
[2] Teo A., Danielson S., Georgeou T. High Performance Machining: A Practical Approach to High Speed Machining. //Annual Conference & Exposition, 2008, P. 13-665.
[3] Sherov K., Ainabekova S., Kuanov I., Myrzakhmet B., Bekzhanov Y., Gabdyssalik R., Mazdubay A., Kamarov A., Sherov A. Research of temperature distribution in the process of thermo-frictional cutting of titanium alloy TI-5553 //Journal of Applied Engineering Science, 2022, 20(2), P. 400 - 407, DOI: https://doi.org/10.5937/jaes0-32723
[4] Sherov K., Kuanov I., Imanbaev Ye., Mussayev M., Karsakova N., Mardonov B., Makhmudov L. The Investigation and Improvement of the Hardness of the Clad Surface by Thermal Friction Milling Methods //International Journal of Mechanical Engineering and Robotics Research, 2022, Vol. 11, No. 10, P. 784-792. DOI: https://doi.org/10.18178/ijmerr.11.10.784-792
[5] Donenbayev B.S., Filippova T.S., Sherov K.T., Oryntayeva G.J. Calculation of the Economic Efficiency of the Rotary-Friction Boring Method//Material and Mechanical Engineering Technology, 2020, 3(3), P. 4–8
[6] Sherov K., Tussupova S., Sikhimbayev M., Mussayev M., Ainabekova S., Imanbayev Ye., Karsakova,N., Abisheva N. Simulation of the thermal state of the blank surface layer at thermal-friction turn-milling //IOP Conference Series: Materials Science and Engineering, 2021, 1047(1), 012017. DOI: https://doi.org/10.1088/1757-899X/1047/1/012017
[7] Mardonov B.T., Sherov, K.T.,Toirov M.Sh., Makhmudov L.N., Yakhshiev Sh.N., Kongkybayeva A.N., Shezhau K. Features of Engineering Methods of Research Results on Butt Welding on Metal Pipelines //Material and Mechanical Engineering Technology, №1, 2024, P. 3-8. DOI 10.52209/2706-977X_2024_1_3
[8] Wu C., Chen F., Long, X. The self-excited vibration induced by friction of the shaft-hull coupled system with the water-lubricated rubber bearing and its stick-slip phenomenon //Ocean Engineering, 2020, 198, 107002.
[9] Sihimbaev M.R., Sherov K.T., Zharkevich O.M., Alimbaev S.T., Mekhtiev A.D. The development and analysis of the machining attachments for the decrement of oscillations of a boring bar in the process of the refinement of high-accuracy apertures. Journal of Vibroengineering, 2014, 16(2), P. 1022–1032.
[10] Li F., Liu J., Hu B., Jin H. Three-dimensional stability lobe diagram construction in milling process with considering multiple modes //Research scuare, 2023, P. 1 - 15 https://doi.org/10.21203/rs.3.rs-2998903/v1
[11] Astakhov V. P. The assessment of cutting tool wear //International journal of machine tools and manufacture, 2004, 44(6), 637-647.
[12] Toshov J., Sherov K., Baratov B., Mussayev M., Baymirzaev B., Esirkepov A., Ismailov G., Abdugaliyeva G., Burieva J. Ways To Optimize The Kinetic Parameters of Tricone Drill Bits. Material and Mechanical Engineering Technology, 2024, №1, P. 35-45. DOI 10.52209/2706-977X_2024_1_35
[13] Sherov K., Sagitov A., Tusupbekova G., Sherov A., Kokayeva G., Kossatbekova D., Abdugaliyeva G., Karsakova N. Experimental Study of Wear Resistance Improvement of Modular Disk Milling Cutter by Preliminary Pre-Processing Method //Designs 2025, 9, 30. https://doi.org/10.3390/designs9020030
[14] Mussayev M., Sherov K., Kassymbabina D., Abdugaliyeva G., Donenbayev B., Kardassinov S., Karsakova N., Tussupova S. Research of wear and increasing wear resistance of the working part of busbar punching tools by surfacing method //Journal of Applied Engineering Science, 2024, Vol. 22, No. 3, P.654-664. DOI:10.5937/jaes0-51175
[15] Zharkevich O.M., Shlyakhov S.V., Nurzhanova O.A., Imasheva K.I. Development and Research of a New Reinforced Design of the Mounting Block //Material and Mechanical Engineering Technology, №1, 2025, P.28-35. DOI 10.52209/2706-977X_2025_1_28
[16] Lasemi A., Xue D., Gu P. Recent development in CNC machining of freeform surfaces: A state-of-the-art review. Computer-Aided //Design, 2010, 42(7), 641-654.
[17] Kedgley A. E., Birmingham T., Jenkyn T. R. Comparative accuracy of radiostereometric and optical tracking systems //Journal of biomechanics, 2009, 42(9), 1350-1354.
[18] Khidhir G. I., Baban S. A. Efficiency of dissimilar friction welded 1045 medium carbon steel and 316L austenitic stainless steel joints //Journal of Materials Research and Technology, 2019, 8(2), P.1926-1932.
[19] Astakhov V. P. Effects of the cutting feed, depth of cut, and workpiece (bore) diameter on the tool wear rate //The International Journal of Advanced Manufacturing Technology, 2007, 34(7), P.631-640.
[20] Abdallah M., Elkeelany O. A survey on data acquisition systems DAQ //International Conference on Computing, Engineering and Information, 2009, P. 240-243
[21] Dudescu M. C. Post-processing of the experimental data using MATLAB //International Workshop “Advanced Researches in Computational Mechanics and Virtual Engineering, 2006, P. 18-20.
[22] Cooley J. W., Lewis P. A., Welch P. D. The fast Fourier transform and its applications //IEEE Transactions on Education, 2007, 12(1), P.27-34.
[23] Krattiger D., Wu L., Zacharczuk M., Buck M., Kuether R. J., Allen M. S., Brake M. R. Interface reduction for Hurty/Craig-Bampton substructured models: Review and improvements //Mechanical Systems and Signal Processing, 2019, 114, P.579-603.
[24] Park J. B., Jeon Y., Ko, Y. Effects of titanium brush on machined and sand-blasted/acid-etched titanium disc using confocal microscopy and contact profilometry //Clinical Oral Implants Research,2015, 26(2), P.130-136.

Information of the authors

Juraev Musurmon Avlaqulovich, Associate professor Almalyk branch of Tashkent state technical university
E-mail: musurmonjorayev666@gmail.com

Alikulov Djavlon Ergeshevich, Professor of Tashkent state technical university
e-mail: aje8391@mail.ru

Kardassinov Sayat Mamyrbaevich, Associate professor Kazakh Automobile and Road Institute
e-mail: sa-yat@yandex.kz

Tuyboyov Oybek Valijonovich, Head of the Department at Technology Transfer office under the Ministry of Higher Education, Science and Innovation of the Republic of Uzbekistan
e-mail: oybektuyboyov85@gmail.com

DOI 10.52209/2706-977X_2025_4_10 **IRSTI 55.09.81** **UDC 621.762**

Evaluation of Wear of Gas-Flame and Ion-Plasma Sealing Coatings with 0.3% Yttrium under Thermomechanical Loading Conditions

Fasol Y.O[1]., Kubich V.I[1]., Cherneta O.G[2]., Yurov V.M.[3]., Rabatuly M.[4*]
[1]National University Zaporozhye Polytechnic, Zaporozhye, Ukraine
[2]Dnieper State Technical University, Kamenskoye, Ukraine
[3]Vostok LLP, Karaganda, Kazakhstan
[4] Abylkas Saginov Karaganda Technical University, Karaganda, Kazakhstan
*corresponding author

Abstract. The article presents the results of investigation of tribological characteristics of gas-flame and ion-plasma sealing coatings of KNA-82 system with yttrium content of 0.3% used in gas turbine engine assemblies. The tests were carried out in four stages modelling different operating conditions: without heating (22°C), under medium heating (350°C), after the samples were aged at 1100°C and after repeated high-temperature loading. To evaluate the wear resistance of the coatings, linear wear, reduced wear and conditional linear wear were analysed as a function of temperature and pressure in the contact zone. It was found that both types of coatings show a tendency to stabilise the wear process under thermomechanical loading. It was found that at 1100°C the wear of ion-plasma coating is 10% lower than that of gas-flame coating under constant mechanical loading and 34% lower under step loading. A significant difference in the behaviour of the coatings was found: the gas-flame coating shows a hyperbolic decrease in the reduced wear with parallelism of the curves in the range of 350-1100°C, which indicates the stability of the wear mechanism, whereas the ion-plasma coating is characterised by instability of the wear mechanism with pressure and temperature changes.

Keywords: sealing coatings, yttrium, tribotechnical characteristics, wear resistance, thermomechanical loading, KNA-82, gas turbine engines, high-temperature resistance.

Introduction

Sealing coatings are special composite materials applied to stator elements of gas turbine engines to create effective radial seals with rotating parts. These coatings work on the principle of controlled wear - in contact with the rotor blades they work up, forming a minimum radial gap, which reduces leaks of working gas and increases the efficiency of the engine [1].

Increasing the operating temperature of sealing coatings is an important technical task dictated by modern trends in aircraft engine building. Increasing the operating temperatures of gas turbine engines allows to significantly increase their thrust and efficiency. According to research data, increasing the temperature in the combustion chamber by 50°C can increase the engine efficiency by 12.5% [2]. At the same time, to ensure reliable operation of the engine, it is necessary that all its elements, including sealing coatings, retain their functional properties at elevated temperatures.

Traditional nickel-based sealing coatings of the KNA-82 type retain their serviceability up to temperatures of 900-950°C, but modern and advanced engines require materials capable of reliable operation at temperatures of 1100-1200°C [3]. The alloying of coatings with rare-earth metals, in particular yttrium, is one of the effective ways to increase their high-temperature resistance. The presence of these elements in the coating composition promotes the formation of stable protective oxide films, which increase the resistance to gas corrosion and erosion wear [4]. Tribological properties of sealing coatings determine their ability to controlled wear in interaction with rotating turbine blades and are crucial for the efficient operation of gas turbine engines. Research in this area is focused on a comprehensive assessment of the friction coefficient, energy intensity of wear and the character of wear surface formation.

The authors in [5] found that gas-flame coatings of Co-Ni-Cr-Al-Y system with 0.1% yttrium at 20-200°C have 1.9 times higher wear than ion-plasma coatings. However, in the range 350-450°C, gas-flame coatings withstand 1.5 times higher contact pressures with 2 times lower conditional linear wear. At 400-800°C, the wear of gas-flame coatings decreases 2 times slower. At 1100°C the wear properties of both types of coatings become almost identical, although the surface layers of ion-plasma coatings can be destroyed due to structural-phase transformations.

Earlier in [6-8], the feasibility of studying coatings with yttrium content of 0.1; 0.3 and 0.5% was substantiated. The evaluation of wear of gas-flame and ion-plasma coatings with 0.3% yttrium under thermomechanical loading conditions is a logical continuation of these studies.

Test results [6] showed that coatings with 0.3% yttrium have an optimal combination of tribological characteristics. Gas-flame coatings with such yttrium content demonstrate maximum resistance to mechanical fracture - 25-40% higher than other compositions. Under static high-temperature loading (1100°C), the mass gain of gas-flame coatings is 30-35%, which is 2 times higher than that of ion-plasma coatings.

The friction coefficient of gas-flame coating with 0.3% yttrium stabilises at the level of 0.77-0.82, which indicates high structural homogeneity and strength of cohesive bonds. This makes this coating composition promising for application in high-temperature units of GTE.

The aim of the work is to obtain surface wear characteristics of coatings formed by gas-flame and ion-plasma methods with yttrium content of 0.3% in the initial composition and their tribotechnical evaluation depending on the modelled mechanical pressure and temperature.

1. Research methodology

For tribotechnical tests were used coatings of the composition KNA-82 nickel (base), silicon, aluminium and solid lubricants (graphite and boron nitride), which were forged on small-sized samples rings in the gas-flame method, then coating No. 1, and ion-plasma method, then coating No. 2.

The experimental equipment used in [5] was used to simulate the heat and mechanical loading of the investigated coatings. The elements of the test chamber and the investigated coatings, which were preformed on the specimen-rings 2 are shown in Figure 1. The equipment was installed on a test bench for testing generator sets of automotive engines Hiradastechniki GepgyaraU-808 series No. 326 with two modes of controlled change of drive shaft speed.

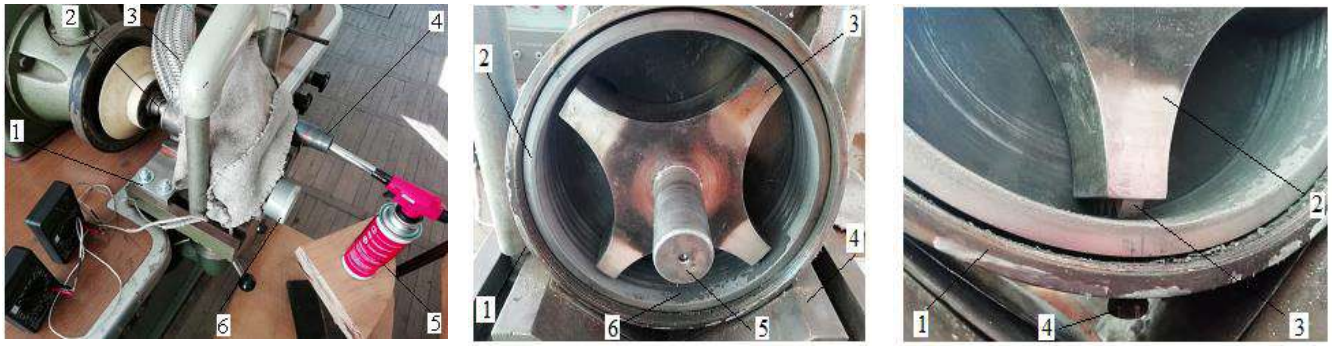

a) b) c)

1 – chamber body; 2 – sample-ring; 3 – rotor; 4 – supporting frame stand; 5 – rotor bearing shaft; 6 – coating wear products; c – rotor wing with a plate: 1 – sample-ring; 2 – rotor wing casing with internal groove; 3 – plate with knife edges; 4 – bottom screw for fixing the sample-ring

Fig. 1 – Generalview (a) ofthetestchamber (b) andcounterbodies (c):

The method of measuring linear wear is shown in Figure 2. In this case, the following characteristics were taken to evaluate the wear:

- linear wear h, which was recalculated into the reduced wear h1000 to the friction path of 1000 m. The necessity of such recalculation was determined by the change of rotor speed 5 (Fig. 1 b) at change of modes of mechanical loading of the coating surface and different time of duration of the tests;
- conditional linear wear hu = h1000/pcr. Average pressure in a friction zone pcp=0,5(pmin+pmax). Necessity of introduction of such parameter was determined by change of specific pressure in a friction zone. The minimum and maximum values of mechanical pressures were determined in accordance with the areas of the end faces of plates 3 (Fig.1 c), which were increased at the end of the experiment: pmax - before the test; pmin - after the test.

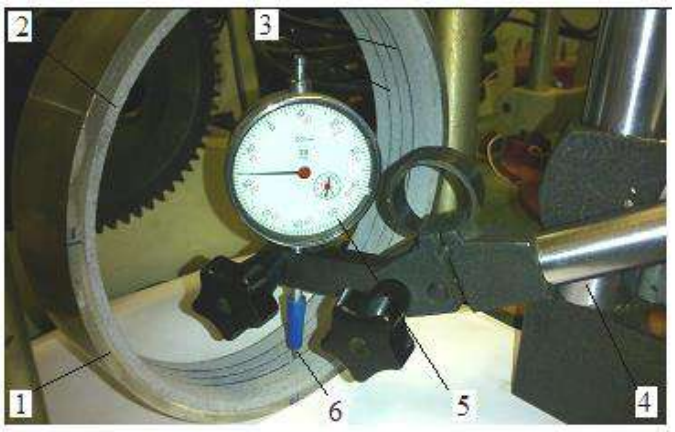

1 - sample-ring body; 2 - coating; 3 - wear tracks; 4 - tripod; 5 - indicator head; 6 –stylus

Fig. 2 - Measurement of linear wear

When modelling the thermal and mechanical loading of the investigated coatings, the possible four stages of their contact interaction with gas turbine blades, unfolded in time and predictably characteristic of their operating conditions, were reproduced separately [6, 7]. At the same time, the mechanical loading was modelled as constant and stepwise with possible levels determined by the contact areas in the friction zone and the pressing force. Based on the technical capabilities of the stand, where the test chamber was mounted, as well as the mass and geometrical parameters of the pressure plates 3 (Fig. 1 c), the modes of force and velocity loading of the friction contact zones were determined.

The following conditions and modes of modelling of heat-mechanical loading of the investigated samples were inherent to the stages.

Stage No. 1: No heating of possible contact interaction zones T=22 ºC, constant mechanical pressure on the surface of coatings: primary minimum - 2,45 MPa for coating No. 1 and 1,7 MPa for coating No. 2 - experience No. 1, secondary maximum - 11,4 MPa for coating No. 1 and 5,5 MPa for coating No. 2 - experience No. 2. The test time is 1 minute. Rotor rotation frequency 300 min-1.

Stage No. 2. Heating up in the chamber and contact interaction of surfaces at a steady temperature T=300-476 ºC. Test No.1 - constant mechanical pressure on the surface of coating No.1 - 3.24 MPa, on coating No.2 - 2.56 MPa. Test time 53 min (of which 48 min of chamber warming up and 5 min at the specified temperature). Rotor rotation frequency 600 min-1. Test No. 2 - step loading with average mechanical pressures on coating No. 1 - 4,61 MPa, on coating No. 2 - 3,1 MPa. Test time 26 min (of which 23 min warming up the chamber and 3 min at the specified temperature). Rotor rotation frequency 600 min-1 and 1200 min-1. The test time at each of the specified frequencies was 1.5 min.

Stage No3. Separate endurance of sample-rings with coatings at temperature T-1100 ºC for 3 hours with the subsequent test at heating of friction contact zones at the established temperature T=372-476 ºC. Test No.1 - constant mechanical pressure on the surface of coating No.1 - 6 MPa, on coating No.2 - 4.22 MPa. Test time 35 min (of them 20 min of chamber warming up and 15 min at the specified temperature). Rotor speed 600 min-1. Test No. 2 - step loading with average mechanical pressures on coating No. 1 - 5.61 MPa, on coating No. 2 - 4.9 MPa. Test time 25 min (of which 22 min warming up the chamber and 3 min at the specified temperature). Rotor rotation frequency is 600 min-1 and 1200 min-1. The test time at each of the specified frequencies was 1.5 minutes.

Stage No4. Heating of friction contact zones of plate scallops with deepened layers of coatings up to a steady temperature T=305-412 ºC and their interaction under stepwise loading with average mechanical pressures for coating No.1 - 6.69 MPa, for coating No.2 - 3.87 MPa. Deepened layers were obtained as a result of mechanical grinding of the surface at the depth of maximum plunge after the third stage of testing. The test time was 40 min (of which 38 min of chamber warm-up and 2 min at the specified temperature). Rotor speeds of 600 min-1 and 1200 min-1. The test time at each of the specified frequencies was 1 minute [9, 10, 11].

2. Results and discussion

Processing of data on wear of surfaces of coating materials allowed to obtain the following results, Table 1.

According to the data given in Table 1 for stages №1-№3 graphs are constructed, Fig.2. These graphical dependences display the predicted regularities of wear variation of coatings depending on pressure and temperature of the interaction medium [12].

In accordance with the data shown in Fig.2 c the following should be noted.

For both coatings with increasing pressure at Tcr=22 ºC is characterised by a decrease in the reduced wear, which may indicate the tendency of the structures to elastoplastic deformation, which leads to pressurisation of the layers and an increase in their resistance to fracture.

Table 1. Summary data on wear characteristics of coatings

Coatingnumber	Condition, regime (experience)	Option	Temperatureofinteraction			
			Stage №1 22 °C	Stage №2 350 °C	Stage №3 1100 °C	Stage №4 1100 °C
№1	1	h_{1000}, μm	73±20	33±7,3	10,4±3,4	40,3±16
		h_y, μm ·MPa^{-1}	29,8	10,2	1,73	6,02
	2	h_{1000}, μm	123±33	41±13*	20,2±5,3*	-
		h_y, μm ·MPa^{-1}	10,8	8,9*	3,6*	-
№2	1	h_{1000}, μm	54±20	37±5,3	9,3±2,45	44,3±16
		h_y, μm ·MPa^{-1}	32,1	14,45	2,2	11,4
	2	h_{1000}, μm	107±26	35±14*	13,3±3,6*	-
		h_y, μm ·MPa^{-1}	19,45	11,3*	2,7*	-

*Note. * - steploading.*

The character of change in the reduced wear shown in Fig. 2 a, b indicates the unequal nature of its reduction with heating (stages #1-#3) for both coatings.

Thus, for coating No.1 a hyperbolic reduction of the reduced wear was determined by two curves, the parallelism of their sections is preserved in the temperature range from 350 ºC to 1100 ºC. This may indicate the reproducibility (repeatability) of the dynamics of deformation of the structures of coating No.1 with increasing pressure and temperature.

I.e. it is possible to speak about constancy of wear mechanism manifestation without changing the parameter (s) of its estimation. For example, such a parameter can be the strength of cohesive bonds between the components of coating No. 1.

For coating No.2, both hyperbolic reduction of the reduced wear, which appears at high initial pressures p=5.5MPa in the friction zone, and angular linear reduction, which appears at lower initial pressures p=1.7MPa in the friction zone, are determined, Fig.2 b. In this case it is inappropriate to speak about parallelism of plots in the temperature range from 350 ºC to 1100 ºC. This may indicate the non-reproducibility (non-repeatability) of the dynamics of deformation of the structures of coating No.1 with increasing pressure and temperature. I.e. it is possible to speak about inconstancy of wear mechanism manifestation - there is a change of parameter (s) of its estimation. For example, such a parameter can be the strength of cohesive bonds between the components of coating No.1.

Heating of coatings up to Tcp=350 ºC causes reduction of their conditional linear wear, Fig. 2 c. At the same time, the modelled pressure in the friction zone, which changes due to the wear of the plate scallop ends, does not cause a sharp change in the wear tendencies of the coatings at this stage. Decrease of conditional wear of coatings occurs both at insignificant increase of pressures (coating No. 1 - line 3, coating No. 2 - line 1) and at their decrease (coating No. 1 - line 4, coating No. 2 - line 2). This indicates that both coatings adapt to tangential loading in the frictional interaction zone in different ways during the warm-up phase to an average temperature of 350 ºC. Coating No.2 at lower pressures is more prone to propagation of destructive stress fields per unit contact area of 1 mm^2, which do not match the strengths of cohesive bonds between its components in the material. The stresses arising in the surface layers of coating No.2 are greater than the strength of cohesive bonds, which causes its greater wear both at Tcr=22 ºC and at Tcr=350 ºC.

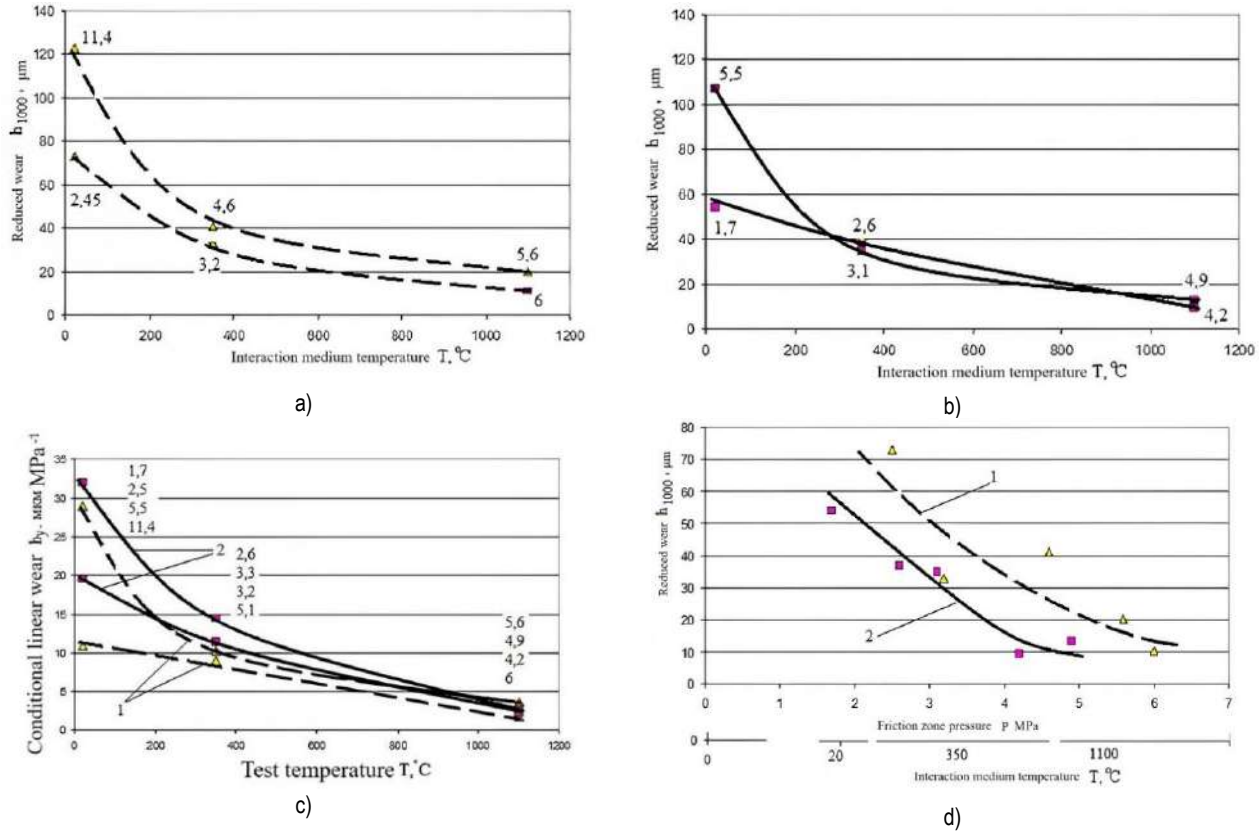

a - reduced linear wear of coating No.1; b - reduced linear wear of coating No.2; c - distribution of conditional linear wear;
1 - coating No.1; 2 - coating No.2; d - reduced wear at pressure in the friction zone. NumbersnearthepointsdenotepressureinMPa

Fig 2. - Dependence of coating wear types on the interaction temperature

Heating at constant load (stages No.1, No.2) predetermines a big difference in conditional wear of coatings. If at Tcr=22 ºC coating No.1 had a conditional wear of 1.1 times less than coating No.2, then at Tcr=350 ºC coating No.1 already had a wear of 1.42 times less than coating No.2. That is, the difference increased by 1.27 times, or by 27% [11].

However, during step loading and holding at Tcr=350 ºC (step #2) the opposite occurs. Conditional wear of coating No.1 decreases by 1.3 times. This may indicate the formation of some safety margin in the layers of coatings by cohesive bonds between their components, within which the stresses caused by tangential deformation loading are balanced. If to estimate the indicated safety margin, then at step loading and holding at Tcr=350 ºC (stage No.2) it is 1.27 for coating No.1 and 1.37 for coating No.2. Thisisevidencedbytheratiosofconditionalwear, whichareforcoating No.1 - 10.2/8, forcoating No.2 - 14.45/10.5.

The data shown in Fig.2 c for stage No3 indicates the following. Firstly, exposure of both coatings at 1100 ºC predetermines the range of conditional linear wear variation from 1.73 to 3.6 μm-MPa^{-1}, which occurs at the pressure range

from 4.2 to 6 MPa. Secondly, in comparison with stage No.2, the range of variation of conditional linear wear for both coatings is wider and ranges from 8.9 to 11.3 μm-MPa-1 and takes place at lower pressures - from 2.6 MPa to 5.1 MPa. This once again confirms the significance of the influence of long-term high-temperature exposure on the structural-phase transformations occurring in the layers of coatings, which determine the adaptability of frictional interaction zones to mechanical loading with large average pressures [13].

The data shown in Fig. 2 d for stages №1-№3 indicate the following.

Firstly, the rate of reduction of the reduced wear in both coatings in the range of pressure increase from 2 MPa to 4 MPa is practically the same, and makes 18 μm-MPa-1, which indicates the equality of the rates of destruction (change) of cohesive bonds between components in coatings No.1 and No.2. However, their quantity is different. In coating No.1 they are more due to the separation of fragments in the form of wear particles. In coating No.2 there was a smaller number of wear particles due to subsidence of structures, which predetermined an increase in the strength of cohesive bonds between components in its near-surface layers.

Secondly, there are no pressure ranges within which steady wear of the coatings takes place, except for the emerging preconditions for coating No. 2 at pressures from 4.5 MPa and presumably higher. For coating No.1 such preconditions can be observed starting from a pressure of 6 MPa. However, due to the lack of experimental data on wear at higher pressures for coatings No. 1 and No. 2, taking into account the structural-phase transformations manifested after exposure at 1100 ºC, it is premature to testify about reaching the steady wear.

The evaluation of wear (Table 1) at stage No.4 indicates the following.

The reduced wear of coating No.1 in comparison with stage No.3 increased by 3.9 times, for coating No.2 - by 4.8 times. The conditional wear of pavement No.1 compared to stage No.3 increased by a factor of 3.5, for pavement No.2 - by a factor of 5.2. These data show a significant decrease in the resistance of surface layers of both coatings to failure under the action of step loads. This indicates that long-term high-temperature exposure does not provide the same flow of structural-phase transformations in the layers of both coatings in depth [14].

Conclusions

As a result of the conducted researches the tendencies of change of wear characteristics of coatings, caused by unequal manifestation of their physical and mechanical properties, heterogeneously distributed on their body, have been determined. Thus both coatings are inclined to stabilisation of process of wear at adaptability to thermomechanical loading that is indicated by the identical character of display of the received regularities of change of characteristics of wear.

It is determined that taking into account the average statistical variability of the investigated wear characteristics, which is 15-20% at the temperature of 1100 ºC, which is the average statistical operating temperature of the power compartment of the gas turbine unit, there is a tendency to decrease the wear of coating No.2. Reduction of wear of coating No.2, in comparison with coating No.1 makes ≈10% at constant mechanical loading, and ≈34% at modelling of step loading.

Furthermore, the study demonstrates that the differing structural responses of gas-flame and ion-plasma coatings to combined thermal and mechanical loads have practical implications for their application in gas turbine engines. While both coatings exhibit a tendency toward wear stabilization, the ion-plasma coating shows superior adaptability under stepwise loading conditions, which are typical in operational cycles of gas turbines. This suggests that for components exposed to variable mechanical pressures and high temperatures, ion-plasma coatings with 0.3% yttrium can provide enhanced durability and prolonged service life, reducing maintenance requirements and improving the overall reliability of the engine assemblies.

References

[1] Zhang B., Li J., Li W., Ji H. Influence of Geometric Tooth Shape Parameters of Labyrinth Seals on theFlow Law and the Algorithm for Designing Straight Grate Teeth //Russian Physics Journal, 2021, 64(6), P. 1122–1129. DOI: 10.1007/s11182-021-02432-0.

[2] Enache M., Carlanescu R., Mangra A., Florean F., Kuncser R. Investigation of Flow through a Labyrinth Seal //*Incas Bulletin*, 2021, 13(2), 51–58. DOI: 10.13111/2066-8201.2021.13.2.6

[3] Ullah A., Khan A., Bao Z.B., Yang, Y.F., Xu M.M., Zhu S.L., Wang F.H. Temperature Effect on Early Oxidation Behavior of NiCoCrAlY Coatings: Microstructure and Phase Transformation //Acta MetallurgicaSinica(English Letters), 2021, 35(6). DOI: 10.1007/s40195-021-01310-5.

[4] Jojith R., Sam M., Radhika N. Recent advances in tribological behavior of functionally gradedcomposites: A review. Engineering Science and Technology // International Journal, 2021, 25(5) DOI:10.1016/j.jestch.2021.05.003.

[5] Kubich V., Pavlenko D., Fasol Y., Syvachuk O. Comparison of High-Temperature Wear Resistance of Gas-Flame and Ion-Plasma Sealing Coatings with 0.1% Yttrium //Tribology in Industry, 2024, Vol. 46, No. 3, P. 486-498.DOI:10.24874/ti.1587.11.23.03

[6] Kubich V., Fasol Y. Defining tests of heat-resistant yttrium-containing sealing coatings for high-temperature gas-erosion resistance //Problems of Friction and Wear, 2023, №3 (100), P. 40-48. DOI: 10.18372/0370-2197.3(100).17893

[7] Kubich V., Fasol Ye, Cherneta O., Yershina A.K, Sakipov N.Z Resistance of heat-resistant yttrium-containing sealing coatings to mechanical fracture when forming cutting paths //Eurasian Physical Technical Journal, 2024, Vol. 21, No. 3(49), P. 81–92. https://doi.org/10.31489/2024no3/81-92

[8] Kubich V., Fasol E., Cherneta O. Influence of high-temperature loading conditions on the change in the physical state of yttrium-containing coatings //Problems of Friction and Wear, 2024, № 1(102). P. 14-22. https://doi.org/10.18372/0370-2197.1(102).18398.

[9] Boguslaev V. O., Greshta V. L., Tkach D. V., Kubich V. I., Sotnikov E. G., Lekhovitsera Z. V., Klymov O. V. Evaluation of the Tribotechnical Characteristics of Therma-Barrier Sealing Coatings under Critical Loads //Journal of Friction and Wear, 2019, Vol. 40, No. 1, P. 80–87.

[10] Boguslaiev V.O., Greshta V.L., Kubich V.I., Fasol Ye.O., Lekhovitser V.O.Effect of alloying heat-resistant packing coatings on their tribotechnical, physical and mechanical properties //Naukovyi Visnyk Natsionalnoho Hirnychoho Universytetu, 2020, (6), P. 41–47
[11] Fakhrullin R. F., Tursunbayeva A., Portnov V. S., L'vov Yu. M. Ceramic Nanotubes for Polymer Composites with Stable Anticorrosion Properties //Crystallography Reports, 2014 (7), Vol. 59, 1107–1113. DOI: https://doi.org/10.1134/S1063774514070104
[12] Zhetessova G., Zharkevich O., Pleshakova, Ye., Yurchenko V., Platonova Ye., Buzauova T. Building mathematical model for gas-thermal process of coating evaporation //Metalurgija 55(1), 2016, P. 63-66
[13] Zhetesova G.S., Dandybaev E.S., Zhunuspekov D.S., Zhekibaeva K.K. Improvement of the Organization of Maintenance And Repair of Dump-Cars //Material and Mechanical Engineering Technology, 2020, 1, P. 33–38
[14] Zhetessova G., Nikonova T., Gierz Ł., Berg A., Yurchenko V., Zharkevich O., Alexey K. A. Comparative Analysis of the Dynamic Strength Properties of the Long Guides of Intelligent Machines for a New Method of the Thermal Spraying of Polymer Concrete //Appl. Sci., 2022, 12, 10376.

Information of the authors

Fasol Yelyzaveta Oleksandrivna, senior lecturer at the department of physical materials science national university «Zaporizhzhia Polytechnic»
e-mail: selvluna@gmail.com

Kubich Vadim Ivanovich, PhD, associate professor, associate professor of the department of automobiles, heat engines and hybrid power plants national university «Zaporizhzhia Polytechnic»
e-mail: schmirung@gmail.com

Cherneta Oleg Georgievich, PhD, associate professor, associate professor of the department of automobiles and automotive industry Dniprovsky State Technical University
e-mail: OCherneta@gmail.com

Yurov Viktor Mikhailovich, candidate of physical and mathematical sciences, associate professor, leading construction manager of LLP "Vostok"
e-mail: exciton@list.ru

Rabatuly Mukhammedrakhym, PhD, acting associate professor, acting associate professor of the department of development of mineral deposits, Abylkas Saginov Karaganda Technical University
e-mail: mukhammedrakhym@gmail.com

DOI 10.52209/2706-977X_2025_4_16 **IRSTI 55.57.33** **UDC 631.3**

Methods for Identifying the Mechanical Properties of Wheat Grain in the Context of Normal Impact

Marcinkiewicz J.*
Poznan University of Technology, Faculty of Civil and Transport Engineering, Poland
*corresponding author

Abstract. This article has a review-empirical character. The first part synthesizes methods for identifying the mechanical properties of seeds used in bench tests, with particular emphasis on measuring the force–time course, contact time, and the coefficient of restitution under impact conditions. The limitations of non-standardized procedures and apparatus requirements-stemming from very short contact times and the diverse morphology of grain are discussed. The second part presents original experiments on a gravitational test bench for free fall of grain onto a piezoelectric force sensor, together with simultaneous velocity recording using a high-speed camera. Normal impacts of winter wheat (cv. Memory) with a flat metal surface were analyzed for 400 grains at four moisture levels (7–16%) and varied impact velocities. We observed an increase in peak force with impact speed, a non-linear decrease in the coefficient of restitution with increasing speed and moisture, and a lengthening of contact time with moisture. The compiled data serve as a reference for calibrating contact models, including discrete element method models, and as a basis for selecting loading ranges in the design of machine working elements; the methodology, , which combines review and experimental verification, helps reduce the number of costly full scale trials.

Key words: coefficient of restitution (CoR); force–time relationship; dynamic impact forces; agricultural machinery; winter wheat grains

Introduction

Modernizing existing machines [1] and designing new solutions in agricultural mechanization require reliable data on mechanical interactions in the system comprising the machine and the processed material. In the classical approach, a complete picture is obtained only at the stage of costly full scale prototype tests, which slows design iterations and increases the risk of incorrect design decisions [2, 3]. This problem is particularly evident in machines intended for the transport and dosing of plant derived granular materials, from sowing through harvesting and threshing to storage, packaging, and processing, where cereal grains are among the key working media.

The motion of a single kernel in seeder mechanisms and in conveying ducts involves numerous short duration impacts with elements of complex geometry. Accurately capturing these interactions in field studies or even in traditional laboratory experiments is difficult because contact times are very short, the response is sensitive to grain orientation, and the material is variable in shape, size, and moisture content.

For seed material, correct identification of static and dynamic loads is crucial, because excessive values can lead to internal and external damage that reduces germination and growth. The aim of this paper is to review research methods that enable the identification of the mechanical properties of grain under impact conditions, serving as a prelude to the development of a test stand and the planning of detailed, accurate experiments. The resulting synthesis is intended to support both the design and optimization of engineering solutions and the calibration of numerical models, such as the discrete element method, which in turn reduces the number of costly full scale tests and shortens the machine development cycle.

1. Wheat grain

From a nutritional standpoint, wheat holds a leading position among cereals, so understanding the properties of its kernels is of particular importance. Cereal grains, as plant material, have a complex morphological and anatomical structure that directly determines their physico mechanical properties. These are influenced by size, shape, chemical composition, moisture content, gluten and protein content, vitreousness, and density, which affect the condition of the endosperm [4 - 7]. Geometrically, the grain is highly variable: length about 5 to 10 mm, mass 30 to 50 mg, an elongated shape that is laterally flattened; the cross section ranges from evenly rounded to triangular, with variability both between cultivars and within a single ear [4]. Common features include a ventral groove reaching halfway into the cross section, an embryo surrounded by a scar at the boundary of the ventral and dorsal sides, and a brush at the apex [7]. Externally, the grain is protected by a fruit seed coat composed of several layers, including an aleurone layer; waxy compounds present in the coat limit water permeability and facilitate long term storage [8, 9]. The endosperm, which constitutes about 80 percent of the mass, is made up of protein starch cells, and its cohesiveness translates into grain strength [8].

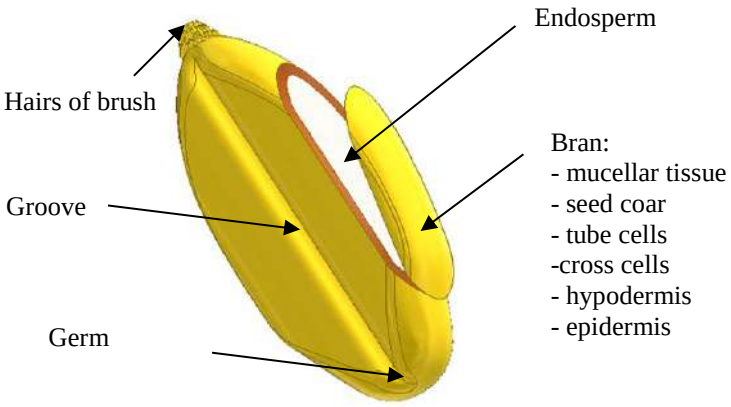

Fig. 1. - Diagram of a whole wheat [10]

Such morphology, and its variability in dimensions, shape, the layered seed coat, and endosperm traits, directly affect the course of collisions with working elements and the contact parameters. Therefore, as a direct consequence of the foregoing, bench studies with controlled geometry and measurement of short duration phenomena are necessary to reliably determine contact model parameters and to account for the material's morphological diversity.

2. Contact problem for cereal grain

Modeling contact forces in collisions poses a substantial cognitive challenge, because the system response is governed by complex processes of energy transfer and dissipation, which makes rigorous mathematical analysis difficult. Constructing dynamic contact models therefore requires extensive theoretical considerations, and the resulting hypotheses must each time be verified experimentally using appropriately chosen measurement setups. The collision of a cereal grain is a short lived and violent phenomenon: on a very small time scale there is an exchange of momentum, intense energy dissipation, and large changes in velocity and contact forces [11]

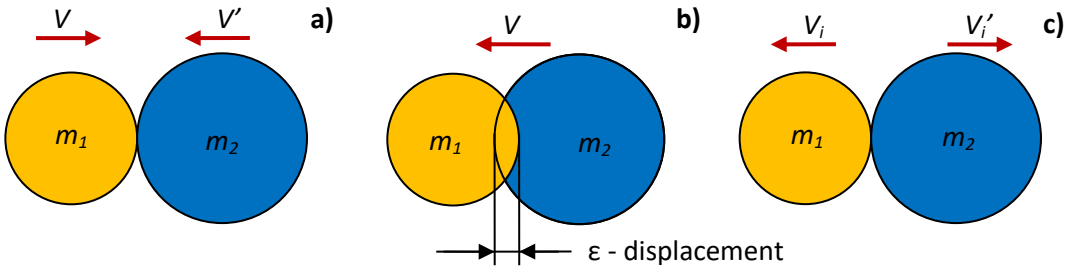

a) the initiation of contact, b) the movement of objects relative to each other until it ceases, c) the termination of contact [12]

Fig. 2. - Phases of contact

It should be described as a continuous process with a finite duration, in which local deformations occur in the contact zone with elastic, plastic, or elasto plastic character, energy is dissipated including in friction and micro slip, and vibrations and stress waves propagate throughout the system [13 - 17]The contact can be divided into two phases. In the loading compression phase, which begins at the moment of first contact, equal and opposite compressive forces act on both sides of the contact point and oppose the relative motion of the bodies [18]. This phase continues until the relative velocity at the contact point reaches zero; for two bodies of masses m and m′ and velocities just before impact V and V′, the common velocity of the system at the end of compression is:

$$V_w = \frac{mV + m'V'}{m + m'}$$

If the material is fully elastic, the unloading restitution phase follows compression immediately and ends at the moment the bodies separate [19]. This description applies both to the collision of two comparable masses in motion and to an impact against a surface treated as rigid [20]. In the second phase the deformed bodies tend to recover their original shape and the contact forces decrease; however, the separation of the bodies does not have to mean a full return to the initial state, because depending on the material properties permanent deformations and delayed restitution are possible,

occurring partly after contact has ceased. For an ideally elastic system without energy losses, the kinematic and dynamic relations follow directly from the conservation of momentum:

$$mV_0 + m'V_o' = mV_i + m'V_i'$$

where V_0, V_0' are the velocities before the collision;

V_i, V_i' are the velocities after the collision.

An illustration of material differences is the comparison of force as a function of time for a normal impact: an elastic impact yields an approximately symmetric trace (compression and rebound times are similar, with a shorter contact time), whereas elasto plastic and plastic impacts show pronounced asymmetry, a longer compression phase, and a greater overall contact time; the share of energy dissipation increases and the ability to "bounce" decreases [21]. This qualitative picture underpins the choice of a contact model and the estimation of its parameters (for example, stiffness, damping, and plasticity thresholds), whose values require bench tests with synchronized force time records and kinematic characteristics to enable their determination and verification.

3. Methods for identifying the mechanical properties of seeds

The mechanical properties of plant based materials are understood as their response to applied external loads, resulting from elastic, plastic, and viscous behavior. Reliable identification of these properties requires precise laboratory tests that determine material constants and the curves describing the relationship between load and deformation [22, 23]. At present there are no general international guidelines that would unambiguously standardize measurements of the basic physical properties of seeds. In practice, many procedures derive from classical strength of materials, which, given the complex structure of biological samples, is not always fully adequate in terminology or methodology [8].

The complexity of cereal grain structure, evident in irregular shapes and sizes, variable water content, and a multilayered anatomical structure, makes an unambiguous assessment of strength characteristics difficult. For this reason, many studies have been conducted on seeds with geometry closer to a sphere, for example pea [24], lentil, soybean, rapeseed [25], and bean [26]. In research on granular materials two principal approaches are adopted, depending on how the medium is treated. The first is based on tests performed on a bulk granular mass [27], and the second on tests of single seeds [28]. These approaches should be regarded as distinct and complementary, because they provide independent mechanical characteristics that are not directly convertible into one another.

The choice of approach depends on the aim of the work. It may be the organization of knowledge and identification of features for a systematic treatment, the preparation of data for engineering calculations, or, increasingly, the calibration and validation of simulation models [8]. The outcome of such studies is sets of material constants and curves that describe the relationship between excitation and deformation. These data form the basis for identifying and parameterizing effective mechanical characteristics in constitutive models of an empirical or theoretical nature, which is crucial for further analyses of contact and impacts of seeds with working elements [8].

3.1. Studies on single grains

Previous work on identifying the parameters that describe the strength and mechanical characteristics of granular masses captures material behavior well during storage and transport, but attempts to transfer those generalized characteristics to the behavior of a single kernel have shown no simple correspondence [8]. Hence the need for detailed identification of mechanical properties at the level of an individual seed. The literature recognizes two main paths: indirect methods and direct methods [29].

In the indirect approach, strength is inferred from the grain's response to an excitation applied in a technological process or under laboratory conditions. The excitation may take the form of a precisely defined parameter or be the effect of a process such as threshing, transport, drying, cleaning, or sorting [30]. The influence of loading is evaluated after the sample is unloaded and often relies on inspection of the surface for macroscopic structural damage, for example dents, cracks, or breaches of the coat. Although quick, this diagnosis is subjective, has limited repeatability, and does not provide information on the internal state [8]. For this reason laboratories readily use complementary techniques. A colorimetric method can reveal coat damage and deeper fissures: the sample is immersed in a dye that penetrates defects, then the dye is washed out and the extinction of the resulting solution is measured, which correlates with the level of damage [29]. When assessment of internal structure is required, X ray methods are used. The test is non destructive, so the same sample can then undergo biological tests. An integrative indicator of the effect of loading on the vital functions of seeds is biological resistance, understood as the ability to maintain viability and vigor for germination and growth [31 - 35].

Indirect methods, however, do not provide the unambiguous and complete characteristics needed to build constitutive models that reproduce contact in numerical analyses, for example in the DEM environment. Much higher precision of identification is obtained with direct methods, in which a single grain is subjected to strictly defined excitations and its response is recorded. Two loading regimes are distinguished: quasi static and dynamic. In quasi static tests, compression, tension, and creep are most common. The dominant solution is to measure the relationship between displacement and load, from which a stress strain curve is determined. This type of test corresponds well to the frequent technological situations involved in processing and storage of the material [8].

Studies under dynamic loading conditions are described much less often, even though they are closest to real impacts in seeder mechanisms and conveying systems. The limited number of reports results from the very short durations involved and the small sizes and irregular shapes of the objects, which impose high requirements on apparatus and

measurement procedures. In practice, nonstandard test stands are used. In one approach a moving grain strikes a fixed obstacle, and in the other a hammer strikes a fixed grain. Both variants make it possible to determine key contact quantities, provided that impact speed, contact time, and the force history are controlled precisely so that the results can be used to identify the parameters of models describing collisions of single seeds.

3.2. Dynamic loads

Issues concerning the behavior and mechanical properties of cereal grains under dynamic loading are addressed relatively rarely. This is primarily due to the small size of the grains and to measurement difficulties, because the processes change rapidly and require specialized, costly recording equipment. As in quasi static tests, no uniform method for assessing mechanical properties has yet been developed for dynamic loads. Consequently, the available publications present results obtained under diverse experimental conditions, differing in sample preparation, grain orientation, interaction velocities, and the design of the test stands.

The earliest studies focused on indirect methods, in which the influence of excitation was evaluated through the subsequent biological usefulness of the seeds [36 - 40]. The scope of research was sometimes extended to include cyclic loading, carrying out fatigue like tests. In practice, simple impact rigs were used, which, following Mohsenin's proposal, are divided into two basic types: freely seated grain and supported grain (Fig. 3) [41]. This division organizes descriptions of the test stands and facilitates comparisons of results obtained in different dynamic configurations.

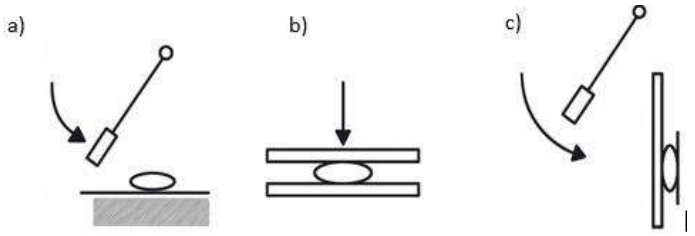

a) unsupported; b, c) supported [41]

Fig. 3. - Placement of the grain during dynamic tests

In the supported configuration, hammer type test stands are used to apply excitations at velocities on the order of 1 to 3 m s^{-1} [41]. Structurally, the sample is stably seated on an anvil plate, and the excitation is generated by a pendulum or, in more advanced solutions, a push rod crank mechanism with an electric drive, as in Frączek's stand [42]. For multiple impacts, which better reflect processing conditions, the sample must be immobilized between a backing plate and a pressure plate to ensure repeatable orientation in successive cycles [41]. In such setups the hammer acts on the grain via the pressure plate, and both force and kinematics can be recorded with sensors integrated into the head (the operating scheme is shown in Fig. 4).

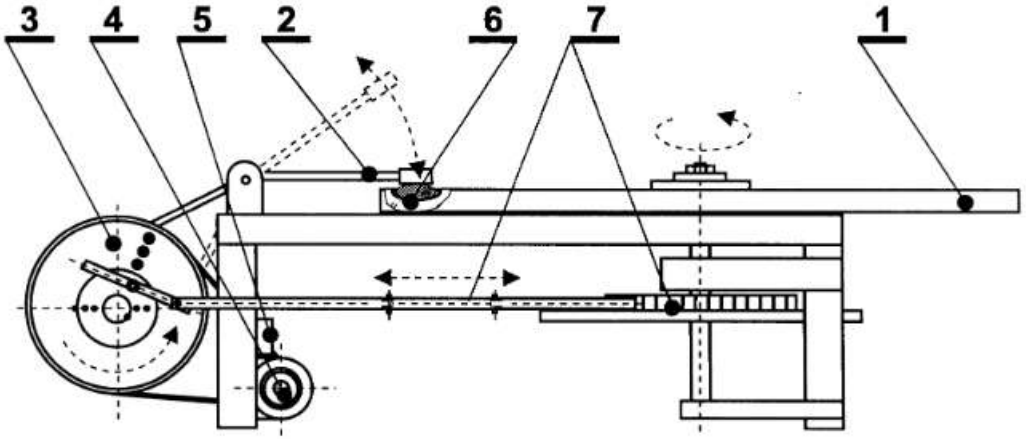

1 - rotating disc, 2 - hammer arm, 3 - crank lever mechanism, 4 - motor, 5 - drive belt, 6 - grain, 7 - rotary ratchet mechanism [42]

Fig. 4. - Test stand with one sided support

To reproduce higher energy phenomena characteristic of threshing or cleaning units, rotating hammer rigs are used. In Bilanski's design [33], employed among others by Niewczas [43], the exciter is a short rotating arm ending with a hammer, and the test grain is introduced into the path by a launcher synchronized with the rotation. In simpler variants, a lifting table serves this function. Such stands make it possible to achieve impact velocities from 3 to 40 m s^{-1} [41] and to assess the threshold energy of damage; for wheat, complete structural breakup has been shown above about 25 m s^{-1} [43]. Bilanski [33] observed increased resistance to impact damage with increasing moisture and a dependence on grain orientation relative to the loading direction.

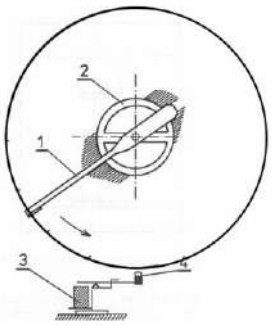

1 - hammer, 2 - drive, 3 - grain launcher, 4 - grain [43]

Fig. 5. - Rotor test stand

An important area of research is the direct identification of the force history during impact. Kustermann [44] developed a test rig with a hammer driven electrically by a push rod crank assembly (Fig. 6), in which the striking head was equipped with a piezoelectric force sensor. The setup enabled impact velocities in the range of 0.1 to 20 m s^{-1} and simultaneous measurement of the motion of both the hammer and the grain, which made it possible to obtain full F(t) records for maize kernels.

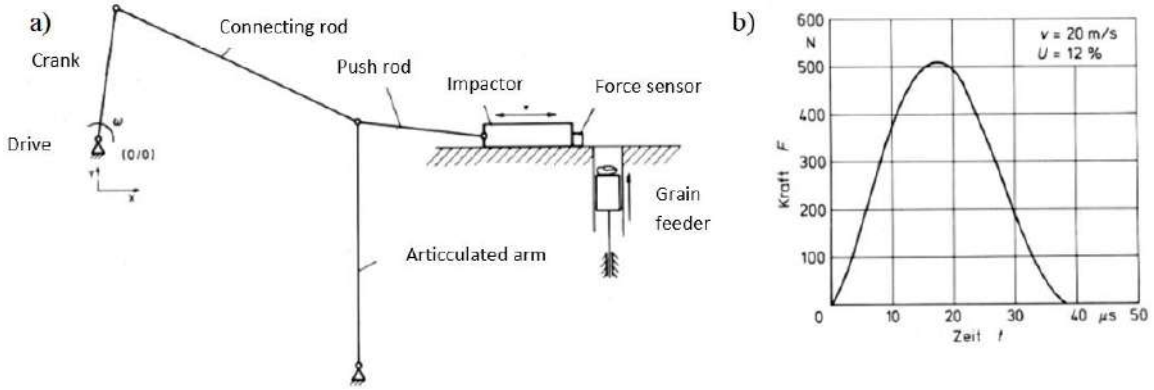

(a) schematic of the test rig, (b) example force measurement at an impact velocity of 20 ms^{-1}

Fig. 6. - Kustermann's studies [44]

In Poland, Kęska's spring arm launcher (Fig. 7) [45] enabled studies on maize, pea, lupine, vetch, and wheat with a maximum speed of about 10 m s^{-1}. Force was recorded with a PCB piezoelectric sensor with a natural frequency of 70 kHz, and pre and post impact velocities were measured with photoelectric sensors [46]. This made it possible to determine regression relations for F_max and for contact time as functions of speed and moisture, as well as to record typical force histories.

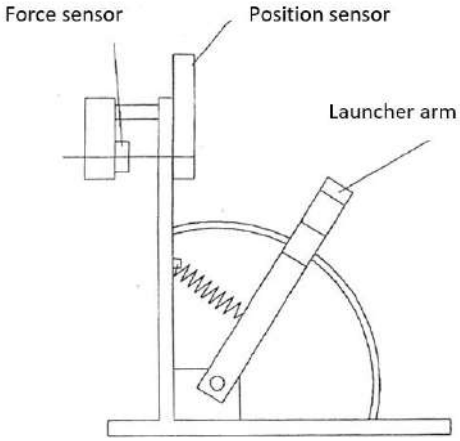

Fig. 7. - Schematic of the test stand [45]

Among the many research efforts, Kęska drew attention to issues related to the proper selection of measuring apparatus. In a 2021 article [46], he pointed out the risk of difficulties in interpreting signals recorded from a piezoelectric force sensor during dynamic measurements of hard, low moisture grains. Based on results showing the impact force

impulse, the author noted the form of the trace, in which, in addition to the main reading indicating the maximum force reached, numerous subsequent decaying oscillations can be observed. A characteristic feature of the phenomenon is that the oscillations occur after the grain has rebounded and, despite the lack of contact between the grain and the sensor surface, they persist for a longer time. According to the author's findings, these oscillations resulted from the sensor's own vibrations excited by a sufficiently short force impulse, which he demonstrated by performing numerous simulations for various contact stiffness parameters for the grain sensor interface. As a result, there is a risk of a significant difference between the sensor's measurement signal and the true contact force history (Fig. 8). Thus, the author indicated that to obtain reliable measurements of the impact force history, one should use impact force sensors of special design with a high resonance frequency [46].

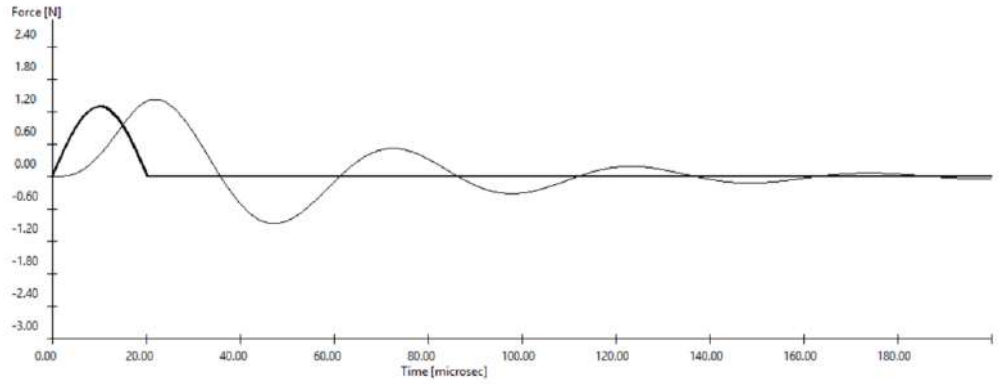

Fig. 8. - Impact force history (thick line) and sensor measurement signal (thin line) for a small dry grain. Contact stiffness k2=1e5 N/m, frez=20 kHz [46]

The most commonly used solution today for identifying the force history during collisions of cereal grains is the free fall method. This approach to studying dynamic phenomena has been presented for years by numerous researchers, largely because the measurement method offers a major advantage in the simplicity of the test stand's construction. The method gained popularity in studies of traditional engineering materials [47 - 50], and was later adapted for testing plant derived materials [51 - 56].

One of the most recent grain studies in Poland using a gravitational test stand was carried out on rapeseed at the Institute of Agrophysics in Lublin. The stand shown in the figure consisted of a simple support column on which a pneumatic gripper was mounted to release the seed sample onto the surface of a piezoelectric sensor. The setup allowed adjustment of the nozzle height from 1 to 100 mm, yielding a maximum impact velocity of 2 m s^{-1}. For velocity measurement, the system was equipped with high speed cameras. The experiments made it possible to analyze in detail the impact force history and to characterize its dependence on the velocity at the moment of contact, determining the coefficient of restitution. Example results from these tests are illustrated in Fig. 9.

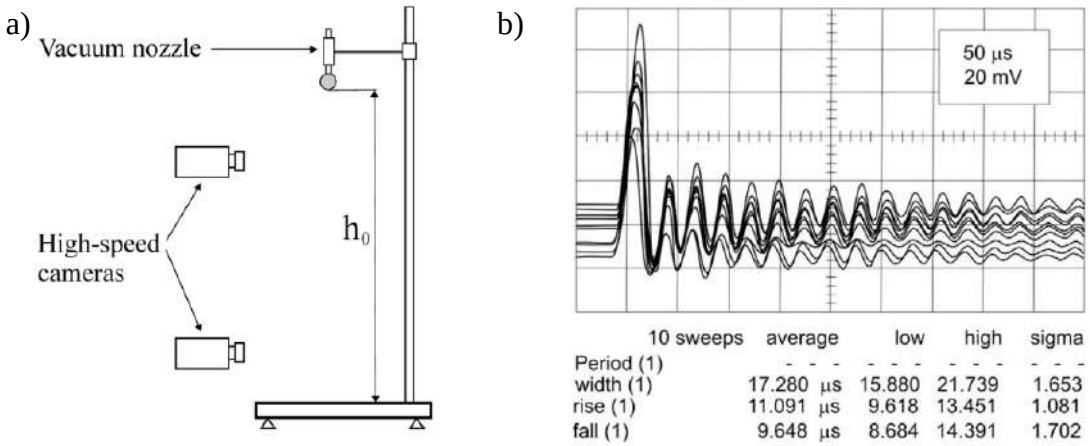

a) test stand, b) example impact force history for a rapeseed grain [51]

Fig. 9. - Measurements using the free fall method

Recording only the force history over time does not provide all the information needed to characterize the physico mechanical processes occurring in the tested object during its impact with an obstacle. For this reason, years of research aimed at a more comprehensive understanding of phenomena in plant derived materials under dynamic excitation led to the development of more complex measuring apparatus capable of recording, simultaneously, both the applied excitation and

the sample's response in the form of deformation. Work in this area was initiated, among others, by Jindal and Mohsenin, who defined an experimental technique for testing the dynamic strength of food materials. They designed a new test stand, drawing on experience with hammer type impact rigs in the form of pendulum impact testers. They justified this choice by, among other things, the greater precision in controlling the imposed excitation parameters compared with a freely falling grain or a falling mass, as well as by the higher precision in determining the point of contact and the ability to use very low impact energy levels [12].

The core of the pendulum impactor developed by the researchers was an arm with a counterweight mounted on a bearing supported axis (Fig. 10). For measuring the position of the pendulum arm, the setup was equipped with angular displacement sensors. The forcing force was identified indirectly by measuring impact deceleration with a piezoelectric accelerometer mounted at the height of the striking head. The adopted design solutions provided a maximum excitation speed of 1 m s^{-1}. Using the newly developed device, the researchers carried out some of the first comprehensive dynamic measurements of the properties of maize kernels by identifying their dynamic hardness. The results showed a slight effect of strain rate on the determined dynamic hardness, but a significant effect of grain moisture content [51].

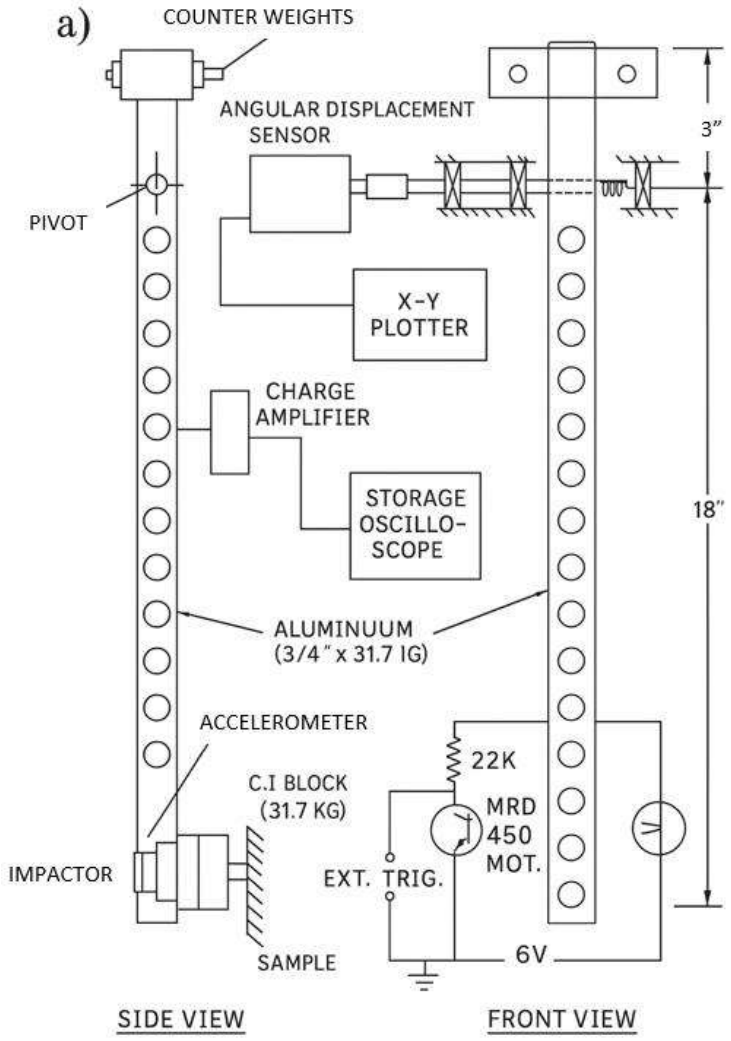

Fig. 10. - Jindal and Mohsenin test stand

Over the years, the above approach has been modified. As a result of work by a few researchers, alternative solutions have appeared to increase measurement precision. Some of the most recent studies on the influence of dynamic excitation on selected cereal grains were carried out at the University of Krakow. The researchers Frączek and Ślepek [41] focused on seeking an objective indicator for assessing the resistance of wheat to damage under repeated dynamic loads. In their studies, they analyzed the deformation of individual kernels at different moisture levels.

To this end, they developed a special impact apparatus (Fig. 11). In the device, the main working element was a movable hammer pin driven by a spring as the exciter. The spring was coupled to a ratchet mechanism that allowed it to be tensioned and then released abruptly, generating a dynamic motion of the hammer pin, which struck the tested grain sample via a measuring head. The measuring head, built as a strain gauge sensor assembly, enabled precise recording of the forcing forces. To measure deformations occurring in the tested sample, the stand incorporated an optical displacement sensor that tracked the motion of the hammer pin. The adopted design allowed excitations with a speed of 0.005 m s^{-1}.

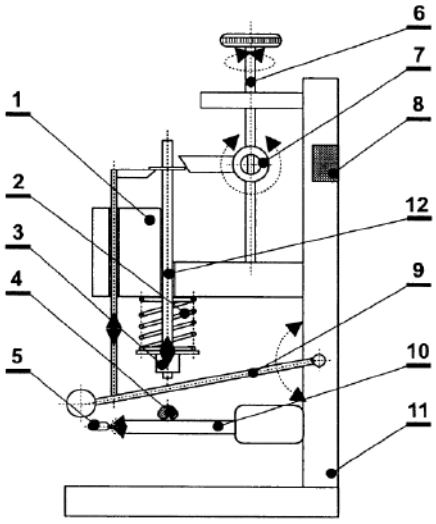

1 - optical displacement sensor, 2 - tension spring, 3 - strain gauge force sensor, 4 - grain, 5 - adjustment screw, 6 - pawl screw, 7 - pawl, 8 - electronic amplifier, 9 - tensioning lever, 10 - measuring table, 11 - housing, 12 - hammer pin [41]

Fig. 11. - Schematic of the impact apparatus

The studies carried out on the above apparatus provided many important insights. Among other things, the effect of successive excitations on the sample was determined, showing that the largest changes in grain elasticity occur between the first and fifth impact. The occurrence of fatigue strengthening of the material and its dependence on moisture were identified [41]. Moreover, the researchers were able to determine force deformation relationships in the form of hysteresis loops with a highlighted area representing changes in kinetic energy (Fig. 12). However, the reported data concerned relatively small ranges of excitation velocities, and the plotted deformation excitation characteristics were presented only symbolically, as they were not the main focus of the study. As a result, the work did not provide the full information needed for rheological modeling of the grain's response to excitations accompanying its impact with a machine's working surface, leaving room for further research.

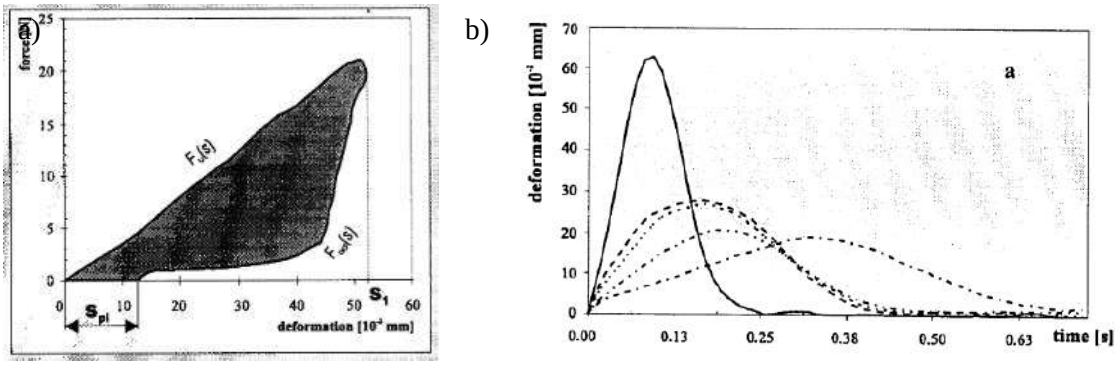

a) force deformation relationship, b) deformation of the tested sample

Fig. 12. - Example results of wheat grain studies by Frączek and Ślepek[41];

4. Empirical studies of contact force histories in the system comprising plant grain and the surface of a working unit

Following the literature review focused on identifying the mechanical properties of grain under impact conditions, a research stand based on a gravitational drop setup was adopted for further development. This solution combines structural simplicity with precise control of impact velocity by selecting the drop height and with simultaneous recording of the force history, the coefficient of restitution, and the contact time. The stand makes it possible to synchronize force measurement with video recording of grain velocity and orientation.

First, attention was focused on characterizing the test material itself, namely wheat grain, for which the principal physical parameters were measured. The resulting characteristics provided basic information needed to select measurement groups of grains that would ensure reliable and repeatable experimental results at later stages. Next, the effort focused on proper identification of the force history during the impact of a single grain with a flat surface, during which the impact impulses accompanying dynamic interactions were measured. The planned experiment provided information that serves as boundary conditions for the target research.

For the experiments, the test material was winter wheat of the cultivar Memory, which is currently one of the more commonly grown wheats in Poland. This relatively new cultivar, characterized by excellent yield potential, is classified in the highest quality groups A/B. The grain used in the study was purchased from a seed center as certified seed, meaning that it was obtained from special laboratory fields intended for the cultivation of seed material.

Before the preliminary tests, the test material was characterized in terms of physical features that affect the measurements, that is, its mass, moisture content, and main dimensions.

As a result of the measurements, the following material characteristics were determined [12]:

- average grain mass: 0.045 ± 0.008 g,
- base moisture: 7 %,
- grain length: 6.41 ± 0.5 mm,
- grain width: 3.04 ± 0.38 mm.

4.1 Test stand

As part of the undertaken work, a specialized research stand was constructed in the form of a system for dropping a grain onto a force sensor (Fig. 13). The stand comprised the following components: an aluminum frame serving as a support column; a transparent grain guide; a piezoelectric force sensor; a high speed camera; lighting; a measurement amplifier; and a computer for data acquisition and processing [12]. A piezoelectric force sensor was used to measure the force history. The control and measurement system employed an HBM GEN2tB amplifier, which enabled recording of measurement data at a frequency of 1,000,000 Hz. In addition, a Chronos 1.4 high speed camera was used to measure the velocity of the grain during impact.

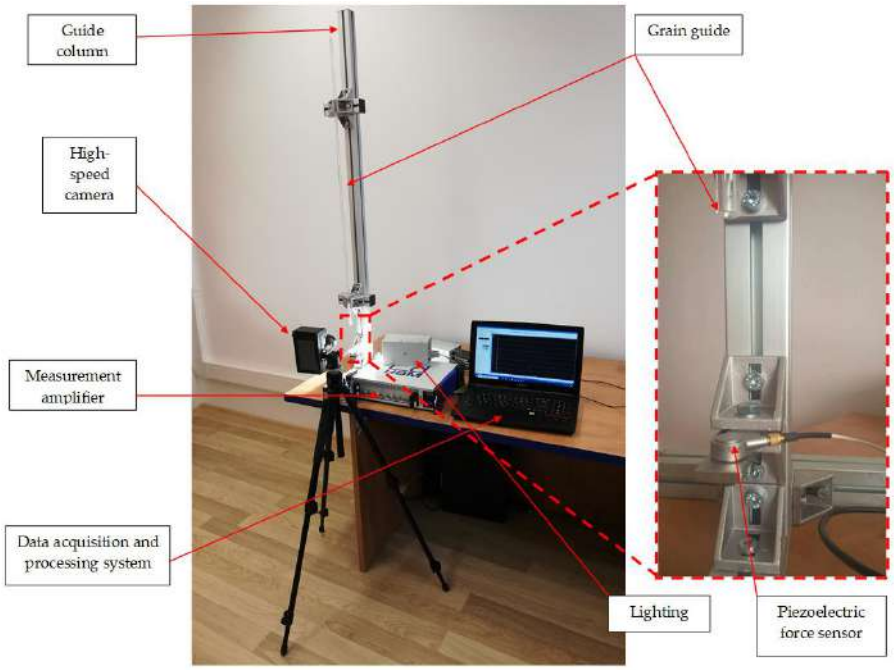

Fig. 13. - View of the impact test stand

The vision system enabled image recording at a resolution of 640×240 pixels with a frame rate of FPS = 8,816 frames per second. The recorded field of view covered the distance between the outlet of the transparent guide and the measuring surface of the force sensor. To determine velocity, a method was used that tracks reference points on the surface of the moving grain, assuming for the calculation that these points move in the same direction at the same speed relative to the observer, that is, the camera. Because during free fall the object may rotate due to, among other things, air resistance, the notional geometric center of the grain was adopted as the point satisfying these assumptions. With a stable camera setup, it was assumed that the velocity calculated relative to the camera equals the velocity relative to the force sensor. This approach made it possible to determine the flight time of the grain, Δt, by counting the number of frames, FR, in the recorded sequence, from which the instantaneous velocity was computed.

The stand made it possible to carry out a series of repeatable tests in which a single grain was dropped via the transparent guide onto the surface of the piezoelectric sensor. The experiment was performed for four moisture levels of the test material: 7, 10, 13, and 16 percent. For each moisture level, measurements were taken on 100 randomly selected wheat grains. The impact velocity was adjusted in the range from 1.5 to 4.5 m s^{-1}. Lower velocity ranges were achieved by free drop from an appropriately selected height between 200 and 1,000 mm [12].

The velocity range was established with reference to the results of Segler (1951), who determined a limiting permissible air velocity for pneumatic transport of wheat grain equal to 27.5 m s^{-1}. Above this value, structural damage is observed that reduces biological value and germination capacity. According to measurements carried out at the Department

of Working Machines of Poznan University of Technology for wheat [57, 58], air velocities of about 27.5 m s^{-1} in the seed tube of a pneumatic seeder correspond to grain velocities of about 4.5 m s^{-1}, which justifies the adopted range of impact velocities [12].

4.2 Results

Using the developed stand, a series of measurements was carried out to identify contact forces during impacts of wheat grain with a flat metal surface. The recordings made it possible to reconstruct single impact characteristics at various impact velocities; example force-versus-time traces are shown in Fig. 14.

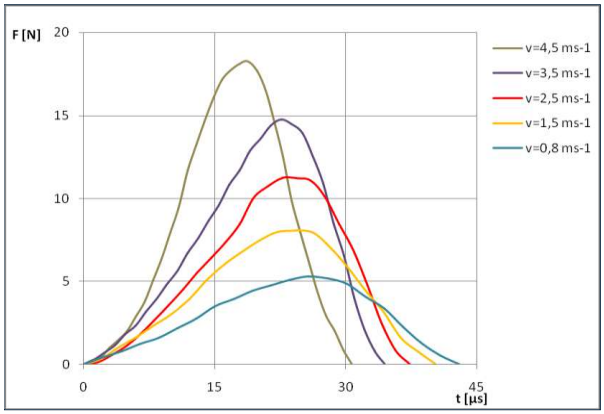

Fig. 14. - Comparison of example impact force histories for wheat grain at 10 percent moisture

The study was performed on a sample of 400 randomly selected grains, dropped at different velocities and for four moisture levels. To make a preliminary determination of interdependencies among the analyzed quantities, linear and nonlinear regression models were estimated. This approach yielded a complete dataset needed to compute the coefficient of restitution R, which characterizes the dissipation of energy during impact and is an important parameter describing the elasticity of the system; for plant materials it is equivalent in significance to viscoelastic damping parameters. To calculate R, the recorded force histories F(t) were approximated and written as finite polynomial functions, separately for the compression and restitution phases, and then used for integration to obtain the force impulse and the pre and post impact velocities, from which the coefficient of restitution R was computed.

Key measurement data were tabulated (Tables 1 to 4), including impact velocity v, restitution coefficient R, peak force Fmax, and contact time t_c. The results show that grain moisture is the leading factor governing the course of the impact. As moisture increases, the contact time with the flat surface increases systematically, while the peak interaction force decreases and the restitution coefficient declines. The response of the system therefore shifts from a shorter, more elastic impact toward one with a clearly larger share of plastic deformation and viscoelastic damping, which yields a longer compression phase and greater energy dissipation. As a consequence, higher moisture grains bounce less, and the impulse transmitted to the working element is lower but stretched in time.

This trend is consistent with the material structure: increasing water content reduces the effective stiffness of the endosperm and modifies the properties of the coat, which facilitates local plasticization and prolongs contact relaxation. Practically, strategies for limiting mechanical damage should consider moisture conditioning and the selection of surface material and roughness so as to reduce peak loads while maintaining control over contact time. The collected force time curves, contact times, and restitution values form a coherent dataset for calibrating contact models, for example DEM, and for selecting safe operating ranges in conveying and metering systems, especially where short duration impacts dominate over sliding friction.

Table 1. Summary of results for 7 percent moisture

Velocity	**Coefficient of restitution**	**Force**	**Contact time**
$m*s^{-1}$	**-**	**N**	**µs**
v	R	F	t
1,5	0,56±0,02	6,27±0,5	32,30±0,0002
2,5	0,51±0,02	10,34±0,5	29,37±0,0002
3,5	0,48±0,02	14,37±0,5	27,45±0,0002
4,5	0,47±0,02	18,38±0,5	26,03±0,0002

Table 2. Summary of results for 10 percent moisture

Velocity	**Coefficient of restitution**	**Force**	**Contact time**
m*s^{-1}	**-**	**N**	**µs**
v	R	F	t
1,5	0,53±0,02	5,65±0,5	42,05±0,0002
2,5	0,47±0,02	9,73±0,5	35,82±0,0002
3,5	0,43±0,02	13,91±0,5	31,50±0,0002
4,5	0,41±0,02	18,19±0,5	29,01±0,0002

Table 3. Summary of results for 13 percent moisture

Velocity	**Coefficient of restitutioncji**	**Force**	**Contact time**
m*s^{-1}	**-**	**N**	**µs**
v	R	F	t
1,5	0,48±0,02	5,13±0,5	49,96±0,0002
2,5	0,44±0,02	8,84±0,5	45,11±0,0002
3,5	0,41±0,02	12,55±0,5	42,06±0,0002
4,5	0,41±0,02	16,39±0,5	40,12±0,0002

Table 4. Summary of results for 6 percent moisture

Velocity	**Coefficient of restitution**	**Force**	**Contact time**
m*s^{-1}	**-**	**N**	**µs**
v	R	F	t
1,5	0,45±0,02	3,78±0,5	64,12±0,0002
2,5	0,40±0,02	6,76±0,5	56,33±0,0002
3,5	0,38±0,02	9,94±0,5	51,83±0,0002
4,5	0,37±0,02	13,20±0,5	48,64±0,0002

Conclusion

The aim of this work was to review research methods for identifying the mechanical properties of grain under impact conditions and to indicate methodological solutions that enable reliable data collection for design and modeling. Against the background of transport and dosing of granular materials, it was shown that variability in grain morphology and very short contact times hinder the use of classical measurement procedures. The state of the art in indirect and direct methods was synthesized, highlighting the limitations of visual and colorimetric assessments and the benefits of single grain tests in quasi static and dynamic configurations. A lack of uniform standards for seeds was noted, leading to limited comparability of some results.

In the methods section, the choice of a gravitational drop setup was justified as a solution that combines structural simplicity with control of impact velocity and the ability to record force and motion simultaneously. Attention was drawn to critical aspects of data acquisition, including the need to use impact force sensors with high natural frequency and to synchronize force recording with video capture to control grain orientation and eliminate measurement artifacts.

Empirical studies on wheat grain confirmed the usefulness of the adopted methodology. Force versus time histories were recorded; contact time and peak forces were determined; and the coefficient of restitution was calculated from pre and post impact velocities. A monotonic increase in peak force with impact velocity was demonstrated, as well as a decrease in the coefficient of restitution with increasing velocity and moisture. Contact time increased with moisture, which is consistent with a shift in the deformation mode toward a more viscoelastic response. The results were summarized in tables, yielding a coherent input dataset for the calibration and verification of contact models, including models used in DEM simulations.

The considerations and results presented have direct application. They enable the determination of load ranges for machine working elements, the reduction of biological damage to seeds, and the shortening of the design cycle through better grounded calibration of numerical models. At the same time, they point to areas requiring further work: expanding the range of impact velocities, analyzing oblique impacts and contact with surfaces of varied roughness and materials, systematically studying the effect of grain orientation, and standardizing measurement protocols and uncertainty reporting. Including these elements in subsequent stages will help build a clear bridge between experiment and modeling and consistently reduce the number of costly full scale tests while increasing the safety of seed transport and dosing processes.

References

[1] Warguła Ł., Kukla M., Krawiec P., Wieczorek B. Reduction in operating costs and environmental impact consisting in the modernization of the low-power cylindrical wood chipper power unit by using alternative fuel //Energies, 13(11), 2995, 2020.
[2] Warguła Ł., Lijewski P., Kukla M.. Influence of non-commercial fuel supply systems on small engine SI exhaust emissions in relation to European approval regulations //Environmental Science and Pollution Research, 29(37), 55928-55943, 2022.
[3] Warguła Ł., Lijewski P., Kukla M. . Effects of changing drive control method of idling wood size reduction machines on fuel consumption and exhaust emissions //Croatian Journal of Forest Engineering: Journal for Theory and Application of Forestry Engineering, 44(1), 137-151, 2023.
[4] Figiel A., Właściwości mechaniczne ziarna polskiej pszenicy twardej //Inżynieria Rolnicza, 134(9), s. 23-30, 2011.
[5] Fortes M., Okos M. R., Changes in physical properties of corn during drying //Trans. ASAE, 23(4), s. 1004-1009, 1980.
[6] Glenn, G.M., Younce F.L., Pitts M.J., Fundamental physical properties characterizing the hardness of wheat endosperm, //Cereal Sc., 1991, 13, P. 179-194,
[7] Evers A.D., Bechtel D.B., Microscopic structure of the wheat grain, in: Wheat: Chemistry and Technology eds: Pomeranz, Y., American Association of Cereal Chemists, Inc., Minnesota, USA, 1988.
[8] Fulcher R.G., Duke T.K.R. Whole-grain structure and organization: implications for nutritionists and processors Whole-Grain Foods in Health and Disease eds: Marquart, L., Slavin, J., Fulcher, R., American Association of Cereal Chemists, Inc., Minnesota, 2002.
[9] King R. Water uptake in relation to pre-harvest sprouting damage in wheat: Grain characteristics' //Australian Journal of Agricultural Research, 1984, 35, P. 337-345,
[10] Frączek J., Kaczorowski J., Ślipek Z., Horabik J., Molenda M., Standaryzacja metod pomiaru właściwości fizyczno-mechanicznych roślinnych materiałów ziarnistych, Lublin, 2003.
[11] Han I. Gilmore B.J. Multi body impact motion with friction analysis, simulation, and validation //Journal Mechanical Design, 1993, 115. P. 412–422,
[12] Marcinkiewicz J. Modelowanie sił Kontaktowych w Układzie ZIARNO roślinne–Powierzchnia Zespołu Roboczego w Aspekcie Zjawisk o Przebiegu Dynamicznym. Doctoral Dissertation, Politechnika Poznańska, Poznań, Poland, 2023.
[13] Flickinger D.M., Bowling A. Simultaneous oblique impacts and contacts in multibody systems with friction //Multibody System Dynamic, 2010, 23, P. 249–261,
[14] Goldsmith W., Impact: The theory and physical behaviour of colliding solids, Edward Arnold Ltd, London, England, 1960.
[15] Haug E.J., Wu S.C., Yang S.M., Dynamics of mechanical systems with coulomb friction, stiction, impact and constraint addition deletion - I theory, Mech Mach Theory, 21, P. 401–406, 1986.
[16] Rodriguez, A., Bowling, A., Solution to indeterminate multipoint impact with frictional contact using constraints, Multibody System Dynamic, 2012, 28(4), P. 313–330
[17] Wriggers P. Computational contact mechanics, 2nd edn. Springer, Berlin, 2006.
[18] Ivanov A.P. Dynamics of systems with mechanical collisions, (Moscow: International Education Program), 1997.
[19] Morozow S.J., Soudarenijetieł, Kłasiczeskaja teoria udara, cz. 1, Archangielsk, 2001.
[20] Panovko Y.G. Introduction to the theory of mechanical impact, Science, Moscow, 1977.
[21] Stronge W. Impact Mechanics (2nd ed.), Cambridge University Press, 2018. DOI:10.1017/9781139050227.
[22] Mohsenin N.N. Characterization and failure in solid foods with particular reference to fruits and vegetables //Journal of Texture Studies, 1977, 8, P. 169-193
[23] Mohsenin N.N. Physical properties of plant and animal materials, Gordon and Breach Science Publishers, New York, 1970.
[24] Kuwabara G., Kono K. Restitution coefficient in a collision between 2 spheres //Japanese Journal of Applied Physics, 1987, 26(8), P. 1230-1233
[25] Hu G., Hu Z., Jian B., Liu L., Wan H. On the determination of the damping coefficient of non-linear springdashpot system to model Hertz contact for simulation by discrete element method //Journal of Computers, 6(5), 2011, P. 984-988
[26] Oomah B.D., Ward S., Balasubramanian P., Dehulling and selected physical characteristics of Canadian dry bean (Phaseolus vulgaris L.) cultivars //Food Research International, 2010, 43(5), P. 1410-1415 DOI: 10.1016/j.foodres.2010.04.007.
[27] Selech J., Ulbrich D., Włodarczyk K., Kowalczyk J., Adamkiewicz J. The prototype of stream amplifier used in transport of polydisperse medium //Procedia Engineering, 2017, 192, P. 777–781. https://doi.org/10.1016/j.proeng.2017.06.134
[28] Ślipek Z., Złobecki A., Wpływ obciążeń wielokrotnych na uszkodzenia ziarna, Zeszyty Problemowe //Postępu Nauk Rolniczych, 1992, 402, P. 197-203
[29] Woźniak W., Grundas S., Niewczas J., Zastosowanie metody kolorymetrycznej i rentgenograficznej w badaniach uszkodzeń mechanicznych ziarna pszenicy, Annales Universitatis Mariae Curie-Skłodowska, Sectio AAA, Physica, 46/47, P. 469-475, 1991/1992.
[30] Jankowski S. Surowce mączne i kaszowe, WNT, Warszawa, 1988, ISBN 83-204-0981-0.
[31] Grzesiuk S., Górecki R., Fizjologia plonów. Wprowadzenie do przechowalnictwa, Wydawnictwo ART Olsztyn, 1994, ISBN 83-86497-01-7.
[32] Bechtel D.B., Abecassis J., Shewry P.R., Evers A.D., Development, structure, and mechanical properties of the wheat grain, in: Khan, K., Shewry, P.R., (ed.) //Wheat Chemistry and Technology, 2009, 4, P. 19-49,
[33] Kołowca J., Ryś S., Ślipek Z., Problemy pomiaru opisu niektórych cech fizycznych zbóż, Materiały Sympozjum biologii nasion i nasiennictwa KRGiHR, PAN, Puławy, 1979. p. 60
[34] Kołowca J., Ryś S., Ślipek Z., Wartość biologiczna ziarna pszenicy poddawanego działaniu obciążeń dynamicznych, Materiały Sympozjum biologii nasion i nasiennictwa KFGiHR, PAN, Puławy, 1979, P 60 -61
[35] Kołowca, J., Zeszyty Problemowe WSR w Krakowie, Rolnictwo, 1972, 14, P. 48 - 56
[36] Grundas, S., Horabik, J., Kuczyński, A., Zachowanie się ziarna pszenicy podczas cyklicznych obciążeń statycznych //Roczniki Nauk Rolniczych, Warszawa, 1980, 74-C-2, P. 177-187
[37] Kołowca J., Wpływ obciążeń mechanicznych na uszkadzalność i wartość biologiczną ziarna pszenicy, rozprawa habilitacyjna Akademia Rolnicza, nr 70, Kraków, 1979.
[38] Lutek K., Opracowanie konstrukcji przyrządu do badania odporności płodów rolnych na uszkodzenia mechaniczne, Maszynopis, Akademia Rolnicza Lublin, 1966.
[39] Ślipek Z., Złobecki A., Frączek J., Metoda oceny uszkadzalności ziarna przy uszkodzeniach wielokrotnych, Zeszyty Problemowe Postępu Nauk Rolniczych, 1994, 415, P. 187-195.

[40] Ślipek Z.,Metodyka oceny uszkadzalności ziarna pszenicy przy obciążeniach dynamicznych, Zeszyty Naukowe Akademii Rolniczej, Kraków, I, 1983.
[41] Fraczek J. A Test stand for fatigue testing of plant materials (in Polish), Zeszyty Problemowe Postawowych Nauk Rolniczych, 1995, 426, P. 53-63.
[42] Fraczek J., Ślipek Z., Influence of moisture content and number of mechanical impacts, upon the energy and sprouting capacity of wheat grains //International Agrophysics, 1998, 12(2), P. 97-101
[43] Niewczas J. Ocena uszkodzeń mechanicznych ziarna pszenicy wykrywanych techniką rentgenograficzną //Acta Agrophysica, 1994, 2
[44] Kustermann M., Stossartige Belastung von Maiskörner, Grundlagen der Landtechnik, 1987, 37(4), P. 121-131.
[45] Kęska W., Badania przebiegu sił przy zderzeniu nasion niektórych roślin uprawowych z powierzchniami roboczymi maszyn rolniczych, Prace Przemysłowego Instytutu Maszyn Rolniczych, 1996, 41(2), P. 17-21,
[46] Kęska W., Marcinkiewicz J., Gierz Ł., Staszak Ż., Selech J., Koszela K., Simulation Verification of the Contact Parameter Influence on the Forces' Course of Cereal Grain Impact against a Stiff Surface //Appl. Sci., 2021, 11, 466 https://doi.org/10.3390/app11020466.
[47] Shivakumar K.N., Elber W., Illg W., Prediction of Impact Force and Duration Due to Low-Velocity Impact on Circular Composite Laminates //ASME Journal Application Mechanics, 1985, 52(3), P. 674–680 DOI: https://doi.org/10.1115/1.3169120.
[48] Thornton C. Coefficient of restitution for collinear collisions of elastic perfectly plastic spheres //ASME Journal Application Mechanical, 1997, 64, P.383–386
[49] Nikonova T., Zharkevich O., Baimuldin M., Dandybaev E., Sichkarenko A., Kotov E. Developing a measuring system for monitoring the thickness of the 6 m wide HDPE/LDPE polymer geomembrane with its continuous flow using automation equipment //Applied Sciences (Switzerland), 2021, 11(21), 10045
[50] Xie J., Dong M., Li, S., Shang,Y., Fu Z. Dynamic characteristics for the normal impact process of micro-particles with a flat surface //Aerosol Science and Technology, 2018, 52(2), P. 222-233
[51] Horabik J., Beczek M., Mazur R., Parafiniuk P., Ryżak M., Molenda M. Determination of the restitution coefficient of seeds and coefficients of visco-elastic Hertz contact models for DEM simulations //Biosystems Engineering, 2017, 161, P. 106-119
[52] Szwed G., Pecen J., Sosnowski S. Measurement and analysis of impact of spring rape seeds //Acta Agrophysica, 2003, 2(95-1), P. 221-229
[53] Szwed G., Pecen J. Wyniki badań współczynnika restytucji niektórych nasion roślin uprawnych, Inżynieria Rolnicza, 2006, 4(79), P. 289-295
[54] Wojtkowski M., Pecen J., Horabik J., Molenda M. Rapeseed impact against a flat surface: Physical testing and DEM simulation with two contact models //Powder Technology, 2010, 198(1), P. 61-68
[55] Kilikevicius A., Bacinskas D., Selech J., Matijosius J., Kilikeviciene K., Vainorius D., Ulbrich, D., Romek D. The Influence of Different Loads on the Footbridge Dynamic Parameters //Symmetry, 2020, 12(4), 657-1-657-21
[56] Zhan Z., Yaoming L., Zhenwei L., Zhiqiang G. DEM simulation and physical testing of rice seed impact against a grain loss sensor //Biosystems Engineering, 2013, 116(4), P. 410-419
[57] Gierz Ł., KęskaW., Gierz S. Badania laboratoryjne czasu transportu ziarna pszenicy w przewodzie nasiennym siewnika //Journal of Research and Applications in Agricultural Engineering, 2012, 57(1), P. 37-40
[58] Gierz Ł., Kęska W. Badania symulacyjne i laboratoryjne czasu transportu ziarna rzepaku w przewodzie nasiennym siewnika //Journal of Research and Applications in Agricultural Engineering, 2012, 57(2), P. 73-78

Information of the author

Marcinkiewicz Jacek, PhD, Eng, assistant professor, Poznan University of Technology
e-mail: jacek.marcinkiewicz@put.poznan.pl

DOI 10.52209/2706-977X_2025_4_29 **IRSTI 55.51.29** **UDC 631.3**

Mobile Overpass with a Movable Foundation: Ensuring Trench Stability Under Traffic Loads

Kadyrov A.S.[1,2], Kukesheva A.B.[2*], Bakytov Y.S.[3]
[1]QarTech Innovation and Industrial Hub, Karaganda, Kazakhstan
[2]Abylkas Saginov Karaganda Technical University, Karaganda, Kazakhstan
[3] Borusan Makina Kazakhstan LLP FE
*corresponding author

Abstract. The aim of this study is to develop a mobile overpass design with a movable damping foundation that ensures safe and continuous traffic flow during the repair of underground utilities. The scope of the research includes the analysis of loads on the overpass foundation and the development of an engineering solution to prevent trench collapses. The study examines vertical and horizontal loads acting on the support foundation and proposes an original movable foundation structure using thixotropic and viscoplastic materials. The research methodology is based on the application of rheological models to describe the behavior of materials that absorb the kinetic energy of vehicles. The obtained results demonstrate the effectiveness of the proposed solution in reducing the risk of trench slope instability, enhancing safety, and improving deternmental conditions. The developed structure can be applied in urban construction and in the organization of temporary road infrastructure.

Keywords: mobile overpass, damping foundation, viscoplastic medium, thixotropy, load, trench stability.

Introduction

During the repair of urban underground utilities, traffic flow is inevitably disrupted, forcing vehicles to detour via alternative routes. This is typical for maintenance works on heating networks, water supply systems, communication lines, and power grids. Forced detours increase vehicle mileage, raise traffic intensity on adjacent streets, and, as a result, lead to higher fuel consumption and increased concentrations of harmful substances in the air. Atmospheric pollution with nitrogen oxides, carbon monoxide, soot, and fine particulate matter (PM2.5 and PM10) enhances the aerogenic load on the human body and is accompanied by the development of systemic inflammatory responses, as well as dysfunctions of the respiratory and cardiovascular systems [1, 2].

The most vulnerable groups to the effects of polluted air are populations with weakened immune reactivity and chronic diseases. Even a moderate increase in the concentration of harmful impurities in such patients can trigger decompensation of existing pathologies and elevate the risk of adverse outcomes, as confirmed by clinical data indicating reduced lung function, impaired microcirculation, and an increased incidence of acute cardiovascular events [3, 4].

Our review of previous studies shows that two fundamentally different approaches are used to reduce the negative impact of road transport on the urban environment. The first approach is aimed at combating air pollution caused by engine operation using physical methods [5, 6]. These physical purification methods include ultrasonic, electrical impulse, and laser-based effect, which allow a reduction in the toxicity of exhaust gases [7, 8]. The second approach focuses on preventing the formation of traffic congestion, which is one of the main causes of increased emissions. The most effective engineering solution in this direction is recognized as the use of mobile overpasses, which make it possible to maintain uninterrupted straight-line traffic over excavation zones and prevent the growth of traffic congestion [9,10].

Thus, reducing the environmental burden under conditions of urban repair works requires the joint development of both exhaust gas purification technologies [11] and infrastructure solutions that ensure the continuity of traffic flows. The developed design of a mobile overpass with a damping foundation constitutes a contribution to the second direction and is aimed at eliminating one of the key causes of air quality deterioration – the formation of prolonged detours and additional traffic delays.

The overpass represents both a civil engineering structure and a transportation vehicle at the same time. It is an easily assembled and dismantled structure designed for the rapid creation of temporary detours over roadwork sections (Figure 1) [12].

Fig.1 – Overpass Structure

The load-bearing capacity of the overpass is based on a three-dimensional metal truss. Its spatial framework, consisting of longitudinal, diagonal, and vertical elements, forms a rigid frame built on a stable triangular lattice. This geometry ensures high structural strength and even distribution of weight loads (Figure 2).

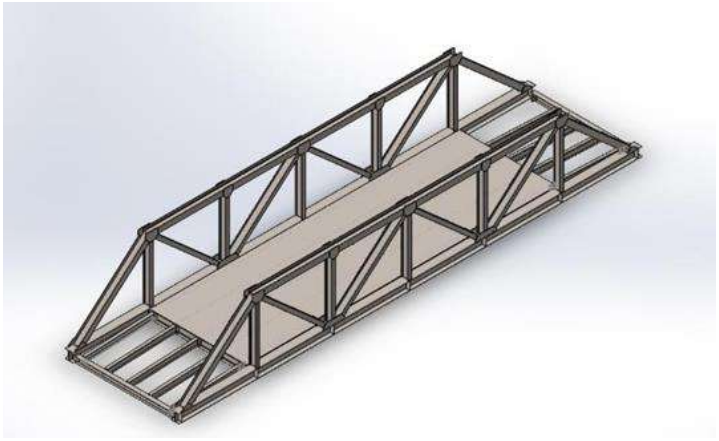

Fig. 2 – Load-Bearing Capacity of the Overpass

A key feature of the overpass is its transport-support system. Instead of stationary supports, the overpass rests on two central wheel trolleys. These dual-axle modules with pneumatic tires serve a dual purpose: in transport mode, they function as a chassis for relocation (Figure 3a), and in operational mode, they are elevated above the road surface (Figure 3b). During operation, damping materials can be placed under the supports [13].

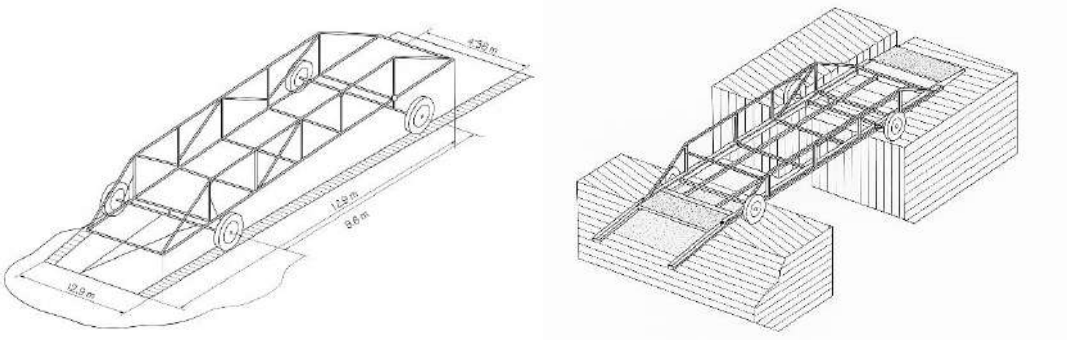

a) overpass diagram in transport position above the trench

b) overpass diagram in operational position above the trench

Fig.3 – Transport-Support System of the Overpass

Based on the above, the aim of this study is to develop and justify the design of a mobile overpass with a movable damping foundation that reduces horizontal loads on trench walls while ensuring safe and continuous traffic flow during underground utility repairs.

To achieve this aim, the following objectives were set:

- to study the nature of vertical and horizontal loads that arise during the operation of temporary overpasses;
- to analyze the threat of trench slope instability caused by horizontal forces;
- to develop a structural solution for a movable support using thixotropic and viscoplastic materials.

The scientific novelty of the work lies in the development and justification of a mobile overpass design with a movable damping foundation, in which a viscoplastic thixotropic material (e.g., bentonite slurry) is used for the first time as an active element to absorb horizontal loads on trench slopes. An original engineering model of a support interacting with a flowable medium is proposed. This medium is capable of changing its internal structure under the influence of the kinetic energy of the moving vehicle, enabling stress redistribution and preventing foundation failure.

The practical significance of the research lies in the potential application of the proposed design for the safe and rapid creation of temporary crossings during urban underground utility repairs. The development reduces the risk of emergencies, lowers costs for trench reinforcement, and ensures stable traffic flow without the need for prolonged detours, thereby enhancing the efficiency and environmental sustainability of urban infrastructure solutions.

2. Materials and Methods

During the operation of the overpass, the foundations beneath the vehicle supports are subjected to vertical and horizontal loads (Figure 4).

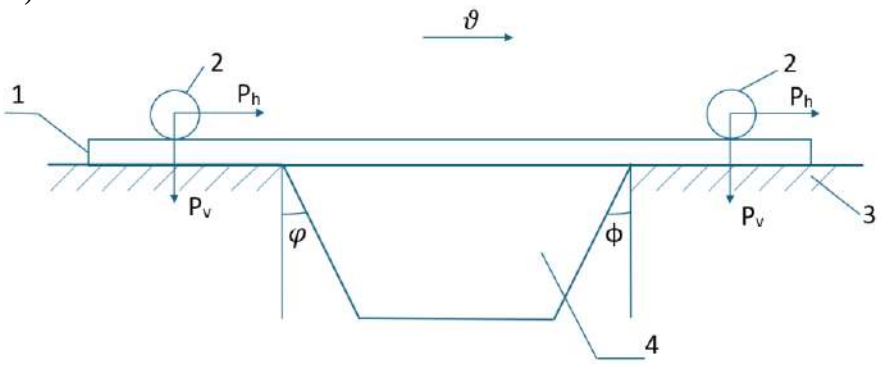

1 – overpass frame; 2 – moving mass (vehicle); 3 – foundation (mass of soil above the overpass support); 4 – sloped trench; P_h and P_v – horizontal and vertical components of the load on the overpass foundation, respectively; φ – trench slope angle; ϑ– direction and speed of the vehicle movement.

Fig. 4 – Diagram of Forces Acting on the Overpass Supports

Vertical loads are determined by the weight of the vehicle, while horizontal loads arise from the vehicle's movement across the overpass in the direction of velocity ϑ. Horizontal displacements pose a risk of trench instability, which can lead to accidents or even disasters.

The stability of trench slopes has been addressed in several studies [14,15]. We propose an engineering solution involving a mobile foundation for the overpass support [16].

The support consists of a semicircular component made of metal-reinforced concrete, plastic, or wood, featuring horizontal grooves along its body. It is placed in a ground recess filled with viscoelastic or simultaneously elastic and flowable materials such as coal slurry, clay solution, fine sand, or used oil, and is secured at the top to the overpass [17,18].

Figure 5 shows the general view of the design, where: 1 – recess, 2 – flowable material, 3 – overpass support, 4 – support fastening elements, 5 – semicircular element made of reinforced concrete, plastic, or wood, 6 – horizontal grooves.

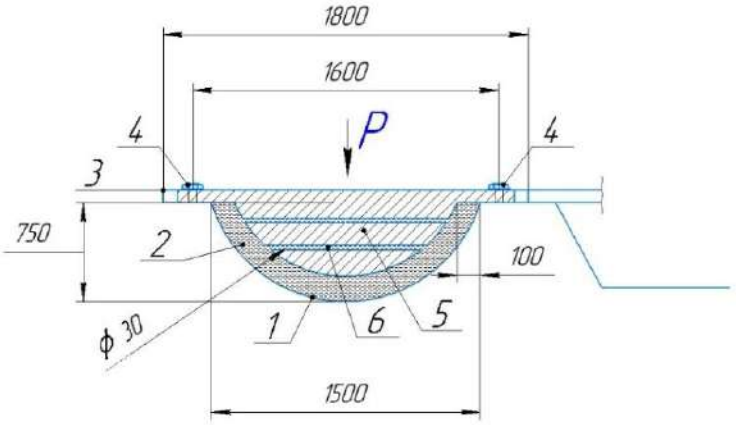

Fig. 5 – General View of the Structure

The geometric parameters of the damping foundation are determined based on the presented structural layout. The excavation depth is h=0.75h = 0.75h=0.75 m, which ensures the required volume of thixotropic material and a sufficient thickness of the damping layer. The surface width of the excavation is b=1.80 m, while the effective width of the load application zone is 1.60 m. The length of the support along the trench is taken as L=1.50 m, which corresponds to the design size of the curved element and the soil contact area.

The supporting element is designed as a curvilinear semicircular ring with a radius of R=0.75 m, which follows from the diameter of 1.50 m indicated in the drawing. The wall thickness of the semicircular ring is t≈0.10 m, providing sufficient structural stiffness with minimal weight. The horizontal grooves, intended for the flow of the thixotropic medium and energy dissipation, have a width of s≈0.03 m and are arranged with a spacing of l≈0.10 m.

The support element is curved in the vertical plane in such a way that the tangent to its outer contour forms an angle with the horizontal equal to the internal friction angle of the soil (Figure 6).

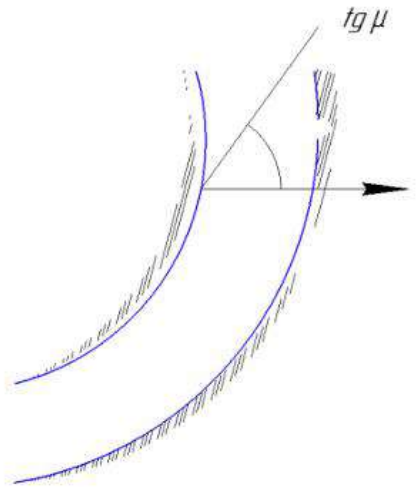

Fig.6 – Support Element

The operation of the support functions as follows: when a vehicle drives onto the overpass, pressure is transmitted to the wall of the recess through the flowable elastic material. This material dampens the loads by absorbing kinetic energy, reducing viscosity, and partially flowing through the horizontal grooves in the metal, reinforced concrete, plastic, or wooden semicircular support element into the rear part of the recess. In this way, the flowable material acts as a hydraulic damper powered by the kinetic energy of movement .

This allows for a reduction in the distance between the support and the recess, as well as the load R on trench wall A, without increasing the risk of collapse. The upper part of the support is used for attachment to the overpass structure. The side sections of the support contain threaded connections for bolts (Figure 5), where: 7 – overpass structure, 8 – side sections of the support, 9– rubber coating of the overpass.

The clay solution poured into the circular recess is a thixotropic liquid, which can be described using various rheological models depending on the amount of energy applied to it.

The operational efficiency of the damping foundation of the mobile overpass is primarily determined by the rheological properties of the filling material. In this regard, the selection of the filler must be based on a set of engineering criteria:

- pronounced thixotropy – the ability of the material to разрушать its structure under shear and restore it at rest, ensuring cyclic absorption of dynamic loads [19];
- the presence of a yield stress τ_0 and a stable range of plastic viscosity μ, allowing the damping performance to be predicted;
- environmental safety, absence of toxicity and aggressive impact on soil and groundwater;
- technological efficiency – ease of preparation, dosing, injection into the excavation, and subsequent pumping out after completion of works; stability of properties over a wide range of temperatures and humidity.

Bentonite thixotropic slurry, widely used in geotechnical and drilling technologies, most fully meets these requirements [20]. Its behavior is well described by the viscoelastic–plastic Bingham model, which is characterized by the presence of a yield stress τ_0 and plastic viscosity μ.

At stresses below τ_0, the bentonite slurry behaves as an elastic solid (gel), enabling stabilization of the support zone. When τ_0 is exceeded, it transitions into a viscoplastic fluid state that absorbs shear energy. This makes it an optimal damping material for reducing horizontal loads [21].

The parameters of bentonite slurries ($\tau 0$=10–20 Pa, μ=0.02–0.08 Pa·s) reported in [22, 23] fully satisfy the requirements of the developed structure and ensure a predictable level of energy dissipation.

Various alternative media were also considered; however, their application is limited by the following drawbacks:

- coal slurry – prone to rapid sedimentation, unstable in composition, and may contain toxic inclusions [24];
- fine sand – is not a thixotropic material and behaves as a granular medium, providing no plastic energy absorption [25];
- waste oil – significant environmental risks (contamination of soils and aquifers), absence of recoverable structure [26];
- natural clay slurries – may be used, but their properties are less stable and more difficult to control [27].

Thus, bentonite slurry possesses an optimal combination of thixotropy, environmental safety, technological efficiency, and predictable rheological characteristics. These features make it suitable for use as the basic damping material in the developed mobile overpass structure.

The application of a damping foundation based on bentonite slurry requires compliance with a specific technological sequence that ensures both operational safety and the possibility of repeated use of the thixotropic medium. The technology includes the following stages:

1. Preparation of the working zone and formation of the excavation. Before installation of the support, the excavation of the design depth is carried out using an excavator or hydromill. The excavation geometry corresponds to the dimensions of the curvilinear supporting element. The bottom of the excavation is leveled, and, if necessary, a sand–clay bedding layer is applied to reduce filtration losses [28].

2. Installation of the supporting semicircular ring. The curvilinear support is installed into the prepared excavation and fixed by lateral connections to the bridge structure. The tightness of the contact zone is ensured by the close fit of the support contour against the excavation walls.

3. Filling the excavation with thixotropic slurry. Filling is performed from a tanker truck equipped with a pumping unit. The bentonite slurry is supplied by gravity flow or under slight pressure through a flexible hose. The filling rate is regulated to achieve the required degree of filling and to prevent the formation of air voids. The complete filling time of a single excavation with a volume of 1.1–1.2 m³ is approximately 3–5 minutes.

4. Operation of the damping foundation. During the operation of the overpass, periodic monitoring of the level and condition of the bentonite slurry is carried out through technological openings. Due to its thixotropic properties, the slurry remains stable, resisting filtration and sedimentation. Slight compaction may occur during rest periods, but under dynamic loading the structure rapidly liquefies, providing the required damping effect.

5. Completion of works and extraction of the slurry. After the end of overpass operation, the slurry is pumped back into the tanker using a submersible or diaphragm pump. The extraction time is 5–7 minutes per excavation. Residual slurry traces are washed out with water, which is also collected and transported to the base.

6. Reuse and disposal of the slurry. The bentonite slurry can be reused after adjusting its density and viscosity at the production base. Such regeneration minimizes raw material consumption and reduces environmental impact. If disposal is required, the slurry fully complies with safety requirements for handling thixotropic clay mixtures and can be disposed of in accordance with current regulations.

Thus, the proposed technology for the application of the damping foundation ensures rapid execution of works, multiple reuse of the material, and full compliance with environmental requirements, thereby enhancing the practical applicability of the developed mobile overpass structure.

3. Results

A methodology has been developed for determining the horizontal force transmitted to the trench wall by a vehicle while passing over a mobile overpass, and a comparative analysis of loads has been performed for two support configurations: a rigid fixed support and a support with a damping thixotropic foundation.

The calculations were carried out for a vehicle with a mass of m=3 t, moving at a speed of v=20 km/h, with an entry angle of α=5°, a trench depth of ht=1.8 m, and the following soil parameters: unit weight γ=18 kN/m³, internal friction angle φ=26°, and cohesion c=12 kPa.

For the rigid support configuration, it is assumed that the horizontal component of the wheel load is almost entirely transmitted through the support element to the trench wall. In this case, the horizontal force is determined by the following expression:

$$P_{hr} = mgsin5^{\circ} + \frac{m\vartheta^2}{R}, \quad (1)$$

where m is the vehicle mass,

α=5° is the entry slope angle,

R is the radius of trajectory curvature (considered as a parameter of the dynamic amplification factor according to design standards).

The first term of the expression describes the horizontal projection of the vehicle weight on the slope, while the second term represents the dynamic component associated with the change in velocity during motion along the inclined section.

For a vehicle mass of m=3000m = 3000 kg and gravitational acceleration g=9.81g = 9.81g=9.81 m/s², we obtain mg=29,430 N. The horizontal component of the weight on a slope with α=5° is:

For a speed of v=20 km/h (v≈5.55 m/s), the dynamic component is:

$$\frac{m\vartheta^2}{R} \approx 3000 \cdot \frac{5{,}55^2}{25} \approx 3700 \text{ N}, \quad (2)$$

The total horizontal force for the rigid support is therefore:

$$P_{hr} = 2560 + 3700 = 6260 \text{ N}$$

which corresponds to almost complete transmission of the load to the trench wall and may lead to a reduction in its stability.

When using a support with a damping thixotropic layer, part of the transmitted energy is dissipated through shear deformation of the viscoplastic material layers and destruction of its structure, as a result of which the effective horizontal force is reduced. In this case, the following relationship can be written:

$$P_{hd} = P_{hr} - F_{damp}, \tag{3}$$

where F_{damp} is the damping force caused by the rheological properties of the bentonite slurry.

To estimate F_{damp}, the Bingham model is used, according to which the shear stress in the slurry layer is determined as:

$$\tau = \tau_0 + \mu \frac{d\vartheta}{dy}, \tag{4}$$

and the resulting damping force is calculated by integration over the contact area between the support and the slurry:

$$F_{damp} = \int_{A_1}^{A_2} (\tau_0 + \mu \frac{d\vartheta}{dy}) dA, \tag{5}$$

where τ_0 is the yield stress of the bentonite slurry (12–18 Pa),

μ is the plastic viscosity (0.02–0.08 Pa·s),

A is the contact area.

Based on the calculation of the damping force F_{damp} generated in a bentonite slurry layer with a thickness of 40–60 mm under shear caused by the horizontal load from the vehicle, a dimensionless load reduction coefficient k was obtained:

$$k = \frac{P_{hd}}{P_{hr}} = 0{,}4 - 0{,}6, \tag{6}$$

The coefficient k=0.4–0.6 was obtained using the Bingham rheological model, estimation of shear stresses, and the equivalent shear area. Taking into account the thixotropic breakdown of the slurry structure and energy dissipation, it was established that the thixotropic interlayer absorbs 40–60% of the horizontal load, which is consistent with data for similar viscoplastic media in engineering applications.

Then,

$$P_{hd} = \mathrm{k} \cdot P_{hr} = (0{,}4 – 0{,}6) \cdot 6\,260 \approx 2\,500 – 3\,750 \text{ H}, \tag{7}$$

Accordingly, the absolute reduction in the load on the trench wall is:

$$\Delta P = P_{hr} - P_{hd} \approx 6260 - (2500 – 3750) = 2510 – 3760 \text{ H}, \tag{8}$$

which corresponds to a 40–60% reduction in the horizontal force.

To assess the effect of vehicle speed on the load magnitude, calculations were performed for three typical speeds of 10, 20, and 30 km/h. The final values are summarized in Table 1.

Table 1. Horizontal force P_{hr} for different support types

Speed, km/h	P_{hr} for rigid support, N	P_{hd} for damping support, N	Load reduction, %
10	3,900	1,600–2,350	40–60
20	6,260	2,500–3,750	40–60
30	9,200	3,700–5,500	40–60

Figure 7 (to be inserted later) shows the dependence of the horizontal force on vehicle speed for two support configurations: curve 1 corresponds to the rigid support, and curve 2 corresponds to the support with a damping thixotropic foundation.

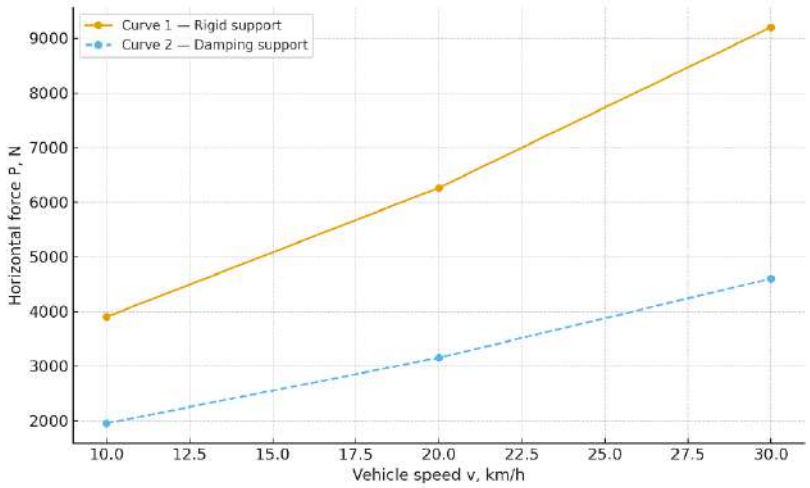

Fig. 7. – Dependence of the horizontal force on vehicle speed

The graph clearly demonstrates that as the vehicle speed increases, the difference between the two support configurations becomes more pronounced, while the use of a damping interlayer makes it possible to significantly limit the growth of the dynamic component of the load.

The performed calculations confirm that the application of a thixotropic damping foundation under the supports of the mobile overpass ensures a reduction in the horizontal force transmitted to the trench walls by 40–60%, which substantially increases their stability and reduces the risk of soil displacement and loss of slope stability under transport loading.

Conclusion

The conducted study has shown that traditional mobile overpass structures supported by rigid fixed foundations are subject to significant horizontal loads возникающим during vehicle movement on inclined surfaces. These loads are directly transmitted to the trench walls and may lead to a reduction in their stability, an increase in plastic deformations, and the risk of local collapses, especially under conditions of dense urban underground utilities.

The proposed design of a mobile overpass with a movable damping foundation filled with a thixotropic viscoplastic material fundamentally changes the nature of interaction between the support and the soil base. It has been demonstrated that bentonite slurry, due to its pronounced thixotropic properties, is capable of transitioning from a gel state to a viscoplastic state upon reaching the yield stress, thereby absorbing and dissipating a significant portion of the transmitted energy.

The developed method for calculating horizontal loads made it possible to quantitatively assess the efficiency of the damping layer. It was established that the use of a thixotropic interlayer reduces the horizontal force acting on the trench wall by an average of 40–60% compared with the rigid support configuration.

The developed technology for slurry filling, condition monitoring, and subsequent extraction ensures the practical applicability of the proposed solution in an urban environment. This makes it possible to reduce the need for additional trench wall reinforcement, accelerate repair operations, and decrease traffic delays that directly affect the environmental situation in the city.

Thus, the proposed mobile overpass design with a damping foundation represents an effective engineering solution aimed at improving safety, reducing operational risks, and enhancing environmental conditions during underground utility works.

Aknowledgments. This research was supported by the QarTech Innovation and Industrial Hub (Karaganda Region, Kazakhstan)

References

[1] Yessenbayeva A., Kadyrova I., Aukenov N., Shaimardanov N., Apsalikov B., Massabayeva M., Kazymov M., Shakhanova A., Mussazhanova Zh. Biomarkers of immunothrombosis and polymorphisms of IL2, IL6, and IL10 genes as predictors of the severity of COVID-19 in a Kazakh population // PLoS ONE, Vol. 18, Issue 6, 2023. – p. 61–67.

[2] Akhmaltdinova L., Sirota V., Babenko D., Zhumaliyeva V., Kadyrova I., Maratkyzy M., Ibrayeva A., Avdienko O. Proinflammatory cytokines and colorectal cancer – the impact of the stage // Wspolczesna Onkologia, Vol. 24, Issue 4, 2021. – p. 207–210.

[3] Ospanov O., Yeleuov G., Kadyrova I., Bekmurzinova F. The life expectancy of patients with metabolic syndrome after weight loss: Study protocol for a randomized clinical trial (LIFEXPE-RT) // Trials, Vol. 20, Issue 202, 2019. – p. 1–7. DOI: 10.1186/s13063-019-3304-9

[4] Kadyrova I.A., Mindubaeva F.A., Grjibovski A.M. Prediction of outcomes after stroke: A systematic review // Human Ecology (Russian Federation), Vol. 4, Issue 10, 2015. – p. 55–64.

[5] Kadyrov A., Kryuchkov Y., Sinelnikov K., Ganyukov A., Sakhapov R., Kukesheva A. Studying the process of the internal combustion engine exhaust gas purification by an electric pulse // Communications – Scientific Letters of the University of Žilina, Vol. 24, Issue 4, 2022. – p. 275–287. DOI: 10.26552/com.C.2022.4.B275-B287
[6] Ibatov M.K., Kadyrov A.S., Pak I.A., Kadyrova I.A., Askarov B.S. The results of experimental studies of the capacitive equipment of ultrasonic cleaning of exhaust gases of vehicles // Ugol, Vol. 21, Issue 2, 2020. – p. 73–78.
[7] Pak I. Experimental study of the ultrasonic muffler efficiency for improving the exhaust gas cleaning system of internal combustion engines of automobiles // Material and Mechanical Engineering Technology, Vol. 6, Issue 2, 2024. – p. 53–63.
[8] Ilesaliev D.I. Design of ultrasonic technology to improve the efficiency of car exhaust gas cleaning system // Material and Mechanical Engineering Technology, Vol. 6, Issue 2, 2024. – p. 3–7.
[9] Kadyrov A., Ganyukov A., Balabekova K. Development of constructions of mobile road overpasses // MATEC Web of Conferences, Vol. 108, 16002, 2017. – p. 1–4. DOI: 10.1051/matecconf/201710816002
[10] Kadyrov A., Balabekova K., Ganyukov A., Akhmediyev S. The constructive solution and calculation of elements of the unified module of the mobile bridge overcrossing // Transport Problems, Vol. 12, Issue 3, 2017. – p. 59–69. DOI: 10.20858/tp.2017.12.3.6
[11] Sarsembekov B.K., Kadyrov A.S., Kunayev V.A., Issabayev M.S., Kukesheva A.B. Experimental comparison of methods for cleaning car exhaust gas by exposure using ultrasound and laser radiation // Material and Mechanical Engineering Technology, Vol. 6, Issue 3, 2024. – p. 44–54.
[12] Kadyrov A.S., Ganyukov A.A., Amanbayev S.Sh., Bogdanova A.A. Development of mobile communal overpasses applied during repairing of urban communal networks // Material and Mechanical Engineering Technology, No. 3, 2023. – p. 11–14. DOI: 10.52209/2706-977X_2023_3_1
[13] Ganyukov A.A., Sinelnikov K.A., Kabikenov S.Zh., Karsakova A.Zh. Research and calculation of the deformed state of the roadway mobile overpass //Material and Mechanical Engineering Technology, Vol. 6, Issue 3, 2024. – p. 88–95.
[14] Kim H.J., Won D.H., Kang Y.J., Kim S. Structural stability of cable-stayed bridges during construction // International Journal of Steel Structures, Vol. 17, Issue 2, 2017. – p. 443–469.
[15] Roy K. Structural damage identification using mode shape slope and curvature // Journal of Engineering Mechanics, Vol. 143, Issue 9, 2017. – 04017110.
[16] Kadyrov A.S., Suleev B.D., Ganyukov A.A., Kadyrova I.A. Temporary support for a bridge crossing: Patent No. 2020/0841.1, Republic of Kazakhstan. Published in Bulletin No. 10 on 11.03.2022. Filed on 07.12.2020. – Priority documents: RU 2297489 C2 (20.04.2007); KZ 2131 U (14.04.2017); BY 2560 U (30.04.2006).
[17] Sherov K.T., Absadykov B.N., Sikhimbayev M.R., Togizbayeva B.B., Esirkepov A. Investigation of the stress-strain state of components of a hydraulic impact device // News of the National Academy of Sciences of the Republic of Kazakhstan. Series of Geology and Technical Sciences, Vol. 1, Issue 457, 2023. – p. 260–269.
[18] Kadyrov A.S., Ganyukov A.A., Altynbaev A.Z. Analysis of research and characteristics of physical and mechanical properties of clay thixotropic solutions // Material and Mechanical Engineering Technology, Vol. 2, Issue 2, 2024. – p. 15–19.
[19] Kyzylbaeva E.Z., Kukesheva A.B., Kunaev V.A. Mathematical model of plate movement in thixotropic mud // Material and Mechanical Engineering Technology, Vol. 2, Issue 2, 2020. – p. 26–30.
[20] Rinaldi V.A., Clariá Jr J.J. Time dependent stress–strain behavior of bentonite slurries; effect of thixotropy // Powder Technology, Vol. 291, 2016. – p. 311–321.
[21] Souza G.S.D., Luporini S., Rigoli I.C. Rheological characterization of bentonite dispersions with xanthan for oil well drilling fluids // Materials Research, Vol. 20, Suppl. 2, 2017. – p. 159–166.
[22] Chen M., Liu B., Li L., Cao L., Huang Y., Wang S., Cheng X. Rheological parameters, thixotropy and creep of 3D-printed calcium sulfoaluminate cement composites modified by bentonite // Composites Part B: Engineering, Vol. 186, 2020. – 107821.
[23] Larson R.G., Wei Y. A review of thixotropy and its rheological modeling // Journal of Rheology, Vol. 63, Issue 3, 2019. – p. 477–501.
[24] Ma S., Wu G., Meng X., Zhou R., Chu R., Miao Z., Qi Y. Characteristics of coal sludge slurry prepared by a wet-grinding process // International Journal of Mining Science and Technology, Vol. 26, Issue 5, 2016. – p. 947–953.
[25] Li L., Zhang Y., Tian Y. The application of fine sand in subgrades: A review // Applied Sciences, Vol. 14, No. 15, 2024. – 6722.
[26] Guo L.P., Han X., Lei Y., Wang L., Yu P.F., Shi S. Study on the thixotropy and structural recovery characteristics of waxy crude oil emulsion // Petroleum Science, Vol. 18, Issue 4, 2021. – p. 1195–1202.
[27] Ren Y., Yang S., Andersen K.H., Yang Q., Wang Y. Thixotropy of soft clay: A review // Engineering Geology, Vol. 287, 2021. – 106097.
[28] Kadyrov A., Zhunusbekova Z., Ganyukov A., Kadyrova I., Kukesheva A. General characteristics for loading the working elements of drilling and milling machines when moving in the clay solution // Communications – Scientific Letters of the University of Žilina, Vol. 23, Issue 2, 2021. – p. 97–105. DOI: 10.26552/COM.C.2021.2.B97-B105

Information of the authors

Kadyrov Adil, d.t.s., QarTech Innovation and Industrial Hub, Abylkas Saginov Karaganda Technical University
e-mail: adil.suratovich@mail.ru

Kukesheva Aliya, PhD, Abylkas Saginov Karaganda Technical University
e-mail: aliya.kukesheva@bk.ru

Bakytov Yelkhan, service engineer, Borusan Makina Kazakhstan LLP Fe
e-mail: ebakytov@borusan.com

DOI 10.52209/2706-977X_2025_4_37 **IRSTI 55.42.27** **UDC 621.01**

Dynamic Analysis of Machine Aggregates with Compound Belt Transmissions

Yunusov S.Z.[1]*, Kenjayev S.N.[1], Kasimova D. A.[2]
[1]Tashkent State transport University, Tashkent, Uzbekistan
[2]Andijan Institute of Technology, Andijan, Uzbekistan
corresponding author

Abstract: This article examines the dynamic characteristics of the PD-type feeding system in the 4DP-130 cotton cleaning machine when utilizing a composite belt drive. The study focuses on analyzing angular velocity oscillations and technological resistances by developing and solving a mathematical model using Mathcad software. Key parameters investigated include belt tension force (M_c), deformation of the composite pulley's elastic element (M_0), stiffness (c), and dissipation (b).
The findings indicate that the structural features of the composite belt drive contribute to partially absorbing dynamic loads, thereby reducing stresses on the shafts within the drive system. Additionally, an increase in the shafts' moments of inertia was found to prolong the machine assembly's startup time. Based on these results, the study provides recommendations on the interrelation of parameters such as M_c=100 Nm, M_0=4 Nm, c=20 Nm/rad, and b=8 Nms/rad, and their impact on the machine's dynamic performance.

Key words: belt transmissions, dynamic analysis, machine aggregates, feeder machine, fiber separation machine, moments of inertia, transmission ratios.

Introduction

The efficient operation of a working shaft in a technological process primarily depends on the dynamic parameters of the machine unit, including the moments of inertia of the masses, the dissipation properties of the elastic elements, and the influence of technological loads. To accurately determine these parameters, it is essential to study the dynamics of the machine unit with a belt transmission in both transient (static) and steady-state operating modes.

When conducting a dynamic analysis of a machine unit with a belt transmission, several key issues can be addressed:

- investigating external technological resistance: this involves examining how external factors-such as the weight force of the links, frictional forces, and the inertia force of the mechanism-affect the motion characteristics of both the driving and driven pulleys;
- reducing dynamic loads: identifying methods to minimize dynamic loads on the driving and driven pulleys while maintaining the required motion modes. This includes analyzing and regulating the relationships between motion regime parameters and the dynamic parameters of the machine unit under the influence of both external and internal forces.

Dynamic analysis of machine aggregates is crucial in studying the working mechanisms of technological machines, as it enables the assessment of how variations in external parameters affect the operation of the machine aggregate.

1. Analysis of scientific works and literature

A number of scientists, in their scientific research, do not consider dynamic factors based on static stresses and their extended models based on the accepted calculated models of reliability of belt drive machine units in failure or "stop" mode. In this case, dynamic equations for the system, taking into account dynamic loads and material properties, were proposed and studied depending on time. This takes into account the dynamic dependence of the machine unit during the "stopping" process and improper maintenance [1-3].

During operation in belt transmission, forces can be axial, transverse, and rotational. The analysis of forced and free oscillations occurring in a belt transmission was studied by comparing existing models. The influence of initial tension, the angular velocity of the shafts, bending stiffness, and reaction forces on the supports was discussed. Oscillations arising in belt drives were also considered, and the complex influence of factors was studied [2-7].

Material itself and the attenuation of vibration energy through the external tension system were taken into account. Using a closed system of equations of eigenvalues of the system, the dynamic problem of the hybrid model was solved. In this case, the numerical modeling method was used to account for the effectiveness of calculations. For each oscillatory mode, the optimal attenuation value has been determined. Analysis of the obtained results did not show that it is at this value that the oscillation is damped most rapidly [4,9,10].

In his research, M. I. Belov, based on experimental studies, studied the dependence of the values of the tractive forces arising in a belt drive consisting of driving and driven pulleys and a flat belt on the relative slippage of the belt on the pulley and the efficiency of the belt drive. A mathematical model has been developed that allows for a theoretical assessment of the dependence of the belt's traction capacity on the operating mode in the zone of elastic slippage of the belt along the pulley in the belt drive [5, 8, 10].

2. Main theoretical part

As an example of a machine aggregate with a belt transmission and composite pulleys, we consider the kinematic diagram of the 4DP-130 fiber separator machine, one of the key technological machines used in cotton processing plants. This machine features a PD-type composite feeder and serves as an illustrative model for the study. The kinematic diagram of the machine is presented in Figure 1 [11].

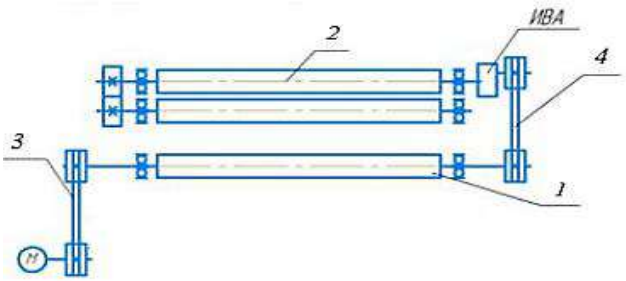

1 - spiked drum, 2 - feeding shaft, 3,4 - belt transmission

Fig. 1. - Kinematic diagram of the PD feeder machine unit of the 4DP-130 fiber separation machine

When the recommended composite driving pulley belt transmission is applied in the PD-type feeder of the 4DP-130 saw gin machine, this machine aggregate consists of a five-mass system (Figure 2).

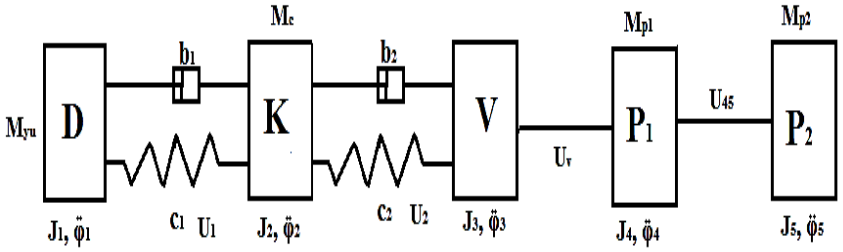

Fig. 2. - Dynamic model of the PD feeder machine unit of the 4DP-130 fiber separation machine with the recommended belt drive

In this case, the first mass represents the electric motor, the second mass corresponds to the spiked drum, the third mass denotes the IVA-type variator, while the fourth and fifth masses represent the PD-type feeder shafts. We assume that the specific elasticity of the belt remains constant in this scenario.

The external forces acting on the machine aggregate's mechanical system vary in nature and play different roles in the torsional-vibrational process. Initially, before the influence of external forces, the system is in equilibrium. However, when external forces are applied, they disturb this equilibrium, causing restoring forces to emerge as the system attempts to return to its original state. These restoring forces arise due to deviations from equilibrium and drive the system back toward its initial condition, leading to oscillations within the system.

Given that the pulleys in our case are composite (incorporating an elastic element), we assume that torsional-vibrational movements occur in the belt-driven machine. Here, restoring forces play a crucial role, acting as the primary factor in these oscillations. These forces originate from the elastic element of the pulley and exhibit an elastic nature.

In a linearly deformable system, the restoring force due to elasticity is proportional to the torsional deformation of the system. The connections between elastic elements are defined by a single parameter-the stiffness coefficient, which characterizes the rigidity of the elastic element within the pulley.

It should be noted that, in addition to restoring forces, frictional forces also arise within the elastic element. These frictional forces contribute to the dissipation (or dispersion) of mechanical energy, and are referred to as dissipative forces. In this context, the dissipative force in the elastic element of the compound pulley absorbs part of the system’s energy and reduces torsional vibrations in the shaft.

The characteristics of both restoring and dissipative forces depend entirely on the material properties of the elastic element within the belt drive pulley.

Furthermore, another category of forces, known as excitation forces, emerges during the operation of a belt-driven machine with composite pulleys. These forces are represented by explicit time-dependent functions, meaning they do not directly depend on the system's movement but actively influence it. For example, the unbalanced rotation of the driving shaft transmits a force to the conveyor belt, which serves as an excitation force.

As the mass of material transported by the conveyor belt periodically fluctuates, unbalanced rotation occurs in the driving shaft. In this scenario, external forces include the torque acting on the motor shaft and the loads exerted on the driving shaft, which are set into rotational motion through the belt drive.

I.S. Pinchuk, in his research on asynchronous motors, proposed treating these motors as dynamic mechanical systems [12,13].

$$\dot{M}_d = 2\dot{M}_k\omega_c - 2M_kP\dot{\varphi}_d - \omega_cS_kM_d \quad (1)$$

where M_d and M_k represent the torque of the electric motor and its critical value, respectively;

S_k is the critical slip in the electric motor; ω_c is the rotational frequency of the motor shaft.

The differential equations of motion for the belt-driven machine aggregate in the given system were derived using the second-order Lagrange equation [14].

$$\frac{d}{dt}\left[\frac{\partial T}{\partial \dot{\varphi}_i}\right] - \frac{\partial T}{\partial \varphi_i} + \frac{\partial \Pi}{\partial \varphi_i} + \frac{\partial \Phi}{\partial \dot{\varphi}_i} = M_i(\varphi_i) \quad (2)$$

where T – the kinetic energy of the system;

Π – the potential energy of the system;

Φ – Rayleigh's dissipative function;

φ_i – generalized coordinate;

$\dot{\varphi}_i$ – generalized velocity;

$M_i(\varphi_i)$ – generalized force.

The transmission ratio of the machine aggregate, including the drive mechanism of the feeding shafts, is determined as follows:

$$U_1 = \frac{\dot{\varphi}_1}{\dot{\varphi}_2};\ U_2 = \frac{D_2EF}{D_1(EF - S_0(e^{f(\beta \pm \Delta\beta)} - 1))}\sin\alpha;\ U_3 = U_v = \frac{\dot{\varphi}_3}{\dot{\varphi}_4};\ U_{45} = \frac{\dot{\varphi}_4}{\dot{\varphi}_5}; \quad (3)$$

where u_1, u_2, u_3, u_{45} – transmission ratios between the corresponding masses; $\dot{\varphi_1}$ – angular velocity of the electric motor shaft, $\dot{\varphi_2}$ – angular velocity of the spiked drum, $\dot{\varphi_3}$ – angular velocity of the IVA-type variator shaft, $\dot{\varphi_4}$ and $\dot{\varphi_5}$ – angular velocities of the feeder shafts; D_1 – diameter of the driving pulley in the belt transmission with a composite pulley, D_2 – diameter of the driven pulley in the belt transmission with a composite pulley; S_0 – initial tension force of the belt; F – cross-sectional area of the belt; E – modulus of elasticity; β – belt wrap angle around the pulley; $\Delta\beta$ – variable wrap angle of the composite driving pulley; f – coefficient of friction.

We accept the angular displacements of the rotating masses of the machine aggregate for generalized coordinates as φ_1, φ_2, φ_3, φ_4, and φ_5. The kinetic energy of the considered system has the following form:

$$T = \frac{J_1\dot{\varphi}_1^2}{2} + \frac{J_2\dot{\varphi}_2^2}{2} + \frac{J_3\dot{\varphi}_3^2}{2} + \frac{J_4\dot{\varphi}_4^2}{2} + \frac{J_5\dot{\varphi}_5^2}{2} \quad (4)$$

where J_1, J_2, J_3, J_4, J_5 – moments of inertia of the electric motor and working parts.

The potential energy of the system is a homogeneous quadratic form of generalized coordinates and is written as follows:

$$\Pi_1 = \frac{1}{2}[c_1 \cdot (\varphi_1 - U_1 \cdot \varphi_2)^2];\Pi_2 = \frac{1}{2}[c_2 \cdot (\varphi_2 - U_2 \cdot \varphi_3)^2] \quad (5)$$

For the given system, the Rayleigh dissipative function is expressed as follows:

$$\Phi_1 = \frac{1}{2}[b_1 \cdot (\dot{\varphi}_1 - U_1 \cdot \dot{\varphi}_2)^2];\ \Phi_2 = \frac{1}{2}[b_2 \cdot (\dot{\varphi}_2 - U_2 \cdot \dot{\varphi}_3)^2] \quad (6)$$

where c_1, c_2, b_1, and b_2 are the stiffness and dissipations of the belt drive.

We determine the conditions of the Lagrange equations:

a) derivatives of the kinetic energy of the machine aggregate

$$\frac{d}{dt}\left(\frac{\partial T}{\partial \dot{\varphi}_1}\right) = J_1\ddot{\varphi}_1;\ \frac{d}{dt}\left(\frac{\partial T}{\partial \dot{\varphi}_2}\right) = J_2\ddot{\varphi}_2;\ \frac{d}{dt}\left(\frac{\partial T}{\partial \dot{\varphi}_3}\right) = J_3\ddot{\varphi}_3;\ \frac{d}{dt}\left(\frac{\partial T}{\partial \dot{\varphi}_4}\right) = J_4\ddot{\varphi}_4;\ \frac{d}{dt}\left(\frac{\partial T}{\partial \dot{\varphi}_5}\right) = J_5\ddot{\varphi}_5 \quad (7)$$

b) partial derivatives of displacements from the potential energy

$$\frac{\partial \Pi_1}{\partial \varphi_1} = c_1 \cdot (\varphi_1 - U_1\varphi_2);\ \frac{\partial \Pi_1}{\partial \varphi_2} = -c_1U_1 \cdot (\varphi_1 - U_1\varphi_2);$$
$$\frac{\partial \Pi_2}{\partial \varphi_2} = c_2 \cdot (\varphi_2 - U_2\varphi_3);\ \frac{\partial \Pi_2}{\partial \varphi_3} = -c_2U_2 \cdot (\varphi_2 - U_2\varphi_3) \quad (8)$$

c) partial derivatives of the dissipative function with respect to velocities

$$\frac{\partial \Phi_1}{\partial \dot{\varphi}_1} = b_1 \cdot (\dot{\varphi}_1 - U_1 \cdot \dot{\varphi}_2);\ \frac{\partial \Phi_1}{\partial \dot{\varphi}_2} = -b_1 U_1 \cdot (\dot{\varphi}_1 - U_1 \cdot \dot{\varphi}_2)$$
$$\frac{\partial \Phi_2}{\partial \dot{\varphi}_2} = b_2 \cdot (\dot{\varphi}_2 - U_2 \cdot \dot{\varphi}_3);\ \frac{\partial \Phi_2}{\partial \dot{\varphi}_3} = -b_2 U_2 \cdot (\dot{\varphi}_2 - U_2 \cdot \dot{\varphi}_3) \quad (9)$$

d) moment:

$$M(\varphi_1) = M_d;\ M(\varphi_2) = M_c;\ M(\varphi_3) = M_c + M_0 Sin(at);$$
$$M(\varphi_4) = M_{34} - M_{p1};\ M(\varphi_5) = M_{45} - M_{p2} \quad (10)$$

where M_c – the tension force moment of the belt in the belt drive;

M_0 - the moments of the deformation forces of the flexible element of the composite pulley,

M_{34} and M_{45} are the fourth and fifth moments of a five-mass machine unit, representing the moments generated on the feeder shafts due to technological resistance.

For this machine aggregate, the mathematical model recommended by A.E. Levin [15] was used to determine the dynamic mechanical characteristics of the electric drive, based on the second-order Lagrange equation. The system of differential equations describing the motion of the machine aggregate is as follows:

$$\dot{M}_d = 2\dot{M}_k \omega_c - 2M_k P \dot{\varphi}_d - \omega_c S_k M_d;$$
$$J_1 \ddot{\varphi}_1 = M_d - c_1(\varphi_1 - u_1\varphi_2) - b_1(\dot{\varphi}_1 - u_1\dot{\varphi}_2);$$
$$J_2 \ddot{\varphi}_2 = u_1 c_1(\varphi_1 - u_1\varphi_2) + u_1 b_1(\dot{\varphi}_1 - u_1\dot{\varphi}_2) - c_2(\varphi_2 - u_2\varphi_3) - b_2(\dot{\varphi}_2 - u_2\dot{\varphi}_3) - M_c;$$
$$J_3 \ddot{\varphi}_3 = u_2 c_2(\varphi_2 - u_2\varphi_3) + u_2 b_2(\dot{\varphi}_2 - u_2\dot{\varphi}_3) - M_c + M_0 Sin(at);$$
$$J_4 \ddot{\varphi}_4 = u_3 M_c - M_{34} - M_{p1};\ J_5 \ddot{\varphi}_5 = u_{45} M_{45} - M_{p2} \quad (11)$$

During the operation of a belt-driven machine aggregate with composite pulleys (incorporating an elastic element), the entire system is subjected to periodic loading. This influences the reduction of oscillations in the working shaft and causes variations in the transmission ratio of the belt drive due to the impact of external technological resistance (working force).

In our study, we analyze the dynamics of a belt-driven machine aggregate with composite pulleys under two key operating modes:

- the startup mode of the system;
- the steady-state operation of the system.

3. Main practical part

Particular attention is given to angular velocity oscillations and technological resistance in the machine aggregate's drive mechanism. The primary objective of this dynamic analysis is to determine the motion laws governing the system's components and the associated resistances while considering the acting forces. Next, let us examine the forces acting on the belt-driven machine aggregate with composite pulleys.

Investigation of the motion modes of the parameters of the 4DP-130 cotton cleaning machine drive system with a composite driving pulley belt transmission and the forces acting on the system using a computer. The dynamic problem of the proposed flat belt drive composite machine aggregate was implemented in the *"Mathcad"* software using modern computer technologies and a numerical method for solving the system of linear differential equations.

To solve the mathematical model of the flat belt drive composite machine aggregate in computer programs, we introduce some notations and define the following designations:

$$M_g(t) = y_1(t);\ \dot{M}_g(t) = \dot{y}_1(t);$$
$$\varphi_1(t) = y_2(t);\ \dot{\varphi}_1(t) = \dot{y}_2(t) = y_3(t);\ \ddot{\varphi}_1(t) = \dot{y}_3(t);$$
$$\varphi_2(t) = y_4(t);\ \dot{\varphi}_2(t) = \dot{y}_4(t) = y_5(t);\ \ddot{\varphi}_2(t) = \dot{y}_5(t);$$
$$\varphi_3(t) = y_6(t);\ \dot{\varphi}_3(t) = \dot{y}_6(t) = y_7(t);\ \ddot{\varphi}_3(t) = \dot{y}_7(t);$$
$$\varphi_4(t) = y_8(t);\ \dot{\varphi}_4(t) = \dot{y}_8(t) = y_9(t);\ \ddot{\varphi}_4(t) = \dot{y}_9(t);$$
$$\varphi_5(t) = y_{10}(t);\ \dot{\varphi}_5(t) = \dot{y}_{10}(t) = y_{11}(t);\ \ddot{\varphi}_5(t) = \dot{y}_{11}(t)$$

After determining the parameters, calculations for the equation of motion of the composite machine unit with a flat belt transmission were performed using the "Mathcad" software.

The selection of the electric motor was based on the research results provided in [11]. The movement of the working part of the flat belt drive composite machine aggregate mechanism is carried out using a 4A132S4Y3 asynchronous electric motor, which has the following parameters:

P=2,2 kVt- nominal power of the motor; n=1456,5 min^{-1} - nominal rotational speed of the motor shaft; $M_к=M_н \cdot 3=43{,}36$ Nm, $M_к$ – critical (maximum) torque of the motor shaft; $M_n=9550 \cdot (P/n)=9550 \cdot (2{,}2/1456{,}5)=14{,}46$ Nm, M_n – nominal torque of the motor shaft; $f_c=50$, Gs- frequency; P=2- number of pole pairs.

The calculation of the required parameters and coefficients of the motor was carried out using the following formulas [11]

System rotational frequency: $\omega_c=2\pi f_c=314$ rad/s. Nominal angular velocity of the electric motor shaft: $\omega_n=\pi n/30=3{,}14 \cdot 1456{,}5/30=152{,}447$ rad/s. Angular velocity of the electric motor rotor in ideal no-load operation:

$\omega_o=2\pi f_c/P=2\cdot3,14\cdot50/2=157$ rad/s. Moment of inertia of the electric motor rotor: $J_1=0,028$ kg·m^2. Nominal slip value: $S_n=2,9\%$. Critical slip value: $S_k=19,5\%$. Mine the moments of inertia of the shafts of the PD type feeding device of a belt-driven saw machine by calculating them, where:

spike drum: d = 400 mm; L = 4000 mm; thickness S = 4 mm; GOST 10704-91.

$$V = d \cdot L \cdot S = 0,4 \cdot 4 \cdot 0,004 = 0,0064\ m^3;$$

When the steel density is ρ=7700 ÷ 7900 kg/m^3,

$$m = \rho \cdot V = 7850 \cdot 0,0064 = 50,24\ kg$$

$$J = m \cdot r^2 = 50,24 \cdot (0,2)^2 = 2,0096\ kg \cdot m^2$$

- feeder drums: d=140mm; L=4000mm; S=3mm.

$$V = d \cdot L \cdot S = 0,14 \cdot 4 \cdot 0,003 = 0,00168\ m^3;$$

$$m = \rho \cdot V = 7850 \cdot 0,00168 = 13,188\ kg$$

$$J = m \cdot r^2 = 13,188 \cdot (0,07)^2 = 0,065\ kg \cdot m^2$$

IVA-type variator shaft: d=40mm; r=20mm=0,02m; L=0,5m; m=4,9325kg; F=12,566 sm^2, GOST 2590-2006

$$J = \frac{1}{2} m \cdot r^2 = \frac{4,9325 \cdot (0,02)^2}{2} = 0,00099\ kg \cdot m^2$$

Moments of inertia of all shafts of the machine aggregate: J_1 = 0,028 kgm^2; J_2 = 2,0096 kgm^2; J_3 = 0,099 kgm^2; J_4 = 0,065 kgm^2; J_5 = 0,065 kgm^2

To find the relationship between the dynamic parameters of the machine aggregate and its motion modes, we apply the following variations to the values:

- rigidity coefficient of the flexible element: c=20÷40 Nm/rad
- dissipation coefficient of the flexible element: b=8÷16 Nms/rad

The range of variation of the coefficient values characterizing the flexible element was determined based on experimental results for different types of rubber [16].

When studying the dynamics of the PD feeder machine aggregate of the 4DP-130 fiber-separating machine with the recommended composite belt drive, the influence of the composite pulley parameters on the operation of the feeder rollers and the variator shaft was analyzed [7]. In this study, the transmission ratio between the electric motor and the pinned drum was taken as $U_1 = 2$, the average transmission ratio of the variators as $U_3 = 10$, and the transmission ratio between the feeder shafts as $U_{45} = 1$.

From the kinematic scheme of the PD-type feeder of the saw gin and the corresponding dynamic model of the aggregate, it can be observed that the proposed belt drive is installed between φ_2 and φ_3. If φ_4 and φ_5 are considered as the working shafts of the feeder, then the technological resistances from seed and cotton can be taken into account through M_{p1} and M_{p2}. The values of M_{p1} and M_{p2} depend on the loads exerted by seed and cotton.

It is known from the technological process that the feeder shafts rotate at the same angular velocity. Therefore, it can be assumed that their loads are also identical. The main issue of interest is the effect of the loads generated by the technological resistances in the feeder rollers on the angular accelerations of the variator shaft. In studying the dynamics of the considered machine aggregate, to account for the random technological resistances generated by seed due to cotton, we used the mathematical expression $M_c + M_0 \sin(\alpha t)$ in the calculations.

4.Results and discussions

In the analysis of the given dynamic model (Figure 2), the transition process of the machine aggregate under the influence of external loads is of interest, particularly the establishment of oscillations in the angular velocities of the working shaft masses. The main parameter in this case is the time spent on the transition process (Δt), which depends on the parameters of the machine aggregate. When the technological resistance changes, it affects the masses $M_d, \ddot{\varphi}_1, \ddot{\varphi}_2,$ and $\ddot{\varphi}_3$, causing a sharp decrease in their values. After a certain period, these oscillations subside, and this exact time Δt is considered as the time required for the velocity transition process.

In analyzing the data obtained from studying the dynamics of the flat belt drive composite machine aggregate, the variation and interrelation of the belt tension force (M_c), the deformation (M_0) and stiffness (c) of the flexible element of the composite pulley, as well as dissipation (b), are taken into account. The variated values are presented in Table 1 below.

Table 1. Data obtained from studying the dynamics of the flat belt drive

M_c (Nm)	80	100	120
M_0 (Nm)	4	8	12
c (Nm/rad)	20	30	40
α (grad)	π/2	π/4	π/6

In the belt drive system with a composite pulley containing a flexible element, the variation in belt tension (M_c) is considered as a factor affecting the load changes on the working shaft. It is known that changes in belt tension are primarily influenced by variations in the torsional moment on the shafts. The fluctuation in tension depends on the coefficient of friction generated between the belt and the pulleys. The belt tension force (M_c) formed during operation can be analyzed based on a harmonic (sinusoidal) law, reflecting the nature and magnitude of load variations.

The dynamic problem of the proposed flat belt drive composite machine aggregate was solved using a system of linear differential equations by employing numerical methods in the *"Mathcad"* software, utilizing modern computer technologies.

Based on the obtained solution, the oscillation range of the velocities and rotational irregularities for each shaft ($\dot{\varphi}_1, \dot{\varphi}_2, \dot{\varphi}_3, \dot{\varphi}_4, \dot{\varphi}_5$) were determined, along with the variation graphs of the angular velocities of the electric motor (M_d). In Figure 3, the belt drive system with a composite transmission is illustrated, showing the torque on the electric motor shaft and the variation graphs of the angular velocities of the shafts.

The operation process of machine units is divided into three stages: "Startup," "Operation," and "Shutdown." It is well known that the highest load occurs during the "Startup" phase, during which the torque (M_d) on the motor shaft reaches its maximum value. At this stage, the inertia moments of the shafts are the primary influencing factor, while technological loads must also be considered.

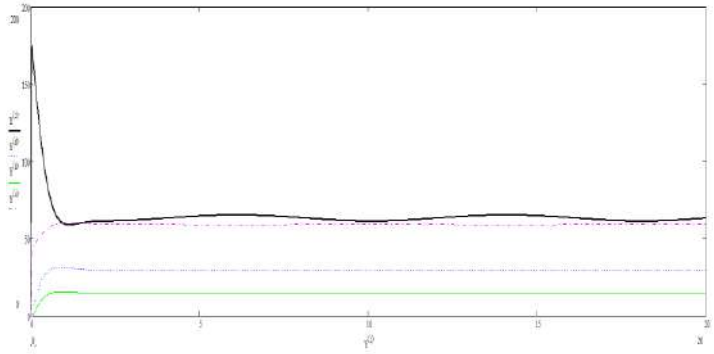

$Y^{(1)}$-time (s); $Y^{(2)}$-torgue on the shaft of the electric motor (Nm); $Y^{(4)}$, $Y^{(6)}$,$Y^{(8)}$-oscilliation rangers of the angular velocities of the first, second and third masses, respectively (*m/s²)*

Fig 3. - Graphs of the variation of the torsional moment on the electric motor shaft and the angular velocities of the shafts in the belt-driven transmission system

We analyze the theoretical research based on the variable values presented in Table 1, considering their interdependencies. The solution was obtained for all variation cases, and to study the results, the oscillation range of the driving motor shaft torque (M_d) and the angular accelerations of the shafts ($\ddot{\varphi}_1, \ddot{\varphi}_2, \ddot{\varphi}_3, \ddot{\varphi}_4, \ddot{\varphi}_5$) during the "Startup" process was examined. The calculated values are summarized in Table 2, where only the values for Mc = 80 are presented. Similarly, the calculated values were also obtained for Mc = 100 and Mc = 120.

Table 2.Oscillation range of the driving motor shaft torque (Md) and the angular accelerations of the shafts

ΔMd		C2=20	C2=30	C2=40
M_0=4	*p/2*	116,43	116,42	116,42
	Δt	1,115	1,15	1,115
	p/4	116,09	116,40	116,08
	Δt	1,13	1,115	1,13
	p/6	115,88	116,07	115,87
	Δt	1,13	1,13	1,125
M_0=8	*p/2*	117,47	117,48	117,49
	Δt	1,125	1,13	1,155
	p/4	116,81	116,82	116,83
	Δt	1,16	1,165	1,155
	p/6	116,37	116,38	116,38
	Δt	1,155	1,155	1,155
M_0=12	*p/2*	118,55	118,56	117,59
	Δt	1,12	1,12	1,16
	p/4	116,90	117,56	117,58
	Δt	1,15	1,16	1,16
	p/6	116,91	116,92	116,92
	Δt	1,15	1,15	1,15

$\Delta\varphi_1$		C2=20	C2=30	C2=40
M_0=4	*p/2*	0,7967	0,7958	0,7958
	Δt	3,07	3,07	3,07
	p/4	0,7219	0,7262	0,7334
	Δt	6,06	6,06	6,06
	p/6	0,6983	0,6975	0,7075
	Δt	9,055	9,055	9,055
M_0=8	*p /2*	1,129	1,131	1,1305
	Δt	3,085	3,085	3,08
	p /4	1,0066	1,0075	1,009
	Δt	6,06	6,06	6,065
	p /6	0,934	0,936	0,935
	Δt	9,07	9,065	9,055
M_0=12	*p /2*	1,4655	1,4661	1,47
	Δt	3,08	3,08	3,08
	p /4	1,2852	1,283	1,2845
	Δt	6,06	6,06	6,06
	p /6	1,1752	1,176	1,176
	Δt	9,055	9,055	9,055

Continuation of table 2

$\Delta\varphi_2$		C2=20	C2=30	C2=40
M_0=4	*p/2*	1,9711	1,9694	1,9695
	Δt	2,685	2,695	2,685
	p/4	1,8836	1,8869	1,882
	Δt	5,63	5,63	5,63
	p/6	1,8525	1,8508	1,8574
	Δt	8,575	8,575	8,575
M_0=8	*p/2*	2,214	2,216	2,18
	Δt	2,76	2,76	2,76
	p/4	2,046	2,049	2,05
	Δt	5,64	5,64	5,635
	p/6	1,984	1,986	1,986
	Δt	8,57	8,57	8,57
M_0=12	*p/2*	2,4638	2,4653	2,4672
	Δt	2,775	2,775	2,775
	p/4	2,2132	2,2157	2,2173
	Δt	5,63	5,63	5,63
	p/6	2,1222	2,1239	2,1239
	Δt	8,575	8,575	8,575

$\Delta\varphi_3$		C2=20	C2=30	C2=40
M_0=4	*p/2*	1,0178	0,9748	0,9748
	Δt	2,455	2,45	2,45
	p/4	0,9609	0,9297	0,8996
	Δt	5,245	5,17	5,17
	p/6	0,9254	0,8734	0,8702
	Δt	8,09	7,97	7,97
M_0=8	*p/2*	1,0505	1,1627	1,1869
	Δt	2,515	2,515	2,525
	p/4	0,882	1,0219	1,0622
	Δt	5,085	5,17	5,24
	p/6	0,8084	0,9631	0,9631
	Δt	7,795	7,97	7,97
M_0=12	*p/2*	1,3502	1,3569	1,3599
	Δt	2,535	2,555	2,555
	p/4	1,0257	1,1445	1,1737
	Δt	5,09	5,17	5,24
	p/6	1,0561	1,0972	1,0972
	Δt	7,965	8,085	8,085

Analysis based on tabulated values shows that the designated startup time for motors ranges from 0,1 ÷ 0.15 seconds. However, considering additional rotating masses, including the parameters of the composite pulley belt drive, this value (*Δt*) increases to the range of 1,1 ÷ 1,2 seconds. Naturally, to reduce the startup time of the flat belt-driven machine unit, it is possible to decrease the moment of inertia of the rotating masses within the machine unit.

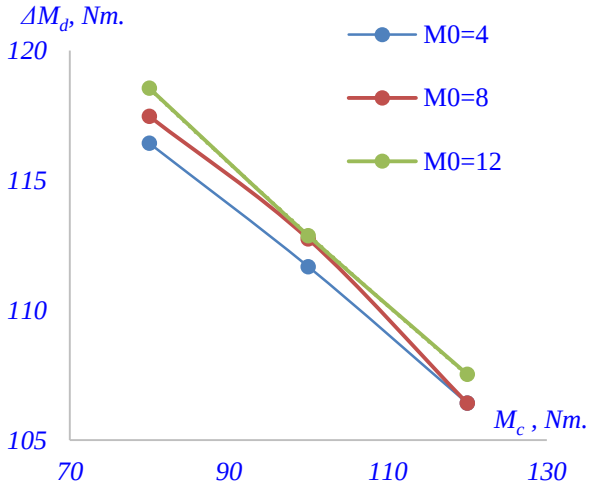

M_0=4 ΔMd	M_0=8 ΔMd	M_0=12 ΔMd
116,432	117,471	118,5524
111,6794	112,7448	112,8725
106,421	106,421	107,5332

Fig. 4. - Graph of the dependence of the engine torque on the belt tension force

The main factor of interest is the effect of the recommended belt drive parameter variations on the dynamics of the machine unit. Based on this, our further analysis is focused on this aspect. In this study, the variation in belt tension (voltage) (M_c) and the deformation of the elastic element due to load (M_0) were considered. Additionally, to account for the stiffness of the elastic element in the composite pulley, the stiffness coefficient (c) and the damping (dissipation) factor (b) were also analyzed (Figure 4). For example, when the value of (M_c) changes from 80 Nm to *120 Nm* and M_0 = *4*, the difference between the peak and nominal values of torque ΔM_d during the "Startup" process decreases from *116,4 Nm* to *106,0 Nm*. However, the time required for the transition (Δt_1) increases from 1,11 seconds to 1,15 seconds.

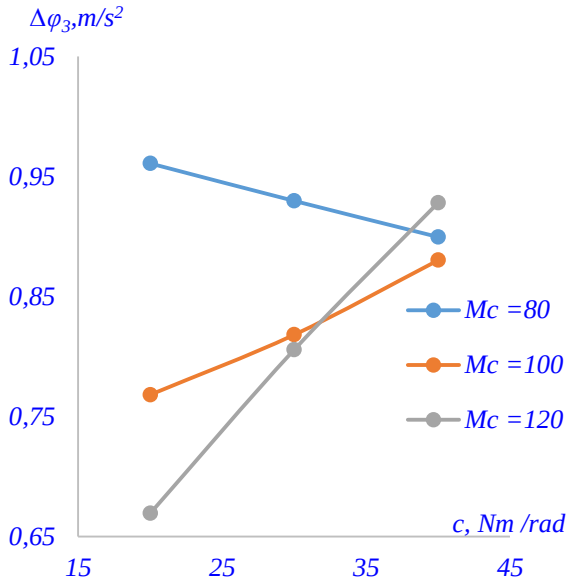

M_c =80	M_c =100	M_c=120
0,9609	0,7681	0,6692
0,9297	0,8181	0,8056
0,8996	0,8802	0,9281

Fig. 5. - The graph of the dependence of $\ddot{\varphi}_3$ on the stiffness coefficient of the elastic element when M_0 = 4 and p/4 is given

The relationship between the parameters of the elastic element, specifically the stiffness "c," was analyzed in the range of 20 Nm/rad to 40 Nm/rad depending on (M_c). The effect is most noticeable in ($\ddot{\varphi}_3$) (Figure 5). For example, when M_c = 80 Nm, the changes in ($\ddot{\varphi}_1$) and ($\ddot{\varphi}_2$) are insignificant, but the value of $\Delta\ddot{\varphi}_3$ decreases from 0,96 m/s² to 0,897 m/s². Conversely, when M_c=120 Nm, the value of $\Delta\ddot{\varphi}_3$ increases from 0,66 m/s² to 0,92 m/s².

If we analyze the variation of M_c based on the harmonic law (Figure 6), i.e., when α changes from π/2 to π/6, with M_c = 80 Nm and M_0 = 4 Nm, ($\Delta\ddot{\varphi}_3$) decreases from 1,01 to 0,92. Similarly, when M_c = 120 Nm and M_0 = 4 Nm, ($\Delta\ddot{\varphi}_3$) decreases from 0,80 to 0,58.

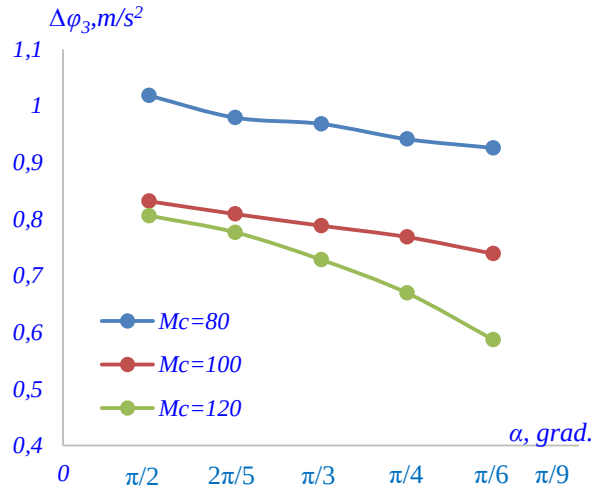

α	M_c=80	M_c =100	M_c =120
π/2	1,0178	0,8313	0,8058
2π/5	0,9789	0,8087	0,7764
π/3	0,9679	0,7881	0,7281
π/4	0,9409	0,7681	0,6692
π/6	0,9254	0,7387	0,587

Fig. 6. - The graph of the dependence of $\ddot{\varphi}_3$ on the harmonic variation of the load M_c.

Conclusion

By utilizing the constructive features of the recommended belt transmission, it is possible to partially absorb (dampen) the dynamic loads generated by the rotating masses within the machine aggregate. This, in turn, helps reduce the loads on the shafts within the drive system. The analysis of the research results indicates that an increase in the inertia moments of the shafts leads to an increase in the "Startup" time of the machine aggregate. In this case, reducing the equivalent inertia moment of the motor shaft has a stronger effect compared to reducing the inertia moments of the subsequent shafts.

Within the scope of studying the dynamics of the above-mentioned flat belt transmission machine aggregate, the conducted research and analysis of the results suggest that it is possible to recommend considering the variation and interrelation of the belt tension force (M_c=*100Nm*), the deformation of the compliant element of the composite pulley (M_0=*4*), stiffness (*c=20* Nm/rad), and dissipation (*b=8* Nms/rad) within the given range.

References

[1] Gao P., Xie L., & Pan J. Reliability and availability models of belt drive systems considering failure dependence //Chinese Journal of Mechanical Engineering, 2019, 32, P.1-12.
[2] Abrate S. Vibrations of belts and belt drives. Mechanism and machine theory, 1992, 27(6), P. 645-659.
[3] Li X. J., Chen L. Q. Modal analysis of coupled vibration of belt drive systems //Applied Mathematics and Mechanics, 2008, 29(1), 9-13.
[4] Lixin Zhang, Jean W. Zu, Zhi-chao Hou Complex Modal Analysis of Non-Self-Adjoint Hybrid Serpentine Belt Drive Systems // Journal of Vibration and Acoustics, 2001, 123(2) DOI:10.1115/1.1356697
[5] Belov M. I. To calculate the belt drive. Universum: Technical sciences, 2017,(5 (38)), P. 16-24.
[6] Wilson A., Green T. Belt Drives in Modern Mechanical Systems: Design and Optimization. Berlin: Springer. 2022. – 356 p.
[7] Yunusov S., Kenjayev S. N., Makhmudova S. A. Shafts of technological machines with combined supports // E3S Web of Conferences, 2023, Vol. 401, p. 01059
[8] Kenjayev S., Yunusov S., Abdurakhimov M., Ahmedova D. Influencing engagement angle on power parameters in flat-belt gears // E3S Web of Conferences, 2023, Vol. 401, p. 05005
[9] Kumaran V. U. Analytical flat belt drive model considering bilinear elastic behaviour with residual strains //Mechanism and Machine Theory, 2023, vol.190, P.123-134
[10] Hamasaki Y. Energy saving technology of flat belts: Meandering control of belts //Toraibarojisuto Journal of Japanese Society of Tribologists, 2018, 63(8), P.532 - 538.
[11] Juraev A. Dynamics of working mechanisms of cotton processing machines. – T.: Fan, 1987. – 168 p.
[12] Juraev A. Modeling the dynamics of machine units of cotton processing machines. – T.: Fan, 1984, 128 p.
[13] Gurin M.A. On the choice of optimal drive parameters of a vibration-impact mechanism. Mechanics of cars. Vol. 33-34. Moscow: Nauka Publ., 1972, pp. 75-84.
[14] Yunusov S. Z. and others. Patent RUzb. FAP00385, Byul. No. 8. 08/29/2008 Working chamber of the saw gin.
[15] Feridman M.V. The moment of inertia of bodies. – M.: Mashinostroenie, 1977. - 511 p.
[16] Yunusov S.Z., Kenjayev S.N., Makhmudova Sh.A., Islamova G.X. Full factorial experiment in research the parameters of a combined shaft of technological machines //E3s Web of Conferences, 2023, 401, 03043. 10.1051/e3sconf/202340103043
[17] Turakulov M., N. Tursunov and S. Yunusov, "New concept of cast iron melting technology in induction crucible furnace", E3S Web of Conferences, 2023, 401, 01060https://doi.org/10.1051/e3sconf/202340101060.
[18] Ziyamukhamedova U., Wasil S., Kumar S., Sehgal R., Wani M. F., Singh C. S., Gupta H. S. Investigating Friction and Antiwear Characteristics of Organic and Synthetic Oils Using h-BN Nanoparticle Additives: A Tribological Study //Lubricants, 2024, 12(1). https://doi.org/10.3390/lubricants12010027.
[19] Tursunov T., Tursunov N., Urazbayev T. Investigation of heat exchange processes in the lining of induction furnaces //E3S Web of Conferences, 2023, 401, 05029 (2) https://doi.org/10.1051/e3sconf/202340105029.
[20] Valieva D., Yunusov S., Tursunov N. Study of the operational properties of the bolster of a freight car bogie //E3S Web of Conferences, 2023, 401, 05017 https://doi.org/10.1051/e3sconf/202340105017.
[21] Toirov O., Tursunov N. Efficiency of using heat-insulating mixtures to reduce defects of critical parts //E3S Web of Conferences 401, 2023, 05018 https://doi.org/10.1051/e3sconf/202340105018.
[22] Urazbayev T., Tursunov N., Tursunov T. Steel modification modes for improving the cast parts quality of the rolling stock couplers", AIP Conf. Proc., 2024, 3045, 060015 https://doi.org/10.1063/5.0197361.
[23] Seydametov S.R., Tursunov N.K., Alimukhamedov S.P. Development of out-of-furnace steel treatment technology for the manufacture of railroad transport parts //AIP Conf. Proc., 2024, 3045, 060022 https://doi.org/10.1063/5.0197429.
[24] Turakulov M., Tursunov N., Yunusov S. Steeling of synthetic cast iron in induction crucible furnace taking into account consumption rate of carburizers //E3S Web of Conferences, 2023, 401, 05012 https://doi.org/10.1051/e3sconf/202340105012.

Information of the authors

Yunusov Saloxiddin Zununovich, d.t.s., professor, Tashkent State transport University
e-mail: ysz1979@mail.ru

Kenjayev Sirojiddin Nematullayevich, doctoral student, senior lecturer, Tashkent State transport University
e-mail: dilafruz.kasimova.19880110@mail.ru

Kasimova Dilafruz Alisherqizi., doctoral student, senior lecturer, Andijan Institute of Technology, Andijan, Uzbekistan
e-mail: xpert_01@bk.ru

DOI 10.52209/2706-977X_2025_4_46 **IRSTI 81.09.03** **UDC 669.11**

Hydrogen Reduction of Mill Scale for Iron Powder Production

Arystanova D.M.[1]*, Zholdubaeva Zh.D.[1], Lopatin V.Yu.[2], Matkarimov S.T[3]
[1]Abylkas Saginov Karaganda Technical University named after, Karaganda, Kazakhstan
[2]National University of Science and Technology MISIS, Moscow, Russia
[3]Tashkent State Technical University, Tashkent, Uzbekistan
*corresponding author

Abstract. This study explores the hydrogen reduction of industrial mill scale as a method for obtaining iron powder suitable for powder metallurgy applications. Mill scale, a by-product of hot rolling, was subjected to reduction in a hydrogen atmosphere at 800 °C, 900 °C and 1000 °C for 60 minutes under isothermal conditions. The chemical composition of the obtained products was analyzed using scanning electron microscopy (SEM) and energy-dispersive X-ray spectroscopy (EDX). The results demonstrate that reduction at 800 °C produces sponge iron with approximately 95 wt.% Fe, accompanied by residual oxygen and calcium. At 900 °C, variations in impurity distribution were observed, reflecting the heterogeneous structure of the raw scale. The highest degree of reduction occurred at 1000 °C, where the iron content exceeded 98 wt.% and no harmful impurities such as sulfur or phosphorus were detected, although localized oxide inclusions remained. The findings confirm the feasibility of recycling mill scale through hydrogen reduction, providing both ecological benefits and economic advantages by converting metallurgical waste into valuable feedstock for powder metallurgy.

Keywords: iron powder, hydrogen reduction, mill scale, waste recycling, powder metallurgy.

Introduction

Mill scale, a solid by-product generated during hot rolling of steel, is composed mainly of iron oxides - hematite (Fe_2O_3), magnetite (Fe_3O_4), and wüstite (FeO) - with a total iron content of up to 70–75%. Despite this, it is often treated as waste, resulting in large-scale storage and associated environmental concerns. Recycling mill scale as a raw material for powder metallurgy aligns with the principles of sustainable metallurgy and the circular economy [1–3].

Hydrogen metallurgy is considered a promising alternative to conventional carbon-based reduction methods. Unlike carbonaceous reductants that introduce impurities and generate CO_2 emissions, hydrogen allows for the production of high-purity metallic iron with significantly lower environmental impact [4, 5]. The thermodynamics of hydrogen reduction are favorable at elevated temperatures, as the equilibrium constants of endothermic reactions increase with temperature, thereby enhancing reduction efficiency [6].

Recent studies have shown the potential of hydrogen reduction in laboratory and pilot-scale conditions. Han and Lee [7] emphasized that the kinetics of hydrogen reduction improve considerably with temperature. Zhang et al. [8] highlighted hydrogen metallurgy as a viable low-carbon pathway for steelmaking. Iwase et al. [9] demonstrated successful hydrogen-based reduction of Fe-containing oxides [10] for powder metallurgy applications [11]. However, research directly targeting the recycling of industrial mill scale into iron powder remains limited, leaving a technological gap.

The aim of this study is to evaluate the reduction behavior of mill scale under hydrogen atmospheres at 800–1000 °C, to analyze the composition of the reduced powders, and to assess the feasibility of this process for industrial powder metallurgy.

1. Materials and Methods

The material used in this study was iron scale, obtained as a by-product of steel production. The scale was received in powder form and mainly consisted of iron oxides. Before the experiments, the powder was carefully prepared and placed in ceramic boats for reduction.

The reduction process was performed in a tubular furnace under a continuous flow of high-purity hydrogen (99.999%). Three different temperatures were selected for the experiments: 800, 900, and 1000 °C. At each temperature, the sample was held isothermally for 60 minutes to ensure sufficient reduction time. The height of the powder layer in the boats was kept at approximately 10 mm to provide uniform heating and effective gas–solid contact.

After reduction, the samples were cooled inside the furnace in a hydrogen atmosphere to avoid secondary oxidation. The obtained powders were then subjected to analysis. Their chemical composition and phase distribution were determined using scanning electron microscopy (SEM) combined with energy-dispersive X-ray spectroscopy (EDX), which allowed both bulk analysis and point microanalysis of selected particles [12].

2. Results and Discussion

The initial scale was reduced at three temperatures: 800, 900 and 1000 °C in the hydrogen environment with the same isothermal holding time of 60 minutes. The height of the powder scale filling in the boat was 10 mm [13]. Figure 1 shows the appearance of the iron sponge made of scale reduced by hydrogen at 800 °C. An assessment of its chemical composition based on energy-dispersive analysis data is given in Table 1.

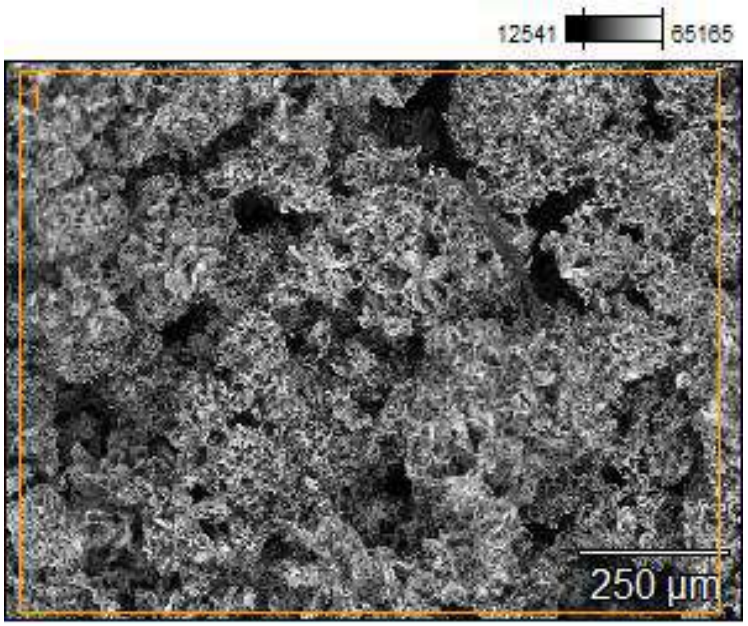

Fig.1. – Iron sponge made of scale reduced by hydrogen at 800 °C

Table 1. Elemental composition of iron sponge made of scale reduced by hydrogen at 800 °C

Element	O	Si	Ca	Mn	Fe
Content, wt. %	1.2	0.5	1.2	1.3	95.8

It can be seen from the presented results that the reduced iron powder has a fairly high content (total) of oxygen and calcium. At the same time, no harmful impurities of sulfur and phosphorus were found in it. Manganese was also found in the composition.

After reduction, the sponge was quite strong (from the point of view of its transportation for subsequent treatment), however, it was easily ground in a rotating ball mill [14].

The results of scale reduction at 900 °C are shown in Figures 2 and 3 (appearance) and in Tables 2 and 3 (chemical composition assessment).

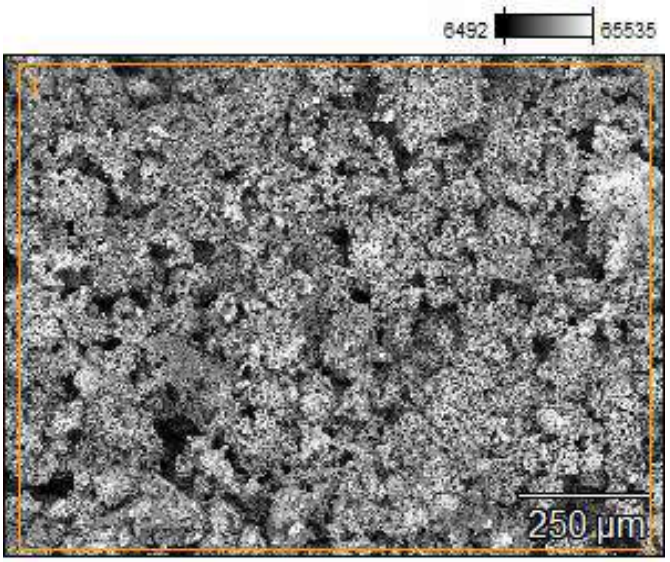

Fig.2. – Iron sponge from scale reduced at 900 °C by hydrogen (first series)

Table 2. Elemental composition of the iron sponge made of scale by oxygen reduction at 900 °C (first series)

Element	O	Si	S	Ca	V	Fe	Ni
Content, wt. %	2.1	0.6	0.5	1.3	4.4	89.8	1.2

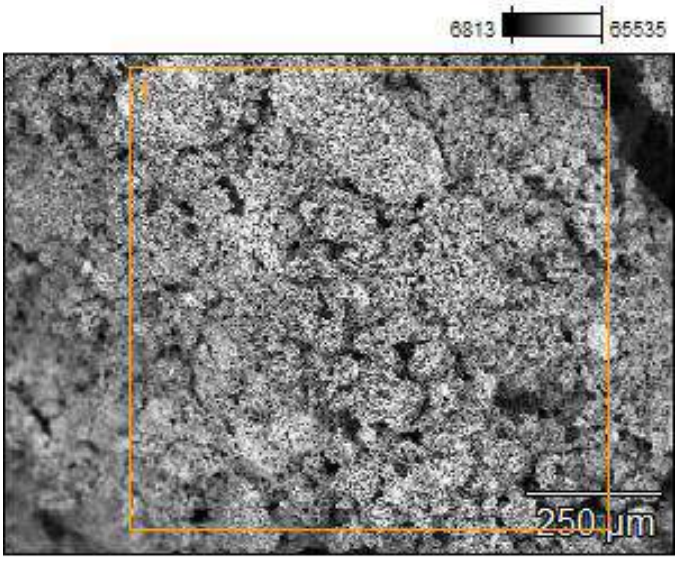

Fig.3. – Iron sponge from scale reduced at 900 °C by hydrogen (second series)

Table 3. Elemental composition of iron sponge obtained using scale reduced by hydrogen at 900 °C (second series)

Element	O	Si	Ca	Mn	Fe
Content, wt. %	1.5	0.6	1.4	1.2	95.3

After scale reduction at 900 °C in the first series, the amount of oxygen and calcium remained virtually unchanged compared to scale reduction at 800 °C. However, in this case, sulfur, vanadium, and nickel were detected in the absence of manganese. The reason for such discrepancies can be that the specified by the fact that impurity elements are present as a separate phase, distributed non-uniformly in the total volume of the scale [15].

This assumption is confirmed by the second series of experiments to determine the chemical composition of the iron powder made of scale reduced at 900 °C. From Table 4 it follows that sulfur, vanadium, and nickel were no longer detected in the powder under study but manganese was detected again. It should be noted that the amount of calcium remained virtually unchanged.

The appearance of the powder obtained using scale of the Qarmet JSC reduced at 1000 °C is shown in Figures 4 and 4. The corresponding results of the chemical composition assessment are presented in Tables 4-6.

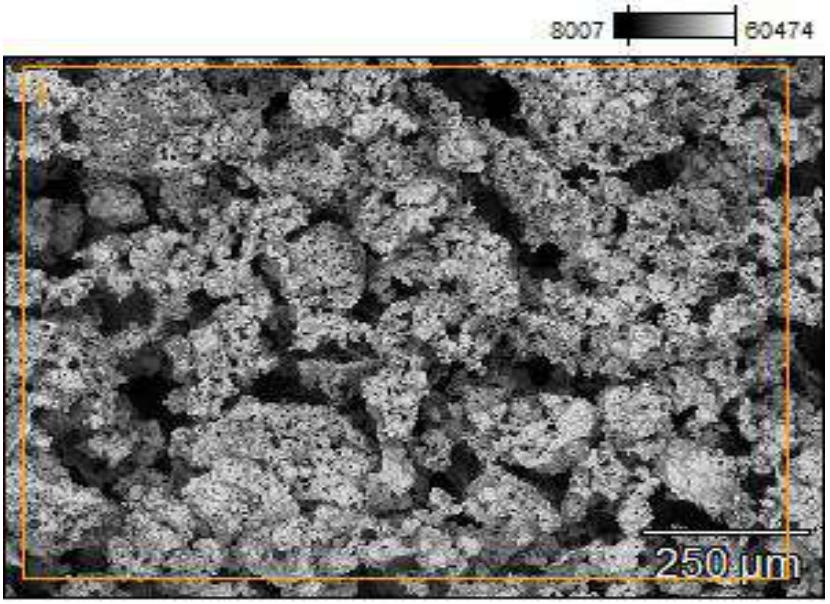

Fig.4. – Iron sponge made of scale reduced at 1000 °C by hydrogen

Table 4. Elemental composition of the iron powder reduced using scale at 1000 °C

Element	Si	Ca	Fe
Content, wt. %	0.3	0.8	98.8

A general assessment of the chemical composition of a relatively large number of particles of iron powder reduced using scale did not show the presence of harmful impurities of phosphorus and sulfur of alloying metals [16]. At the same time, in addition to iron, silicon and calcium impurities were found in the powder.

For a more detailed study of the recovered powder, a point microanalysis of individual particles was carried out (Figure 5).

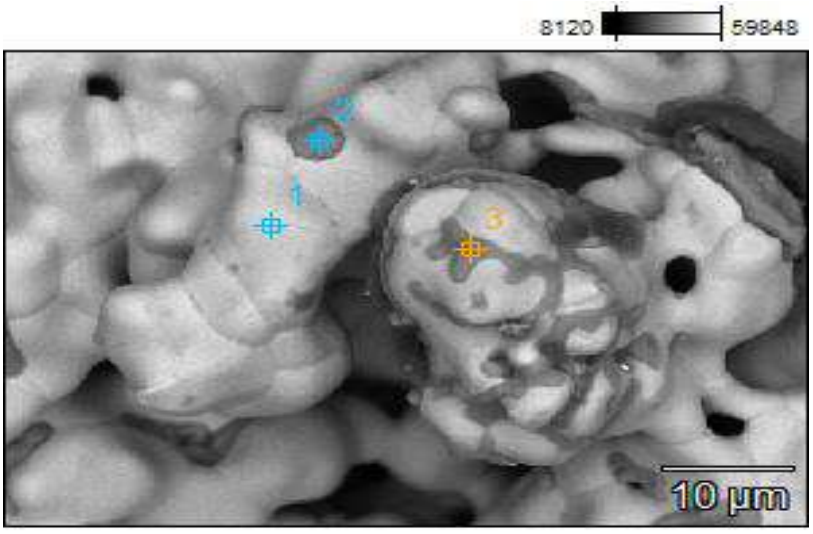

a)

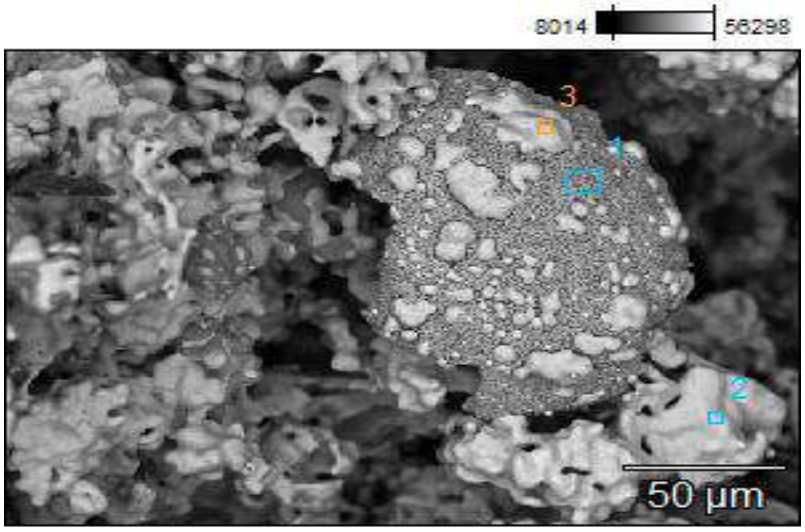

b)

Fig.5. – Powder particles reduced using scale at 1000 °C

Table 5. Elemental composition of the powder particle reduced at 1000 °C using scale (Figure 6, a)

Point	Element	O	Na	Mg	Al	Si	P	Cl	Ca	Mn	Fe
1	Content. wt. %	-	-	-	-	-	-		-	-	100.0
2	Content. wt. %	37.4	0.7	-	0.3	12.0	4.5	-	39.2	2.7	3.1
3	Content. wt. %	32.8	1.3	0.6	-	11.3	1.2	0.4	28.0	1.7	22.7

Table 6. Elemental composition of the powder particle reduced at 1000 °C using scale (Figure 6, b)

Point	Element	O	Mg	Al	Si	Ca	Ti	Cr	Mn	Fe
1	Content. wt. %	0.5	0.8	1.3	2.1	3.8	2.3	24.3	19.6	45.4
2	Content. wt. %	-	-	-	0.3	0.8	-	-	-	98.8
3	Content. wt. %	-	-	-	-	0.8	-	3.0	2.2	93.9

The results show that the particles of the obtained powder were heterogeneous in their chemical composition. The reduced scale powder consists of several phases:

- pure iron (reduction up to 98.8%);
- a complex oxide phase based on iron and the other metallic elements [17];
- a complex oxide phase that does not contain iron.

Conclusions

Industrial mill scale, composed mainly of hematite, magnetite, and wüstite, is confirmed to be a promising secondary raw material for producing iron powder, reducing environmental problems associated with its disposal.

Direct hydrogen reduction at 800 °C resulted in partial conversion to metallic iron. The reduced powder contained residual oxygen and calcium, as well as manganese, indicating incomplete reduction at this temperature.

At 900 °C, variations in the chemical composition of the reduced powders were observed between experimental series. This effect was explained by the heterogeneous distribution of impurity phases within the mill scale. Nevertheless, no harmful phosphorus or sulfur impurities were detected in the final products.

The most efficient reduction occurred at 1000 °C, where the iron content exceeded 98 wt.% and the powders were free from sulfur and phosphorus. However, microanalysis revealed the persistence of oxide inclusions, showing that complete homogeneity was not achieved.

The reduced products exhibited satisfactory mechanical strength for handling and transportation, while remaining friable enough for subsequent milling, making them suitable for powder metallurgy applications.

The results highlight the technical feasibility of applying hydrogen metallurgy to recycle mill scale into high-purity iron powder. Compared with conventional carbonaceous reduction, the hydrogen route offers an environmentally friendly alternative with minimal emissions.

Further optimization, including refining of reduction parameters and potential post-treatment methods, may increase the homogeneity of the powders and broaden their applicability in advanced manufacturing processes.

Acknowledgments. The authors gratefully acknowledge Karaganda Technical University and NUST MISIS for providing laboratory support and analytical facilities.

References

[1] Singh R., Kumar S. Recycling of mill scale for sustainable steel production //Journal of Cleaner Production, 2021, 290, 125198 https://doi.org/10.1016/j.jclepro.2021.125198

[2] Gupta R., Kumar A. Utilization of mill scale waste for sustainable metallurgy //Materials Today: Proceedings, 2022, 62, 3895–3902 https://doi.org/10.1016/j.matpr.2022.02.317

[3] Zhang H., Liu Y., Wang G. Hydrogen metallurgy: A low-carbon pathway for ironmaking. Journal of Sustainable Metallurgy, 2023, 9(2), 412–425 https://doi.org/10.1007/s40831-023-00792-4

[4] Luidold S., Antrekowitsch H. Hydrogen as a reducing agent: Thermodynamic possibilities //JOM, 2027, 59(8), 58–62 https://doi.org/10.1007/s11837-007-0091-y

[5] Han Y., Lee H.G. Thermodynamics and kinetics of hydrogen reduction of iron oxides //ISIJ International, 2020, 60(12), 2760–2768 https://doi.org/10.2355/isijinternational.ISIJINT-2020-180

[6] Iwase M., Watanabe K., Inoue A. Hydrogen reduction behavior of Fe-based oxides for powder metallurgy applications //Journal of Alloys and Compounds, 2022, 918, 165727 https://doi.org/10.1016/j.jallcom.2022.165727

[7] Fan Z., Sun H. Characterization of iron powders produced by hydrogen reduction of iron oxides //Powder Metallurgy, 2020, 63(1), P. 38–45. https://doi.org/10.1080/00325899.2020.1711645

[8] Bazlov A., Strochko I., Ubyivovk E., et al. Structure and properties of amorphous quasi-high-entropy alloys //Metals, 2023, 13(7), 1464. https://doi.org/10.3390/met13071464

[9] Kovalyova T., Issagulov A., Kovalev P., et al. Effect of structural anisotropy on impact strength of alloy steels //Metals, 2023, 13(7), 1157 https://doi.org/10.3390/met13071157

[10] Zhetessova G., Nikonova T., Gierz Ł., Berg A., Yurchenko V., Zharkevich, O., Alexey K. A Comparative Analysis of the Dynamic Strength Properties of the Long Guides of Intelligent Machines for a New Method of the Thermal Spraying of Polymer Concrete //Applied Sciences (Switzerland), 2022, 12, 10376.

[11] Zhetesova G.S.; Dandybaev E.S.; Zhunuspekov D.S.; Zhekibaeva K.K. Improvement of the Organization of Maintenance And Repair of Dump-Cars //Material and Mechanical Engineering Technology, 2020, 1, P.33 - 38

[12] Cantor B. Multicomponent and high entropy alloys //Entropy, 2014, 16(9), 4749–4768 https://doi.org/10.3390/e16094749
[13] Liu S., Zhang J., Gao F. Hydrogen-based reduction of iron oxide concentrates: Process optimization and kinetics //Minerals Engineering, 2023, 189, 107946 https://doi.org/10.1016/j.mineng.2023.107946
[14] Kumar A., Sharma P. Green hydrogen applications in iron and steel industry //Renewable and Sustainable Energy Reviews, 2023, 178, 113296 https://doi.org/10.1016/j.rser.2023.113296
[15] Wu X., Li C., Huang Z. Reduction behavior of hematite fines with hydrogen at different temperatures //Metallurgical Research & Technology, 2022, 119(5), 507 https://doi.org/10.1051/metal/2022050
[16] Chen Y., Wang L., Zhao Y. Microstructural evolution during hydrogen reduction of magnetite //Materials Characterization, 2022, 192, 112346 https://doi.org/10.1016/j.matchar.2022.112346
[17] Gao H., Sun, J., Li M. Advances in hydrogen metallurgy for sustainable ironmaking //Journal of Mining and Metallurgy B: Metallurgy, 2023, 59(1), 1–12 https://doi.org/10.2298/JMMB230101001G

Information of the authors

Arystanova Diana Mukhamedzhanovna, doctoral student, Abylkas Saginov Karaganda Technical University
e-mail: d.arystanova97@mail.ru

Zholdubaeva Zhumagul Diusenbaevna, PhD, associate professor, Abylkas Saginov Karaganda Technical University
e-mail: zh.zholdubaeva@ktu.edu.kz

Lopatin Vladimir Yurevich, c.t.s., associate professor, National University of Science and Technology MISIS
e-mail: lopatin63@mail.ru

Matkarimov Sohibjon Turdalievich, PhD, associate professor, Tashkent State Technical University
e-mail: sohibtm@gmail.com

DOI 10.52209/2706-977X_2025_4_52 **IRSTI 55.57.99** **UDC 631.361.7**

Optimization of Energy Consumption in Combined Melon Drying through Mathematical Modeling

Kaldanov Zh.[1*], Jingilbaev S.[1], Penov N.[2], Kairbaeva A.[1], Zharylkapova Zh.[1].
[1]Almaty technological university, Almaty, Kazakhstan
[2]University of food technology, Plovdiv, Bulgaria
*corresponding author

Abstract. This study examines the optimization of energy consumption in the combined melon drying process, which includes convective heating and infrared radiation. A mathematical model of heat and mass transfer based on the Fourier and Fick equations was developed to predict the dynamics of temperature and humidity. Experimental optimization allowed us to determine the optimal drying conditions: temperature 65°C, air humidity 60%, infrared radiation power (IR) 60% and an air flow velocity of 1.5 m/s. This unit provides an effective balance between drying speed, product quality and energy consumption, consuming only 1.12 kWh/kg of evaporated moisture. Compared with traditional convective drying, this method reduces drying time by 30-40% and energy consumption by 28%. The accuracy of the model is confirmed by the maximum deviation of 6.7% between the experimental data and the simulation results. Given the potential of this technique to increase energy efficiency while maintaining product quality, it is recommended for use in the food industry. In the course of future research, the modeling of mass transfer will be improved, the effect of air flow velocity will be evaluated, and the technology's application to other agricultural products will be expanded.

Keywords: melon drying, combined drying, infrared radiation, convective heating, mathematical modeling, optimization of energy consumption.

Introduction

Drying is a fundamental process in the food industry that prolongs the shelf life of products by reducing moisture content. However, traditional drying methods such as convective (hot air) and infrared drying have significant disadvantages, including high energy consumption, risk of overheating, uneven drying, and potential deterioration in quality (Priyanka, S. Abhay, M.)[1]-[2]. As global energy consumption increases and production efficiency requirements increase, the development of energy-efficient technologies combining multiple drying methods is becoming increasingly relevant.

Hybrid approaches combining convective heating with infrared radiation show significant prospects. Studies by Christian, K.A. Man, Z. and Russian scientist Kuznetsov, A.A. show that these combined methods can reduce energy consumption by 15-30% and reduce drying time by 20-25% while preserving the taste of the product[3]-[5]. Despite its widespread use, convective drying requires significant energy expenditure and often leads to uneven moisture removal. In contrast, infrared drying is more energy efficient, but requires precise parameter control to prevent thermal damage (Abhay, M.)[2].

Numerical modeling of heat and mass transfer helps optimize drying processes. The research of Tzempelikos D., Salagnac P., Kaya A. shows that modern computational models, especially those based on finite difference methods, can predict the dynamics of humidity and temperature with deviations of only 4-11%[6]-[8]. Improved models, including heat and mass transfer mechanisms, allow for more precise optimization of drying conditions, reducing energy consumption by 15-40%[7].

Despite significant progress, some problems remain unresolved. Existing models often do not fully account for variables such as product composition, moisture content, temperature fluctuations, and type of heat exposure. In addition, discrepancies between theoretical predictions and experimental data indicate the need for more accurate models. Fine-tuning the parameters is crucial to minimize energy consumption while maintaining product quality.

Research hypothesis: Numerical modeling allows accurate prediction of energy consumption and optimization of melon drying conditions, achieving a balance between efficiency, product quality, and resource conservation.

Based on this hypothesis, the purpose of this study is to determine the optimal drying conditions for melons that minimize energy consumption while maintaining product quality through the development and experimental validation of a mathematical model of combined convective-infrared drying.

To achieve this purpose, the following research tasks were formulated:

- develop and validate a mathematical model of combined melon drying using experimental data;
- perform numerical modeling of the drying process based on fundamental heat and mass transfer equations;
- experimentally evaluate energy consumption under various combined drying modes;
- compare theoretical calculations with experimental results to refine optimization strategies.

This study provides a comprehensive analysis of the drying process, including a detailed description of the research object, mathematical modeling methodologies, numerical forecasts of energy consumption, and experimental verification. The results obtained are aimed at creating a scientifically based approach to optimizing melon drying, which ultimately will reduce energy costs and increase production efficiency in the food industry.

1. Materials and methods

The object of the study.

The study examines the Gulabi melon variety, which is widely used in processing due to its high sugar content and dense structure, which are favorable for drying. The main physico-chemical characteristics of fresh melons include:

- average fruit weight: 1.5–3.0 kg;
- initial humidity: 85-88%;
- Final humidity: 12-18%;
- Average density: ~0.95 g/cm3;
- Dry matter content: 10–14%;
- Sugar content: 12-14%.

For experiments, the melon was cut into 5×5×5 mm cubes. This particle size ensures uniform drying by reducing the path of moisture diffusion. Before drying, standard preparation of raw materials was carried out, including cleaning (removing the peel and seeds, washing), cutting into preset fragments, monitoring the initial mass and moisture content in the samples (using a laboratory moisture meter) and mixing the batch to equalize the properties of the samples. Such preparation meets the standards of the food industry, ensuring reproducibility and comparability of experimental results[9].

Description of the drying system. The experiments were carried out using a combined laboratory-scale drying system (Fig. 1), which combines convective heating and infrared radiation. This system allows precise control of temperature, infrared frequency and air flow velocity. This technology optimizes the distribution of thermal energy, increasing the energy efficiency of the drying process.

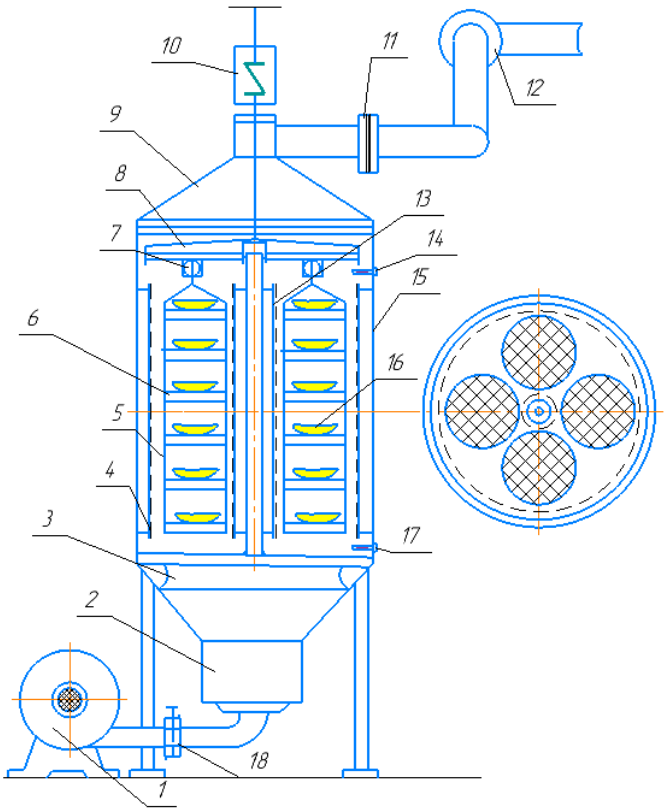

1 - fan; 2 - air heater; 3 - diffuser; 4 - external ir emitter; 5 - product cassette; 6 - mesh tray; 7 - servo motor; 8 - transverse support; 9 - removable cover; 10 - electronic dynamometer for analysis of drying kinetics; 11 - flexible flange; 12 - rotating flange; 13 - internal ir emitter; 14 - upper temperature sensor; 15 - system housing; 16 - dried product; 17 - lower temperature sensor; 18 - flap valve.

Fig.1. - Laboratory combined drying system

The laboratory drying chamber is designed to study the process of dehydration of melons using combined convective and infrared heating. The system includes electric heaters (30-90 °C) and infrared (IR) radiation (wavelength 1.2–2.5 microns) to optimize the distribution of thermal energy.

The main components include a fan for supplying heated air, an air heater for preheating, and a diffuser for evenly distributing the airflow. Both external and internal IR emitters provide additional heating for the product. Melon samples are placed on mesh pallets inside the food cassettes, which promotes uniform drying. The system is also equipped with servomotors to regulate the air flow, a removable cover for easy access and a rigid body with a transverse support for stability.

Precise temperature control is provided using the upper and lower sensors (±0.5°C), and the humidity in the chamber (10-60%) is regulated using an electronic hygrometer (±1%). A laboratory filter is used to control emissions, and the intensity of the air flow (0.5–2.5 m/s) is regulated by a flap. Energy consumption is recorded by an electronic wattmeter, and the change in product weight is monitored using analytical scales (±0.01 g). The system is designed for a maximum load of 5 kg.

The principle of operation and tested drying modes. The drying process begins when the fan directs the heated air through the air heater into the chamber. At the same time, infrared radiators are activated, transmitting thermal energy to melon samples both convectively (through an air stream) and radiationally (by IR radiation).[10]. The flexible duct provides a controlled discharge of the treated air.

Three drying modes were tested to evaluate the drying efficiency:

- gentle drying: 50°C, IR radiation power 30%;
- balanced drying: 65°C, IR radiation power 60%;
- Intensive drying: 80°C, 90% IR radiation power.

Optimization was carried out based on drying speed, energy consumption and the quality of the final product (moisture content, color, texture)[11]. The experimental results were compared with numerical models of heat and mass transfer, which made it possible to verify the accuracy of the model[12].

The laboratory system provides a controlled environment for studying the melon dehydration process, allowing precise temperature and humidity control. By testing various drying modes, the system allows a comprehensive assessment of their impact on product quality and energy efficiency, contributing to the further development of drying technologies.

Mathematical modeling.

The combined drying process was mathematically described using a system of coupled differential equations describing heat and mass transfer.

The heat exchange model.

The thermal behavior of melon samples was modeled using the Fourier heat equation in differential form for an unsteady temperature field[13]:

$$\frac{\partial T}{\partial t} = \alpha\left(\frac{\partial^2 T}{\partial x^2} + \frac{\partial^2 T}{\partial y^2} + \frac{\partial^2 T}{\partial z^2}\right), \quad (1)$$

where T is the product temperature (°C);

t is time (s);

x, y, z are spatial coordinates (m);

$\alpha = pck$ is the heat transfer coefficient (m^2/s);

k is the thermal conductivity (W/m·K);

p is the density (kg/m^3);

c is the specific heat (J/kg·K).

The model of mass transfer.

The diffusion of moisture was described using Fick's second law for unsteady diffusion:

$$\frac{\partial W}{\partial t} = D\left(\frac{\partial^2 W}{\partial x^2} + \frac{\partial^2 W}{\partial y^2} + \frac{\partial^2 W}{\partial z^2}\right), \quad (2)$$

where W is the local moisture content (kg of water per kg of dry matter);

D is the effective coefficient of moisture diffusion (m^2/s), which depends on temperature.

The dependence of D on temperature obeys the exponential Arrhenius law:

$$D = D_0 exp\left(\frac{-E_a}{RT^*}\right), \quad (3)$$

where D_0 is the preexponential coefficient (m^2/s);

E_a is the diffusion activation energy (J/mol);

R is the universal gas constant (8,314 J/mol·K);

T is the absolute temperature (K).

Boundary conditions.

On the sample surface (x=0x = 0x=0), heat transfer obeys a boundary condition of the third kind (convective heat transfer):

$$-k\frac{dt}{dx}\Big|_{x=0} = h\big(T_\infty - T(0,t)\big), \quad (4)$$

where h is the coefficient of convective heat transfer ($W/m^2 \cdot K$);

T_∞ is the air temperature in the drying chamber (°C).

Similarly, mass transfer on a surface is described as follows:

$$-D\frac{dW}{dx}\Big|_{x=0} = \beta\big(W_\infty - W(0,t)\big), \tag{5}$$

where β is the mass transfer coefficient (m/s);

W_∞ is the equilibrium moisture content on the surface (determined by air humidity).

Inside the sample (x > 0), the initial conditions were set as:

T(x, 0) = T₀ = 25°C (uniform initial temperature throughout the sample)
W(x, 0) = W₀ = 0.85 kg/kg = 85% (uniform initial moisture content on wet basis)

Numerical solution method.

The system of equations was solved using the finite difference method. To increase the stability and accuracy of calculations, the Crank-Nicholson scheme was implemented in MATLAB (an implicit method of second-order central differences in space and first-order in time).

The main stages of modeling:

1. Sampling - the sample was divided into a computational grid with a space step of 1 mm and a time step of 1 s;
2. Iterative calculations - the distribution of temperature and humidity was calculated at each time step;
3. Boundary conditions were applied - heat and mass transfer on the surface was taken into account;
4. Convergence check - the simulation was completed when the average moisture content reached the target value (~15%).

Thermal and physical properties of melon. The following parameters were used in the model, obtained on the basis of experimental data and literature:

- thermal conductivity: k ≈ 0.45 W/m·K;
- density: r≈950 kg/m^3;
- Specific heat capacity: c≈3600 J/kg·K;
- Effective moisture diffusion coefficient (at 60°C): D≈1.5×10-10 m^2/s;
- Coefficient of convective heat transfer: h≈15-25 W/m^2·K (depends on the air flow velocity);
- Diffusion activation energy: E_a≈35 kJ/mol.

These values correspond to those obtained during fruit drying studies.

Checking the model.

The accuracy of the model was confirmed by comparing the simulation results with experimental data on drying time, final moisture content, and energy consumption. The average deviation between the theoretical and experimental values was 5-7%, which corresponds to the accuracy range of 4-11% obtained in the course of similar studies on fruit drying.

The developed numerical model accurately predicts the drying process of melons, which makes it a reliable tool for optimizing drying conditions and estimating energy consumption under various processing scenarios.

3. Results and discussion

The results of the numerical simulation were first analyzed with an emphasis on the distribution of temperature and humidity inside the melon sample during drying, as well as on the calculated energy consumption under various drying modes. The simulation covered a 1-hour time interval corresponding to the active drying phase, during which the moisture content in the sample decreased to about 20%.

Figures 2 and 3 show the calculated temperature and moisture distribution fields inside the sample after 60 minutes of drying, based on the numerical model. The analysis of these results is given below.

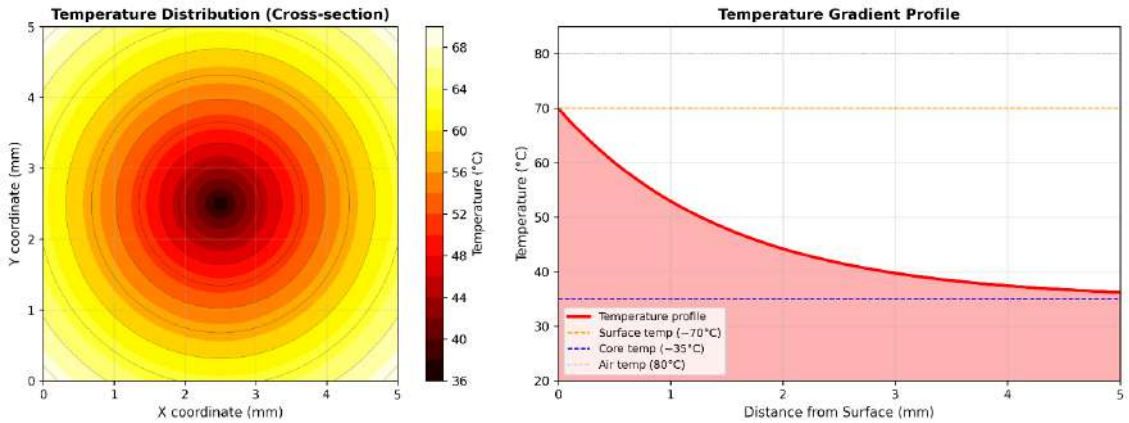

Fig.2. — Temperature distribution in a melon sample

2.1 Analysis of the temperature field

After an hour of drying, the surface temperature of the melon sample rises to about 70 °C, approaching the air temperature in the drying chamber, which is 80 °C. However, there is a clear temperature gradient from the surface to the center:

- the outer layers heat up significantly due to direct contact with hot air and infrared radiation;
- in contrast, the core remains significantly colder, with temperatures ranging from 30°C to 40°C.

This discrepancy indicates a limited penetration of heat into the product during a given drying time. In order for the core to reach the optimal drying temperature, a longer drying time (more than 1 hour) is required.

In order to minimize the internal temperature gradient and achieve more uniform heating, the drying process can be optimized using:

- increasing the air flow rate,
- increasing the power of infrared radiation or
- the introduction of a dynamic drying profile that gradually adjusts the heating intensity over time.

Such changes will help to balance the surface temperature and the internal temperature, contributing to the uniform removal of moisture and improving the overall product quality.

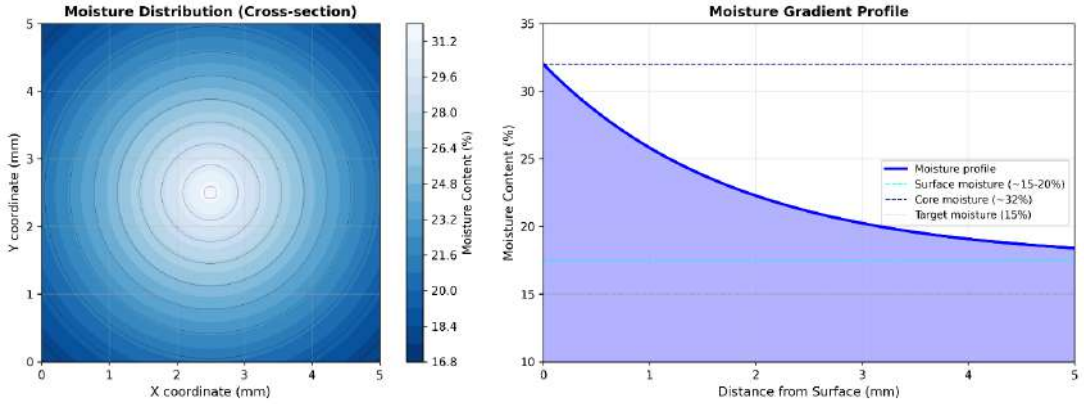

Fig.3. - Moisture distribution in a melon sample

2.2 Analysis of the humidity field

Evaporation of moisture during drying occurs mainly from the surface of the melon sample. After an hour, there is a significant decrease in the moisture content in the outer layers to about 15-20% (mass fraction). At the same time, more than 30% of moisture remains in the core, which indicates a sharp internal gradient.

This uneven distribution is the result of limited diffusion of internal moisture to the surface, which cannot fully compensate for the rate of surface evaporation during the observed time period. Consequently, a pronounced moisture gradient is formed along the thickness of the sample.

To achieve uniform dewatering, it is necessary to increase the drying time so that the internal moisture has more time to migrate outward and evaporate effectively.

To accelerate the redistribution of moisture and reduce the internal gradient, the following process optimizations can be considered:

- increasing the intensity of infrared heating at the final stage of drying;
- increase the air flow velocity to stimulate mass transfer.

To evaluate the optimal drying parameters, numerical modeling was used, during which three different drying modes with different air temperatures, infrared radiation intensity and air flow velocity were analyzed. For each mode, the model calculated the drying time required to achieve the target moisture content of ~15%. These results are summarized in table 1.

Table 1. Melon drying modes and estimated duration of the process (model-based data)

№	Drying mode (characteristics)	Temperature, °C	IR radiation intensity, %	Air flow velocity, m/s	Drying time (estimated), h
1	Gentle (protective)	50	30	1,0	2,36
2	Balanced	65	60	1,5	1,69
3	Intensive	80	90	2,0	1,31

The data clearly demonstrate that an increase in air temperature from 50°C to 80°C, combined with a higher intensity of infrared radiation and air flow velocity, significantly reduces drying time from about 2.36 hours to 1.31 hours with the same level of moisture removal.

However, such accelerated drying in the most intensive mode does not guarantee optimal product quality. Analysis of temperature and humidity fields shows that at a temperature of 80 ° C and an infrared radiation intensity of 90%, there is an increased risk of overheating of the surface and overdrying, which can worsen the taste and texture of melons.

In contrast, mode 2 (65°C, 60% infrared, 1.5 m/s) is a balanced drying strategy. It provides relatively fast drying (~1.7 hours) while reducing thermal stress, which helps maintain product quality:

- mode 3 (80°C / 90% IR radiation) provides the fastest drying (~1.3 hours), but carries the greatest risk of product spoilage;
- mode 1 (50°C / 30% IR) is the most gentle, effectively preventing overheating, but requires the most time (~2.4 hours);
- mode 2, by comparison, reduces drying time by about 30% compared to the gentle mode without compromising quality, making it a practical compromise between speed and product preservation.

This theoretically optimal set of parameters for mode 2 will be confirmed at the next stage of the study through experimental testing.

3. The results of the experiment

The experimental tests were carried out using the same three drying modes — gentle, balanced and intensive, which were previously analyzed in the numerical model. The data obtained during these tests include:

- The total drying time required to reach the final humidity of 15-16%%;
- Energy consumption of the drying system;
- The output of the dried product, measured by the output of dry matter.

For a visual comparison, the experimental results are presented in Table 2 along with the predictions of the model.

Table 2. Comparison of experimental data and model forecasts (melon, 5 kg of feedstock)

Indicator	Experimental	Model forecast	Deviation, %
Initial Moisture Content, %	85	85	0
Final Moisture Content, %	16	16	6,7
Drying Temperature, °C	50/65/80	50/65/80	0
Drying Time, h	2,5/1,7/1,3	2,36/1,69/1,31	5,9/0,6/–0,8
Total Energy Consumption, kW * h	4,4/3,6/3,1	4,2/3,5/3,0	4,8/2,9/3,2
Dried Product Yield, kg	0,85/1,05/1,25	0,88/1,08/1,22	–3,4/–2,8/2,5

Note: The deviation was calculated using the formula $\frac{(Experiment-Model)}{Model} \times 100\%$. *A negative value indicates that the model slightly overestimated the observed experimental result.*

3.1 Analysis of experimental data

The experimentally measured initial and final humidity levels corresponded to the targets defined in the model, while in all drying modes the final moisture content reached approximately 15-16%, which corresponds to the goals of the process.

The drying time observed during the experiments fully corresponded to the predictions of the model. The largest deviation, about 5.9%, occurred in mode 1, while mode 2 showed an almost perfect match with a deviation of only 0.6%, which confirms the high accuracy of the simulation.

In practice, energy consumption per cycle was slightly higher, exceeding model values by 3-5% in all modes. This discrepancy can be explained by the inevitable loss of heat to the environment and the limitations of the efficiency of laboratory equipment.

The final weight of the dried product ranged from 0.8 to 1.3 kg (from 5 kg of raw melon), depending on the drying mode. These results also fully corresponded to the forecasts of the model, while the deviations remained within ~ 3%, which confirms the reliability of the model in assessing moisture loss.

Minor discrepancies between theoretical and experimental results are probably due to:

- uneven air flow in the drying chamber;
- sensor errors;
- simplifications in the model, including assumptions about uniform initial conditions and ignoring the effects of shrinkage.

All deviations were within acceptable limits, and the average modeling error was ~3-7%, which corresponds to the expected accuracy of modern food drying simulations described in the literature. This confirms the experimental verification of the mathematical model and allows it to be used to predict and optimize drying conditions (see comparative data in Table 2).

3.2 Optimal drying mode

Experiments have confirmed that mode 2 (65°C, 60% IR intensity) provides the best overall performance, balancing drying speed, energy efficiency, and product quality.

In mode 2:

- drying time ≈ 1.7 hours;
- total energy consumption ≈ 3.6 kWh (for 5 kg fresh melon);
- specific energy consumption ≈ 1.12 kWh per kg of evaporated moisture;
- the yield of dried product is ≈ 1.05 kg (from 5 kg of fresh melon).

Mode 3 (80°C / 90% IR radiation) provided the shortest drying time (~1.3 hours) and lower energy consumption (~3.1 kWh), as well as a slightly higher yield (due to a decrease in the final humidity of ~12%). However, it was associated with a high risk of overheating of the surface and loss of quality.

Mode 1 (50°C / 30% IR radiation) provided excellent product quality, but required more drying time (~2.5 hours) and consumed more energy (~4.4 kWh), which made it less economical.

Thus, mode 2 represents an optimal compromise, reducing drying time by about 30% compared to the gentle mode while maintaining high product quality and reasonable energy consumption.

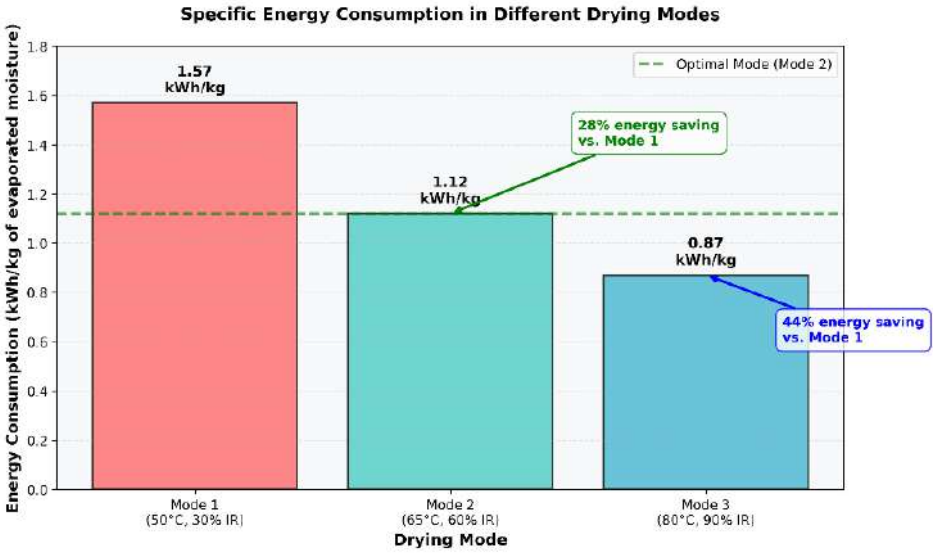

Fig.4. — Specific energy consumption per 1 kg of evaporated moisture in different drying modes

Figure 4 shows the specific energy consumption per kilogram of evaporated moisture (kWh/kg) in three drying modes.

The experimental results show a clear trend: as the drying temperature and the intensity of infrared radiation increase, the specific energy consumption decreases significantly:

- Mode 1 (50°C, 30% IR): ~1.57 kWh/kg of evaporated moisture;
- Mode 2 (65°C, 60% IR radiation): ~1.12 kWh/kg of evaporated moisture;
- Mode 3 (80°C, 90% IR radiation): ~0.87 kWh/kg of evaporated moisture.

This means that in the most intensive drying mode (Mode 3), approximately 44% less energy is consumed per unit of moisture removed than in the gentle mode (Mode 1).

However, this energy saving has its drawbacks. Higher temperatures and IR radiation levels increase the risk of overdrying, which can degrade the taste, color, and texture of the final product.

Mode 2 is the optimal compromise, offering:

- ~28% energy savings compared to gentle convective drying (mode 1);
- preservation of taste, texture and appearance.

These results confirm the practical suitability of mode 2 for industrial applications, providing high energy efficiency without compromising product quality.

Conclusions

In the course of this study, a mathematical model of combined melon drying based on heat and mass transfer equations was successfully developed and tested. Comparison with experimental results (see Table 2) confirmed the high accuracy of the model prediction, while deviations in key parameters remained within ~6-7%. For example, the model predicted a final moisture content of 15%, while the experiment showed a 16% deviation of 6.7%, which corresponds to international standards for modeling the drying process.

The optimal drying mode, which provides a balance between energy efficiency and product quality, was determined as follows: air temperature 65 °C, infrared radiation power of about 60%, air flow velocity of about 1.5 m/s. Under such conditions, the drying process takes about 1.7 hours for 5 kg of raw melon, and the specific energy consumption is about 1.12 kWh per kilogram of evaporated moisture.

An increase in temperature to 80 °C and infrared radiation power to 90% additionally reduces drying time (~1.3 hours) and energy consumption (~0.87 kWh/kg of evaporated moisture), but this can negatively affect the quality of the product, including loss of nutrients, changes in taste and color. Therefore, such intense conditions are not recommended for sensitive products unless they are accompanied by mitigation measures such as lowering the temperature during the final drying phase.

On the other hand, gentle drying at 50°C with an IR intensity of 30% ensures the highest product quality, but is significantly less energy efficient. It takes about 2.5 hours and consumes about 1.57 kWh/kg of evaporated moisture, which

is about 40% more energy than the optimal mode. Thus, this mode is less suitable for industrial enterprises where energy efficiency is a priority.

The hybrid drying method combining convective and infrared heating has demonstrated clear advantages, including a 28% reduction in total energy consumption and a 30-40% reduction in drying time compared to traditional convective methods, while maintaining competitive product quality. These results confirm the energy-saving potential and industrial practicality of infrared convective drying systems.

The improved mathematical model effectively simulates the dynamics of internal heat and moisture in the melon during drying and can be used as a reliable tool for optimizing industrial drying processes. The results obtained correspond to current trends in energy-efficient food processing and demonstrate the applicability of this methodology in food production enterprises, fruit canning operations and in small-scale production, where they seek to increase yields and reduce energy costs.

The practical significance of this study lies in the fact that it provides food manufacturers with a scientifically based approach to reduce drying costs by 20-30% while improving the quality of dried products through more controlled and uniform moisture removal. The introduction of combined drying systems contributes to the development of sustainable, energy-efficient agro-industrial technologies and is an important step towards more environmentally friendly food production.

Thus, the study confirms that combined drying of melons, based on proven mathematical modeling, is an effective and expedient method for increasing drying efficiency. Further research and pilot tests will help improve the methodology and expand its scope of application in the food industry.

Acknowledgements. The authors sincerely thank their colleagues for their valuable contribution to the implementation of this study to Dr. N.A. Umbetaliev, associate professor, for expert advice in the field of mathematical modeling of heat and mass transfer, critical analysis of boundary conditions and recommendations aimed at improving the accuracy of numerical modeling, to Dr. K.K. Kuzembaev, associate professor, for organizing the experimental part of the study, setting up equipment for combined drying processes and processing energy consumption data, to Dr. M.A. Adilbekov, associate professor, for theoretical substantiation of the Fourier and Fick equations, verification of numerical methods for solving differential equations, and evaluation of the stability of computational algorithms.

Their professional support played an important role in ensuring the scientific validity and practical significance of the results presented in this study.

References

[1] Priyanka S. Infrared drying of food materials: the latest achievements //Food Engineering Reviews, 2020, Vol. 11, Issue 3, P. 142-158.
[2] Abhay M. A systematic review on the recent advances of the energy efficiency improvements in non-conventional food drying technologies //Trends in Food Science & Technology, 2020, Vol. 100, P. 67-76.
[3] Christian K.A. et al. Advances in the Application of Infrared in Food Processing for Improved Food Quality and Microbial Inactivation. //Foods, 2024, Vol. 13, Issue 24, P. 4001.
[4] Man Z. et al. Convective air drying characteristics and qualities of non-fried instant noodles. //International Journal of Food Engineering, 2015 DOI:10.1515/ijfe-2015-0108
[5] Kuznetsov A.A. Analysis of a hybrid packed bed dryer assisted by infrared radiation for processing acerola (Malpighia emarginata D.C.) residue. //Journal of Food Engineering, 2019, Vol. 114, P. 235-244.
[6] Tzempelikos D. et al. Numerical modelling of heat and mass transfer during convective drying of cylindrical quince slices //Journal of Food Engineering, 2014.
[7] Salagnac P. Numerical modeling of heat and mass transfer in porous medium during combined hot air, infrared and microwaves drying. //International Journal of Heat and Mass Transfer, 2004, Vol. 47, Issue 19-20, P. 4479-4489.
[8] Kaya A. Numerical modeling of heat and mass transfer during forced convection drying of rectangular moist objects //International Journal of Heat and Mass Transfer, 2006, Vol. 49, Issue 17-18, P. 3094-3103.
[9] George W. Latimer, Jr. Official methods of analysis of AOAC INTERNATIONAL. 22nd ed., 2023.
[10] Khoruz E., Bozkurt H., Karatash H., Maskan M. Kinetics of drying apricot halves in a combination dryer with hot air and infrared radiation. //Journal of Food Science and Technology, 2017, Vol. 54, Issue 12,. - p. 4111-4120.
[11] Zhu Yu., Peng Z. Processing and quality characteristics of apple slices with simultaneous infrared dry blanching and dehydration. //Journal of Food Engineering, Vol. 90, Issue 4, 2009. - p. 441-452.
[12] Doymaz I. Evaluation of Mathematical Models for Prediction of Thin-Layer Drying of Banana Slices. //International Journal of Food Properties, 2010, Vol. 13, Issue 3, P. 486-497.
[13] Incropera F.P., DeWitt D.P., Bergman T.L., Lavine A.S. Fundamentals of Heat and Mass transfer. 8th ed., 2017.

Information of the autors

Kaldanov Zhassulan, doctoral student, Almaty technological university
E-mail: dtn.jason@mail.ru

Jingilbaev Seit, doctor of technical sciences, professor, Almaty technological university
E-mail: d.seit@mail.ru

Penov Nikolai, professor, University of Food Technology, Plovdiv, Bulgaria
E-mail: npenov@yahoo.com

Kairbaeva Ainura, PhD doctor, associate professor of «Almaty technological university»
E-mail: erkenovna111@mail.ru

Zharylkapova Zhansaya, master of technical sciences, lecturer of «Almaty technological university»
E-mail: zhansaya_06z@mail.ru

DOI 10.52209/2706-977X_2025_4_60 **IRSTI 55.57.53** **UDC 631.535**

Development and Application of Sea Buckthorn Harvesting Machinery

Wu X.[1], Yurchenko V.[2*], Wang W.[1], Lei J.[1], Wang J.[3]
[1]Shihezi University, Shihezi, Xinjiang, China
[2]Abylkas Saginov Karaganda Technical University Karaganda, Karaganda, Kazakhstan
[3]Xinjiang Silk Road Sea Buckthorn Technology Co, Ltd, Tacheng, China
[*]corresponding author

Abstract. As the country with the richest sea buckthorn resources in the world, China has played an important role in sea buckthorn planting and industrial development in recent years. With the expansion of sea buckthorn cultivation area, the harvesting efficiency and quality of this economic crop have attracted the attention of growers and researchers. This paper reviews the current development and application of sea buckthorn harvesting machinery, analyzing the technological advancements both domestically and internationally that enhance harvesting efficiency and reduce labor intensity. Given China's complex terrain and the diversity of sea buckthorn, this paper proposes a double-ended adjustable-angle harvesting tool module, which can flexibly adapt to different types of sea buckthorn and operational environments, featuring a simple structure and ease of operation. This design provides a new perspective and technical support for the mechanized harvesting of sea buckthorn and other hard-stemmed crops, promoting the development of the sea buckthorn industry towards efficiency and intelligence.

Keywords: sea buckthorn resources; harvesting machinery; double-ended adjustable-angle tool module

Introduction

Sea buckthorn, a plant of the genus Hippophae in the Elaeagnaceae family [1], is characterized by rapid growth, cold resistance, drought tolerance, and salt-alkali resistance [2]. It can quickly establish forests even in “non-suitable forest areas,” such as the soil erosion-prone regions of the Loess Plateau. Sea buckthorn is an excellent species for rapidly restoring vegetation, preventing wind erosion, stabilizing sand, improving soil quality, and enhancing ecological conditions in arid and semi-arid areas [3]. Its nutritional value is also notable, as it contains high levels of vitamin C, which can boost immune function [4]. According to surveys and statistics organized by the Secretariat of the International Sea Buckthorn Association, as of the end of December 2022, sea buckthorn is distributed in about 55 countries worldwide, covering an area of approximately 37.8 million mu [5]. It is widely found in temperate regions, including China, Russia, and Europe [6].

a)

b)

a) unripe sea buckthorn fruit; b) ripe sea buckthorn fruit

Fig. 1. - Sea buckthorn fruit

In September 2021, the Sea Buckthorn Committee of the China National Sand Control and Desert Industry Society released the National Sea Buckthorn Resource Survey Report, which showed that the total area of sea buckthorn forests in China amounts to 19.1044 million mu [7]. Sea buckthorn plays an important role not only in economic development and improving livelihoods but also in ecological restoration, particularly in soil conservation and land reclamation. The sea buckthorn fruit is small with thin skin, closely clustered on thorny branches, and firmly attached, which makes manual harvesting a significant challenge. As the planting area of sea buckthorn continues to expand, traditional harvesting methods are no longer sufficient for large-scale production, making mechanized harvesting a critical factor for scaling up the sea buckthorn industry.

Against this backdrop, researchers have begun to explore mechanized methods for harvesting sea buckthorn fruit. Mechanized harvesting not only improves harvesting efficiency and reduces labor costs but also has the potential to address labor shortages and the limited harvest season, thus supporting the sustainable development of the sea buckthorn industry. However, the research and application of mechanized harvesting technology still face numerous challenges, including the effective design and manufacturing of harvesting equipment, accurate identification and collection of fruit, and the need to

balance harvesting efficiency with fruit preservation. This paper aims to review the development and application of sea buckthorn harvesting machinery both domestically and internationally, analyze the advantages and disadvantages of different machines, and propose a dual-end adjustable-angle cutting tool module design adapted to complex operating conditions, thereby providing reference and technical support for the mechanized harvesting of sea buckthorn.

2. Manual Harvesting of Sea Buckthorn

In the sea buckthorn industry, harvesting is a critical and time-intensive task that directly affects the quality and profitability of the fruit. As one of the most traditional harvesting methods, manual harvesting plays an essential role in the industry's development. Its simplicity and ability to preserve fruit integrity mean that it remains widely used in many regions. A comparison of manual harvesting methods in China and abroad is summarized as follows.

2.1 Manual Harvesting

1) Fruit Picking Method: This simple and direct method relies on manually picking sea buckthorn berries, usually during the ripening period. Workers pluck the fruit from the branches by hand and place it into containers. While easy to operate and suitable for small-scale, sparsely distributed fruit, this method is low in efficiency and can damage both fruit and branches, making it unsuitable for large-scale production. The advantages of this method are its simplicity, but it also presents challenges due to high labor intensity, low efficiency, and reliance on labor resources.

2) Frozen Fruit Shaking Method: This efficient harvesting method requires temperatures below -20°C, but it may lead to frozen cracking or overripe fruit. By tapping the branches with sticks or other tools, the fruit falls to the ground or into containers. This method is suitable for dense, abundant fruit and is relatively simple and efficient. However, to prevent contamination or damage to the fruit, plastic sheets or other materials must be laid out before the fruit matures.

2.2 Manual Tool-Assisted Harvesting

This method uses various hand tools for harvesting, such as handwheel harvesters and branch-cutting harvesters. In the branch-cutting method, branches are manually cut after the sea buckthorn ripens, then frozen and shaken to obtain the fruit. Although this approach is flexible, it remains inefficient. September is typically a busy agricultural season, leading to a labor shortage, so manual harvesting with tools remains less efficient and adaptable than mechanized methods.

A survey of community harvesting efficiency is shown in Table 1[8].

Table 1. Production efficiency of sea buckthorn fruit in mass harvesting belt

Total fruit harvest (kg)	Number of fruit pickers (person)	Fruit picking days (days)	Fruit picking efficiency	
			[kg/(h • person)]	[kg/(d • person)]
5300	120	4	5.1	33.2

3. Development of Mechanized Sea Buckthorn Harvesting

With the expansion of sea buckthorn cultivation and increasing demand, traditional manual harvesting can no longer meet efficiency and cost requirements. Sea buckthorn is known for its small fruits, short stems, and growth characteristics of clinging to thorny branches. When ripe, the fruit is very fragile and can easily break with slight contact, creating significant challenges for harvesting and hindering the industry's transition to large-scale industrialization [9-10]. To address these issues, it is necessary to design and optimize harvesting devices based on sea buckthorn's harvesting needs, crop characteristics, and agronomic requirements to achieve mechanized harvesting. This approach can reduce harvesting costs, free up labor, improve efficiency, and meet raw material demands for enterprises. Additionally, it prevents random pruning of trees that can lead to reduced yields and resource waste in subsequent years [11].

Researchers are therefore dedicated to developing various mechanized harvesting technologies to increase production efficiency and reduce labor costs. Both domestic and international efforts have led to the development of diverse harvesting equipment for sea buckthorn, ranging from simple spring vibration devices to complex pneumatic suction harvesters, as well as integrated machines capable of simultaneous branch cutting and vibration. Countries such as Russia, Canada, and Germany were early pioneers in the research and development of sea buckthorn harvesting machinery. Russia began developing such equipment in the 1950s and has continued to refine it over the decades[12]. These machines not only enhance harvesting efficiency but also reduce labor intensity, making a significant contribution to the development of the sea buckthorn industry. Meanwhile, China has also been actively exploring this field, introducing, assimilating, and adapting advanced foreign technologies while strengthening research and innovation to gradually establish a comprehensive mechanized harvesting system for sea buckthorn. The development and application of these machines provide strong support for the sustainable growth of the sea buckthorn industry and lay the groundwork for future improvements and innovations in sea buckthorn harvesting technology.

3.1 International Research Progress

Canadian researchers Danny D. Mann and Donald S. Petkau developed a clamping and vibration-based sea buckthorn harvesting device (as shown in Figure 2), which consists of a telescopic pole, clamping mechanism, springs, rotating platform, and telescopic cylinder. By clamping the sea buckthorn tree and shaking a part of the plant, the applied force on the trunk, branches, or leaves causes the fruit to detach from the stem. Although this vibrating harvester is highly

efficient, it has a low harvest rate and can cause some damage to the sea buckthorn tree [13].

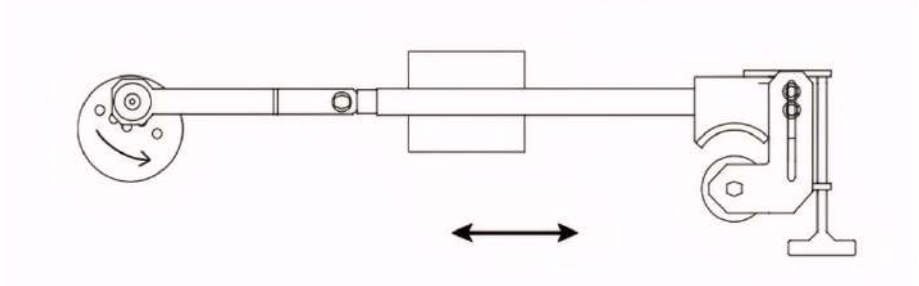

Fig. 1. - Holding device of Russian sea buckthorn harvester

The German company Kranemann GmbH developed a sea buckthorn cutting harvester [14] (as shown in Figure 3) equipped with adjustable deflectors, a circular saw, a reel, an elevator, and a container. The popular harvesting method in Germany involves cutting branches, freezing them, and then shaking off the frozen berries. During harvesting, the machine moves along rows of sea buckthorn, with the deflectors adjusting to the growth habits of the shrubs. The deflectors can travel under drooping branches, lifting the mower deck via the reel. The reel, installed with a curved profile, aligns the branches and guides them to the set position for cutting, where a circular saw trims the berry-laden branches, which are then transported to a container. This method is efficient and adaptable to various sea buckthorn varieties. However, it requires leaving some branches with leaves intact post-harvest, as sea buckthorn branches need 2-3 months to regrow and adapt. Without sufficient leaves, many sea buckthorn plants could die over winter, leading to a substantial decrease in the following year's yield. Additionally, this harvester requires a row spacing of at least 3 meters, making it suitable only for commercial plantations with one-year harvest intervals.

Fig. 3. - Structure of sea buckthorn fruit cutting machine

The MII70-6 air-sucking sea-buckness-picking machine developed by the Moscow Academy of Agricultural Science Machinery (as shown in Figure 4), with a supporting power of 36.6kW or more tractors, is mainly composed of universal transmission shaft, pulley assembly, vacuum pump, harvesting container tank, fruit box, vacuum tube and picking and other parts. At work, the tractor power through the drive shaft to drive the vacuum pump to produce enough negative pressure, so that the special picking head to form an suction flow, pick the sea buckthorn fruit, after being sucked into the harvest container, through the separator to separate the fruit, branches and leaves, and finally into the fruit box to complete the harvest. The machine is usually equipped with 6 picking heads, which can work for 6 people at the same time, and the daily picking efficiency is about 1000kg, which is suitable for harvesting large-fruit sea buckthorn [15].

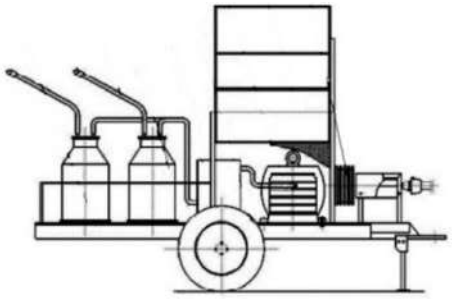

Fig.4. - Structure diagram of air-suction sea buckthorn fruit harvester

3.2 Domestic research progress

Since 1997, the Inner Mongolia Academy of Forestry has focused on research into sea buckthorn harvesting technology and associated machinery. Building on Russian sea buckthorn harvesting technology, and taking into account the distribution, terrain, and cultivation conditions of sea buckthorn in China, the academy developed two proprietary sea buckthorn harvesting machines, as shown in Figure 5. The first is a spring vibration and variable-frequency vibration suction combination harvester powered by a small gasoline engine, suitable for large-scale artificial sea buckthorn forests on gentle slopes. The second is an electric, spring-vibration, and variable-frequency vibration backpack harvester designed for natural sea buckthorn forests and capable of harvesting on sloped terrain. Through patent development and technological improvements, two prototype harvesters based on different principles were developed, integrating suction devices with mechanical spring and variable-frequency vibration mechanisms. These machines are adaptable for harvesting various types of small forest fruits, including sea buckthorn, goji berries, and nanking cherries. These innovations provide efficient and flexible solutions for harvesting sea buckthorn and other small forest fruits [16].

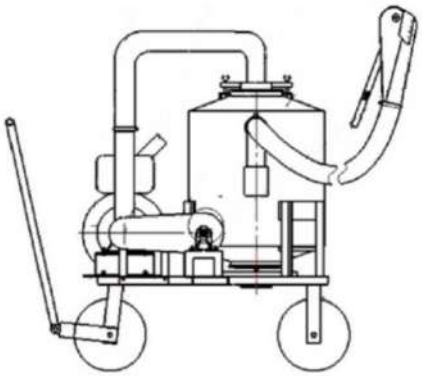

Fig. 5. - Spring Vibration and Suction-Type Sea Buckthorn Fruit Harvester

Wang Min, Cao Silin, and others designed a mechanical vibration-type sea buckthorn harvesting machine in response to the rapid development of the sea buckthorn processing industry, where there are currently no mature tools for fruit picking[17]. The design is intricate, consisting of key components such as a vibrating head, machine body, crank-slider mechanism, flexible shaft, and gasoline engine, as shown in Figure 6. The crank-slider mechanism includes a telescopic shaft, crank, and gear pair, which enables complex motion conversion. Its working principle is quite ingenious: after starting the gasoline engine, power is transmitted through the flexible shaft to the crank-slider mechanism, converting rotational motion into the linear reciprocating motion of the vibrating head. The vibrating head drives the telescopic shaft to shake off the sea buckthorn fruits, facilitating the harvesting process. The shaken fruits are collected by a gathering device, perfectly achieving the automation of sea buckthorn harvesting.

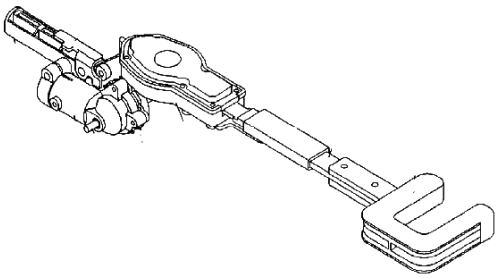

Fig.6. - Schematic Diagram of Mechanical Vibration-Type Sea Buckthorn Harvesting Machine

Zhai Zhiyuan, Lei Jin, and their research team successfully developed the first domestic self-propelled sea buckthorn reciprocating pruning and harvesting machine based on German sea buckthorn cutting and harvesting technology[18]. This machine integrates multiple innovative designs, including a fully functional cabin control system (covering walking, steering, branch displacement, cutting, and lifting), an efficient pruning device (comprising a branch displacement wheel, cutter, and branch gathering system for branch separation, combing, and cutting), a flexible walking chassis (hydraulically driven rear wheels with flexible steering of front wheels, and a ground clearance of 1200 mm), as well as a grading, lifting, and storage system (first-level lifting of branches to a storage box, and second-level lifting to an accompanying vehicle). The harvester optimizes space utilization through a three-segment folding design, making it easier to transport. Its fully hydraulic drive control characteristics are suitable for the complex working conditions of sea buckthorn shrubs, significantly improving operational efficiency and quality, and achieving an automated process from cutting to collection.

Further research based on sea buckthorn planting patterns and growth characteristics involved detailed parameter measurement and data analysis, providing foundational data support for sea buckthorn growth management. However, the machine still has several shortcomings in practical applications, such as non-adjustable position and speed of the branch displacement wheel leading to poor combing effects, mismatches between manual operation and pruning results causing

harvesting losses, tool fatigue and chipping issues affecting service life, poor adaptability to plants of different heights, and insufficient stability during slope operations, which require further optimization in subsequent research.

Fig.7. - Self-Propelled Sea Buckthorn Reciprocating Pruning and Harvesting Machine

4. Discussion

A review of the research progress on sea buckthorn harvesting machinery both domestically and internationally reveals that there are different technological paths and adaptations in the development of sea buckthorn harvesting machinery. In countries such as Russia, Canada, and Germany, the development of sea buckthorn harvesting machinery began earlier and is more technologically mature, with significant achievements in mechanical types such as air suction, cutting, and clamping vibration systems. These machines excel in improving harvesting efficiency and reducing labor input and intensity; however, they often have higher requirements regarding planting modes and terrain conditions. In contrast, domestically, advanced foreign technologies have been introduced, digested, and absorbed, leading to independent research and development that gradually forms sea buckthorn harvesting machinery with independent intellectual property rights.

A performance comparison of various sea buckthorn harvesting machines is shown in Table 2.

Table 2. Comparison of Sea Buckthorn Harvesting Machines

Type	Country/Developer	Working Principle	Harvesting Efficiency	Fruit Damage Rate	Advantages	Disadvantages
Clamping Vibration Harvester	Canada (Danny D. Mann et al.)	Vibrates the fruit off by clamping the trunk	High	Relatively High	High harvesting efficiency	Low clean rate, destructive to the tree
Cutting Harvester	Germany (Kranemann GmbH)	Cuts branches and shakes off the fruit after freezing	30 kg/h, 80% drop rate	5%	High harvesting rate, suitable for multiple varieties	Some damage to trees, requires 2-3 months to recover
Air Suction Fruit Picker	Russia (Moscow Agricultural Scientific Machinery Institute)	Uses vacuum suction to collect fruits into a container	Approximately 1000 kg/day	Moderate	Suitable for large sea buckthorn, allows for 6 people working simultaneously	Requires high-power tractor, high cost

Contanuation of the table 2

Type	Country/Developer	Working Principle	Harvesting Efficiency	Fruit Damage Rate	Advantages	Disadvantages
Spring Displacement-Air Suction Combined Harvester	China (Inner Mongolia Academy of Forestry)	Vibrates to drop fruits and collects them using air suction	Moderate	Medium-Low	Suitable for large flat areas and various small fruit varieties	Not suitable for complex terrain
Mechanical Vibration Harvester	China (Wang Min, Cao Silin et al.)	Converts rotational motion to linear reciprocating motion of the vibrating head to shake off fruits	Moderate	Moderate	Simple design, suitable for small to medium-scale harvesting	Lower level of automation
Self-Propelled Reciprocating Pruning and Harvesting Machine	China (Zhai Zhiyuan, Lei Jin et al.)	Automatically walks, prunes, and collects, suitable for shrub areas	High	Moderate	High degree of automation, suitable for densely planted shrubs	Component lifespan issues, insufficient stability on slopes

Various types of sea buckthorn harvesting machines each have their advantages in different structural designs and working principles, making them suitable for different harvesting needs and terrain conditions. Clamping vibration harvesters and air suction fruit pickers are characterized by high efficiency, but they face issues such as significant damage to the tree and high equipment costs. In contrast, cutting harvesters are considered commercially viable due to their high harvesting rate and low fruit damage, though they have higher requirements for tree recovery. The domestically developed spring displacement-air suction combined harvester and self-propelled reciprocating pruning and harvesting machine offer flexibility in adapting to different terrains and environments, making them particularly suitable for the complex terrain conditions of sea buckthorn forests in China. However, they still require optimization in terms of component durability and operational stability. Overall, the development direction of sea buckthorn harvesting equipment aims to balance harvesting efficiency, fruit protection, and tree health while further enhancing automation and adaptability to meet the demands for large-scale mechanized harvesting in the sea buckthorn industry.

Specifically, for harvesting deciduous shrubs like sea buckthorn, the design and optimization of cutting devices are crucial for improving harvesting efficiency and quality. Researchers both domestically and internationally have developed various high-efficiency and adaptable cutting devices through innovation, such as reciprocating dual-action knives, sliding-cut and shearing combinations, bionic blades, and finite element analysis, which have significantly improved cutting efficiency and quality. However, research on disk-type cutting mechanisms specifically for sea buckthorn remains insufficient and needs to be strengthened further.

5. Development

Sea buckthorn branches are characterized by high lignification and hardness, categorizing them as hard-stemmed crops[19]. During the harvesting of sea buckthorn, it is necessary to harvest the branches, leaves, and fruits together to improve harvesting efficiency. The mechanical properties of sea buckthorn branches and the cutting methods of the tools are particularly important, as they directly affect the quality of the harvesting process [20].

Currently, research reports on specialized sea buckthorn branch and fruit harvesting machines in China are relatively limited, and there is also a lack of studies on cutting devices for sea buckthorn branches. However, there is a wealth of research on harvesting machinery for other hard-stemmed crops, such as corn and sugarcane. Therefore, this paper analyzes and references harvesting machinery for hard-stemmed crops.

Wang Bingpeng and colleagues analyzed the optimal cutting parameter combinations for sea buckthorn branches by designing a cutting test platform using blades from other stem crops [21]. This test platform utilized a reciprocating dual-action knife structure and conducted experiments on factors affecting the cutting of sea buckthorn branches, as well as multi-factor response surface cutting tests. Ultimately, the study revealed the variation laws of the main factors affecting sea buckthorn cutting and determined the optimal cutting parameter combinations. The cutting experiments for sea buckthorn branches provide significant reference value for this research; however, the experimental methods differ from the operational conditions of harvesting machines in complex field environments.

Ni Chang'an and colleagues explored the performance and power consumption of several types of disk cutters

during the cutting of corn stalks [22]. The experiment selected three types of cutters: straight knife, serrated knife, and star-toothed knife, analyzing how their structures and operating parameters affect cutting results. The results indicated that the straight knife cutter performed best in terms of power consumption and is suitable for cutting smaller diameter corn stalks, while the star-toothed knife consumed the most energy under the same conditions. Additionally, cutting power consumption is related to the speed of the cutting tool and the forward speed of the machine. The research also pointed out that the idle power consumption of disk cutters is relatively high; thus, practical designs should focus on simplifying the transmission structure and ensuring reliability to reduce energy consumption and improve operational efficiency.

Qing Shangle and colleagues mainly studied the kinematic characteristics of a single disk cutter during the sugarcane harvesting process [23]. By establishing motion equations and models, they analyzed how the structural parameters of the cutter and the geometric parameters of the sugarcane affect the cutting results, determining the conditions for avoiding missed cuts and ensuring that the cutting disk does not contact the sugarcane. The results showed that the maximum speed ratio for avoiding missed cuts is related to the structural parameters of the cutter and not the motion parameters, and that the speed ratio decreases as the disk angle increases and increases as the blade angle increases; the disk angle should not exceed 20°. The maximum speed ratio for avoiding contact is related to the diameter, tilt angle, and cutting position of the sugarcane, where a tilt angle exceeding 40° is detrimental to harvesting.

Based on an in-depth analysis of previous research, this paper proposes a design for a disk-type sea buckthorn harvesting knife module with dual-end adjustable angles, aiming to optimize the flexibility and efficiency of sea buckthorn harvesting operations. This module consists of a single cutting tool and a main frame, with the control mechanism including a cutting motor and a steering motor. The adjustment mechanism achieves micro-adjustment of the angles of the dual-end tools through cams, gears, and racks on a central support frame. Users can precisely adjust the working angles of the two cutting tools to meet the harvesting needs of different sea buckthorn varieties and complex terrains.

The innovation of this design lies in utilizing high-speed, smooth circular saws to cut sea buckthorn, while using a DC motor and a brushless motor to control steering and cutting, respectively, in order to meet a wider range of harvesting needs. The angle adjustment of the tools can adapt not only to the branch structures of different sea buckthorn varieties but also optimize cutting performance by changing the entry angle, improving the smoothness of the cutting surface and the overall quality of the harvest. Compared to traditional fixed-angle tools, the proposed module offers a simple structure, convenient operation, and strong adaptability, promising a more efficient solution for the harvesting of sea buckthorn and other stem crops.

As shown in Figure 8.

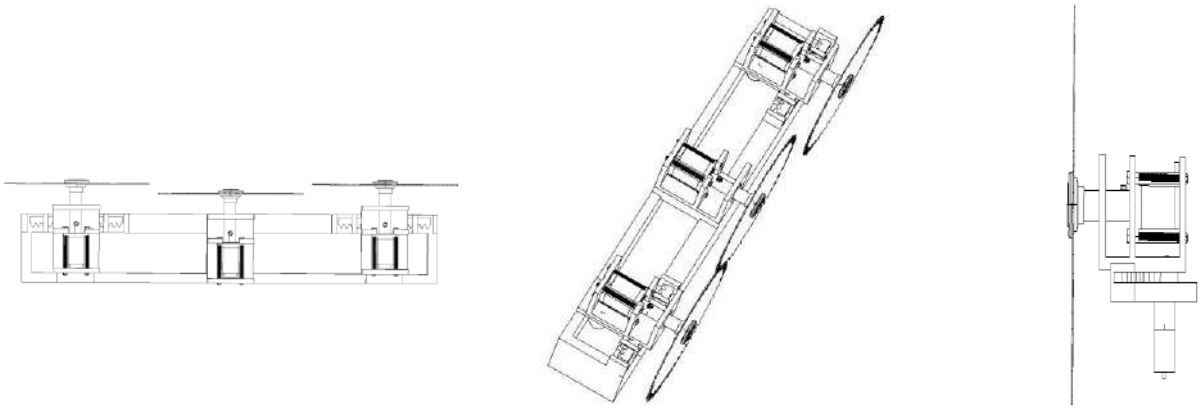

a) b) c)

a) Top view; b) Isometric view; c) Side view of single-point cutting tool

Fig. 8. - A dual-end adjustable-angle saw-type sea-buckthorn harvesting tool module

Conclusion

This review thoroughly explores the transition of sea buckthorn harvesting machinery from traditional manual methods to mechanization, analyzing the developmental process and challenges involved. It also provides an in-depth discussion on the strengths and weaknesses of various domestic and international harvesting technologies, particularly in terms of efficiency, fruit protection, and adaptability.

By conducting a detailed comparison of advanced equipment from countries like Canada, Germany, and Russia (e.g., clamping vibration, cutting, and air-suction harvesting machinery), this article provides a nuanced understanding of the technical benefits and practical contexts in which these machines can enhance harvesting efficiency and reduce labor costs. The effectiveness of these technologies across diverse planting models, terrain conditions, and operational scales has gradually driven the replacement of traditional manual harvesting with mechanized solutions, thus serving as a pivotal force in advancing the sea buckthorn industry.

Considering China's diverse terrain and the variability of sea buckthorn varieties, this review further examines the advancements in domestically developed harvesting machinery, with a focus on innovations from regions such as Inner

Mongolia and Ningxia that address specific local challenges. Building upon foreign technologies, China has gradually developed an independent machinery system tailored to small forest fruits, significantly boosting harvesting efficiency and operational flexibility. The development emphasizes strategic adaptation to local conditions while fostering indigenous innovations.

Based on these developments, a dual-end adjustable-angle harvesting cutter module for sea buckthorn is proposed. This module utilizes an adjustable design with efficient cutting and steering motors that independently control the cutting and entry angles, thereby optimizing performance for different sea buckthorn varieties and working environments. This innovative design aims to address the limitations of traditional fixed-angle cutters, particularly their inability to adapt to varying operational environments. It enhances flexibility, smooth operation, and fruit protection, thereby improving overall harvesting quality. Compared to traditional fixed-angle equipment, this module efficiently handles complex working conditions while featuring a straightforward structure and easy operation. It significantly improves sea buckthorn harvesting efficiency and quality, providing a strategic advancement for the mechanized harvesting of sea buckthorn and other rigid-stemmed crops, offering new insights and practical directions for future technological development. This innovative design is intended to address the limitations of traditional fixed-angle cutting tools, which struggle to adapt to diverse operating environments, thereby improving harvesting flexibility, smoothness, and fruit protection. Compared with conventional fixed-angle equipment, the proposed module not only operates efficiently under complex working conditions but also features a simple structure and ease of operation. It significantly enhances the efficiency and quality of sea buckthorn harvesting, offering a new direction and practical reference for the mechanized harvesting of sea buckthorn and other hard-stemmed crops in the future.

This innovative design is intended to address the limitations of traditional fixed-angle cutting tools, which struggle to adapt to diverse operating environments, thereby improving harvesting flexibility, smoothness, and fruit protection. Compared with conventional fixed-angle equipment, the proposed module not only operates efficiently under complex working conditions but also features a simple structure and ease of operation. It significantly enhances the efficiency and quality of sea buckthorn harvesting, offering a new direction and practical reference for the mechanized harvesting of sea buckthorn and other hard-stemmed crops in the future.

Funding. This study was supported by the Financial Science and Technology Plan of XPCC (Grant No.: 2024AB043) and the Tianshan Elite Cultivation Programme Corps Rural Development Core Talent Development Project.

References

[1] Liu Xin, Zhu Dan, Wei Wenyi, et al. Study on the Stability of Sea Buckthorn Cloudy Juice // China Brewing, 2018, 37(6): 136-139.
[2] Zhang Jinhong. A Brief Discussion on the Promotion of Large Sea Buckthorn Cultivation Technology in Weichang County // Urban Construction Theory Research (Electronic Version), 2013(23).
[3] Hu Jianzhong, Tu Xiaoning, Wen Xiufeng. Suitable Site Types for Planting Sea Buckthorn in the Energy Development Zone of Shanxi, Shaanxi, Inner Mongolia, and Gansu, and Related Suggestions // China Soil and Water Conservation, 2009(4): 42-43.
[4] Jin Feng. Understanding Vitamin C //Chinese Food & Nutrition, 2006(1): 47-48.
[5] International Seabuckthorn Association. Survey and Statistics on Seabuckthorn Distribution across the Globe (as of December 2022). Available at: https://isahome.net/news.php?id=659. Accessed November 8, 2024.
[6] Fu L, Su H, Li R, et al. Harvesting technologies for sea buckthorn fruit // Engineering in Agriculture Environment & Food, 2014, 7(2): 64-69.
[7] Yang Yulan. National Sea Buckthorn Resource Background Survey Report[EB/OL]. https://www.gov.cn/xinwen/2022-06/10/content_5695086.htm, 2022-06-10.
[8] Gu Yukai, Jin Zhengping, Jiang Tonghai, Gao Fujiang, Wang Xiaowei, Wang Keqin, Wang Shiping, Jin Shuyuan. Application Research on Fruit Harvesting with Small Branches for Sea Buckthorn in China // International Sea Buckthorn Research and Development, 2004, 2(1): 4-8.
[9] Wang Mingzhu. Harvesting Technology of Sea Buckthorn Branches and Fruits // Farmer's Friend, 2013(06): 86.
[10] Wang Min, Cao Silin, He Yichuan, et al. Design of Mechanical Vibration Type Sea Buckthorn Harvester // Agricultural Mechanization Research, 2013(01): 109-111.
[11] Cao Silin, He Yichuan, Wang Min, et al. Current Situation and Considerations on Mechanized Harvesting Technology of Sea Buckthorn Fruit // Agricultural Mechanization Research, 2012(05): 12-15.
[12] Li Min. The Status and Role of Sea Buckthorn in the Development of Western China //Sea Buckthorn, 2002, 15(3): 1-4.
[13] Danny D. Mann, Donald S. Petkau, et al. Removal of sea buckthorn (Hippophae rhamnoides L.) berries by shaking // ResearchGate, 2001, 01.
[14] Dr. Friedrich Höhne. Proceedings of the 3rd European Workshop on Sea Buckthorn EuroWorkS2014[C]. Finland: Natural Resources Institute Finland, 2015.
[15] Liu Lei, Niu Changhe. Current Status and Analysis of Sea Buckthorn Harvester Development // Xinjiang Agricultural Mechanization, 2010(1): 35-37.
[16] Liang Jianping. Introduction of Intelligence: Sea Buckthorn Fruit Harvesting Technology and Supporting Machinery //Inner Mongolia Forestry Science and Technology, 2008, 34(4): 61-62.
[17] Wang Min. Design of Mechanical Vibration Type Sea Buckthorn Harvester // Agricultural Mechanization Research, 2013(1): 109-111.
[18] Zhai Zhiyuan. Design and Experiment of Cutting and Conveying Device for Sea Buckthorn Harvester // Lei Jin: College of Mechanical and Electrical Engineering, Shihezi University, 2024.
[19] Wang Tao, Yan Xiaoli, Mi Guopeng, et al. Research Status of Cutting Devices for Hard-Stemmed Crops //China Agricultural Mechanization Journal, 2023, 44(8): 34-39+74.
[20] Li Xiaoqiang, Wang Fene, Guo Weijun, et al. Analysis of Factors Affecting Cutting Force of Cabbage Stalks // Transactions of the Chinese Society of Agricultural Engineering, 2013, 29(10): 42-48.

[21] Wang Bingpeng, Lei Jin, Qin Xinyan, et al. Analysis and Experiment of Cutting Parameters for Sea Buckthorn Branches with Double-Action Knives // Transactions of the Chinese Society of Agricultural Engineering, 2023, 39(10): 26-36.
[22] Ni Chang'an, Lin Gongzhen, Ji Jiangtao, Liu Shiduo, Zhang Yuxian, Chen Dongsheng. Experiment and Analysis of Cutting Corn Stalks with Disc Cutter // Journal of Luoyang Institute of Technology, 1995, 12(4): 25-30.
[23] Qing Shangle, Ou Yinggang, Liu Qingting. Kinematics Analysis of Single Disc Basecutter of Sugarcane Harvester // Transactions of the Chinese Society for Agricultural Machinery, 2006, 37(1): 52-54.

Information of the authors

Wu Xiaoyu, master student, College of Mechanical and Electrical Engineering Shihezi University
e-mail: wuxy@stu.shzu.edu.cn

Yurchenko Vassiliy, professor, Abylkas Saginov Karaganda Technical University
e-mail: juvv76@mail.ru

Wang Weibing, professor, College of Mechanical and Electrical Engineering Shihezi University
e-mail: wwbshz@163.com

Jin Lei, associate professor, College of Mechanical and Electrical Engineering Shihezi University
e-mail: jinlei@shzu.edu.cn

Wang Junyang, Xinjiang Silk Road Sea Buckthorn Technology Co, Ltd
e-mail: 19318318323@163.com

DOI 10.52209/2706-977X_2025_4_69 **IRSTI 81.09.09** **UDC 634.613**

Carbon Pellets Prepared from Self-Adhesive Properties of Pre-Carbonized Date Palm Leaves *(Phoenix dactylifera L.)*: X-ray DiffractionAnalysis and Applications

Abbas F.M.[1*], Khalofa A.[2], Abbas H.M.[2], Al-ahmd Z.A.[1], Abdelrahman A.E.[3]
[1]King Khalid University, Abha, Saudi Arabia
[2]Ministry of Science Higher Education and Scientific Research, Sudan
[3]Act Center for Research, Singa, Sudan
*corresponding author

Abstract. Carbon pellets (CPs) were prepared from the self-adhesive properties of date palm leaves (Phoenix dactylifera L.) and converted into pellets by applying (5 to 21) metric tons of pressure, before being carbonized at 1000 °C in a nitrogen environment using a multi-stipe heating profile. Characterizations of CPs produced were carried out in terms of Young's modulus (YM) and crystallite dimensions, specific surface area, and porosity. A microscopic cross-linking model based on crystallite dimensions (d002, Lc, and La) was also used to estimate YM, spring length (Sp) between two cubic granulars of the carbon microstructure structure, specific surface area, and porosity as a class of X-ray diffraction application, by assuming that the changes in YM for carbon pellets as a function of compression occur similarly as a function of heat treatment temperature. Results of the X-ray diffraction pattern show that the structure of the CPs is turbostatic, and its crystallite dimensions are improved by compressive pressure. The estimated YM from a microscopic cross-linking model was in good agreement with that measured by ultrasonic techniques, showing that the behavior of the YM is related to the crystallite dimensions. The results also found that the degree of stiffness as a function of compression pressure is equal to that of heat treatment temperature, proving that the changes in YM as a function of compression pressure occur similarly as a function of heat treatment temperature. The results also show that the data of specific surface area and porosity, estimated from microscopic cross-linking, are in good agreement with the measured data. The Sp is reduced with increasing compression pressure, and above 12 metric tons of pressure the CP observed the stress broadening behavior. These results can conclude that the crystal dimensions can play an essential role in the phenotypic and description of CP pellets, indicating the applicability of the microscopic cross-linking model to estimate the physical properties of carbon materials.

Keywords: carbon pellets, date palm leaves, compression pressure, crystallites dimensions, Young's modulus, surface area, porosity, spring length.

Introduction

Carbon materials have attracted great attention in the last decade because of their numerous applications, such as catalysts and catalyst supports [1], capacitor electrodes [2], fuel gas storage [3] (Sawant et al., 2017), Supercapacitor [4] and electromagnetic wave absorption [5]. The carbon material is generally available in three main forms; these are powder, granular, and pellet forms [6]. Frequently, carbon materials have been developed in various physical forms, from reliable products such as powder, granules, and pellets, with or without binder to increase their industrial applications [7]. Also, the pellet form can provide a more fundamental understanding of the physical properties of carbon and the interactions that occur at its surface [6, 7]. The pellet form is date palm leaves [8]. On the other hand, the surface area is an important characteristic of carbon and activated carbon material that greatly determines the properties and applications. It has found carbon material with a high surface area allowed to store electrical charge to produce a double layer capacitor [9]. Therefore, there are many carbonaceous materials that have been tested for a high surface area by potassium hydroxide treated grape seed of (1222 m^2/g) [10], oil palm leaves of 1685 m^2/g and date palm leaves (1308-1658). Frequently, conversion of the biomass precursor into a fine grain powder by heat treatment temperature and ball milling process is one of the most common to improve self-adhesive properties before being pelletized as a pellet by a different compression pressure to improve its surface area and physical behaviour [7]. In addition, biomass materials can be converted into several products, such as biofuel, bio-oil, biogas, and bio-solid (Wong et al., 2020), wood plastic composite reinforcement, polymer-wood flour [11, 12].

Among them, date palm leaves (Phoenix dactylifera L.) biomass (DPLB) is a by-product derived from the date palm tree, referring to lignocellulose biomass, composed of cellulose, hemicelluloses, and lignin is maen products [13](Dhyani and Bhaskar, 2018), emerged as a promising precursor of carbon and activated carbon materials for being renewable, vastly available, ecologically suitable, and a high carbon content [13, 14][7]. Traditionally, it is made into baskets, fans, crates, boxes, hats and fuel sources, and further used to produce liquid phenolic acid [15]. It has been found that the lignin compound is early burn at low temperature [13] and the hemicelluloses is burned at the mediem temperature. So far, the domment structure of the final product is related to the cellulose compound. In the present work, date palm leaf biomass has been used as a raw material to prepare solid carbon. Also, recently, it has been used to prepare activated carbon and carbon pellets with a high surface area with excitable mechanical and electrical properties [7, 16, 17]. It is well known that X-ray interference intensity offers more or less direct details of the crystal structure and the crystallite dimensions. It has been found that analysis of certain carbon structures can be made in terms of the crystallite dimensions (d002 Lc and La) of the graphite-like crystallites that are randomly distributed and oriented throughout the samples [16]. Therefore, an

empirical microscopic cross-linking model based on crystallite dimensions and volume fraction has been proposed by Emmerich and Luengo to estimate Young's modulus of carbon material as a function of heat treatment temperature as a class of the X-ay diffraction application [18]. By assuming that the bulk of the carbon matrix is made up of two phase-granular structures (micro-crystallites and cross-links), and at the microstructural level, Young's modulus is controlled by its crystallite dimensions. In addition, there are many experimental modeling and theoretical equations that have been used to evaluate the mechanical properties of carbon material [19, 20] and to correlate porosity with elastic modulus [21] electric conductivity with the bulk density in terms of percolation theory [8] and surface area with crystallite dimensions [8]. In the present work, conventional techniques have been to characterize carbon such as ultrasonic techniques, X-ray diffractions in terms of crystallite dimensions, Young's modulus, and further estimated by the microscopic cross-ling module by assuming that the changes in Young's modulus for carbon samples as a function of compression pressure occur similarly as a function of heat treatment temperature. Additionally, the porosity and surface area of the CP were estimated based on bulk density and staking order, and the microscopic cross-ling module models. The objective of this work is to prepare solid carbon pellets from date palm levers and characterize the crystallite dimensions, Young's modulus, porosity, and surface area as a function of compression pressure. An X-ray diffraction program (Trace version 5) has been applied to measure crystallites dimenstion to assess the accuracy. Reference glassy carbon (Sigradur-K) was used to calibrate the ultrasonic signal. The aim of this study is to systematically examine the influence of compression pressure on the crystallite dimensions, Young's modulus, surface area, porosity, and microstructural behaviour of carbon pellets produced from pre-carbonized date palm leaves. Further, to confirm the validity of the microscopic crosslinking model in predicting their physical properties.

1. Materials and Methods

1.1 Sample Preparation

Saudi Arabia date palm leaves (Phoenix dactylifera L) waste materials were collected near rural areas, urban areas and cities in southern Saudi Arabia. Raw palm leaves were washed thoroughly to remove dust and contamination and dried at 100 °C for 2 hours. Then held in a box furnace (MPA6/ 400 °C) equipped with vacuum champers (Eyela, A-35), and heated at 280 °C for four hours, causing a considerable weight loss with an average of 32 % present. The date palm leaves (DPLs) were cut into small pieces, washed thoroughly with hot distilled water to remove dust and impurities and dried in an oven at 100 ˚C for 2 hours. Then the dried leaves were carbonated at 280 C in a vacuum chamber for 4 hours, to cause them to shrink and break the palm leaves microstructure and realize no carbon content [22]. The average weight loss was about 32%, mainly due to the loss of volatile components and tar [13, 15]. The pre-carbonized date palm leaves were converted into a fine grain powder using the micro-hammer cutter for 20 hours of milling time and sieved to pass through a 70-micron sever. The sifted grain powders were stored in clean, self-sealing plastic bags in silica gel until use. About 2 g of grain powder was converted to grain pellets by applying 5 to 21 metric tons of pressure in a mold of 2.1 cm in diameter and 8.5 cm in length, without adding any binder. All grain pellets exhibited an excellent self-adhesive property, before being carbonized at 1000 ºC in a nitrogen environment using a multistep heating profile by using equipment (Vulcan Box Furnace 3-1750). The heating schedule was reported elaswored [16] then the system was automatically allowed to cool down naturally to room temperature, and the obtained carbon pellets were washed thoroughly with distilled and hot distilled water to remove impurities and dried at 100 ˚C for 2 hours. The pellet's dimensions before and after the carbonization process were measured by a digital micrometer and the bulk density was determined by the ratio of its mass to volume. Results are given as the averages of 5 replicates of each sample were analyzed as a function of compression pressure.

1.2 Ultrasonic Measurement

The longitudinal velocity (*V*) and *YM* of solid carbon pellets were determined using an Ultrasonic pulsar receiver (Model 500 PR) operating at 25 MHZ and equipped with PICO ADC-200 software. The pulsar section produces electrical pulses that are converted into ultrasonic signals using identical transducers. Petroleum jelly was applied as a coupling medium at the probe sample interface. Reference glassy carbon (Sigradur-K) was used to calibrate the ultrasonic signal and measure Young's modulus (*YM*). The glassy carbon scale (Sigradur K) agreed well with the value given by the supplier with an error of < 1%. *YM* equation for the one-dimensional form of the wave equation in a weak attenuation region is given by:

$$YM = \rho V^2 \quad (1)$$

1.3 X-Ray Diffraction (XRD)

The wide angle XRD diffraction measurements were performed using (Bruker Advanced Solution AXS D8) operated at 40 kV and 30 mA, with Cu Kα- X-ray radiation. The pellets were scanned at 2Ɵ between 20^o and $70^{o,}$ with a step size of 0.04^o. The diffraction spectrum was corrected for instrumental line broadening and fitted into a symmetrical Gaussian distribution curve. The crystallite dimension of the solid carbon pellets, such as the d-spacing stack diameter (L_a) and stack height (L_c) were calculated from the full width at half maximum (FWHM) of the diffraction peaks (002) and

(100) using the well-known the Bragg's and Deby-Sherrier equations (1) and software Trace 1.4 X-ray diffraction program Varian 5 from Diffraction Technology PTG LTD, Australia to evaluate measurement accuracy.

$$L_{c,a} = \frac{K\lambda}{\beta_{c,a}\cos\theta} \tag{2}$$

where θ is the scattering angle position, λ is the wavelength of X-ray diffraction, K is a shape factor which is equal to 0.9 for L_c and 1.84 for L_a, $\beta_{c,a}$ is the width of a reflection at half-height expressed in radians. It is well known that X-ray interference intensity offers direct relationships between d_{002} and L_a can be deduced by assuming a well-known condition for large L_a and $\frac{1}{L_a}$ approaches zero, and that d_{002} and $\frac{1}{L_a}$ should follow a linear equation given as [16] (Abubaker, 2023).

$$d_{002} = 3.354 + \frac{9.5}{L_a} \tag{3}$$

where 3.354 Å is the value representing the interlayer spacing of the pure graphite structure.

1.4 Microscopic Cross-Linking Model

A microscopic cross-linking model to estimate YM is proposed by Emmerich and Luengo (1993) considering that the structure of carbon pellets was assumed to be made of granular cubic volume structure reviewed elseward [8, 18].

.

$$YM = \gamma\left(\frac{1}{L^2}\right)\left(\frac{10}{6}\right)^n\left(\frac{X^{\frac{2}{3}}}{1-X^{\frac{1}{3}}}\right) \tag{4}$$

where, γ is a factor that has dimension of force and represents the degree of stiffness of the carbon material, L is the cube root of the mean grain volume and is given as:

$$L = \left[(\frac{\pi}{4})(L_a)^2 L_c\right]^{\frac{1}{3}} \tag{5}$$

$$f_1 = \frac{1}{L^2} \tag{6}$$

where La is the stack diameter and Lc is the stack height of the grain cell and 10/6 is a factor related to strength. n is the order of strength, which is given as:

$$n = \log\left(\frac{(L_c/d_{002})+1}{(L_c/d_{002})_i+1}\right)\frac{1}{\log 2} \tag{7}$$

$$f_2 = \left(\frac{10}{6}\right)^n \tag{8}$$

$$n = \frac{1}{\log 2}\log\left[\frac{\left(\frac{L_C}{d_{002}}\right)+1}{\left(\frac{L_C}{d_{002}}\right)_i+1}\right] \tag{9}$$

where i is denoted as a structural parameter of the carbon sample taken at the initial value (for a carbon pellet prepared with 5 metric tons of pressure is considered as an initial value:

$$f_3 = \frac{X^{\frac{2}{3}}}{(1 - X^{\frac{1}{3}})} \tag{10}$$

Equation (3) can be rewritten as:

$$\rho V^2 = \gamma \left(\frac{1}{L^2}\right)\left(\frac{10}{6}\right)^n \left(\frac{X^{\frac{2}{3}}}{1-X^{\frac{1}{3}}}\right) \tag{11}$$

$$\text{Let } H = \gamma \left(\frac{1}{L^2}\right)\left(\frac{10}{6}\right)^n \tag{12}$$

Substitute the value of volume fraction as:

$$\left(\frac{X^{\frac{2}{3}}}{1-X^{\frac{1}{3}}}\right) = \left(\frac{\left(\frac{\rho}{\rho_g}\right)^{\frac{2}{3}}}{1-\left(\frac{\rho}{\rho_g}\right)^{\frac{1}{3}}}\right) \tag{13}$$

After substitution equation (9) finished to a polynomial equation (10)

$$\left(\rho^{\frac{2}{3}}\right)\left(\rho_g^{\frac{1}{3}}\right) - \left(\rho^{\frac{1}{3}}\right)\left(\rho_g^{\frac{2}{3}}\right) + \frac{H}{V^2} = 0 \tag{14}$$

1.5 Specific Surface Area (SSA)

The surface area (SA) of porous material can be given as:

$$SSA = \frac{\mathbf{2}}{\boldsymbol{\rho L_c}} \tag{15}$$

Substitute equation (15) into Equation (14). The surface area finished to the following polynomial equation (16):

$$\left(\frac{1}{SSA}\right)^{\frac{2}{3}}\left(\frac{2}{L_c}\right)^{\frac{2}{3}}\rho_g^{\frac{2}{3}} - \left(\frac{1}{SSA}\right)^{\frac{1}{3}}\left(\frac{2}{L_c}\right)^{\frac{1}{3}}\rho_g^{\frac{1}{3}} + \left(\frac{H}{V^2}\right) = 0 \tag{16}$$

1.6 Porosity (B)

Porosity can be estimated from direct measurement of bulk density as:

$$\rho = \rho_g(1 - B) \tag{17}$$

Substitute equation (18) into polynomial equation (14):

$$(1 - B)^{\frac{2}{3}} - (1 - B)^{\frac{1}{3}} + \frac{H}{\rho_g V^2} = 0 \tag{18}$$

All the polynomial equations were solved by Mathcad programs to asses' accuracy

1.7 Spring Length (S_p) Between the Cubic Granular Volume Structure

The spring length (S_p) between cubic granular volume structures of the carbon sample is given as [18].

$$S_p = L\left(\frac{1-X^{\frac{1}{3}}}{X^{\frac{1}{3}}}\right) \tag{19}$$

$$d_{002} = 3.354 + \frac{9.9}{L_a} \tag{20}$$

2. Results and Discussion

2.1 Bulk Density and Young's Modulus

The bulk densities of the pellets were recorded before and after the carbonization process showing that the bulk solid density increased, but the apparent density decreased slightly after carbonization despite losing considerable weight and significant volume shrinkage. The carbon yield of the carbon pellets varied from 27.29 % to 32.20 % with the increase in the compression pressure. A similar result has been found for activated carbon based on olive stones activated by phosphoric acid (31%-36 %) [23]. The density of the solid carbon pellets increased rapidly with compression up to 15 metric tons of pressure and subsequently decreased. These results are consistent with the expectation that a green body containing less volatile volumes will develop a better microstructure and stronger inter-particle bonding during carbonization. In addition, the increased compaction pressure reduces the intergranular distance by reducing the voids, forming a solid bond that can improve the mechanical properties of the carbon pellets produced [8]. A compression pressure of 10-21 metric tons of pressure yielded CPs with acceptable mechanical properties. YM of the CPs produced were found in the range of activated carbon from date palm leaves treated with KOH (10 GPa -5GPa) [7]. It has been suggested that the crystalline structure in the CP is first damaged or not well-developed below 11 metric tons of pressure and recrystallization occurred above 11 metric tons of pressure during the carbonization process. The overall properties of the carbonized date palm leaves can be improved by increasing the pallarization pressure. Further comparison, pressure improves the ordering and orientation of crystallites in the direction of the fiber axis. These result in better mechanical properties of the final carbon produced. Table 1 shows that Young's modulus for the CPs increased with the compression from 5 to 21 metric tons of pressure.

Table 1. Carbon pellets Before Carbonization and After Carbonization Process

Grain Pellets				Carbon Pellets				
CP(MT)	T_1 **(mm)**	D_1 **(mm)**	ρ_1 **(g/cm^3)**	T_2 **(mm)**	D_2 **(mm)**	ρ_2 **(g/cm^3)**	YM_1 **(*GPa*)**	**Carbon Yield %**
05	0.275	2.707	1.2439	1.99	19.60	1.063	2.81±0.145	26.40
07	0.264	2.716	1.3452	1.82	19.57	1.072	3.33±0.155	27.29
09	0.258	2.717	1.408	1.77	19.51	1.124	4.72±0.210	28.98
10	0.253	2.712	1.4669	1.79	19.45	1.212	5.21±0.261	29.66
11	0.251	2.703	1.4954	1.81	19.37	1.222	5.37±0.269	30.45
13	0.25	2.707	1.5051	1.80	19.37	1.293	5.48±0.119	31.87
14	0.248	2.71	1.5278	1.79	19.38	1.256	5.92±0.274	30.63
15	0.247	2.704	1.5436	1.77	19.34	1.281	5.79±0.289	30.48
16	0.246	2.714	1.5505	1.79	19.41	1.244	6.32±0.310	30.38
17	0.245	2.71	1.5654	1.77	19.38	1.298	6.39±0.316	30.95
19	0.244	2.712	1.5771	1.79	19.39	1.323	6.89±0.345	32.28
21	0.244	2.709	1.5789	1.77	19.37	1.276	7.11±0.356	30.41
SIG-K^s						1.540	35.75	
SIG-K^m						15.40	34.90	
A							10.15-5.35	
B								31-36.8

Note: S is for suppler and M is for masearrment, A is for activated carbon from date palm leaves treated wit potassume hydroxide and B is for activated carbon from olive stons [23].

2.2 X-ray Diffraction (XRD)

Figure 1 represents the X-ray diffraction profile of the CP produced. The diffraction intensity, initially at (002) and (100) reflection of Bragg's peaks, was broad with higher background intensities profiles showing that typical structure is turbostratic [3, 16] diffraction profile has been corrected to the background line and fitted to the Gaussian distribution curve, as shown in Figure 1. The Gaussian distribution shows the diffraction intensity profile is broad and overlapped, consisting of Bragg's peaks, (101) (002), (100), and (111), reflection plan, corresponding to diffraction angles of 14.37° 25.55°, 45.22o and 54.20°, respectively. After correction, the diffraction intensity and Bragg's peaks were the same as in a graphite-like structure, and the layer separation was slightly further apart than in graphite as shown in Figure 1.

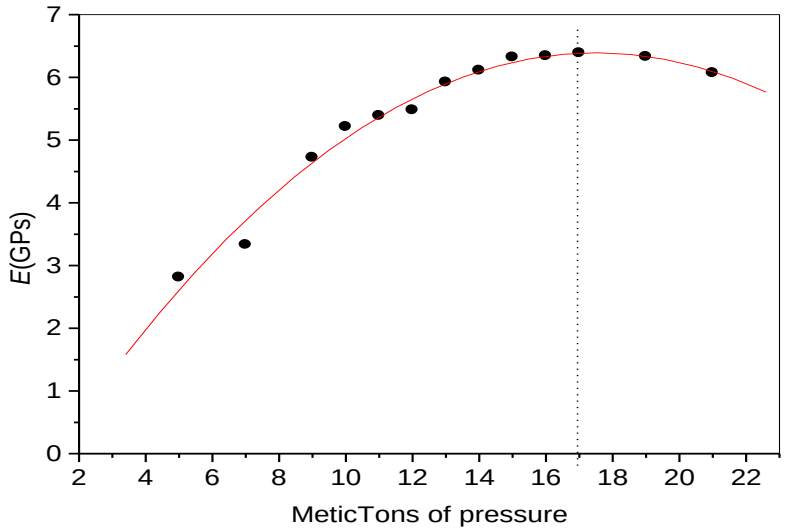

Fig. 2. - X-ray diffraction pattern of carbon pellets fitted using a Gaussian distribution, showing broad turbostratic peaks corresponding to (101), (002), (100), and (111) reflections

Table 2. Crystallite dimensions (Lc, La, and d002) of carbon pellets (CPs) prepared under different compression pressures, compared with activated carbon from date palm leaves (A) and commercial activated carbon (AC-Type H)

CP(MT)	(h k l)		
	(002)	(100)	(002)
	L_c (nm)	L_a (nm)	d_{002} (nm)
05	1.56	2.746	0.370
07	1.61	2.746	0.370
09	1.71	2.914	0.368
11	1.71	3.006	0.367
12	1.61	3.209	0.365
13	1.764	2.914	0.368
15	1.66	3.006	0.367
17	1.82	2.827	0.369
19	1.61	2.596	0.372
21	1.76	2.914	0.368
A	1.65-1.8	2.71-31.5	
Ac-TypeH	0.70	3.2	3.6

Note: A is activated carbon pellets from date palm leaves activated from KOH. AC-TypeH commercial activated carbon.

Table 2 show that the crystallite dimensions d002 decreased and Lc, and La increased with increasing the compression pressure from 5 to 14 metric tons, showing that an improvement in the crystalline dimensions in the carbon pellets, indicated that the system behaves more like a graphite-like structure. A similar observation on the carbon-based wood stress breading above 16 metric tons of pressure gave the highest values for L_c, and L_a, indicating that it is an optimum compression pressure that can be used to pelletize the grain pellets. While the decrease of Lc, and La above 16 metric tons of pressure gives us information about the reduction in the crystalline structure. The value of L_c, and L_a is close to that of activated carbon made from date palm leaves activated with potassium hydroxide [7] and commercial activated carbon (AC-Type) [24] as shown in Table 1. It is possibly due to stress broadening or overloading causing some crystallite dimensions. Indicating that can improve the crystallite dimensions by compression pressure. The relationship between d_{002}

*a*nd L_a can be deduced by equation (2), which for a large La, 1/ L_a approaches zero and the relationship between d_{002}, vs. 1/ L_a obeys the linear equation as shown in Figure 8. The data fitted very well, as with a slope equal to 9. 9 and a cut axis of 3.354 Å, which is in good agreement with the theoretical equation (3). Indicating that the interlayer spacing is controlled by the stacking orders.

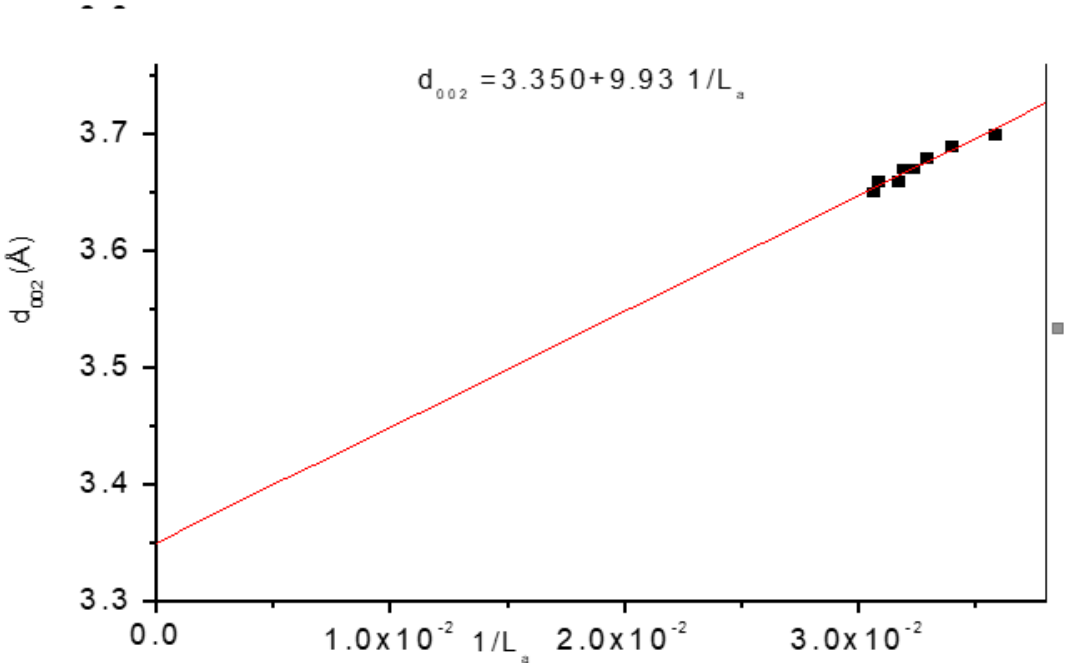

Fig. 3. - Correlation between interlayer spacing (d002) and inverse crystallite diameter (1/La), showing a linear fit consistent with graphite-like stacking behavior

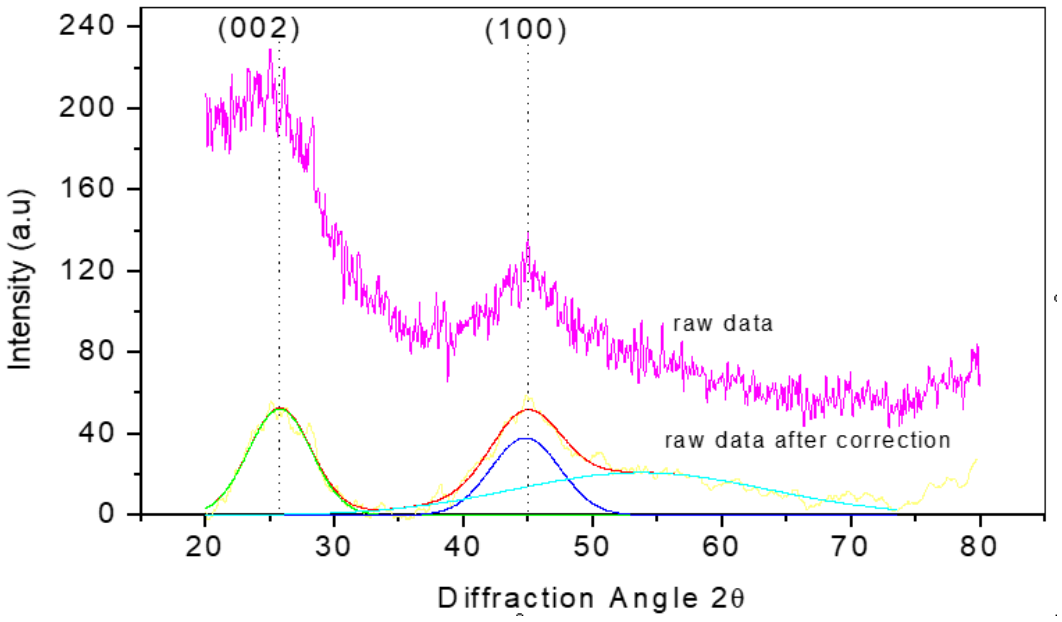

Fig.4. - Gaussian peak fitting of X-ray diffraction signals illustrating the separation of overlapped Bragg reflections for improved crystallite parameter determination

2.3 Microscopic Cross-linking Model

The YM2 was estimated using a microscopic cross-linking model, by fitting data (f_1, f_2, f_3) to YM_1 using equation (20). By adjusting the value of degree of stiffness (γ) until both YM_1 and YM_2 were approximately equal as shown in Figure 4.

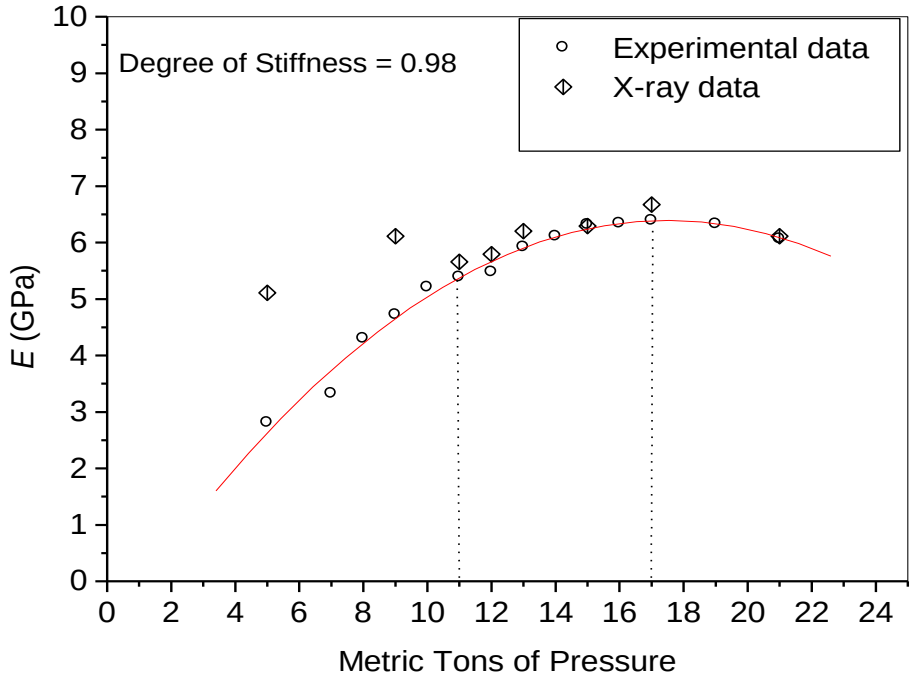

Fig. 5. - The values of the (f1, f2 and f3) were adjusted to fit the experimental data YM1veurses CP (MT) to estimate YM2

The fit seems to be reasonably good for almost all the data points, except for the data samples prepared at compression load below 11 metric tons of pressure.

Table 3. Compression pressure, volume fraction, fitting data (f_1, f_2, f_3) and YM_1 2

CP(MT)	X	f_1(nm^{-2})	f_2	f_3	YM_2(GPa)
05	0.48	2.211	2.136	1.100	5.11
07	0.50	2.211	2.768	1.100	6.32
09	0.54	1.963	2.670	1.116	6.11
11	0.57	1.844	2.779	1.125	-
12	0.58	1.618	3.093	1.145	5.66
13	0.57	1.963	2.892	1.116	-
15	0.57	1.844	3.106	1.125	5.79
17	0.58	2.085	2.920	1.108	6.20
19	0.57	2.474	3.016	1.084	6.29
21	0.56	1.963	2.636	1.116	6.67
γ	0.98 this work				
γ	0.98 [18] (Emmerich and Luengo, 1993)				
γ	0.91 (Fatima et al. 2023)				

Table 3 describes the fitted values of YM_1, f_1, f_2, f_3, and YM_2. The data show that a very good adjustment to the degree of stiffness (γ) of 0.98. The results show that Young's modulus for the carbon pellets increased with the compression pressure. Such an increase in Young's modulus of the carbon pellets can be attributed to the transformation of inter-molecular cross-links between the chain molecules. The value of degree of stiffness (γ = 0.98) was found to be similar to that given by Emmerich and Luengo (1993) for a carbon sample from babassu coconut, estimated as a function of heat treatment temperature (γ = 0.98). These results prove our assumption of the *YM* for the carbon samples as a function of compression pressure occurs similarly as a function of heat treatment temperature. In addition, this result indicates that the degree of stiffness is the same in both carbon samples, even though they were produced from different raw materials and different methods of preparation. This is also close to that of activated carbon-based date palm leaves treated with potassium hydroxide (KOH), (γ = 0.91) [7]. It can be concluded that the crystallite parameters can play a fundamental role

in the phenomenological description of carbon samples, which indicate the applicability of the expression, developed using microscopic cross-linking.

2.4 Specific Surface Area (SSA)

Table 4. The compression pressure, Surface area (SSAo, SSA- , SSA+) and Porosity (*B*,% *B*'+% , *B*'- %) of the carbon pellets

CP(MT)	SSA_o m^2/g	*SSA*- m^2/g	*SSA*+ m^2/g	B%	B+%	B-%
05	1361.1	1489.3	1115.3	49.3	51.8	47.1
07	1333.3	1757.9	1802.9	48.1	50.4	45.7
09	1315.4	1252.5	1849.3	39.0	46.1	41.4
10	1374.2	N	N	N	N	N
11	1430.1	1396.6	2186.5	37.4	43.4	38.7
12	1346.0	1253.0	3998.5	N	N	N
13	1466.0	1424.4	1978.2	35.3	42.2	37.5
14	N	N	N	37.0	42.5	37.8
15	1546.2	1216.0	3869.7	36.0	42.6	37.9
16	N	N	N	37.0	42.4	37.7
17	1424.0	1462.0	3017.1	39.5	43.4	38.7
19	1645.5	1627.8	1733.1	36.1	43.7	39.0
21	1361.1	1320.3	2393.7	49.3	51.8	47.1
A	(1308-1658).					
B	1212			39.0-47.0		
C	1222					

Note: SSA_o is calculated from Equation (15), and (–*SSA*,+*SSA*) are calculated from equation 16. Porosity (*B*,% is calculated from Equation 17 and (*B*'+% , *B*'- %) are calculated from Equation 18 and N is not detected. A is for activated carbon from date palm leaves trated with KOH [8]. B is for activated carbon from olive stons treated with phosphoric acid [23]. C Activated carbon from grape seed treated with KOH (1222 m^2/g) [10].

Table 4 represents the specific surface area (SSA) of the CPs calculated from the bulk density and stacking layer height (L_c) (Equation (16)) and the specific surface area (SSA1) estimated by solving the polynomial equations (12) by using Mathcad mathematical programs to assess accuracy. The data shows that the specific surface area increased consistently with the increasing compression pressure. It seems that activated carbon pellets have an excellent specific surface area of (1333.3 m2 /g - 1466 m^2/g), it is in the range of activated carbon from date palm leaves activated with potassium hydroxide (13073 m^2/g -16583 m^2/g) and higher than the BET surface area (1218 m^2/g) of activated carbon based olive stones activated with phosphoric acid [23]. As shown, the calculated values from the microscopic cross-linking model are in good agreement with the data estimated from the crystallite dimensions and the bulk density, when considering the allowable experimental error. This implies that the compression pressure can control the pore size distribution of the CPs produced, with a high specific surface area achieved by date palm leaves, carbonized at 1000 oC, using multistep heating profiles. These results indicate that the structure of carbon pellets is composed of micropours, mesoporous and macroporus structures. This also shows that it is possible to prepar carbon from date palm leaves without adding any chemical agent with a high surface area.

2.5 Porosity

The porosity calculated by direct bulk density and polynomial equation (18) summarize all data fit very well given the porosity content in the CPs produced in the range of (49.3% - 35.3 %). Similarly, found in activated carbon pellets from date palm leaves treated with KOH (39% -48%) [21]. It is indicated that ithe polynomial equation can be used to estimate the porosity of the carbon material as a function of the crystallite dimensions.

2.6 Spring Length (Sp) Between Two Cubic Granular Volume microstructure Structures

The values of spring length (Sp) between two cubic granular volume structures were calculated using the equation 19). The results show that the Sp decreased linearly with increasing compression from 5 to 11 metric tons of pressure. This feature is best expressed in terms of the fitted linear equationsIt is possibly due to volume shrinkage as well as weight loss of the grain pellets during the pyrolysis mechanism. The values of Sp varied from 0.423 nm to 0.581 nm, which is higher than that of interlayer spacing (d002) in the CPs produced as shown in Table 2. In our opinion, the results in this section demonstrate that the carbon samples are safe from crack and/or collapse during pyrolysis mechanisms and the washing process to remove impurities. Therefore, it is expected that the carbon pellets produced can support any themaroelectrical and mechanical application. Similar observations have been found for activated carbon based on date palm leaves treated with potassium hydroxide [21]. The result from this sample, also suggested that it would be possible that the green bodies would collapse if the Sp in the range of the interlayer spacing (d002). This could be another class of measurement in order to solve the cracking problem in material science research and manufacturing companies. Figure 5 show that the Sp exhibited a fluctuating behavior as a function of compression pressure, with a more gradual change indicating that the

disordered carbon structure formed, allowing some localized deformations, which reflect the range of the stress broadening effect.

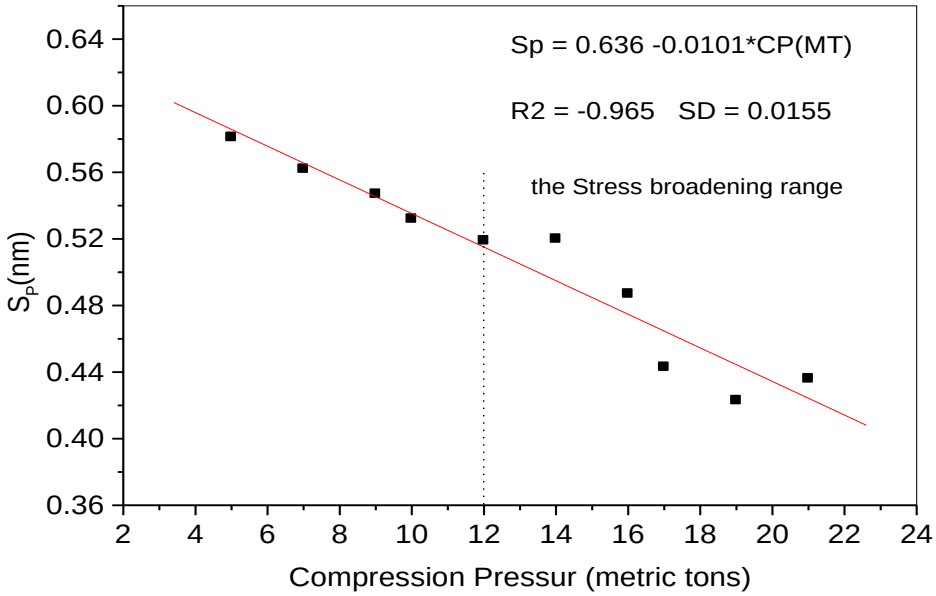

Fig.6. - Variation of spring length (Sp) between cubic granular microstructures as a function of compression pressure, showing a decrease followed by fluctuations attributed to stress broadening

Conclusion

Date palm leaves are found to be suitable for making carbon pellets without binding agents in different compression pressures. XRD diffraction intensity displayed a rising trend of crystallite dimensions with compression load, with d002 and Lc values equal to graphitic-like crystals. The study showed that the increase of palletization pressure resulted in the enhancement of YM, thus, the authors concluded that the bulk density and YM could be controlled by the compression pressure of PCDPLs powder. The microscopic cross-linking model can be used to characterize the YM, surface area and porosity of carbon samples, thus, revealing the origins of the microstructure. It is possible to merge the structural properties of disordered or inhomogeneous materials like carbon for such characterization. The stress broadening effect was noticed when the pressure was above 12 metric tons. The crystallite parameters are of great importance in the phenomenological description of carbon samples, thus proving the validity of the microscopic model.

Acknowledgements

The authors extend their appreciation to Deanship of Scientific Research at King Khalid University for funding this work through General Research Project under grant number (GRP 1/127/44).

References

[1] Lam E., Luong J.H Carbon materials as catalyst supports and catalysts in the transformation of biomass to fuels and chemicals //ACS catalysis, 2014, 4(10), P. 3393-3410.

[2] Pagketanang T., et al. Microporous activated carbon from KOH-activation of rubber seed-shells for application in capacitor electroden //Energy Procedia, 2015, 79, P. 651-656.

[3] Sawant S.Y., et al. Precursor suitability and pilot scale production of super activated carbon for greenhouse gas adsorption and fuel gas storage //Chemical Engineering Journal, 2017, 315, P. 415-425.

[4] Rawat S., Mishra R.K., Bhaskar T. Biomass derived functional carbon materials for supercapacitor applications //Chemosphere, 2022, 286, P. 131961.

[5] Yue J., et al. Biomass carbon materials with porous array structures derived from soybean dregs for effective electromagnetic wave absorption //Diamond and Related Materials, 2022, 126, P. 109054.

[6] Tadda M.A., et al., A review on activated carbon: process, application and prospects. Journal of Advanced Civil Engineering Practice and Research, 2016, 2(1), P. 7-13.

[7] Abbas F.M., et al. Characterization of carbon pellets prepared from date palm leaves (Phoenix dactylifera L.) by compression pressure: X-ray diffraction measurements and applications. 2022.

[8] Abbas F.M., Abdelrahman A.E., Arof A.K. Characterization of the Crystallites Parameters, Specific Sur-face Area, Young's Modulus and Spring Length of the Cubic Granular Volume Microstructures of the Activated Carbon Pellets from Date Palm Leaves Treated with KOH. 2023.

[9] Ishak M., et al. Effect of carbonization temperature on the physical and electrochemical properties of supercapacitor electrode from fibers of oil palm empty fruit bunches //AIP Conference Proceedings, 2015, AIP Publishing LLC.

[10] Okman I., et al., Activated carbons from grape seeds by chemical activation with potassium carbonate and potassium hydroxide. //Applied Surface Science, 2014, 293, P. 138-142.

[11] Dairi B., et al., Morphological, mechanical, and physical properties of composites made with wood flour - reinforced polypropylene/recycled poly (ethylene terephthalate) blends //Polymer Composites, 2017, 38(8), P. 1749-1755.

[12] Haque M.M.-U., et al. Fatigue performance of wet and dry pulverized wood flour reinforced PP composites //Journal of Composites Science, 2019, 3(1), P. 20.
[13] Dhyani V., Bhaskar T. A comprehensive review on the pyrolysis of lignocellulosic biomass //Renewable energy, 2018, 129, P. 695-716.
[14] Supong A., et al., Adsorptive removal of Bisphenol A by biomass activated carbon and insights into the adsorption mechanism through density functional theory calculations // Sustainable Chemistry and Pharmacy, 2019, 13, P. 100159.
[15] Hussain A., et al. Pyrolysis of Saudi Arabian date palm waste: A viable option for converting waste into wealth. 2014.
[16] Abdelrahman A.E., Abbas F.M., Arof A.K. Crystallite Parameters, Amorphous Contents and Surface Functional Groups, Contents of Activated Carbon Prepared from KOH Treated Pre-Carbonized Date Palm Leaves (Phoenix dactylifera L.). 2023.
[17] Abbas F.M., Abdelrahman A.E., Arof A.K. Specific Surface Area and Spring Lengths between Two Cubic Volumes Structure of the Activated Carbon Pellets, from Palm Leaves, Treated with KOH and Carbonized at Different Temperature. 2023.
[18] Emmerich F., Luengo C.,Young's modulus of heat-treated carbons: A theory for nongraphitizing carbons //Carbon, 1993, 31(2), P. 333-339.
[19] Alasfar R.H., et al., A review on the modeling of the elastic modulus and yield stress of polymers and polymer nanocomposites: Effect of temperature, loading rate and porosity //Polymers, 2022, 14(3), P. 360.
[20] Li C., Xian G. Experimental and modeling study of the evolution of mechanical properties of PAN-based carbon fibers at elevated temperatures //Materials, 2019, 12(5), P. 724.
[21 Choren J.A., Heinrich S.M., Silver-Thorn M.B. Young's modulus and volume porosity relationships for additive manufacturing applications //Journal of materials science, 2013, 48(15), P. 5103-5112.
[22] Radenahmad N., et al. A review on biomass derived syngas for SOFC based combined heat and power application //Renewable and Sustainable Energy Reviews, 2020, 119, p. 109560.
[23] Yakout S., El-Deen G.S. Characterization of activated carbon prepared by phosphoric acid activation of olive stones //Arabian journal of chemistry, 2016. 9, P. S1155-S1162.
[24] Faber K., et al. Investigation of the Microstructure of Disordered, Non - graphitic Carbons by an Advanced Analysis Method for Wide - Angle X - ray Scattering //Zeitschrift für anorganische und allgemeine Chemie, 2014, 640(15), P. 3107-3117.

Information of the authors

Abbas Fatima Musbah, professor, King Khalid University, College Science and Art
e-mail: Fatimamusbahabbas@researchergroup.co

Khalofa Ahlam, professor, Ministry of Science Higher Education and Scientific Research
e-mail: ahlam_khalofa12@outlook.com

Abbas Hanan Musbah, professor, Ministry of Science Higher Education and Scientific Research
e-mail: hanan_musbah12@outlook.com

Al-Ahamd Zehbh Ali, professor, King Khalid University
e-mail: zehbh-al-ahamd@outlook.com

Abdelrahman Abubaker Elsheikh, associate professor, director, Act Center for Research
e-mail: 3elsheikh98@outlook.com

DOI 10.52209/2706-977X_2025_4_80 **IRSTI 55.22.19** **UDC 621.793.7**

The Influence of Gas-Dynamic Spraying Temperature on Residual Stresses of the Coating

Olzhataev O.K.[1], Zharkevich O.M.[1,3]*, Allayarov I.S.[1], Rubenkov V.P.[1], Shlyakhov S.V.[2,3]
[1]Abylkas Saginov Kataganda Technical University, Karaganda, Kazakhstan
[2] KurylysMet LLP, Karaganda, Kazakhstan
[3]QarTech Innovation and Industrial Hub, Karaganda, Kazakhstan
*corresponding author

Abstract. This article examines the effect of working gas temperature during gas-dynamic spraying (GDS) on residual stresses in coatings made of CRO ceramics and NiAlSiCr metal composites. GDS is a promising technology for applying protective and restorative coatings in mechanical engineering, preventing component overheating (the substrate temperature typically does not exceed 100-150 °C). The method involves the solid-phase bonding of powder particles, accelerated to supersonic speeds, with the component surface due to their plastic deformation upon impact. The working gas is typically heated to temperatures between 300°C and 700°C. Experiments were conducted using a DIMET 405 setup on St3 steel samples at three gas stagnation temperature settings: 200°C, 300°C, and 400°C. Residual stresses were measured using an IKN-3M-129 stress concentration meter. It was found that increasing the working gas temperature from 200°C to 400°C sharply reduced compressive residual stresses (to -121.75 MPa for NiAlSiCr and -81.125 MPa for CRO at 200°C), followed by a transition to low tensile stresses (to +3.5 MPa for CRO). This is explained by the fact that higher temperatures increase particle plasticity, facilitating their deformation and adhesion. A spraying temperature of 400°C was found to be optimal for minimizing residual stresses, which is important for ensuring the stability and durability of the coating.

Key words: temperature, residual stress, coating quality, plasticity, powder

Introduction.

Gas-dynamic spraying (GDS) is a promising technology for applying protective coatings to various mechanical engineering components. The method involves forming a surface layer through the impact of high-speed particles of the applied powder material on the surface of the substrate (component) [1].

Unlike traditional thermal spraying methods (e.g., plasma spraying), where the material particles are completely or partially melted before impact, with GDS the powder remains solid or is heated to a temperature significantly below its melting point [2]. The working gas (often nitrogen, helium, or compressed air) is heated to a temperature typically between 300°C and 700°C (with GDS). A metal or composite powder (e.g., copper, aluminum, zinc, nickel, and their alloys) with a particle size of 1 to 50 μm is fed into the heated gas stream. The gas flow passes through a specialized Laval nozzle or similar device, where it expands, reaching supersonic speeds (hundreds of meters per second) [3]. Powder particles are entrained in this flow and also accelerate. Upon impact with the surface of the part, the kinetic energy of the particles is converted into thermal and plastic deformation energy. The particles are deformed and solid-state bonding (adhesion) occurs with the substrate and with each other. The key to forming a dense coating is for the particles to reach a critical deposition velocity (but not erosion velocity) [4].

Gas-dynamic spraying is an effective method for restoring the geometry and functional properties of worn, corroded, or damaged parts, often in aircraft, mechanical engineering, shipbuilding, and electrical engineering [5].

GDS is actively used to repair cracks, chips, abrasions, corrosion damage, and to restore the geometric dimensions of mounting surfaces [6].

GDS is used for [7]:

- restoring worn bearing or sealing surfaces on crankshafts, pump shafts, and electric motor shafts;
- repairing cracks, holes, and damaged threaded holes in cylinder blocks, gearbox housings, and hydraulic equipment;
- applying conductive layers (e.g., copper or aluminum) to restore contacts, busbars, or repair windings.
- it is especially effective for restoring aluminum and magnesium parts, as the low process temperature prevents their warping and structural changes;
- repairing piston rods, cylinders, and plungers in hydraulic and pneumatic equipment.

The key advantages of GDS make it the preferred choice for many restoration tasks [8]:

- the substrate (workpiece) remains virtually unheated (the temperature typically does not exceed 100-150°C). This eliminates thermal deformation (warping), oxidation, structural changes, and burnout of alloying elements in the base material of the part;
- produces a high-quality coating with high density (porosity <1-3%) and uniformity, ensuring good adhesion and cohesion;
- the absence of an open flame, high-temperature plasma, and toxic compounds (no metal evaporation) makes the GDS process safe and environmentally friendly compared to some other thermal spraying methods;
- allows you to apply coatings from a wide range of metals (Al, Cu, Zn, Ni, Sn) and their mixtures on various substrates (metals, ceramics, polymers).

Successful use of GDS for component refurbishment requires consideration of a number of process features related to preparation, the process itself, and finishing.

Quality surface preparation is critical to ensuring high adhesion. The surface must be thoroughly cleaned of oil, dirt, rust, and old coatings. Abrasive blasting (sandblasting, shot blasting) is often used to roughen and activate the surface, which promotes mechanical adhesion [9]. Different abrasives are used depending on the material.

Coating quality and deposition rate directly depend on the precise setting of the machine parameters [10]. Gas (air) temperature affects particle plasticity. It is selected below the melting point of the powder, but high enough to ensure plastic deformation upon impact. Gas/air pressure determines the gas flow velocity and, consequently, the particle velocity. Higher pressures provide higher velocities and allow the deposition of harder materials. Powder consumption, like that of wire in other types of thermal spraying, controls the thickness and uniformity of the applied layer [11].

After spraying, the coating may require mechanical processing to achieve the required dimensions and surface finish. The applied layer is then machined or ground to the required geometric parameters (e.g., restoring the bore diameter) [12]. In some cases, to improve hermeticity or corrosion resistance, the sprayed coating can be impregnated with polymers or sealants.

Varying the temperature of the thermal spraying process significantly influences the kinetics and mechanisms of coating formation, which, in turn, determines these key characteristics [13].

The purpose of this article is to study the effect of spraying temperature on residual stresses in CRO and NiAlSiCr coatings, which will enable the development of process recommendations for producing coatings with improved performance properties.

1. Research methodology

1.1 Materials and equipment

Two spherical powders were used for the experiment: CRO (Metacerampowder 28010, Castolin Eutectic, Ireland) and NiAlSiCr (RotoTecPowder, Castolin Eutectic, Ireland) with a particle size of 10 μm.

The coatings were applied to eight St3 steel samples measuring 100 x 20 x 10 mm for each material (Figure 1a, b).

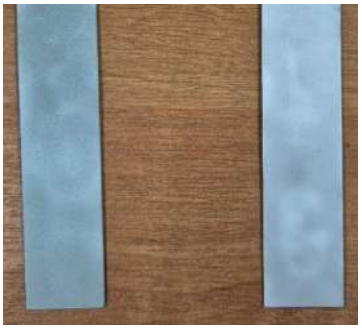

a) b)

Fig.1. – Samples with gas-dynamic coating: a) CRO; b) NiAlSiCr

Before coating, the samples were degreased. The sample roughness was 3 μm.
Powders were applied using a gas-dynamic method using a DIMET 405 system (Figure 2).

Fig. 2 – DIMET 405 Gas-Dynamic Spraying System
(Russia, Obninsk, Obninsk Powder Spraying Center LLC)

1.3 Experimental modes

For the experiment, temperature modes 2, 3, 4 were used, which indicate the gas deceleration temperature in front of the critical section of the supersonic nozzle:

- mode «2» - 300 °C;
- mode «3» - 400 °C;
- mode «4» - 500 °C.

The constants in the experiment were:

- air pressure P_{air} = 5 MPa;
- powder consumption M_{powder} = 30g/min;
- spraying distance s = 20 mm;
- torch travel speed $V_{traverse}$ = 100 mm/s;
- spray angle φ = 30ºC.

1.4 Determination of residual stresses

To determine residual stresses, an IKN-3M-12 stress concentration meter (Figure 3) was used. Under the influence of operating or residual mechanical stresses in a ferromagnetic material (in this case, steel), the metal's domain structure undergoes a restructuring. In zones of maximum residual stress (stress concentrations, defects, and structural inhomogeneities), persistent local changes in magnetic permeability occur. These changes create a self-magnetic field, which is "remembered" by the metal and emerges at its surface. The IKN-3M-12 measures the normal component (Hp) of the strength of this self-magnetic stray field on the surface of the tested object. A zero or minimum Hp value or maximum gradient variability of the field (a change in Hp sign) indicates the presence of a zone with high residual stresses.

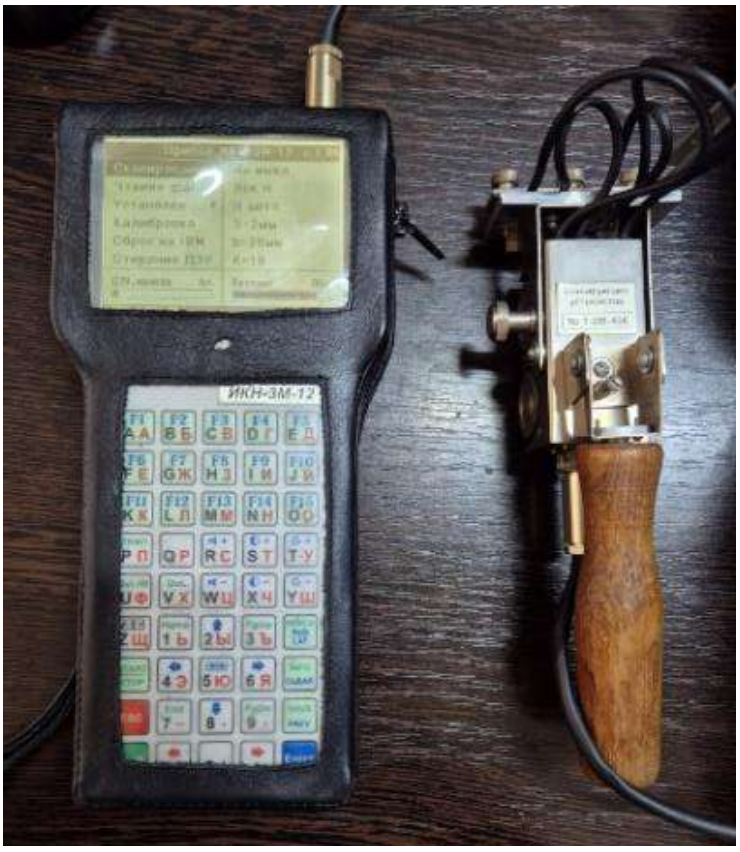

Fig. 3. – Stress Concentration Meter (IKN-3M-12)
(OOO Energodiagnostika, Moscow, Russia)

For each series, residual stress measurements were performed on individual specimens prepared in accordance with ASTM C633

2. Results and discussion

The results for the series of experiments for three different temperatures (200 °C; 300 °C; 400 °C) and two types of coatings (CRO and NiAlSiCr) are presented in Table 1 and Figures 4, 5.

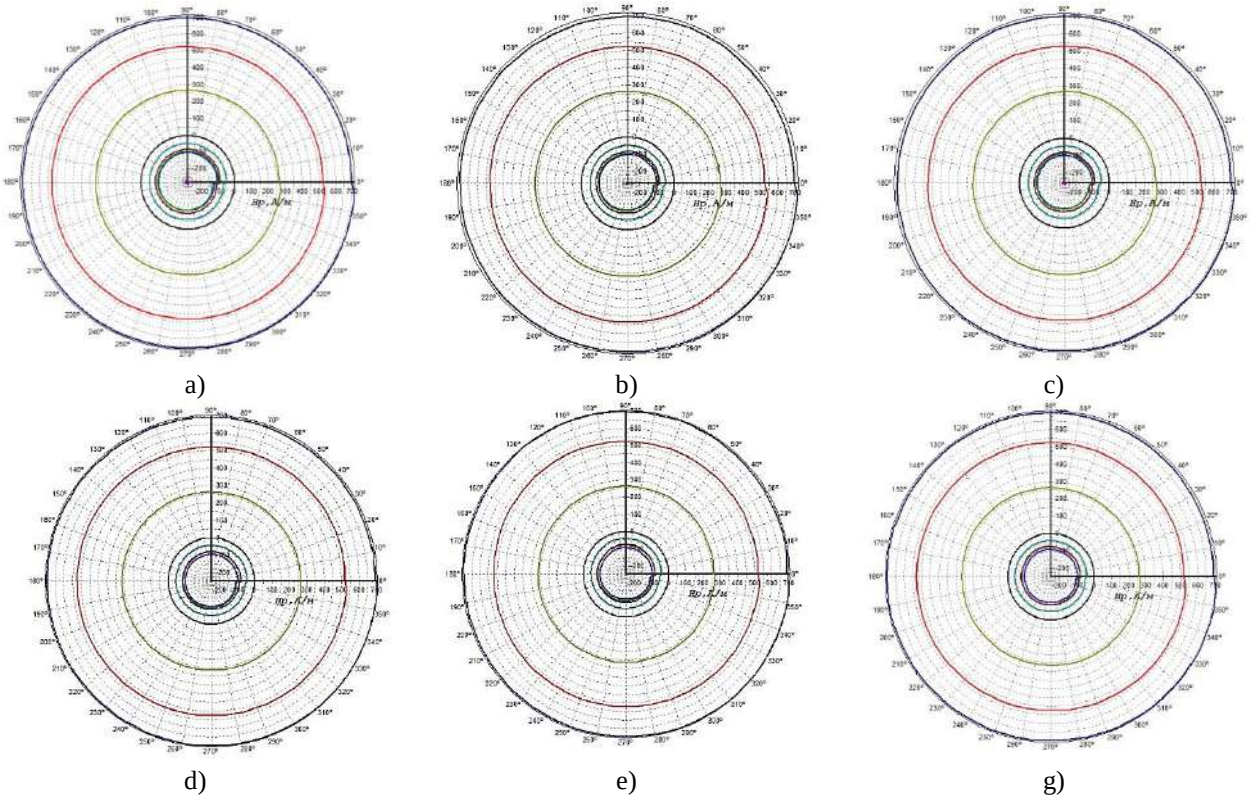

a) b) c)

d) e) g)

a) CRO at T= 200 ºC; b) CRO at T= 300 ºC ; c) CRO at T= 400 ºC; d) NiAlSiCr at T= 200 ºC ; e) NiAlSiCrg at T= 300 ºC ; g) NiAlSiCr at T= 4 00 ºC

Рис.4. – Radial diagram of the distribution of magnetic field strength Hp around the tested coating samples

Table 1. Residual stresses of coatings CRO и NiAlSiCr

Series (T,°C)	T_i, °C	$X_1 \ldots X_8$ (MPa)	Arithmetic mean $\bar{X}_i$ (MPa)	Dispersion S_i^2 (MPa)
CRO				
1	200	-90; -85; -70; -80; -90;-76;-80; -78	-81.125	41.859
2	300	-50; -55;-42;-30; -35; -40; -32; -30	-36.75	82.9375
3	400	5; 7; -1; 10; 8; -2; -4; 5	3.5	23.25
NiAlSiCr				
1	200	-120, -125, -115, -124, -128, -117, -120, -125	-121.75	18.214
2	300	-65, -50, -45, -64, -68, -55, -50, -45	-55.25	98.786
3	400	-15, -10, 5, 10, -5, 5, 12, 10	1.5	86.857

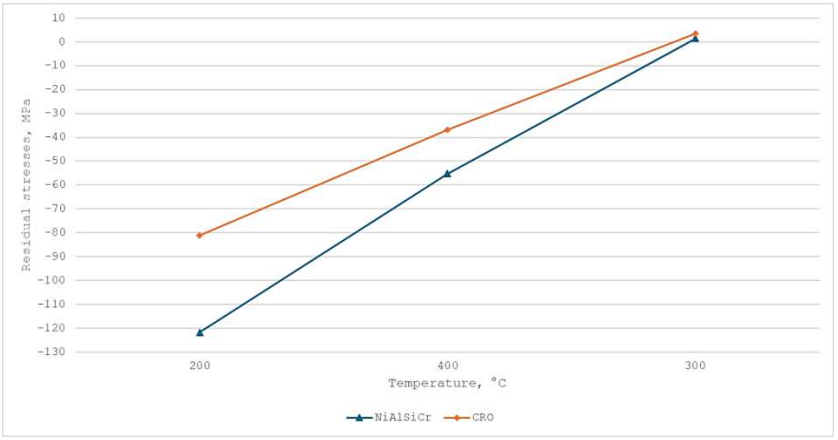

Fig. 5. - Dependence of residual stresses in gas-dynamic coatings on temperature

The graph shows that the CRO coating exhibits lower residual compressive stresses. This can be explained by the fact that CRO is a ceramic coating, which is brittle and exhibits low ductility. During cold gas-dynamic spraying, CRO particles deform significantly less than metal particles. The primary mechanism of coating formation is mechanical adhesion and, possibly, minimal plastic deformation, resulting in lower residual compressive stresses, which typically arise during impact deformation [14].

The NiAlSiCr coating is a metal-composite coating that is ductile. Under high-velocity impact during gas-dynamic spraying, NiAlSiCr particles undergo significant plastic deformation (work hardening) [15]. This deformation is the primary source of residual compressive stresses in cold-sprayed coatings, which are more pronounced than in the CRO coating. To predict, analyze, and manage the mechanical properties of gas-dynamic coatings, regression models were constructed to describe the dependence of residual stresses on temperature.

Since the dependence of residual stresses on temperature on the graph (Fig. 5) appears as a straight line, we use a paired linear regression model in the form:

$$y = a + b \bullet x \quad (1)$$

where y - calculated value of average residual stress, MPa;

x – temperature, °C;

a - free member;

b - regression coefficient.

The regression equations and intermediate data are given in the table 2.

Table 2. Regression analysis of the dependence of residual stresses on temperature in gas-dynamic coatings

Parameter	Coating CRO	Coating NiAlSiCr
Equation	y = -165.06 + 0.423 ·T	y = -243.38 + 0.616 · T
Coefficient b (MPa/°C)	0.423	0.616
Coefficient of determination R^2	0.998	0.997
Statistical significance	Statistically significant because $R^2 \rightarrow 1$	Statistically significant because $R^2 \rightarrow 1$
The actual value of Fisher's F-test (F_{fact})	699.28	447.53
Critical value of Fisher's F-test (F_{crit})	161.45	161.45
Adequacy	Adequate, because (Ffact > Fcrit)	Adequate, because, ($F_{fact} > F_{crit}$)

Both linear regression equations demonstrate very high adequacy and statistical significance for describing the dependence of the average residual stress on temperature in the studied range (200 - 400 °C).

The coefficients of determination (R^2 = 0.998 for CRO and R^2 = 0.997 for NiAlSiCr) confirm that temperature is the primary factor influencing the average residual stress in both coatings.

In both cases, a direct linear relationship is observed (since the b-coefficient is positive), meaning that as temperature increases, the average residual stress increases (becoming less compressive or more tensile).

Conclusions

The following conclusions were reached as a result of the conducted research:

1) Increasing the working gas temperature during gas-dynamic spraying from 200 °C to 400 °C leads to a sharp decrease in compressive residual stresses (≈ -121.75 MPa) followed by a transition to tensile stresses (≈+3.5 MPa);

2) The determination coefficients $R^2_{CRO} \approx 0.998$ (99.8%) and $R^2_{NiAlSiCr} \approx 0.998$ (99.7%) confirm that temperature is the determining factor in the formation of residual stresses;

3) The high observed value of the Fisher criterion ($F_{fact} \approx 699.28$) compared to the critical value ($F_{crit} \approx 161.45$) demonstrates the high adequacy of the constructed regression equation for describing the experimental data;

4) Compressive stresses (-81.125 ÷ -36.75 MPa) for both coatings contribute to increased fatigue strength, but excessively high stresses (-121.75 MPa) can lead to delamination. Zero or low residual stresses are considered optimal for coating stability;

5) A spraying temperature of 400°C is optimal for minimizing residual stresses;

6) The adhesion strength will be further analyzed to finally determine the optimal temperature regime for achieving maximum adhesion strength of the coating to the substrate.

Aknowledgments. This research was supported by the QarTech Innovation and Industrial Hub (Karaganda Region, Kazakhstan).

References

[1] Aleksieieva O., Bozoglu M., Tretiakov P., Toporov A., Antonyuk S. Coating of Refractory Surfaces with Fine TiO_2 Particles via Gas-Dynamic Cold Spraying //Coatings 2024, 14, 1151.

[2] Assadi H., Ga¨rtner F., Stoltenhoff T., Kreye H. Bonding mechanism in cold gas spraying //Acta Materialia, 2003, 51, P. 4379–4394

[3] Kafle A., Silwal R., Koirala B., Zhu W. Advancements in Cold Spray Additive Manufacturing: Process, Materials, Optimization, Applications, and Challenges //Materials, 2024, 17, 5431
[4] Rokni M. R., Nutt1 S. R., Widener C. A., Champagne V. K., Hrabe R. H. Review of Relationship Between Particle Deformation, Coating Microstructure, and Properties in High-Pressure Cold Spray // J Therm Spray Tech, 2017, 5 July
[5] Wu Q., Su J., Zhao W., Li J., Zhang K., Wang L. Determination of Critical Velocity of Cold-Sprayed NiCoCrAlY Coating via Arbitary Lagrangian-Eulerian (ALE) Method of Finite Element Simulation //Coatings 2023, 13, 1992.
[6] Rakhadilov B., Berikkhan K., Satbayeva Z., Zhassulan A., Shynarbek A., Ormanbekov K. Optimization of Cold Gas Dynamic Spray Coatings Using Agglomerated Al–Zn–TiO_2 Powders on Steel //Metals 2025, 15, 1011
[7] Singh H., Chaubey S.K., Singh S., Jhavar S., Desai D.J.K., Mishra V. An Overview of Materials, Parameters, and Applications in Gas Dynamic Cold Spraying // Advanced Materials and Manufacturing, 13 October 2025, P. 253–266
[8] Oyinbo S.J., Tien-Chien J. A comparative review on cold gas dynamic spraying processes and technologies. Manufacturing Review. 2019, 6, 25
[9] Zhetessova G., Nikonova T., Gierz Ł., Berg A., Yurchenko V., Zharkevich O., Alexey K. A. Comparative Analysis of the Dynamic Strength Properties of the Long Guides of Intelligent Machines for a New Method of the Thermal Spraying of Polymer Concrete //Appl. Sci., 2022, 12, 10376.
[10] Zhetessova G., Zharkevich, O., Pleshakova, Y., Yurchenko V.Yu., Platonova Y., Buzauova T. Building mathematical model for gas-thermal process of coating evaporation // Metalurgija , 2016, 55(1), P. 63–66
[11] Nurzhanova O., Zharkevich O., Bessonov A., Naboko Ye., Taimanova G., Nikonova, T. Simulation of the distribution of temperature, stresses and deformations during splined shafts hardfacing //Journal of Applied Engineering Science, 2023, 21(3), P. 837–845
[12] Afandi N., Mahalingam S., Tan A.W.-Y., Manap A., Mohd Yunus S., Sun W., Zulkipli A., Chan X.W., Chong A.I.-X., Om N.I. Remarkable Potential of Cold Spray in Overlay Restoration for Power Plants: Key Challenges, Recent Developments, and Future Prospects //Coatings 2023, 13, 2059.
[13] Dai S., Cui M., Li J., Zhang M. Cold Spray Technology and Its Application in the Manufacturing of Metal Matrix Composite Materials with Carbon-Based Reinforcements //Coatings, 2024, 14, 822
[14] Issagulov A.Z., Kulikov V.Y., Chsherbakova Y.P., Kovaleva T.V., Kvon S.V. The corrosion resistant coating with halloysite nanoparticles //Metalurgija, 2016, 55(3), P/ 426–428
[15] Alekseeva E., Shishkova M., Strekalovskaya D., Shaposhnikov N., Gerashchenkov D., Glukhov P. Performance of Ni-Based Coatings with Various Additives Fabricated by Cold Gas Spraying //Metals, 2022, 12, 314

Information of the authors

Olzhataev Olzhas Kanatovich, doctoral student, Abylkas Saginov Karaganda Technical University
e-mail: olzhasmailru7@gmail.com

Zharkevich Olga Mikhailovna, c.t.s., professor, Abylkas Saginov Karaganda Technical University, QarTech Innovation and Industrial Hub
e-mail: zharkevich82@mail.ru

Allayarov Ilnur Salavtovich, master student, Abylkas Saginov Karaganda Technical University
e-mail: ilnurallayarov55@gmail.com

Rubenkov Vladislav Petrovich, master student, Abylkas Saginov Karaganda Technical University
e-mail: vladrubenkov270202@gmail.com

Shlyakhov Sergey Vladimirovich, m.t.s, chief designer, «Kurylysmet» LLC, QarTech Innovation and Industrial Hub
e-mail: sergey.shlyakhov@yandex.kz

DOI 10.52209/2706-977X_2025_4_86 **IRSTI 55.19.03** **UDC 621.923**

Study of the Influence of the Angle of Inclination of the Axis of Ferroabrasive Grains on the Productivity and Surface Roughness of the Processed Part

Akulovich L.M.[1], Mendaliyeva S.I.[2], Sherov K.T.[2], Toshov J.B.[3], Mussayev M.M.[4*]
[1]Belarusian Agrotechnical University, Minsk, Republic of Belarus
[2]S.Seifullin Kazakh Agro-Technical Research University, Astana, Kazakhstan
[3]Tashkent State Technical University named after I. Karimov, Tashkent, Uzbekistan
[4]Abylkas Saginov Karaganda Technical University, Karaganda, Kazakhstan
*corresponding author

Abstract. The paper presents the results of experimental studies aimed at determining the patterns of influence of the inclination angle of ferro-abrasive grain (FAG) axes on the productivity and surface roughness of parts processed using the magnetic-abrasive method. New approaches to magnetic-abrasive finishing (MAF) are proposed by introducing an additional magnetic field into the working zone. The article includes the results of computer modeling of magnetic field topography achieved through the creation of an additional magnetic field. The behavior, trajectory, and cutting efficiency of ferro-abrasive grains are analyzed. The study suggests relocating the abrasive "brush" to the entry zone of the working gap, enabling a change in the rake angle toward positive values and increasing machining productivity. The experimental results allowed conclusions to be drawn regarding the effectiveness of creating additional magnetic fields and their influence on modifying the rake angle, thereby confirming theoretical principles on the impact of controlling the orientation angle of ferro-abrasive grains relative to the processed surface on improving MAF productivity.

Keywords: magnetic-abrasive finishing (MAF), ferro-abrasive grain, cutting angle, rake angle, ferro-abrasive grain axis, additional magnetic field.

Introduction

Magnetic-abrasive finishing (MAF), as one of the widely used types of finishing processes for parts, currently requires further clarification in studying the cutting process of abrasive grains on part surfaces. Previous studies [1, 2, 3, 4] have shown that the cutting force components in MAF depend on the inclination of the ferro-abrasive grain (FAG) axis relative to the processed surface, the coefficient of friction at the contact point between the FAG and the surface, the hardness of the processed material, and the thickness of the layer removed by an individual grain. The thickness of the removed material is determined by the cutting force component Py, which depends on the level of magnetic induction.

Based on the conducted research, it has also been determined that the cutting forces can be adjusted and technologically implemented by controlling the magnetic induction and the orientation angle of the ferro-abrasive grain relative to the processed surface, which influences the rake angle of the cutting edge [4,5]. Changes in magnetic induction and inclination angle can be achieved by introducing an additional magnetic field [6,7]. Positioning the source of the additional magnetic field alters the direction of magnetic field lines in the entry zone of the working gap, causing the FAG to rotate at an inclination angle ω, which creates conditions for cutting by micro-particles of the abrasive component located on the lateral surface of the ferro-abrasive powder (FAP).

Experimental studies to determine the effect of the modified rake angle of the FAP cutting edges on MAF productivity were conducted on a modernized ЭУ-6 installation equipped with an additional magnetic system. The experimental conditions were as follows: magnetic induction of the primary magnetic system B_p = 0.9 Tl; magnetic induction of the additional magnetic system B_{add} = 0.1 Ts; working gap of the primary magnetic system dp=1 mm; working gap of the additional magnetic system d_{add}=1.5 mm; particle size of ferro-abrasive powder FeTiC D=100–160 μm; main motion speed V=0.9 m/s.

The test samples were piston pins with a diameter of ϕ25 mm, made of 12XH3A steel with a surface layer hardness of 58–62 HRC. The output parameters were surface roughness Ra, μm; and productivity Q, mg/(cm^{2}min). Surface roughness measurements were performed using a Mitutoyo SJ-201P profilometer, and the weight of the samples was measured on Massa-K BK-600 scales with an accuracy of 0.01 g.

Two batches of samples were processed. The initial roughness of the samples was Ra = 1.14–0.97 μm. The first batch was processed without the additional magnetic system, while the second batch was processed with the influence of the additional magnetic field. All samples were treated with a new portion of powder. The experimental results are presented in Table 1.

Table 1. Indicators of productivity and surface roughness when controlling the angle of inclination of ferroabrasive grains and without control

Time processing τ, sec.	*Ra* after MAF, mkm		Efficiency of MAF*Q*, mg/(sm^2×min)	
	Without additional MS	With additional MS	Without additional MS	With additional MS
15	0,75	0,68	25,5	26,2
30	0,4	0,36	17,8	23,3
45	0,25	0,20	14,2	19,7
60	0,2	0,24	11,5	16,1

The MAF setup with an additional magnetic system maintains the initial productivity of the FAP batch for an extended period due to oriented cutting (Fig. 1).

An analysis of the experimental data (Fig. 1) shows that, in the classical MAF scheme, productivity drops sharply after 15 seconds of processing, and by 30 seconds, productivity decreases by 30%–40% compared to the level during the first 15 seconds of processing. In contrast, with MAF utilizing a controlled inclination angle of FAG in the working gap, the productivity decline is more gradual, amounting to only 10%–14% of the productivity observed during the first 15 seconds of processing.

The lowest surface roughness, when controlling the inclination angle of ferro-abrasive grains, is achieved after 45 seconds of processing, whereas with the classical processing scheme, the lowest surface roughness is attained after 60 seconds (Fig. 1).

The results of the experimental studies confirm the theoretical principles regarding the influence of controlling the orientation angle of ferro-abrasive grains (FAGs) relative to the processed surface on improving MAF productivity.

To determine the shape and dimensions of the pole tips, it is necessary to understand the distribution of magnetic field lines in the working gap for various gap geometries. As the amount of ferro-abrasive powder supplied increases, the number of grains in contact with the processed surface also rises, which slows down the rotation of the workpiece. At the same time, as the gap is filled with ferro-abrasive powder, its magnetic permeability increases, leading to a redistribution of the magnetic flux across the gap's cross-section and a reduction in the magnetic induction gradient [8,9].

Let us consider the effect of magnetic field focusing in the working gap on the gradient of magnetic induction. To analyze this, we modeled the operation of the magnetic system using the FEMM 4.2 software.

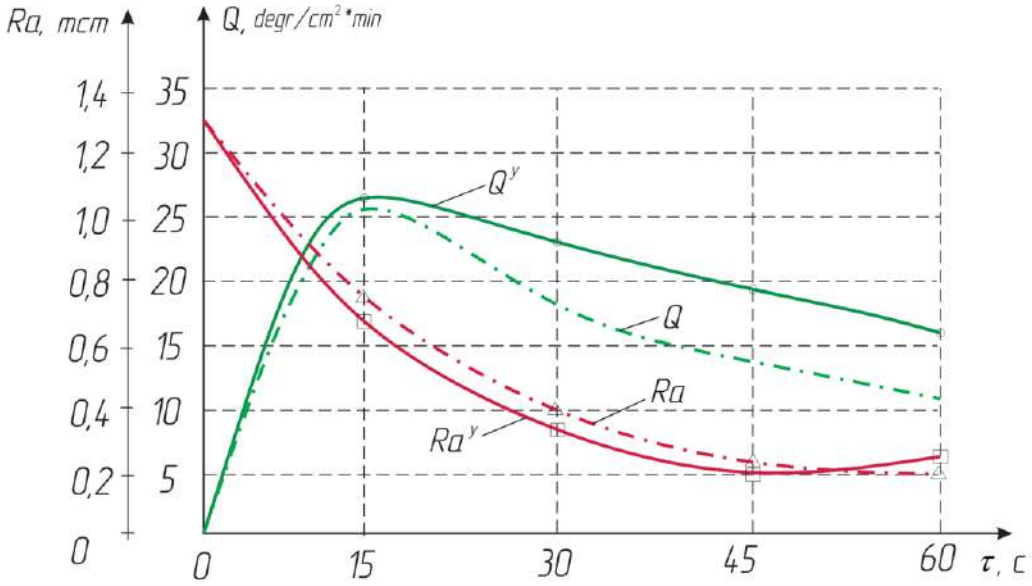

Fig. 1 - Graph of the dependence of Ra roughness and productivity Q from the processing time t. Q and Ra are the MAF performance and surface roughness, respectively, under the classical scheme; Q and Ra are the MAF performance and surface roughness, respectively, when controlling the phase orientation angle

1. Experimental Studies

To achieve controlled oriented cutting, various methods for altering the direction of magnetic field lines were explored. Ferro-abrasive grains that make contact with the processed surface via their abrasive component rotate their central axis perpendicular to the processed surface. This rotation is caused by a torque generated by friction forces at the contact point between the abrasive component of the FAG and the processed surface, which are offset from the grain orientation axis. As the density of ferro-abrasive grains increases, an "expansion" of the abrasive "brush" is observed in the exit zone of the working gap, along with changes in the magnetic field topography.

In this configuration, the FAGs adopt positions where the rake angles become negative. As a result, MAF occurs at cutting angles exceeding 90°.

It is known that as the cutting angle increases, the chip removal process worsens. Furthermore, as the cutting edges of the FAG dull, the process transitions into surface burnishing, which reduces machining productivity. Therefore, to enhance MAF productivity, it is essential to adjust the inclination angle of the FAG axis relative to the processed surface.

To reduce the cutting angle of FAGs by altering the direction of the magnetic field lines, technical solutions have been proposed. These include asymmetric placement of the pole tips of the primary magnetic field relative to the processed surface (Fig. 4a) or installing a source of an additional magnetic field between the pole tips of the primary magnetic field (Fig. 2b) [10,13].

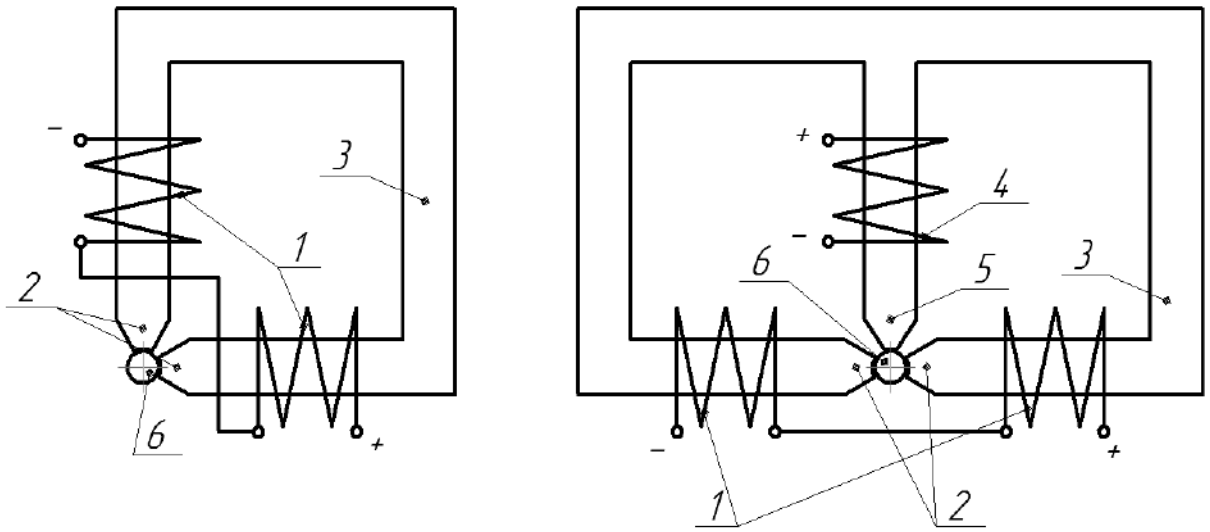

1, 4 – electromagnetic coils; 2, 5 – pole tips; 3 – magnetic core; 6 – workpiece

Fig. 2. – Schemes of MAF with asymmetrically positioned pole tips (a) and with an additional magnetic system (b)

The presence of multiple electromagnetic coils results in the superposition of the primary and additional magnetic fields in the working gap, influencing changes in the cutting angle.

Using asymmetrically positioned pole tips in MAF allows the creation of two zones within the working gap: one for micro-cutting and another for surface burnishing (Fig. 4a) [11,13].

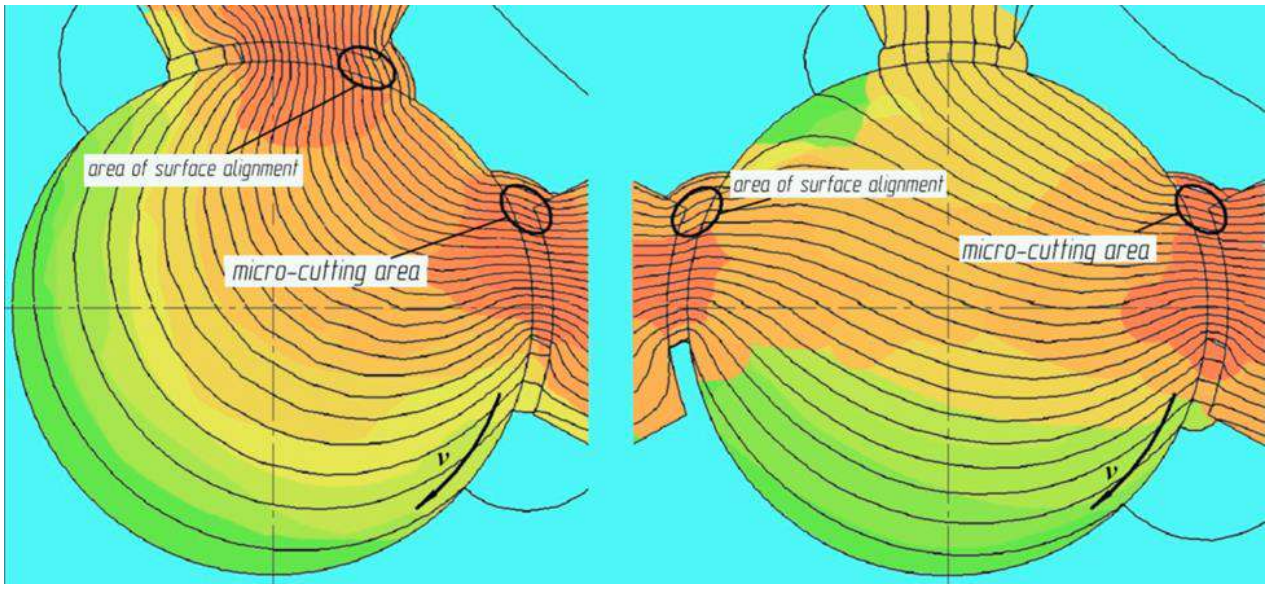

Fig. 3. – Topography of the magnetic field in the working gap
with an asymmetric arrangement of the pole tips (a) and with an additional magnetic system (b) v - main motion speed

This scheme is particularly effective for small material removal tasks when the processing time does not exceed 15 seconds.

The MAF scheme with an additional magnetic field source similarly alters the magnetic field topography in the working gap (Fig. 3b). This configuration focuses magnetic field lines in the entry zone of the working gap, creating conditions for modifying the gradient of magnetic induction within that zone [13].

Positioning the additional pole tip at a 90° angle to the main magnetic core allows adjustments to the magnitude and gradient of magnetic induction in the working gap. This, in turn, alters the direction of the magnetic field lines of the primary magnetic system.

A study of the topography of the magnetic field in the working gap using computer modeling made it possible to establish that an additional magnetic system allows changing the angle of inclination of the magnetic field lines in the area of the entrance to the working gap in the range from 43° to 50° (Fig. 4).

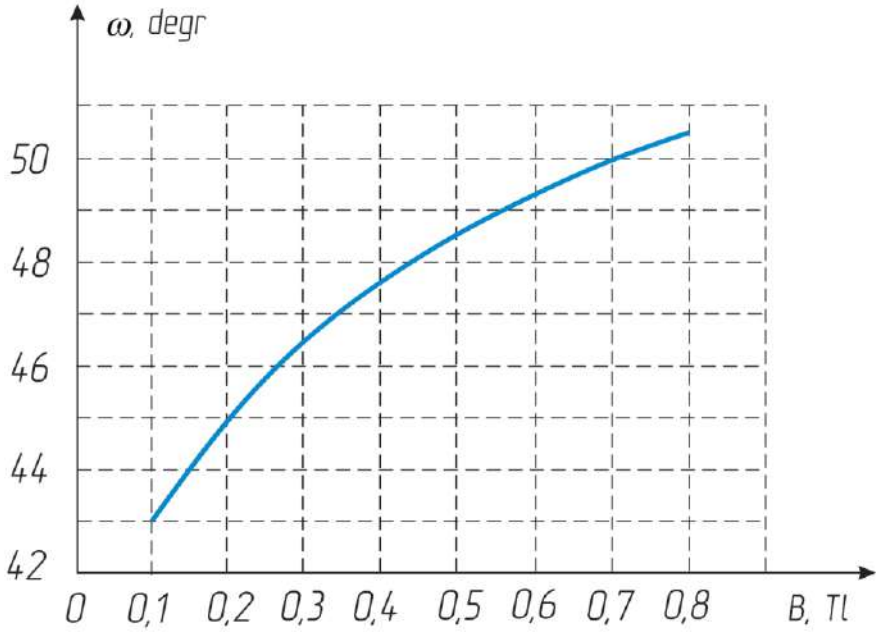

Fig 4. - Dependence of the angle of inclination of the magnetic field lines
in the area of the entrance to the working gap on the magnitude of the magnetic induction of the additional magnetic system

The change in the inclination angle ω of the magnetic field lines in the working gap is described by the equation:

$$\omega = -9.8214B_a^2 + 18.804B_a + 41.615 \quad (1)$$

where B_d - is the magnetic field induction in the working gap of the additional magnetic system, measured in Tesla (Tl).

The inclination angle of the magnetic field lines varies along the perimeter of the working gap: from the entry point to the center of the gap, the angle changes from 43^o to 85^o (Figs. 5 and 6).

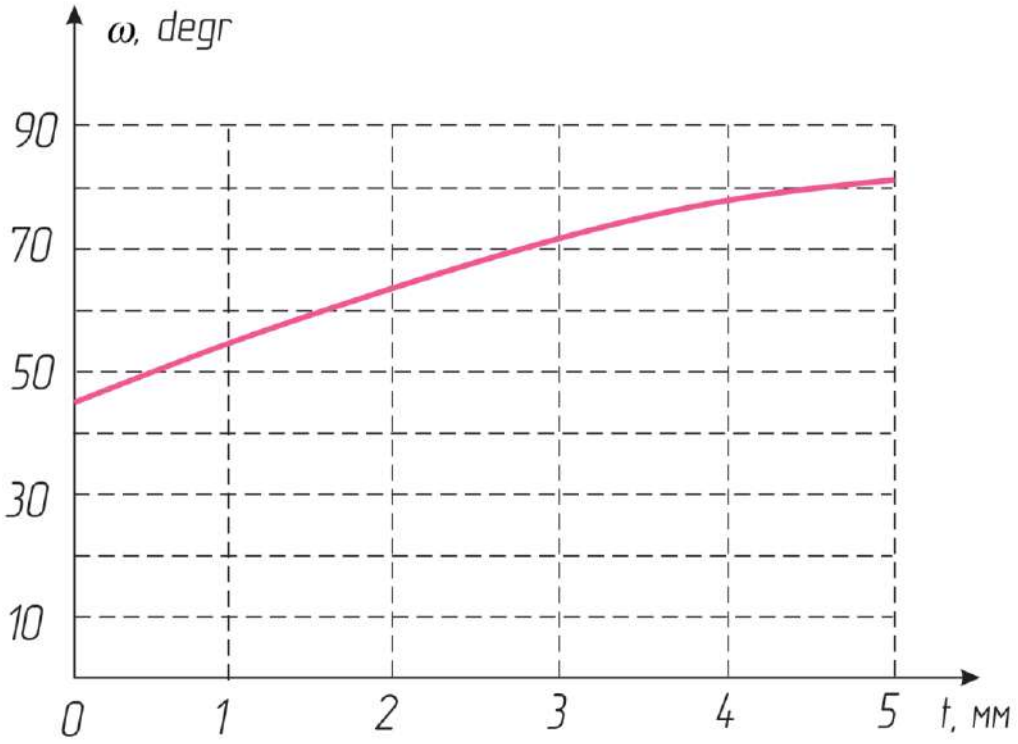

Fig 5. – Dependence of the angle of inclination of the lines of force as they move away from the point of entry into the working gap, v is the speed of rotation of the workpiece

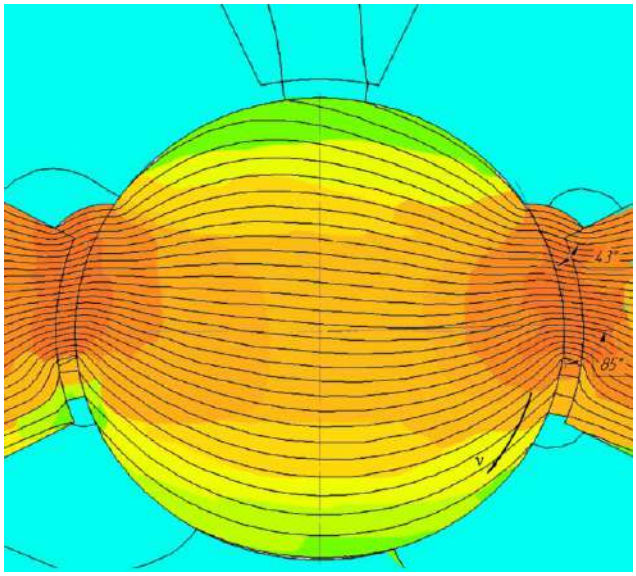

Fig 6. – Computer model of the inclination angle variation of magnetic field lines along the perimeter of the working gap

According to the principle of superposition of magnetic fields, the total change in the inclination angle of magnetic field lines across the working gap cross-section as it approaches the center of the pole tip is described by the equation:

$$\omega = -0.95t^2 + 12.387t + 42.857, \quad (2)$$

where t is the distance from the edge of the pole tip, measured in millimeters (mm).

The magnetic field at a specific point in the working gap, created by multiple sources, equals the vector sum of the fields from each source.

Computer modeling has established that the induction magnitude of the additional magnetic field is limited by the maximum induction of the primary magnetic field. If this limit is exceeded, a branch of the magnetic core at like poles is truncated, and the total magnetic flux closes through the branch with opposite poles. Therefore, the boundary condition for the magnetic induction generated by the additional magnetic system can be expressed as:

$$B_{add} < B_p, \quad (3)$$

where B_{add} and B_p are the magnetic induction magnitudes of the additional and primary magnetic systems, respectively, measured in Tesla (Tl).

The boundary value for the inclination angle of the ferro-abrasive grain (FAG) is 58° [1,13] (Fig 7).

The application of an additional magnetic system to control the inclination of the primary system's magnetic field lines allows the abrasive "brush" to shift toward the entry point of the working gap [14]. It also orients the FAGs to achieve positive inclination angles for their rake surfaces (+γ).

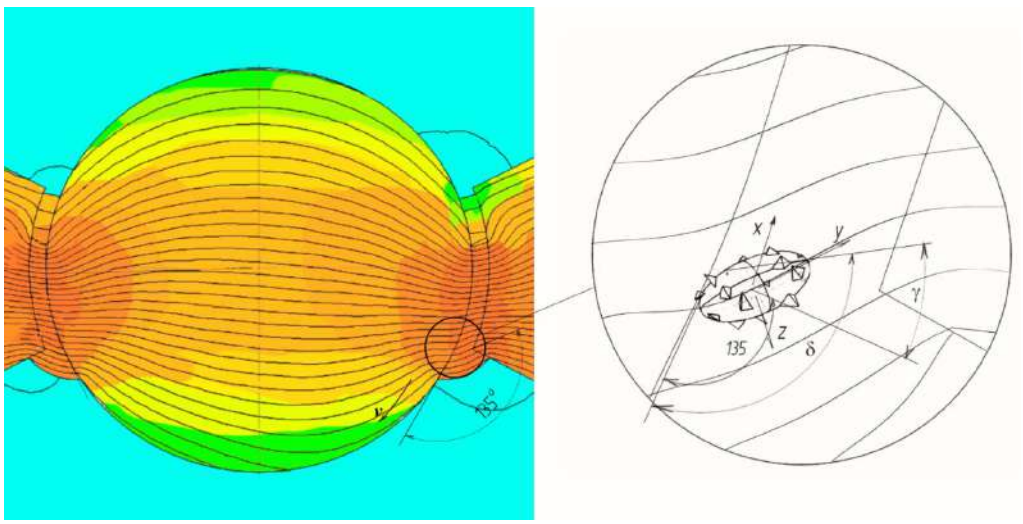

Fig 7. – Computer model of the inclination of magnetic field lines and the position of a ferro-abrasive grain v – primary motion velocity; dP – cutting angle; γ – rake angle

This arrangement of FAGs forms a cutting zone at the entry point of the working gap near one pole tip and a burnishing zone near the other pole tip of the primary magnetic system.

Smooth adjustment of the inclination angle of the magnetic field lines by varying the magnetic induction generated by the additional magnetic system allows control over the cutting intensity and the surface roughness.

Thus, modifying the magnetic field topography in the working gap during MAF of cylindrical surfaces enables the achievement of positive rake angles for the cutting edges of FAGs (Fig. 8) [13].

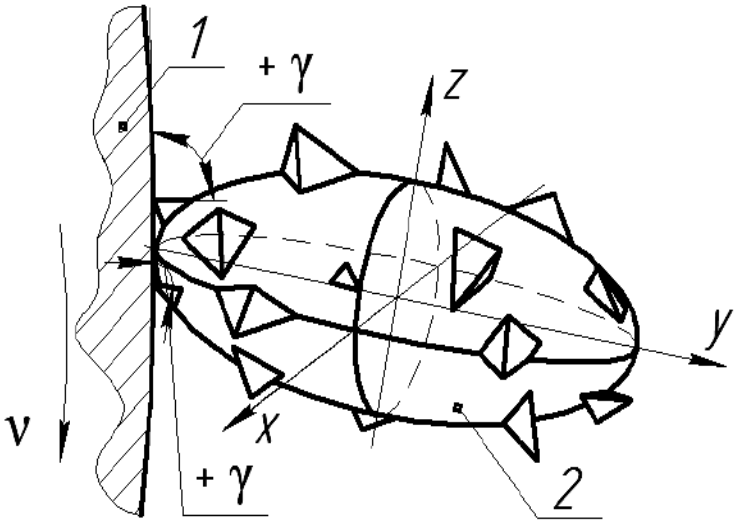

1 – Processed surface; 2 – Ferro-abrasive grain; v – Primary motion velocity; γ – Rake angle

Fig 8. – Micro-cutting scheme with a single ferro-abrasive grain

Thus, the investigation of the magnetic field topography has shown that the formation of the abrasive "brush" leads to a redistribution of the magnetic flux across the working gap.

The developed mathematical model of magnetic flux distribution within the volume of ferro-abrasive grains (FAG) demonstrates that the FAGs act as concentrators of magnetic induction, with the highest values located at sections adjacent to the processed surface. [11,13] As a result, the cutting zone is positioned at the exit of the working gap, and the tangential component of the cutting force moves the FAGs in the direction of the primary motion vector. This increases the rake angle towards negative values, which enhances the burnishing effect of the FAGs on the processed surface and reduces the intensity of the cutting process.

Conclusions

Based on the modeling of the magnetic field topography, it has been proposed to shift the abrasive "brush" to the entry zone of the working gap by creating an additional magnetic field in this area. This approach allows for a significant change in the rake angle toward positive values, increasing metal removal intensity by 30%–40%.

References

[1] Akulovich L.M. Uprochnayushchaya I finishnaya abrazivnaya obrabotka v magnitnom pole detalej selskohozyajstvennyh mashin. – Minsk, , 2022. – 360 c.

[2] Akulovich, L.M., Sergeev, L.E., Mendaliyeva, S.I., Mazdubai A.V., Tussupova, S.O., Ainabekova, S.S. The Mechanism of orientation of Ferro-abrasive grains in the Working Gap during Magnetic Abrasive treatment. Material and Mechanical Engineering Technology. – 2024(2) p.36-43

[3] Absadykov B.N., Sergeev, L.E., Mendaliyeva, S.I. Sherov K.T., Sikhimbayev M.R. The mechanism of action of lubricating and cooling technological means on metal removal during magnetic abrasive processing of parts. News of the National Academy of Sciences of the Republic of Kazakhstan. Vol.4. – 2024. P. 8-16

[4] Akulovich L.M., Sergeev L.E., Mendaliyeva S.I., Sherov K.T. Features of Magnetic Field Modeling for Magnetic-Abrasive Treatment of Complex-Profile Surfaces. Material and Mechanical Engineering Technology, №4, 2022 – P.37-42. DOI https://doi.org/10.52209/2706-977X_2022_4_37

[5] Ahmad S., Singari R, M., Mishra R. S. Development of Al2O3-SiO2 based magnetic abrasive by sintering method and its performance on Ti-6Al-4V during magnetic abrasive finishing Transactions of the IMF. 2021

[6] Zou Y., Satou R., Yamazaki O. and Xie H. Development of a newfinishing process combining a fixed abrasive polishing with magnetic abrasive finishing process Machines. 2021

[7] Anjaneyulu K., Venkatesh G. Experimental investigation of finishing forces on Hastelloy C-276 using UAMAF process. International Journal on Interactive Design and Manufacturing (IJIDeM) 2023

[8] Pak A., Shayegh M., Abdullah A., Choopani Y. Ultrasonic assisted magnetic abrasive finishing of DIN 1.2738 tool steel using vitrified bonded magnetic abrasive particles. Proc. Inst. Mech. Eng. Part E J. Process Mech. Eng. 2023

[9] Khanna N., Airao J., Maheshwari P., Nirala C. K., Outeiro J. Life cycle assessment to reduce environmental and carbon footprints of ultrasonic-assisted turning Sustain. Mater. Technol. 2023
[10] Zhu P., Zhang G., Teng X., Du J., Jiang L., Chen H. Liu N. Investigation and process optimization for magnetic abrasive finishing additive manufacturing samples with different forming angles Int. J. Adv. Manuf. Technol. 2022
[11] Ahmed F., Ahmad F., Kumaran S. T., Danish M., Kurniawan R., Ali S. Development of cryogenic assisted machining strategy to reduce the burr formation during micro-milling of ductile material J. Manuf. Processes. 2023
[12] Rahul Kumar, Venkateswara Rao Komma. Recent advancements in magnetic abrasive finishing: a critical review. Engineering Research Express. 2024. Vol. 6 (2024). https://doi.org/10.1088/2631-8695/ad2ef7
[13] Mayboroda V.S., Doslidzhennya v vlivu viscosti zmashchuvalno-okholzhuyucheshego technologichnogo seredovishcha na vlastivo magnitno-abrasive instrututu, Bulletin of the National Technical University of Ukraine «Kyiv Polytechnic Institute», Vol. 45, pp. 99-102, 2004.
[14] Voroshukho O.N. Technology of Magnetic-Abrasive Processing of External Cylindrical Surfaces with Controlled Orientation of Ferro-Abrasive Grains and Abrasive Brush Regeneration Using a Pulsed Magnetic Field. Abstract of the dissertation. Minsk. – 2019. – 22p
[15] Kumar M., Choudhary A., Ahmad Khan D. Magnetic Assisted finishing of internal surfaces. Engineering Processes. 2024, 66(1),3. Materials of the 5-th International Conference on Innovative Product Desigh and Intelligent Manufactoring Systems (IPDIMS 2023), Rourkela, India, 6-7 December 2023 https://doi.org/10.3390/engproc2024066003

Information of the authors

Akulovich Leonid Mikhailovich, d.t.s., professor, Belarusian Agrotechnical University
e-mail: leo-akulovich.tm@bsatu.by

Mendalieva Saule Ilyinichna, c.t.s, senior lecturer, Seifullin Kazakh Agro-Technical Research University
e-mail: s.mendalieva@kazatu.edu.kz

Sherov Karibek Tagaevich, d.t.s, professor, Seifullin Kazakh Agro-Technical Research University
e-mail:shkt1965@mail.ru

Toshov Javokhir Burievich, d.t.s, professor, Tashkent State Technical University named after I. Karimov
e-mail: javokhir.toshov@yandex.ru

Mussayev Medgat Muratovich, PhD, associate professor, Abylkas Saginov Karaganda Technical University
e-mail: mussayev.medgat@gmail.com

DOI 10.52209/2706-977X_2025_4_93 **IRSTI 81.09.07** **UDC 691.32:621**

Enhancing Fire Resistance of Geopolymer Concrete Through Steel Fiber Reinforcement: Microstructure and Mechanical Behavior at Elevated Temperatures

Abdullah A.F.[1*], Al-Khafaji Z.[2,3*], Falah M.[4]
[1]Technical Engineering College of Kirkuk, Northern Technical University, Kirkuk, Iraq
[2]Universiti Kebangsaan Malaysia, UKM Bangi, Selangor, Malaysia
[3]Scientific Research Center, Al-Ayen University, Thi-Qar, Iraq.
[4]College of Engineering and Engineering Techniques, Al-Mustaqbal University, Babylon, Iraq.
*corresponding author

Abstract. This paper investigates the thermo-mechanical performance of steel fiber reinforced GPC using a combination of fly ash (FA), ground granulated blast furnace slag (GGBS), and ordinary Portland cement (OPC) in binder. The geopolymer matrix was activated with a binary solution containing sodium silicate–sodium hydroxide and the alkaline activator–to–binder by mass for 0.40, with hook-end steel fibers added at volume contents of 0%, 0.5%, 0.75%, and 1.0%. In addition, its mechanical properties such as compressive, split tensile and flexural strengths were tested at room temperature before and after exposure to high temperatures of 250, 500 and 750°C with account for microstructural evolution using X-ray diffraction (XRD) and scanning electron microscopy (SEM) to reveal the effect on thermal degradation and strength maintenance. It is shown that the addition of steel fibers can improve both ambient and residual mechanical properties, and a 1.0% fiber volume fraction has the best strength preservation behavior at all temperatures. However, the residual compressive, tensile and flexural strengths of fiber-reinforced GPC were much higher than that of the plain mix at different temperatures even if a decline with a raise in temperature was inevitable, especially at 750°C presence considerable values, microstructural studies verified that matrix densification is higher developed due to effective crack bridging and promoted interfacial bonding lead adding fibers is responsible for superior fire resistance. These results emphasize the potential of SFRC GPC as an elevated temperature structural fireproof and environmentally friendly building material.

Keyword: Geopolymer Concrete (GPC), steel fibers, elevated temperatures.

Introduction

Ordinary Portland cement (OPC) is the predominant inorganic cementitious material utilized in the contemporary building sector, and its manufacturing process may result in significant environmental contamination. The manufacture of one ton of OPC produces approximately one ton of carbon dioxide (CO2), with the OPC industry accounting for 5–7% of global CO2 releases [1]–[5]. To further promote environmentally conscious and sustainable development, it is essential to identify eco-friendly materials as substitutes for cement-based concrete. Geopolymer was a composite material formed by the interaction of solid industrial byproducts, including fly ash (FA) and ground granulated blast furnace slag (GGBS), which serve as cementitious ingredients, with alkali activators [6]–[8]. The manufacturing technique significantly diminishes energy usage and CO2 releases, establishing it as a novel material with substantial developmental potential [9]–[12]. In comparison to conventional concrete, geopolymer concrete (GPC) offers superior strength, enhanced fire resistance, and improved corrosion resistance [13]–[15]. Nonetheless, its shortcomings, including significant deformation, susceptibility to cracking, and brittleness, are critical considerations that restrict its extensive utilization [16].

Nevertheless, the GPC brittleness has lately led investigators to explore a diverse array of studies. The utilization of short fibers in GPC enhanced performance regarding fire resistance, shrinkage, and ductility [17], [18]. Fibers having a low melting point, like polypropylene [19], are more efficacious since they establish dehydration channels at reduced temperatures. Concrete spalling results from two primary variables: elevated pore pressure and the development of thermal stress [20]. Fibers, steel bars, and other fibrous materials have been utilized to mitigate cracking in concrete through the anti-tensile characteristics [21]. The materials have a thermal coefficient comparable to that of concrete [22]–[24]. The integration of fiber into concrete may markedly enhance its fracture resistance. Consequently, it improved various mechanical characteristics, including tensile, flexural, and impact strength, while simultaneously augmenting the ductility and toughness of the concrete components [25].

High temps influence the physical and mechanical characteristics of concrete. An elevation in temperatures induced by fire may result in irreversible degradation of concrete strength and a decrease in its cross-sectional area owing to the concrete cover spalling. GPC has favorable thermal features, with no spalling seen after exposure to fire [26]. Prior research has shown that GPC samples have superior compressive strength compared to OPC samples under both normal and heat curing conditions [27]–[29].

Exposure of concrete to elevated temperatures leads to spalling, defined as the detachment of surface layers, and external cracking, which occurs due to the evaporation of free water and the degradation of the paste. The events may subject the steel reinforcements inside the concrete to heat, potentially resulting in catastrophic consequences for the concrete structure stability and load-bearing capacity. Moreover, alkalinity decreases due to carbonation, exacerbated by fire, hence increasing the steel rebars corrosion risk [30], [31]. At temperatures above 400 degrees Celsius, the paste commences to contract while the aggregates grow, resulting in a pronounced strain gradient inside the matrix [32]. It

exacerbates cracking inside the matrix and diminishes the adhesion between aggregates and paste, leading to further deterioration of strength. At high temperatures, namely 800-1000 degree centigrade, the breakdown of products of hydration and the chemically-bound water loss cause considerable degradation of the microstructure, resulting in a 60-80% decrease in strength [33].

This study's main objective is to assess the impact of steel fiber volume fraction on mechanical properties and thermal resistance ability of geopolymer concrete mixed with a hybrid FA–GGBS–OPC binder after exposure to elevated temperatures (up to 750°C). The novelty lies in complementary residual compressive, tensile, and flexural behavior investigation alongside comprehensive microstructural analysis, establishing direct correlation between the evolution of geopolymeric phase, fiber-matrix bonding, and post-fire form-stability features. In contrast to the previous studies which have given single measures of either ambient performance or mechanical properties, this work provides a comprehensive thermo-mechanical and microstructural model of steel fibre benefits towards thermal damage resistance and fire resistance in geopolymer concrete.

1. Methodology

1.1 Material Utilized

In this study, Ordinary Portland Cement (OPC) Type I was used a reference binder in the production of geopolymer concrete (GPC), so as to ensure a fair comparison with typical cement based systems; this is universal type cement that being commonly employed for structural applications and its main chemical composition including CaO, SiO_2, Al_2O_3 etc., and physical properties (such as fineness and specific gravity) were analyzed according to the relevant standard test codes listed and presented in Tables 1 and 2. Ground Granulated Blast Furnace Slag (GGBS) [34], GGBS is a non-metallic and free-field by-product of pig iron production that mainly contains calcium silicates and aluminosilicates, the physical properties were described in Tables 1 and 2. Moreover, the Class Ffly ash used was a partial substitute for the cement [35], which complies with the relevant specification and is obtained from EUROBUILD, this being of fine particle size and pozzolanic nature with physical–chemical properties reported in Tables 1 and 2. where the alkaline activator consisted of a mixed aqueous solution of sodium silicate (Na_2SiO_3) and sodium hydroxide (23 wt.% NaOH), with reactivity controlled through the molar ratio of silica dioxide to sodium oxide (modulus SiO_2/Na_2O) which not only determined the Si_x^+ anion concentration in solution, but also affected by water content, leading to changes in viscosity and geopolymerization kinetics; sodium hydroxide was prepared from 99% purity flakes by dissolving them in distilled water to reach the desired molarity and then keeping cooling for at least two hours before usage; such practice makes sure of good stability. To improve workability without increasing the water demand a compliant with ASTM non-chloride high range water reducing superplasticizer, Sika® ViscoCrete®-5930 was added. The coarse aggregates tested for the research were natural river sand as shown in the standard specification, graded as Figure 1 and had a nominal maximum size of 12.5 mm [36], while the fine aggregates are natural river sand which had a maximum particle size of 4.75mm (Figure 2) and they met with the specified grading limit [37]. The tensile behavior of the GPC was also enhanced by the addition of hooked-end high-strength steel fibers with volume fractions ranging from 0% to 1% in increments of 0.5%, with an average diameter around 0.55 mm, a length of about 35 mm, and an aspect ratio of about 64, while its maximum tensile strength could reach up to 1345 MPa.

Table 1. Physical Features

No	Material	Specific Gravity	Specific surface area m^2/kg	Water Absorption %	Dry Loose Unit Weight kg/m^3	Sulfate amount (SO_3) (%)	Material passing through the 0.075 mm sieve
1	FA	2.44	521	-	-	-	-
2	GGBS	2.57	290	-	-	-	-
3	Cement	2.58	372	-	-	-	-
4	Coarse aggregate	2.69	-	1.11	1625	0.088	-
5	Fine aggregate	2.44	-	1.22	1798	0.074	1.84

Table 1. Oxide Composition of Cement, Fly Ash, and GGBS.

Oxides composition	Features		
	FA	GGBS	Cement
CaO	1.52	30.10	62.60
Al_2O_3	22.10	8.78	5.20
SiO_2	62.22	35.40	21.5
Fe_2O_3	7.12	1.97	3.40
MgO	2.34	6.92	2.42
SO_3	0.15	0.41	2.44
Loss of Ignition (L.O.I)	1.55	0.80	1.81

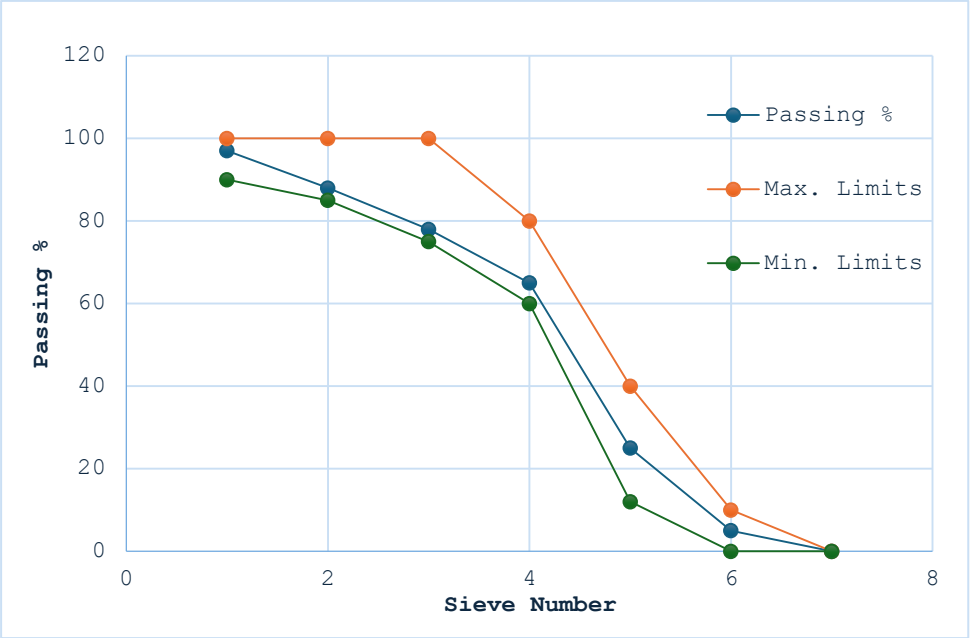

Fig. 7. - Figure 1. Particle size distribution of coarse aggregate.

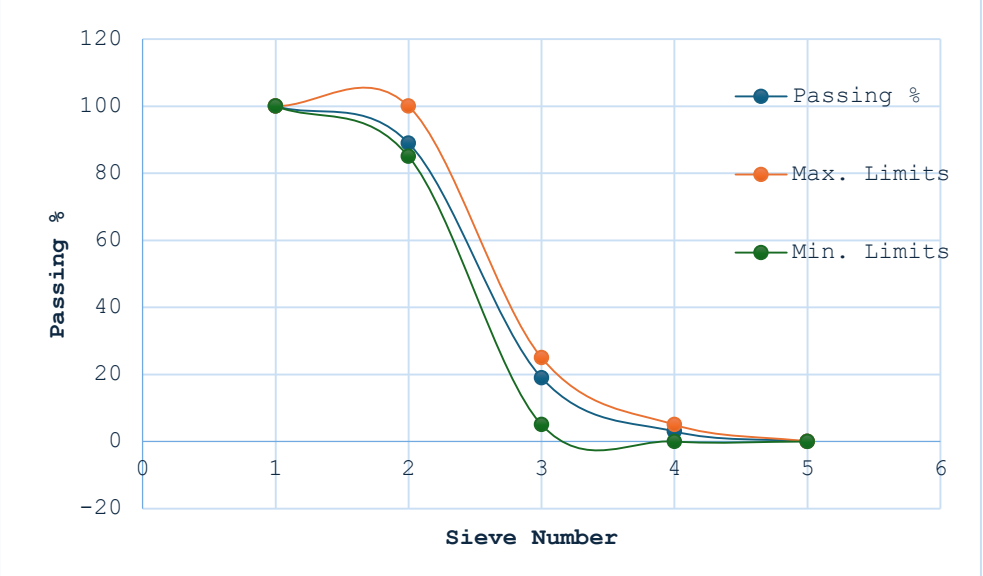

Fig. 8. - Particle size distribution of fine aggregate.

1.2 Mixture of Designations

Geopolymer mortar mix design and preparation following existing practice was defined according to references [38] as well as other standard procedures, considering test mixes handled at the age of 28 days demonstrating that selected mix formulation led to good compromise between workability and mechanical strength. A fixed alkaline activator–to–binder ratio of 0.40 was taken, which is well known to stimulate dense geopolymer gel formation and improved strength development, whereas a sodium silicate to sodium hydroxide ratio of 2.5 was kept for activity and reaction kinetics [38]. The geopolymeric binder system used a mix design that included 50% of GGBS, 40% of Class F fly ash, and 10% of ordinary Portland cement, which allowed obtaining an optimum combination for alkaline activated calcium- and aluminosilicate-rich precursors. The alkaline activator was formulated with constant sodium silicate and sodium hydroxide contents to keep consistency among all combinations. The natural fine and coarse aggregates were added at fixed contents, so that the influence of aggregate effect on other performances is excluded. To study the effect of fibre reinforcement on the properties of the geopolymer, hooked-end steel fibre was incorporated at volumetric proportion 0%, 0.5%, 0.75% and 1.0%. The general mechanism of geopolymerization and the stepwise order of materials reacting after mixing and curing are schematically depicted in Figure 3.

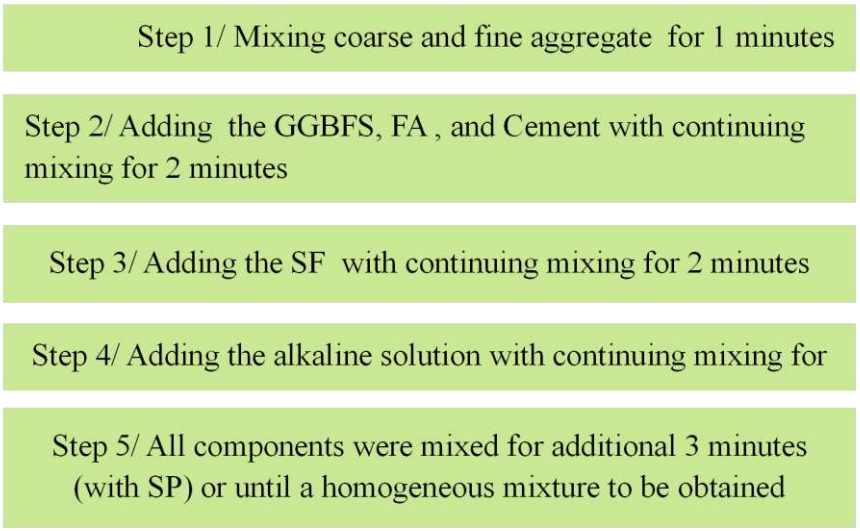

Fig. 9. - Flow chart of GPC mixing procedure steps.

1.3 Tests

X-Ray Diffraction (XRD) analysis

XRD analysis was employed to examine the phase composition and crystallinity of geopolymer cubes comprising 40% fly ash, 50% GGBS, and 10% OPC, treated to different temperature exposures (25, 250°C, 500°C, and 750°C). This approach facilitated the detection of crystalline phases and any phase changes induced by increased temperatures. XRD analysis of diffraction patterns yielded essential insights into the alterations in the geopolymer matrix structure, facilitating the evaluation of stability, the production of new compounds, and the thermal behavior of the material under varying temperature exposures.

Scanning Electron Microscope (SEM)

SEM analysis was performed to investigate the microstructure of heat treated Geopolymer cubes were prepared using 40% fly ash, 50% GGBS and 10% OPC. SEM provided high-resolution images for the assessment of changes in surface morphology and material integrity at various temperatures (25°C, 250°C, 500°C, 750°C). The findings showed the fissure growth, particle packing and structural densification under temperature dependence were plotted against the temperature, providing critical information on the thermal stability, bonding behavior under burning conditions and probable transition corresponding to phase change in geopolymer structure at elevated temperature.

Mechanical Behavior

Mechanical characterization of the geopolymer concrete mixes was performed through a full testing program under ambient temperature (25 °C) and exposure to elevated temperatures (250 °C, 500 °C, and 750 °C) to compare initial versus residual properties. All tests were conducted according to widely regarded ASTM standards to be able to make results repeatable and comparable with ordinary cement-based systems. Compressive strength was measured in cube specimens submitted to uniaxial compression according to the (ASTM C109/C109M) [39]. The splitting tensile strength was tested to indicate the crack resistance and tensile behavior with a cylindrical specimen according to ASTM C496/C496M [40]. Bending strength (modulus of rupture) was evaluated on prismatic specimens loaded in three-point bending, according to ASTM C78/C78M [41].

2 Results and discussion

3

2.1X-ray Diffraction (XRD) analysis

Figure 4 shows the X-ray Diffraction (XRD) of the GPC samples for various curing temperatures (25 °C, 250°C, 500°C and 750°C) which exhibits clear structural transformation. At (25 C°) the XRD pattern shows that an amorphous and crystalline phase mixture obtained in unfired brick, with aluminosilicate gel as a binding matrix reinforced by crystalline fillers as quartz and mullite, together contribute to strength enhancement from hydration products of GGBS such as C-S-Hand C-A-S-H. At 250°C the higher temperature accelerates the geopolymerization process, as a more compact gel and developed crystalline phase that can intensified strength emerged. At 500 °C, a reduction in amorphous phase and increase crystalline phase contribute to better material densification and higher thermal resistance. At 750 °C, formation of an intense crystallinity appears in the structure of GPC with less amorphous phase formed which refers to more completion geopolymerization and considerable content of thermally stable compounds [42]. It reveals that the higher curing temperatures can enhance not only mechanical strength but also thermal stability, thereby facilitating the use of formulations in civil engineering, such as flame-resistant structures as well as high-temperature industry. The variation of temperature had little effect on the XRD patterns of the materials, because the main crystalline phases (quartz (SiO_2), mullite ($Al_6Si_2O_{13}$) from fly ash and hydration products such as calcium silicate hydrate C-H-S and calcium aluminosilicate hydrate C-A-S-H from GGBS are thermally stable within 250-750°C which is examined in this study. Therefore having higher melting point, makes them resistant to phase transition at moderate to high heating conditions [43]. The amorphous phase (the majority of which is aluminosilicate gel) does not significantly change its presence throughout the temperature

regime. While an increase in temperature leads to a shorter geopolymerization reaction time and decreases amorphous content, the main phase also remains the same and therefore diffraction patterns were similar. Since the crystalline components are stable overall and the amorphous phase fairly gradually decreases, no significant change is detected in XRD patterns even with temperature variation [44].

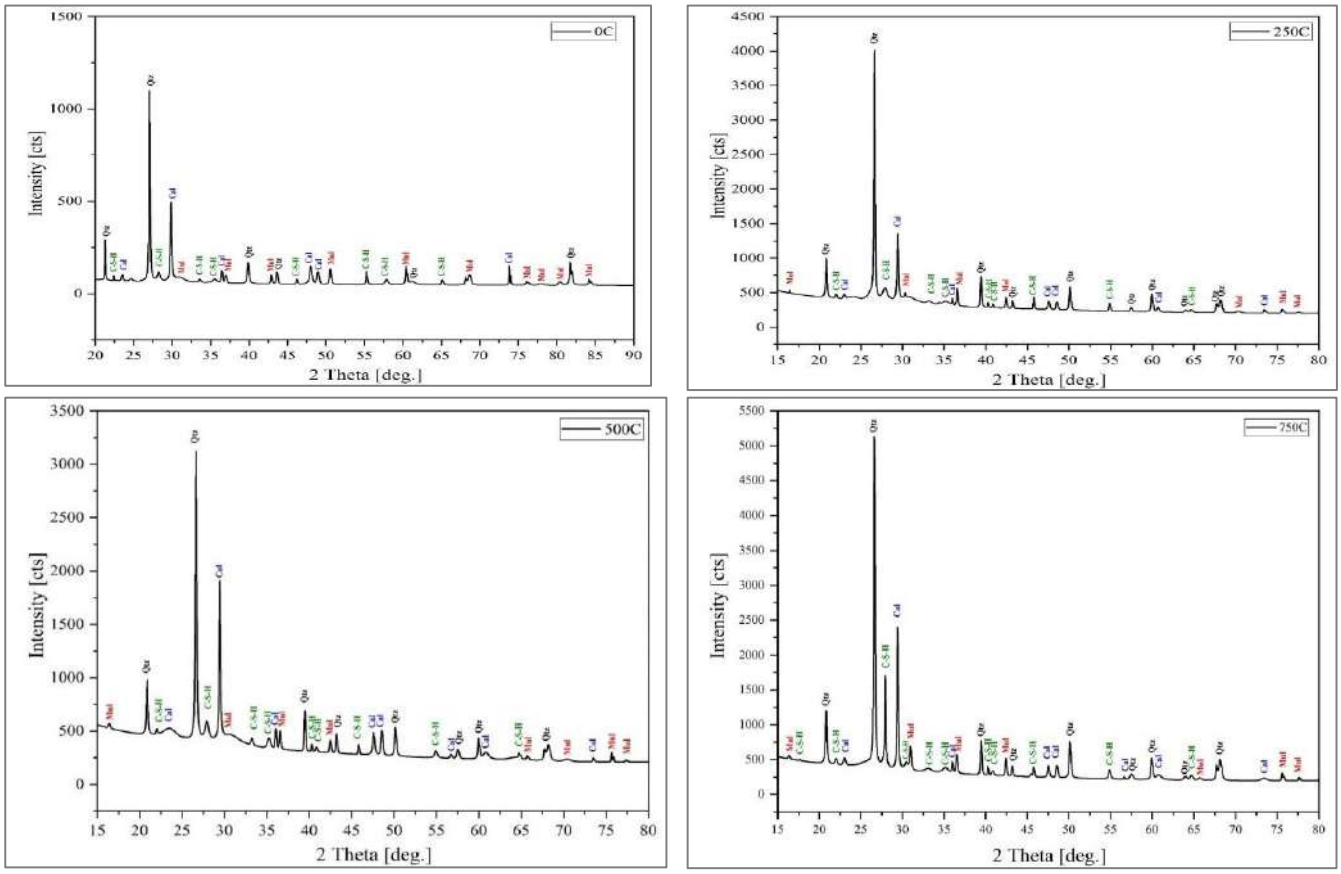

Fig. 10. - XRD pattern for GPC at (25, 250, 500 and 750) °C.

2.2 Scanning Electrons Microscopy (SEM)

The SEM image of GPC with 25°C is illustrated in Fig.5. Here, at lower temperature polycondensation will be slow and there will be little development of binding aluminosilicate gel. The poorly defined matrix in this image shows only incomplete coating of unreacted particles by the gel, resulting in visible porosity and a rough surface texture. Early-age ettringite, a needle-shaped calcium sulfoaluminate hydrate, may exist due to the interaction of GGBS with sulfate. This reaction is passive due to the low temperature and cannot have sufficient role in matrix densification. Increased curing temperatures are necessary to accelerate the disintegration of aluminosilicate components from fly ash and GGBS that eventually assist in developing a compact, cohesive matrix improving mechanical properties. The limited quantity of poor development of the geopolymer gel at 25 °C is a result of the slow kinetics associated with the geopolymerization shown in Figure 5. On cooling, the dissociation of aluminosilicate materials in fly ash and GGBS is severely retarded, which reduces the exposure of reactive species required for gel precipitation. Partial reaction leads to non-reacted spherical fly ash and angular GGBS particles in the matrix, giving rise to porous network. The formation of ettringite is retarded and reduced at low temperatures since calcium, aluminum and sulfate ions are required for the formation of that mineral. GGBS could present these components, though low-temperature limitation of crystalline is not permitted. The microstructure shown in the figure is of a weakly cemented complex and underdeveloped geopolymers system typical for curing at low temperature.

The SEM image of the GPC that has been exposed to 250°C, on the other hand, shows a significant improvement in matrix densification (Figure 6). Elevated temperatures accelerate the process of geopolymerization with increased formation of a denser aluminosilicate gel which can connect more favorably to aggregate particles. The image shows lower porosity, more coalescing structure, and smoother region indicating better adhesion between the particles. Although it is possible that some unreacted fly ash and partly reacted GGBS particles still exist, bulk structure appears more bonded due to enhanced reactivity of the material at this temperature. The stronger bonding results in better mechanical properties, making the geopolymer concrete suitable for structural applications where high strength and long-term durability are required.

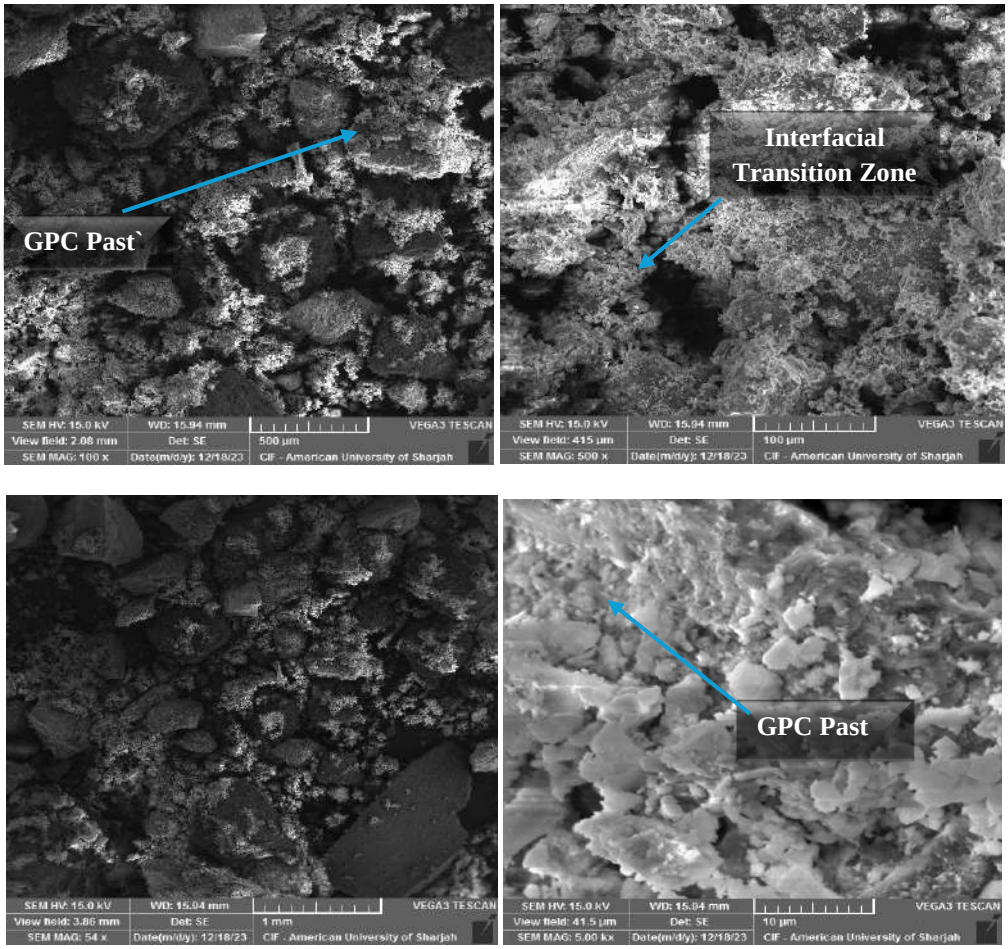

Fig. 11. - SEM image for GPC sample at (25 °C).

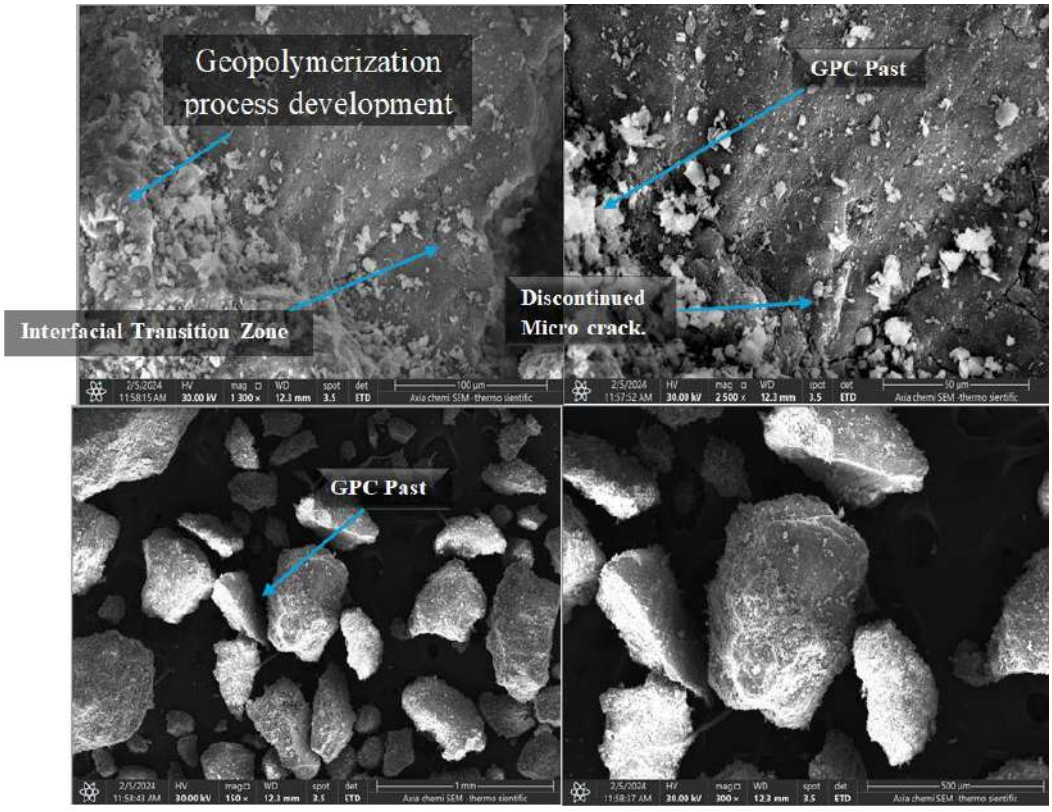

Fig. 12. - SEM image for GPC sample at 250 °C.

Figure 7 shows the SEM image of at 500°C, which reveals a dense and well-bonded matrix with zero visible porosity. The higher temperature itself leads to a more rapid geopolymerization process whereby a dense aluminosilicate network is formed with rougher surface topography, indicating crystallite growth. The presence of C-S-H and C-A-S-H in the matrix enhances its strength, while the coarse- grained appearance suggests that crystallization of these phases is ongoing. Superior microstructure resulting in enhanced mechanical strength and resistance to attack from the environment which is lowered more porosity making GPC 'most suitable for elevated temperature and civil structural applications.

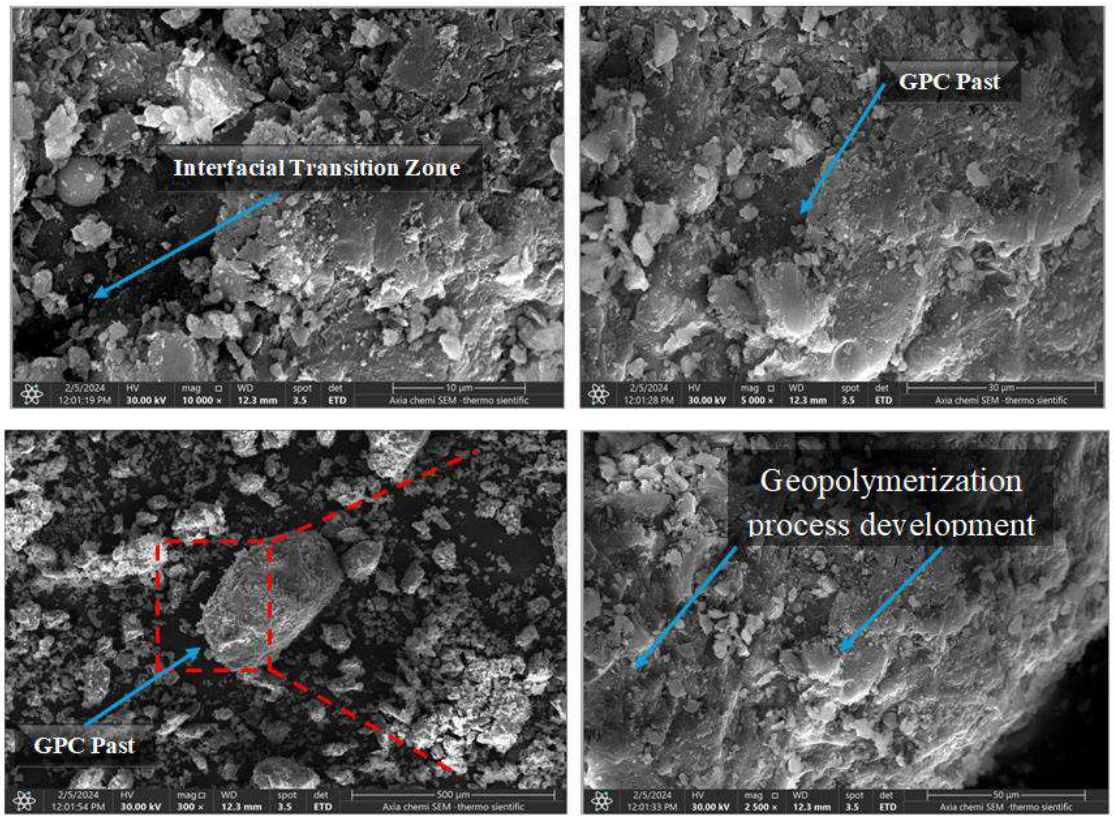

Fig. 13. - SEM image for GPC sample at 500 °C.

The SEM images of the GPC cured at 750°C are displayed in Fig. 8, and its microstructure is a densely packed crystalline structure with sharp-edged particles. The increase in temperature also accelerates geopolymerization and crystallization with a less porous and stronger matrix. The presence of crystalline phases, C-S-H and C-A-S-H, results in good structural improvement, and the remaining fly ash acts as fillers. The surface pattern formed by the broken, namely open, enables heat resistance and dent resistance of the material. The microstructure variation at 750°C makes GC a suitable choice for high performance applications requiring sustainable, thermal, and mechanical properties such as fire resistive construction. The compressive strength of the GPC decreases dramatically with increase in burning temperature. Upon the burning temperature increasing from 25°C to 250°C, the compressive strength is reduced by a half. This significant reduction is attributed to the influence of temperature on the microstructure of the material, where insufficient geopolymerization occurs at lower temperatures and results in an immature binding matrix. The limited interaction between fly ash and GGBS leads to inferior mechanical performance. With the increase in temperature in the chamber to 500°C, layer C loses further 51% of its original compressive strength at 25°C The continuous weakening is due to faster reactions at higher temperatures, leading to dissolution of aluminosilicate components from fly ash and GGBS into a dense matrix but with possible micro-cracking and phase transformations that weaken the material. The SEM analysis at this level shows increased gelation but the general structure is still deteriorating. At elevated temperature of 750°C, the strength is about 70% lower than that at 25°C; higher temperatures favor crystallization with the appearance of crystalline phases comprising calcium silicate hydrate (C-S-H) and calcium aluminosilicate hydrate (C-A-S-H), as shown in the microstructure. However, the excessive crystallinity and potential thermal decomposition makes for a tailorable brittle matrix with poor crush resistance. Despite of the densification, the decrease in mechanical strength makes it less applicable for load–bearing application at elevated temperatures.

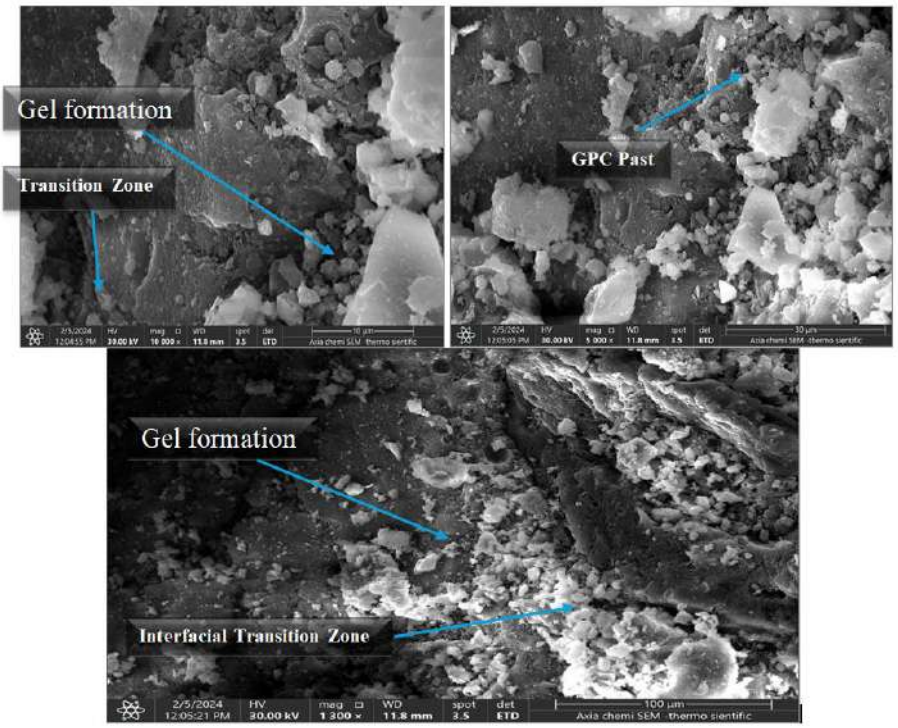

Fig. 14. - SEM image for GPC sample at 750 °C

2.3 Compressive strength

Steel fiber reinforced GPC samples showed higher compressive strength in cube samples compared to those without fibers. The compressive strength increased by 21%, 35% and 59% for S2, S3 and S4 with the addition ratios of steel fibers being 0.5%, 0.75% and 1.0%. Compressive Strength of the Fiber Concrete The use of steel fibers enhanced the compressive strength, with a maximum value being 59 MPa at a fiber ratio of 1.0%, which is approximately consistent to results shown in [45]. The smallest compressive strength for the fiber-reinforced specimens was 40.5 MPa for mix S2 (0.5% of steel fiber), higher than the value obtained in the GPC without steel fibers (38.9 MPa). Residual compressive strength of the steel fiber-reinforced geopolymer concrete mixes subjected to elevated temperatures is shown in figure 9, as compared with those under ambient condition. Addition of steel fibers significantly prepared an improvement in retention of strength at elevated temperature. With the increasing of fiber content, strength decay rate decreased, and higher in volume fractions fibers showed better thermal resistance and remain larger portion of initial strength. At 250°C, there was an increase in the residual strength compared to that at lower volume fraction of fiber, which may be attributed to improved interaction between steel fibers and geopolymer matrix by further polymerization as well as microstructural densification. At room temperature, the compression strength rose from 38.9 MPa (plain mix—S1) to 59 MPa (1%-fiber mix—S4), offering an improvement of around 52%. FRM outperformed SM at higher temperatures. At 750 °C, the strength of S4 (27 MPa) remained more than double that of S1 (12.01 MPa). Similar increases were also recorded at 250°C (from 30.1 MPa to 43.3 MPa) and at 500°C (from 21.3 MPa to 32 MPa). The findings show that both ambient and residual compressive strength increase with an increasing steel fiber content, in which the 1.0% steel fiber results in the largest rate of improvement under all conditions.

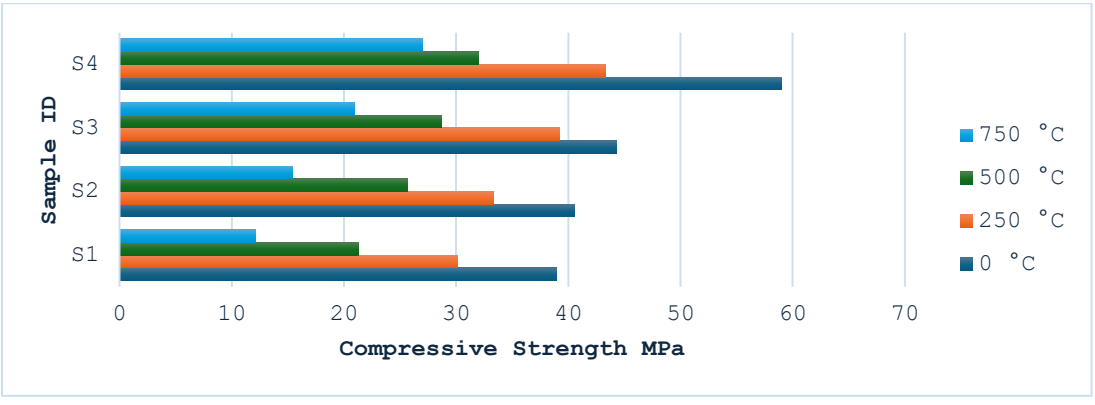

Fig. 15. - Compressive strength for different GPC mixture subject to various temperature

2.4 Tensile strength

As shown in Figure 10, the tensile strength of all samples has also decreased with increasing temperature and exhibits a similar behavior to that observed for the compressive results. Control sample S1 showed tensile forces of 1.89 MPa, 1.4 MPa, and 1.1 MPa at temperatures of 250°C, 500°C and 750°C respectively which are decreased by the value of14%, 36% and 50%. 0.5% by weight steel fibers (S2) addition led to 2.78 MPa, 2.5 MPa and 1.5 MPa of residual tensile strengths, showing loss reduction of 14%, 22% and 53 %, respectively. S3 mixture also showed even further improvement showing a decrement in tensile strength by only 10%, 23% and 28%. Sample S4 showed the best residual compressive strength of 26%, 31%, and 40% at temperatures of 250°C, 500°C, and 750°C, respectively. The tensile strength decreased as the exposure temperature increased. At 250°C, tensile strength increased by 47%, 95%, and 117% for S2 (0.5% SF), S3 (0.75% SF), and S4 (1.0% SF) when compared to S1 (SRM) which demonstrated a similar trend to that of compressive strength. The residual tensile strengths corresponding to the grains layer above 500 °C were 1.4 MPa (S1), 2.5 MPa (S2), 3.16 MPa (S3) and 3.78 MPa (S4), augmenting by of an average value of de un valor medio del 79%, 125% and for SFRM, respectively. The reduced strength of S1 is attributed to the partial deterioration and dehydration mechanism of calcium-aluminosilicate hydrate (C-A-S-H), which could not be supported by an inadequate amount of water for reaction. Ctrl R 0 S1 S2 S3 S4 Resistivities Room temperature Effect of fiber content on the tensile strength The composite fibers all have the same diameter, thus having similar surfaces. The highest value of residual tensile strength (3.3 MPa) was obtained at 1.0% steel fiber, which confirmed the positive role of fiber proportion to temperatures. The tensile strength of GPC decreases with temperature, but by the inclusion of steel fibers its fire resistance is significantly improved. At room temperature, obviously, the strength increases with the content of fibers from 2.2 MPa (0% SF) to 5.51 MPa (1.0% SF). All the mixtures show strength reduction when temperature increases to 250, 500 and 750 °C, however the fiber-reinforced specimens have higher values. At 750°C, it reported a maximum strength of 3.3 MPa for the 1.0% SF mixture which is greater than that obtained from the control sample (1.1 MPa).

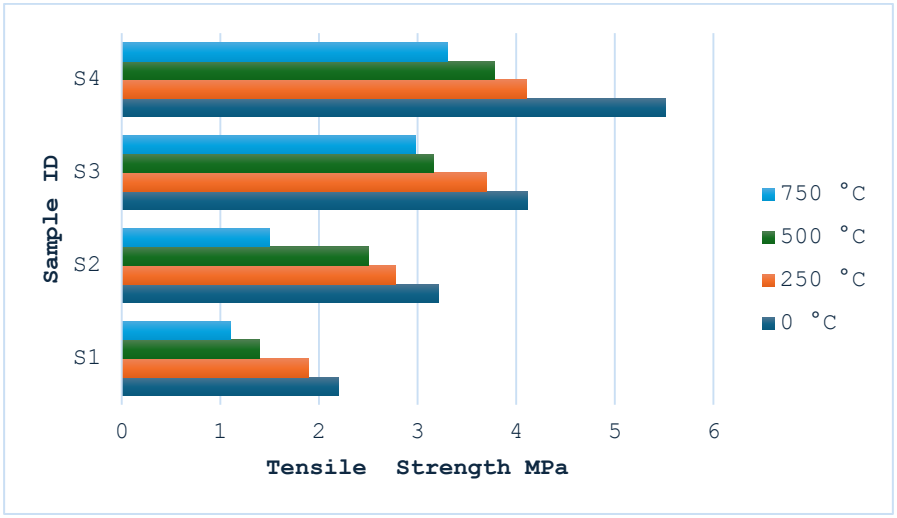

Fig. 16. - Tensile strength for different GPC mixture subject to various temperature

2.5 Flexural Strength

The variation of the flexural strength at elevated temperatures for GPC specimens is illustrated in Figure 11. The loss of strength increases specifically with the temperature when considering all the steel fiber contents. The flexural strength of the control sample (S1) decreases by 14% at 250°C as compared to that at room temperature. The flexural strengths of GPC specimens significantly decreased after exposure to fire, especially at 500°C–750°C; the residual flexural strength was reduced to 66% (S1), and 60%, 41%, and 38% (S2, S3, and S4) at 500 °C. At 750°C, the retained strength was 87% for S1 whereas it decreased to approximately 73%,,71%, and 69% for S2, s3, and S4, respectively. Despite the overall decline, mixtures with steel fibre (S2–S4) showed to continue outperforming the fibre-free mixture (S1) at all exposure levels. This is in accordance with the obtained enhancement of compressive and split tensile strengths. S2 reached the flexural strengths as 5.14, 2.2 and 1.5 MPa after being subjected to temperatures of 250,500 and750°C, respectively. The residual flexural strengths of S2 were 14, 24 and 117% at these temperatures as compared to the pristine GPC (G1-0%SF), while those of S3 were 34, 111 and 168%, and those of S4 were found to be enhanced by 40,137 and 204%, respectively. The findings of the results clearly demonstrate that elevated temperature drastically reduces the flexural strength of all GPC mixes. The amount of reductions is dependent upon the ratio of steel fiber. The control mix with no fiber content (S1) has higher degradation, where the flexural strength drop from ambient temperature 5.25 MPa to 0.69 MPa at only 750 °C, while fiber incorporated concrete of all (S2, S3 and S4) possess larger residual strengths at all temperatures. S4 shows an excellent applicability, maintaining the flexural strength of 2.1 MPa at 750 °C, which is three-fold higher than that of unmodified mixture. This indicates that the heat resistance and structural performance of GPC in fire are enhanced by increasing the steel fiber content. The positive role of steel fibers is due to their ability to control the

crack and improve matrix binding at elevated temperature, in particular. The results confirm that the usage of steel fiber can effectively improve the high-temperature properties of GPC, thereby avoiding its reduced reliability in applications requiring better fire resistance.

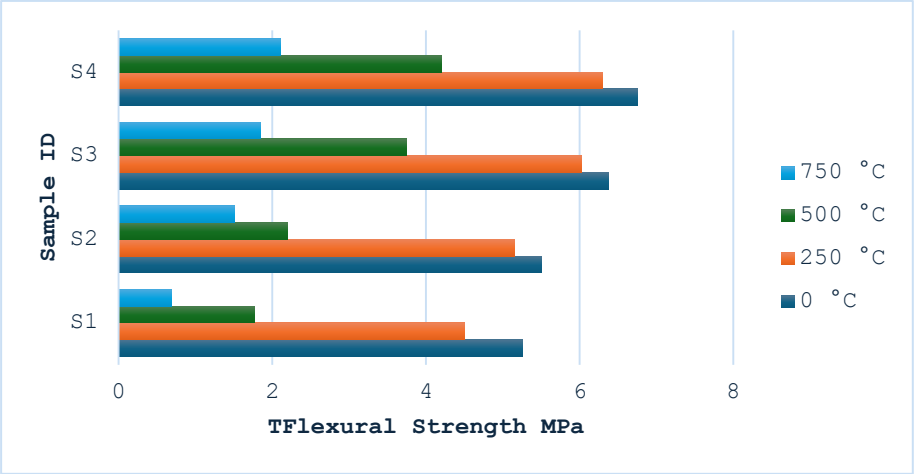

Fig. 17. - Flexural strength for different GPC mixture subject to various temperatures

Conclusion

The results of the experiments conducted demonstrate the importance of reinforcing with steel fibers in acting as an essential element to enhance the thermal mechanical performance of geopolymer concrete at micro and macro level temperatures. It was observed that the use of hooked end steel fibers largely increased compressive, split tensile and flexural strengths, where fiber content of 1.0% has resulting in the highest increments with continues strength retention after thermal attack. At high temperatures, fiber-reinforced GPC achieved significantly higher compressive and tensile residual strengths compared to the plain mix with more than double that exhibited at 750°C whereas plain GPC only showed an increase over 400°C.334 Higher temperature resulted in more geopolymerization gel formation and matrix densification up to intermediate temperatures along with steel fibers acting as a bridge to connect thermally induced microcracks were effectively bonded by steel fibers, increasing bond between fiber/matrix and moving ITZ interface. Even if the fiber-reinforced mixes showed strength loss because of dehydration, crystallization, and microstructure damage at elevated temperature, they were still better than plain cement paste in resisting thermal erosion. In general, this study has shown an SFRGPC to be a viable and durable sustainable fire-resistant material, which is highly potential for load-bearing applications in elevated temperature or fire hazard environments.

References

[1] Ge X., Duran L., Tao M., DeGroot D. J., Li E., Zhang G. Characteristics of underwater cast and cured geopolymers //Cem. Concr. Compos., 2020.

[2] Shubbar A., Nasr M., Falah M., Al-Khafaji Z. Towards net zero carbon economy: Improving the sustainability of existing industrial infrastructures in the UK //Energies, 2021.

[3] Al-Khafaji Z. S., Dulaimi A., Jafer H., Al-Khafaji Z., Atherton W., Hussien S. A. Soft Soil Treated with Waste Fluid Catalytic Cracking as a Sustainable Stabilizer Material //Iraqi Geol. J., 2022

[4] Al-Masoodi Z., Dulaimi A., Jafer H., Al-Khafaji Z., Atherton W., and H. Safa, Soft Soil Treated with Waste Fluid Catalytic Cracking as a Sustainable Stabilizer Material //Iraqi Geol. J., 2022

[5] Hussain A. J., Al-Khafaji Z. S. Reduction of environmental pollution and improving the (Mechanical, physical and chemical characteristics) of contaminated clay soil by using of recycled oil // J. Adv. Res. Dyn. Control Syst., 2020

[6] Al-Husseinawi F. N., Atherton W., Al-Khafaji Z., Sadique M., Yaseen Z. M. The Impact of Molar Proportion of Sodium Hydroxide and Water Amount on the Compressive Strength of Slag/Metakaolin (Waste Materials) Geopolymer Mortar //Adv. Civ. Eng., 2022

[7] Al-Jaberi L. A., Ali A., Al-Jadiri R. S., Al-Khafaji Z. Workability and Compressive Strength Properties of (Fly Ash-Metakaolin) based Flowable Geopolymer Mortar, Electron //J. Struct. Eng., 2023.

[8] Zeini H. A. et al., Random Forest Algorithm for the Strength Prediction of Geopolymer Stabilized Clayey Soil //Sustainability 2023, 15(2), 1408

[9] Rożek P., Król M., Mozgawa W., Geopolymer-zeolite composites: A review //J. Clean. Prod., 2019)

[10] Xu W., Niu X., Zhu Y. Deformation behavior and damage evaluation of fly ash-slag based geopolymer concrete under cyclic tension //J. Build. Eng., 2024

[11] Kaur M., Chawla H., Kwatra N. Effect of different surface preparation techniques on the bond behavior of normal and fiber-reinforced geopolymer concrete //Constr. Build. Mater., 2024

[12] Abdullah A. F., Ezuldin N. Y., Ahmed I. M., Al-Khafaji Z. Enhancing the Sustainability of Concrete Mixes Utilizing Supplementary Cementitious Materials in Renewable Energy Buildings //Eng. Technol. Appl. Sci. Res., 2025

[13] Abdullah A. F., Abdul-Rahman M. B. A.-D., Al-Attar A. A. Investigate the Mechanical Characteristics and Microstructure of Fibrous-Geopolymer Concrete Exposure to High Temperatures // J. Rehabil. Civ. Eng., 2025

[14] Abdullah A. F., Abdul-Rahman M. B. A. D., Al-Attar A. A. A Review on geopolymer concrete behaviour under elevated

temperature influence //J. Sustain. Sci. Manag., 2024
[15] Mardan G. A., Abdul-Rahman M. B. A.-D., Abdullah A. F., Al-Khafaji Z. Thermo-Mechanical Response of Reinforced Geopolymer Hollow Beams Containing Steel Fibers //Math. Model. Eng. Probl., 2025
[16] Dhasmana A., Singh S. P. Long-term mechanical characteristics of fibre reinforced metakaolin-based geopolymer concrete: A review //Mater. Today Proc., 2023
[17] Alomayri T. The microstructural and mechanical properties of geopolymer composites containing glass microfibres //Ceram. Int., 2017
[18] Al-Majidi M. H., Lampropoulos A., Cundy A. B. Tensile properties of a novel fibre reinforced geopolymer composite with enhanced strain hardening characteristics //Compos. Struct., 2017
[19] Zhang S., Horrocks A. R. A review of flame retardant polypropylene fibres //Prog. Polym. Sci., 2003
[20] Khaliq W., Kodur V. Effectiveness of polypropylene and steel fibers in enhancing fire resistance of high-strength concrete columns //J. Struct. Eng., 2018
[21] Ali A. M., Falah M. W., Hafedh A. A., Al-Khafaji Z. S. Evaluation the influence of steel- fiber on the concrete Characteristics //Period. Eng. Nat. Sci., 2022
[22] Shubbar A. A. Properties of cement mortar incorporated high volume fraction of GGBFS and CKD from 1 day to 550 days //J. Build. Eng., 2020
[23] Hamad M. A. et al. Production of Ultra-High-Performance Concrete with Low Energy Consumption and Carbon Footprint Using Supplementary Cementitious Materials Instead of Silica Fume: A Review //Energies, 2021
[24] Shubbar A. A. et al. Early Age and Long-term Mechanical Performance of Mortars Incorporating High-volume GGBS //Advances in Civil Engineering, Springer, 2022.
[25] Mohammadi Y., Singh S. P., Kaushik S. K. Properties of steel fibrous concrete containing mixed fibres in fresh and hardened state //Constr. Build. Mater., 2008
[26] Lahoti M., Tan K. H., Yang E.-H. A critical review of geopolymer properties for structural fire-resistance applications //Constr. Build. Mater., 2019
[27] Y. Ding, J.-G. Dai, and C.-J. Shi, Fracture properties of alkali-activated slag and ordinary Portland cement concrete and mortar // Constr. Build. Mater., 2018
[28] Rickard W. D. A., Van Riessen Performance of solid and cellular structured fly ash geopolymers exposed to a simulated fire //Cem. Concr. Compos., 2014 A.
[29] Sarker P. K., Kelly S., Yao Z. Effect of fire exposure on cracking, spalling and residual strength of fly ash geopolymer concrete //Mater. Des., 2014
[30] Madhkhan M., Saeidian P. Mechanical properties of ultra-high performance concrete reinforced by glass fibers under accelerated aging //Int. J. Eng. Trans. B Appl., 2021
[31] Kashyzadeh K. R., Ghorbani S., Forouzanmehr M. Effects of drying temperature and aggregate shape on the concrete compressive strength: Experiments and data mining techniques // Int. J. Eng., 2020
[32] Horszczaruk E., Sikora P., Cendrowski K., Mijowska E. The effect of elevated temperature on the properties of cement mortars containing nanosilica and heavyweight aggregates //Constr. Build. Mater., 2017
[33] Pillai C. S. et al., Evaluation of microstructural and microchemical aspects of high density concrete exposed to sustained elevated temperature //Constr. Build. Mater., 2016
[34] ACI, 233R-03: Ground Granulated Blast-Furnace Slag as a Cementitious Constituent in Concrete, USA (pp. 44)., 2011
[35] ASTM-C618-12, standard specification for coal fly ash and raw or calcined natural pozzolan for use in concrete, Am. Soc. Test. Mater. West Conshohocken (pp. 17). Philadelphia., 2012
[36] IQS NO.45, Aggregate from Natural Sources for Concrete and Construction. Baghdad, Iraq: Central Organization for Standardization and Quality Control (COSQC), No. 45/1984, 1984
[37] I. S. Specification, No. 45/1984, Aggregate from Natural Sources for Concrete and Construction. 1984.
[38] C. R. ME and A. B. Rao, Behavior of self compacting concrete under axial compression with and without confinement //Int. J. Ethics Eng. Manag. Educ. 1(3)., 2014
[39] A. C109/C109M-16a, Standard test method for compressive strength of hydraulic cement mortars (using 2-in. or [50-mm] cube specimens), West Conshohocken ASTM Int., 2016
[40] ASTM C496/Ca96M-11, Standard Test Method for Splitting Tensile Strength of Cylindrical Concrete Specimens, ASTM Int., 2011
[41] ASTM C78/C78M-22, Standard Test Method for Flexural Strength of Concrete (Using Simple Beam with Third-Point Loading). American Society for Testing and Materials International,United States, 2022
[42] J. Liu, X. Shi, G. Zhang, and L. Li, Study the Mechanical Properties of Geopolymer under Different Curing Conditions //Minerals, 2023
[43] Colangelo F. et al. Thermal cycling stability of fly ash based geopolymer mortars //Compos. Part B Eng., 2017
[44] Gao X., Yu Q. L., Brouwers H. J. H. Properties of alkali activated slag-fly ash blends with limestone addition, Cem. Concr. Compos., 2015
[45] Abdul-Rahman M. B., Al-attar A. A., Younus A. M. Elevated temperature effects on the behavior of one-way fibrous reinforced concrete slabs //Int. J. Eng. Technol., 2018

Information of the authors

Arjan Fakhrulddin Abdullah, PhD, professor, Technical Engineering College of Kirkuk, Northern Technical University (NTU)
e-mail: arjan2006@ntu.edu.iq

Al-Khafaji Zainab, PhD, lecturer, Universiti Kebangsaan Malaysia, Scientific Research Center, Al-Ayen University
e-mail: p123005@siswa.ukm.edu.my

Falah Mayadah, PhD, professor, College of Engineering and Engineering Techniques, Al-Mustaqbal University
e-mail: mayadah.waheed@uomus.edu.iq

DOI 10.52209/2706-977X_2025_4_104 **IRSTI 55.13.17** **UDC 67.02**

Studying the Tribological Properties of Polymer Composite Materials FIlled with Production Waste

Ziyamukhamedova U.[1,2*], Torskaya E.[3], Nafasov J.[1] , Turgunaliyev E.[1], Jalolova Z.[4]
[1]Tashkent State Transport University, Tashkent, Uzbekistan
[2]Kimyo International University in Tashkent, Tashkent, Uzbekistan
[3]Ishlinsky Institute for Problems in Mechanics RAS, Moscow, Russia
[4]Andijan state technical institute, Andijan, Uzbekistan
*corresponding author

Abstract. Currently, numerous studies are being conducted in the field of obtaining thermoreactive polymer composite materials and the production of high-responsibility parts based on them in the field of mechanical engineering. The main advantages of such materials are the low cost of production technology and raw materials compared to metals, replaceable when used as parts, wear resistance, and self- lubricating properties. This article examines the content of fillers and the degree of their influence on the properties of ED-20-based thermosetting polymer composite materials. To ensure the self-lubricating properties of the material in the production of wear-resistant composite materials, "pec" was used as a filler, which is the residual waste formed during the thermal processing of gas. It has been established that the content of carbon-containing pecs in the composite material exceeds 5-6%, and they can change the tribological properties of the composite material to a lesser extent. The morphological analysis of peck and the amount of compounds in its composition have been studied. Mechanical activation of fillers ensures their uniform distribution across the structure of the composite material. The composition of the material with the best tribotechnical properties was determined using experimental studies, and the value of the friction coefficient in wear was reduced to 0.14. In addition, fiber fillers were used to ensure sufficient strength along with the hardness of wear-resistant polymer composite materials, and their optimal amount was determined. The article concludes by examining the prospects of thermosetting polymer-based composite materials and highlighting the advantages of their use.

Keywords: thermoreactive polymer, ED-20, peck, filler, composite, tribological properties, morphology, friction, insole.

Introduction

It is a well-known fact that most of the components used in mechanical systems are made up of metals and their composites. It is also well known that demand for high strength low weight of materials is increasing day by in the industries. Various metallic materials with, Cu, Al, steel, Fe etc. are used use for fabrication automobile components, space components, energy sectors, etc. The cost of fabrication and cost materials of these metallic components is increasing day by day, besides these metallic materials possess high density [1]. The researchers and designers are working to find alternative solutions to these problems. Polymer materials, viz, polyethylene (PE), polypropylene (PP), polytetrafluoroethylene (PTFE). etc. and thermoreactive polymer materials are considered to be promising materials for future application of space, automobile, power plant, railway etc. application due to the fact that these material sposes low weight, high corrosion resistance, low coefficient, etc [2]. Known polymer materials are divided into 2 main groups [3]. They are thermoplastics and reactive plastics. Thermosetting materials are considered high heat resistant material 150-180^{o} C.

Thermoreactive polymers have recently been used for production of many components in railway transportation. These include bush bearings, railway breaking system [4]. These materials are subjected to load in the range of 45- 65 kN, temperature of 55-120^{o} C, and high corrosive environment are mad of high strength metals and their composites. Due to the fact that most of the parts used in the field of mechanical engineering are made of metals [5]. The demand of high strength, high high mechanical, tribological and performance properties is increasing. This leads to an increase in the cost of them and parts based on them. The role of polymer-based composite materials in solving this problem can be called incomparable. However, the correct selection of binders, fillers and reinforcing materials when creating composite materials requires special knowledge, skills and a lot of experimentation [6].

Presently, the polymer composite materials used in the field of railway transport are imported products, their localization and increasing the operational reliability are considered urgent problems. In particular, the bushings that attach the brake suspensions of railway freight wagons are the most widely used imported products in the repair of wagons [7], [8]. Obtaining bushings with high operational properties using the filling and reinforcing components of these bushings based on local raw materials is one of the urgent problems. The main drawback of the bushings used in the braking system of freight cars was considered to be fast wear and, as a result, a lot of time was spent on its repair [9].

Various researchers have carried out researcher's studies on improving the tribological properties and physical mechanical properties of polymer composite materials [10].

Mechanical and tribological properties of three types of polymer-based composites were studied [11]. In this research study three polymer-based composites were developed with the help of 2-3 polymer binds. These include polyesters and epoxy resins. Mechanical properties of these polymers were studied under different conditions of load and sliding velocity [12]. These polymers showed that mechanical properties improve with the addition of binders. Friction and wear properties were improved with coefficient of friction value of as low as 0.3 was obtain. When these polymer-based against counter

body of steel ball. A wear rate of 0-2 mm^3/Nm was obtained of sliding distance test of 200m. However, the complexity of the matrix mixing technology that makes up this composite limits the production of various details.

Chinese researchers studied [13] the properties of polymer composite materials using simple cubic modeling. The reliability of the obtained results is based on hundreds of experiments. However, it should be noted that this method loses its accuracy when the amount of dispersed fillers in the composite materials is from 40% to 85%. As a result, the accuracy of the obtained results is reduced [14].

By adding different types of dispersed metal fillers to polymer composite materials, the tribological properties of the composite can be improved. By adding bismuth oxide to PE, PP, epoxy resins, it is possible to improve the resistance of polymer composite materials to erosion due to friction and to use them as protective materials against various radiation rays [15]. However, due to the high density of bismuth, it is difficult to distribute filler particles uniformly throughout the structure, which is the main disadvantage of this method.

In addition, it is possible to ensure the service life and operational reliability of machine parts by applying wear-resistant polymer-based composite materials as protective coatings to the guiding sections [16-17] of machine-building components.

1 Materials and Methods

1.1 Materials and Preparation of Samples

When preparing samples of composite materials attaching brake suspensions to the side frame of railway cars, ED-20 epoxy resin was obtained from Uzbeksitan, dibutyl phthalate and polyethylene polyamine from Russia, and Angren kaolin AKT-10 which produced in the factory “Angren kaolin” in Uzbekistan as a dispersion filler, and glass fiber as screenings were used as a dispersion filler. used a filler and a multifunctional modifier - oil pyrolysis waste was used as a filler. Table 1 presents the functions of the components used in the preparation of samples within the composite, along with their manufacturers.

Table 1. Information about the components of composite materials

№	Ingredients	Function	Standarts	Manufacturer
1	ED-20	Binder	GOST 10587 - 93	Uzbeksitan, JSC "NAVOIYAZOT" - in Navoi
2	DBF	Plasticizer	GOST 12.1.004 - 91	Russia, "Roshal Plasticizers Plant" LLC
3	PEPA	Hardener	TU 6–02–594–70	Russia, "Roshal Plasticizers Plant" LLC
4	Peck	Filler		Uzbeksitan, Guzar, "Shurtanneftegaz" LLC
5	AKT-10	Filler	O‘z DSt 1056:2004	Uzbeksitan, Tashkent “Angren kaolin” LLC
6	Glass fiber	Reinforcing	GOST 319132011	Uzbeksitan, Tashkent "KANOMA" LLC

Composite components were placed in bins. The dry components measured in the distributor in specified proportions are jointly mechanically activated in the “Vibroplanetary Mechanical Activator” for 30 minutes. At the same time, ED-20 epoxy resin was mixed with DBP in a paddle mixer at a temperature of 60 °C until uniform distribution by volume. Then the mixtures prepared on the technological equipment are mixed in a mechanical mixer until 5-6% fiberglass is added and evenly distributed by volume. At the last stage, the required amount of the PEPA hardener component is added to the prepared mixture, and it is pressed in a press for 15 minutes at a temperature of 140°C - 160°C, under a pressure of 10-30 MPa. Then cool the mold in air for 5-15 minutes and remove the samples from it.

Based on the aforementioned technology for obtaining a thermosetting polymer composite material, samples were prepared based on the compositions presented in Table 1 to determine the tribological properties of the materials.

In this study, samples 01, 02, and 03 were selected to compare the properties of the new composite material and to analyze the influence of dispersed and fibrous fillers on the material properties. The first group of the new composites consists of materials without reinforcement, while the second group comprises composite materials reinforced with glass fibers. The influence of reinforcements and their quantity on the tribological properties of the material was investigated. Additionally, the change in the friction coefficient with an increase in the Pek content was analyzed for composites in both groups.

Table 1. The composition of the samples prepared for the experiment

Name	ED-20, %	DBF, %	PEPA, %	Peck, %	AKT-10, %	Glass fiber, %
01- sample (RK)	83,3	8,3	8,3	-	-	-
02- sample (textolite)	Prototip (Fenolformaldegid smolasi + mato va paxta mahsulotlari)					
Sample 03 (AKPMr)	27,0	2,7	2,7	-	67,6	-
Sample 1 (AKPMr-1)	76,9	7,7	7,7	3,8	3,8	-
Sample 2 (AKPMr-2)	71,4	7,1	7,1	7,1	7,1	-
Sample 3 (AKPMr-3)	66,7	6,7	6,7	10,0	10,0	-
Sample 4 (AKPMr-4)	55,6	5,6	5,6	16,7	16,7	-
Sample 5 (AKPMr-5)	45,5	4,5	4,5	22,7	22,7	-
Sample 6 (AYKPMr-1)	74,1	7,4	7,4	3,7	3,7	3,7
Sample 7 (AYKPMr-2)	66,7	6,7	6,7	6,7	6,7	6,7
Sample 8 (AYKPMr-3)	62,5	6,3	6,3	9,4	9,4	6,3
Sample 10 (AYKPMr-4)	52,6	5,3	5,3	15,8	15,8	5,3
Sample 11 (AYKPMr-5)	43,5	4,3	4,3	21,7	21,7	4,3
Note: RC - Reactoplastic component; AKPMr is an anti-friction reagent-plastic composite material. AYKPMr is an anti-friction-wear-resistant reactive plastic composite material.						

2. Results and discussion

The conditions of friction between the metal-polymer pair were studied in the study of the coefficient of friction and wear intensity in composites based on the ED-20 reagent-plastic binder. The experimental testing process was conducted according to the "ball-disk" scheme according to the ASTM G99 standard. The wear of materials was determined using a 3D profile meter using the "Mikron-Tribo" and "MFT5000" tribiometers. The "Micron-tribo" friction machine, designed for testing friction and wear during rotational and forward-return movements using the "ball-disk" method, was tested on samples with diameters of 50 mm and a thickness of 6-10 mm. Our research conducted friction and wear tests of the samples using the rotational method.

$V = C*L$ - wear.

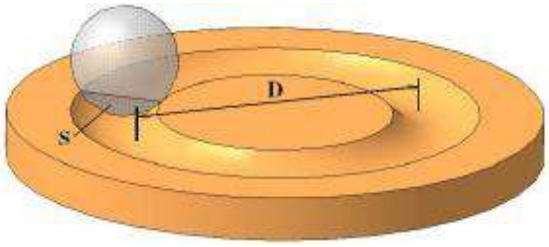

Fig. 1. Test schemes for rotational and forward-reflective friction

D is the diameter of the friction track, S is the cross-sectional area of the track, and L is the length of the track

The wear patterns of samples made of polymer composite materials were investigated using the MFT5000 3D profile.

During the experimental test, when a ball made of St3 steel with a diameter of 5 mm is pressed against the sample with a force of F=5 N, the disk-shaped sample rotates at a speed of n=500 rpm for a time of t = 60 minutes. The standard includes a set of input parameters (load, speed, distance, ball size). In this case, the ball is smaller and the load is lower, while the distance is different.The rotation diameter of the ball on the surface of the sample was set to 40 mm. It was determined that when a sample moves along a circular path with a diameter of 40 mm at a speed of n=500 rpm, the friction distance is 3768 m.

During testing, the magnitude of the friction force is continuously recorded, and the friction coefficient is automatically calculated by recording it graphically on the screen. The test process continues until the ball has fully traversed the specified friction path (L=3768 m).

Next, the linear wear (h) of the composite material was measured using a microscope and the wear intensity of the material was calculated:

$$I_h = h/L$$

where h is the surface thickness lost during linear wear, μm.

The track has the shape of a groove, and linear wear, especially its intensity, cannot be calculated in this way. It is better to measure the shape of the track profile and assess the volumetric wear and its intensity. L is the path of friction, m.

The morphological analysis of PES, used as a filler in the production of wear-resistant polymer composite materials, was conducted using an emission electron scanning microscope FE-SEM-ZEISS-500, Germany. Morphological analysis (Fig. 2.) revealed that peck particles had a plate-like appearance and this appearance was formed as a result of intense impacts of steel spheres during its activation in a vibro-planetary mechanism. When using plate-like particles as fillers in the production of a polymer composite material, their good compaction and strength compared to non-activated aggregates give the composite material high hardness properties. Hardness is the main property that determines the service life of parts operating under wear and tear conditions.

The quantitative content of organic compounds in the peck composition was determined by adsorption chromatography on an Agilent Technologies 7890 gas chromatograph equipped with a 5975 MSD model mass-selective detector. According to the data obtained, the amount of isoparaffin-naphthenic hydrocarbons in its composition is 7.99%, the sum of aromatic and olefinic hydrocarbons is 91.1%, and the amount of resin is 0.9%.

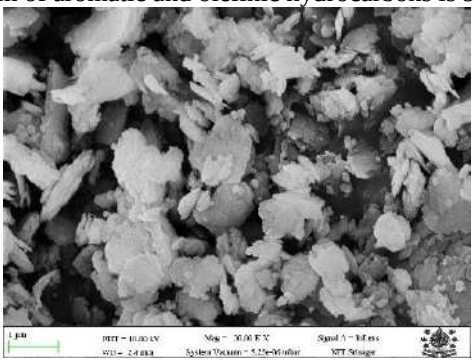

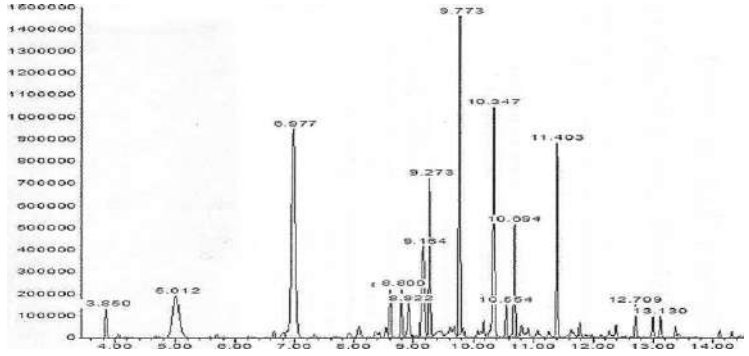

Fig. 2. Morphological (a) and chromatographic analysis of Pek

The amount of fibrous filler in the material was chosen based on research on the change in their friction coefficient. It has been established that increasing the amount of fibrous filler, while increasing the number of fibers located across the surface (Fig. 3), leads to an increase in the coefficient of friction, ensuring electrical conductivity along the surface without the accumulation of tribocharges on the friction surfaces by 6% of the oil content and 5% of the material's operational reliability

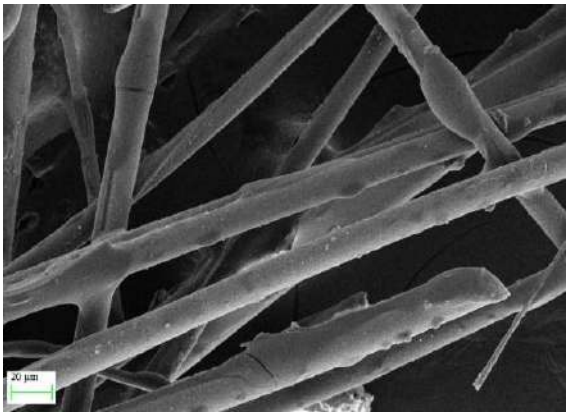

Fig. 3. The structure of the grinding filler (glass fiber) in the composite, (x 1000)

Based on the study of the tribological properties of the materials, optimal compositions of thermoplastic and reactive-plastic composite materials were selected (Table 2) and a 3D profile graph of the wear pattern was analyzed (Fig. 4). As can be seen from the table and profile graph, the reactoplast (AYGPMr-5) heterocomposite material does not lag behind the currently used textolite in terms of its tribological properties. Since the value of the friction coefficient under contact friction in thermoplastic (AYGPMt-3) heterocomposite materials has slightly increased, it is recommended to use these materials as materials resistant to abrasive wear and deformation.

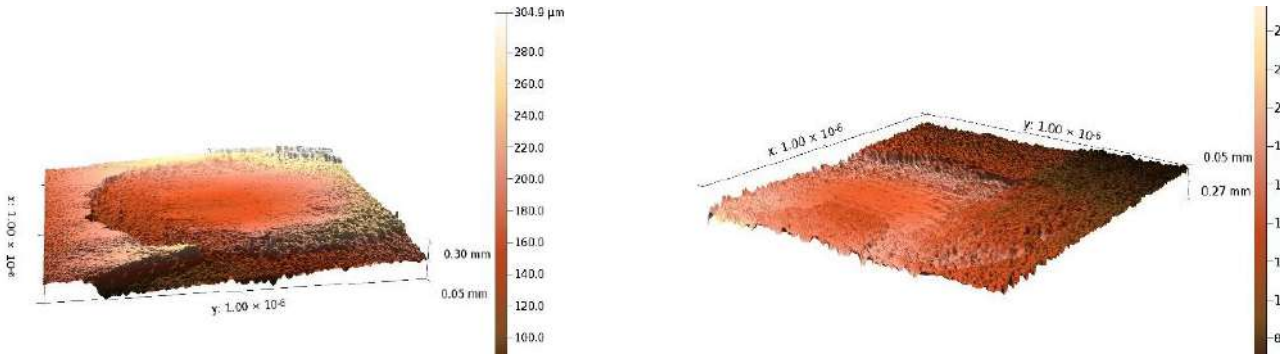

Fig. 4. Profiles of textolite (a) and GKPM (b), determined using a universal tribometer MFT-5000

Currently, railway freight wagons are manufactured based on PT brand textalites with sleeves connecting the brake suspension to the side frame. PT texallite, being an imported raw material, is considered very expensive and rare.

To this end, the wear resistance properties of samples made of heterocomposite polymer materials were compared with textile materials of the standard PT brand, which are currently used to attach the brake suspension of railway freight cars to the side frame, and the samples were tested on metal-polymer systems using a universal tribometer MFT-5000 according to the parameters of real operating conditions.

It is known that the amount of wear caused by friction between the bodies changes directly proportional to the coefficient of mutual friction between them. If the coefficient of friction is small, the material will be resistant to wear. The results obtained show that sample AGPMr-5 has the lowest coefficient of friction (Table 2). However, the absence of a glass fiber filler in its composition does not ensure its resistance to shock loads. This property of the material is ensured by adding 5% glass fiber to its composition (AYGPMr-5).

Table 2. The tribological properties of the samples

Name	Friction path L, m	Linear wear h, μm	Wear intensity I_h , 10^{-8}	Friction coefficient, f
RK	3768	170	4,51	0,42
textolite	3768	140	3,72	0,22
AGPMr	3768	155	4,11	0,35
AGPMr-1	3768	160	4,25	0,4
AGPMr-2	3768	150	3,98	0,32
AGPMr-3	3768	120	3,18	0,26
AGPMr-4	3768	110	2,92	0,16
AGPMr-5	3768	108	2,87	0,14
AYGPMr-1	3768	140	3,72	0,44
AYGPMr-2	3768	135	3,58	0,36
AYGPMr-3	3768	115	3,05	0,28
AYGPMr-4	3768	112	2,97	0,18
AYGPMr-5	3768	110	2,92	0,16

Thus, the tribological properties of heterocomposite materials are not inferior to the tribological properties of PT materials. Consequently, for manufacturing bushings that connect brake suspensions to the side frame of railway rolling stock, it is possible to use a new heterocomposite material. This material can contain 35-45% of ED-20 epoxy resin, 2-5% of dibutyl phthalate, 2-5% of polyethylene polyamine, 20-25% of petroleum waste (pitch), 20-25% of AKT-10 Angren kaolin, and 5-10% of reinforcing glass fibers, all by total mass.

Conclusion

The results of studies conducted on samples obtained by casting in laboratory conditions with a diameter of 5 cm and a thickness of 4-6 mm based on a thermosetting polymer binder (ED-20) revealed the following:

1. It has been established that as a chemical modifier with mechanically activated dispersed fillers, the surface surfaces of oil-bearing heterocomposites are activated, and a strong interstructural bond is formed due to a decrease in the moistening angle of the surface tension of the modifier in the heterogeneous system.

2. Optimal compositions of deformation, abrasion, and wear-resistant heterogeneous polymeric materials based on reactoplastic binders AIGPMr-5 have been proposed, and it has been established that the content of 6% oil pecs in their composition performs a multifunctional function in structure formation, while the content of 5% fiber filler increases tensile strength by 1.8-2 times and deformation resistance by 1.3-1.4 times, ensuring operational reliability.

3. The operational reliability of sleeves made of materials containing AYGPMr-5, obtained by mechanochemical modification using a vibration planetary activator, is ensured by a low coefficient of friction, i.e., equal to 0.16.

Acknowledgments.

The research work was carried out with the financial support of International project AL-7623031217 and «Academic Mobility»

References

[1] Gökçe N., Şevki E. R. E. N., Nodehi M., Ramazanoğlu D., Subaşi S., Gencel O., Ozbakkaloglu T. Engineering Properties of Hybrid Polymer Composites Produced with Different Unsaturated Polyesters and Hybrid Epoxy //Journal of Building Engineering, 2024, 109334.

[2] He L., Dou Z., Zhang,Y., Fu Q., Wu, K. Modelling effective thermal conductivity in polymer composites: A simple cubic structure approach //Composites Science and Technology, 2024, 252, 110592.

[3] Bagheri S., Khalafi H., Tohidifar M. R., Bagheri S. //Thermoplastic and thermoset polymer matrix composites reinforced with bismuth oxide as radiation shielding materials. Composites Part B: Engineering, 2024, 278, 111443.

[4] Kim J., Hwang U., Park I. K., Suhr J., Nam J. D. Non-combustible polymer composites with extremely high filler loading via polytetrafluoroethylene fibrillation //Composites Communications, 2024, 101899.

[5] Ziyamukhamedova U., Evlen H., Nafasov J., Jalolova Z., Turgunaliyev E., Rakhmatov E. Modeling of the process of mechano activation of filler particles in polymer composites // E3S Web of Conferences, 2023, Vol. 401, p. 05027

[6] Khalimov S., Nishonov F., Begmatov D., Mohammad F. W., Ziyamukhamedova U. Study of the physico-chemical characteristics of reinforced composite polymer materials // E3S Web of Conferences, 2023, Vol. 401, p. 05039

[7] Evlen H., Ziyamukhamedova U., Juraev D., Abdukarimov M. Additive manufacturing of bionanomaterials for biomedical applications based on TI6AL4V and PLA: a systematic review // E3S Web of Conferences, 2023, Vol. 401, p. 03040

[8] Mikhaylov A., Diaz J. L. B., Zakharova M., Vinieska V., Münch D., Fohtung E., Kunka D. Micro-reinforced polymer composite materials studied by correlative X-ray imaging //Nano Trends, 2024, 6, 100035.

[9] Ziyamukhamedova U., Bakirov L., Donaev S., Miradullaeva G., Turgunaliev E. Study of structure formation processes in matrices of mixed components with reinforcing natural fillers // E3S Web of Conferences, 2023, Vol. 401, p. 05074

[10] Ziyamukhamedova U., Rakhmatov E., Dustqobilov E., Nafasov J., Ziyamukhamedov J. Development of protective coating compositions for process tanks //AIP Conference Proceedings, 2023, Vol. 2789, No. 1

[11] Li Y., Li H., Kong N., Lu S., Sun C., Tian R., Yang P. Biotribological properties of 3D printed high-oriented short carbon fiber reinforced polymer composites for artificial joints //Biomaterials Advances, 2024, 213888.
[12] Donaev S. B., Ziyamukhamedova U. A., Kenjaeva M., Shirinov G. M., Rakhimov A. M., Abduvayitov A. A. Changes in the electronic structure of the Si surface as a result of ion implantation. In E3S Web of Conferences, 2023, Vol. 383, p. 04040
[13] Ziyamukhamedova U., Bakirov L. Actual contact area of fibrous weight //AIP Conference Proceedings, 2022, Vol. 2637, No. 1
[14] Gadamov D., Ziyamuhammedova U., Miradullaeva G. Chemical resistance of a hydrophobic-hemostable organomineral composite material in aggressive liquid media //AIP Conference Proceedings, 2024, Vol. 3045, No. 1
[15] Gani A., Ibrahim M., Ulmi F., Farhan A. The influence of different fiber sizes on the flexural strength of natural fiber-reinforced polymer composites //Results in Materials, 2024, 21, 100534.
[16] Zhetessova G., Nikonova T., Gierz Ł., Berg A., Yurchenko, V., Zharkevich O., Alexey K. A comparative analysis of the dynamic strength properties of the long guides of intelligent machines for a new method of the thermal spraying of polymer concrete //Applied Sciences, 2022, 12(20), 10376.
[17] Zhetesova G. S., Dandybaev E. S., Zhunuspekov D. S., Zhekibaeva K. K. Improvement of the organization of maintenance and repair of dump-cars //Material and Mechanical Engineering Technology, 2020(1), 33-38.

Infornation of the authors

Ziyamukhamedova Umida, DSc, professor, Tashkent State Transport University**,** Kimyo International University in Tashkent
e-mail: z.umida1973@yandex.ru

Torskaya E., DSc, professor, Ishlinsky Institute for Problems in Mechanics RAS
e-mail: torskaya@mail.ru

Nafasov J., PhD, associate professor, Tashkent State Transport University
e-mail: nafasovz@mail.ru

Turgunaliyev E., PhD, associate professor, Tashkent State Transport University
e-mail: mrelbek@mail.ru

Jalolova Z., doctoral, student, Andijan state technical institute
e-mail: zilolajalolova1108@gmail.com

DOI 10.52209/2706-977X_2025_4_110 **IRSTI 55.21.99** **UDC 621.1.9**

Minimizing Wire Breakage in Wire Electric Discharge Machining Using Multi-Objective Artificial Bee Colony Algorithm

Pawar P. J.[1*], Dalavi A. M.[2], Thorve K. M.[1]
[1]K. K. Wagh Institute of Engineering Education and Research, Nashik, Maharashtra, India
[2]Symbiosis Institute of Technology, Pune, Maharashtra, India
[*]corresponding author

Abstract. Wire breakage in wire electric discharge machining (WEDM) is a serious issue causing in-between stoppage resulting into time loss, wastage of wire, and excessive energy utilization. Hence to achieve higher machining productivity of WEDM process, it is necessary to prevent wire breakage and also to improve material removal rates. Multi-objective optimization for maximizing material removal rate (MRR) and minimizing wire breakage in WEDM process is therefore presented in this work. A novel approach of maximizing tension sustained by the used wire for minimizing wire breakage is presented through an industrial case study. The effect of independent variables such as pulse on time, pulse off time, peak voltage, dielectric fluid pressure, wire feed rate, machine speed, and cutting speed override on dependent variables, wire breakage frequency and material removal rate is studied to formulate the optimization model based on response surface modeling. Multi-objective version of artificial bee colony algorithm is used for optimization. The set of Pareto optimal solutions obtained by this proposed approach provides a ready reference to select most appropriate parameter setting on the machine.

Keywords: WIRE electric discharge machining, wire breakage, material removal rate, multi-objective artificial bee colony algorithm

Introduction

Wire electric discharge machining (WEDM) is an important process, specially used to make complex and intricate shaped components from difficult to machine materials. The wire breakage is one of the major issues frequently encountered while wire electric discharge machining of hard materials like EN19 commonly used for defense applications. While machining if wire breaks, it will stop the operation in serious situation. After breakage all the operation settings has to recover and broken wire has to replace. It is difficult to restart the machining operation from the same work-piece and tool alignment settings. Thus this replacement increases the machining time. Wire breakage also produces a permanent surface damaged on the component surface and also decreases accuracy of the process. This will greatly hamper the machining performance and productivity of WEDM.

The wire breakage in WEDM occurs due to several causes including the thermal loading, high wire tension due to intricate and complex shape of components, impact of electric discharge and large vibrations of wire etc. The machining parameters that affects MRR and wire breakage includes pulse on time, pulse off time, peak voltage, wire feed, flushing pressure, machine speed and cutting speed etc. For the high electric discharge higher pulse on time is required to select which causes the short circuit and wire breakage. On the other hand, higher value of pulse off time reduces the risk of wire breakage but reduces MPR. The peak voltage directly affects the wire breakage. Due to the higher value of peak voltage, heat energy increases which leads to melting and vaporization of wire. The selection of proper wire feed rate results into higher material removal rate, less wire breakage and better surface finish. Flushing pressure refers to the pressure of flushing fluid used to remove the molten slug. The high flushing pressure causes the wire deflection and vibrations, but it is also necessary for better cutting performance. Material removal rate is equally important to achieve higher machining productivity and cost effective utilization of machine. While selecting appropriate parameters for minimum frequency of wire breakage care has to be taken that material removal rate should not be hampered. As these two objectives i.e. minimization of frequency of wire breakage and maximization of material removal rate are conflicting in nature, selection of appropriate process parameters is a challenging task.

Several attempts are made by the researchers for the investigation of wire breakage in WEDM. Kinoshita et al. [1] experimentally studied the conditions of wire breakage and noticed its various reasons and presented a control strategy for prevention of wire breakage by monitoring the pulse frequency. Rajurkar et al. [2] presented the relationship between sparking frequency and wire breakage in WEDM and noticed that wire rupture occurs at high sparking frequency. Based on this a control strategy was suggested to maintain sparking frequency to constant level by on line monitoring. Yan and Liao [3] developed a fuzzy logic based adaptive control optimization system to investigate various performance measures such as material removal rate, surface roughness, and wire breakage. Liao et al. [4] identified two causes of wire rupture namely excess of sparks and sudden rise of sparking frequency. Yan and Liao [5] developed a multi variable three region fuzzy controller for online monitoring of abnormal sparks and sparking frequency to prevent the wire breakage. Luo [6] presented the effect of various WEDM parameters on wire failure and mechanical strength of wire electrode. The study revealed that wire yielding and fracture are the main causes of wire rupture. Inadequate flushing causes the wire temperature increase which also leads to wire failure and the spark pressure directly affects the bow error which also has importance in wire rupture. Guo et al. [7] through simulation modeling of wire vibration observed that under the optimum conditions of discharge energy, discharge frequency, wire tension, and wire span the wire breakage can be minimized. Saha et al. [8]

developed a finite element model for the heat distribution of wire and predicted that the non- uniform heat generated in wire causes the wire breakage; also an optimization process was developed for minimizing the temperature of wire to reduce thermal strain. Cabanes et al. [9] developed a new wire breakage monitoring and diagnosing system by analyzing experimental data to predict the conditions for the wire breakage such as discharge energy, peak current, and ignition delay time. Kumar et al. [10] analyzed the wire electrode surface after the machining of titanium using Energy Dispersive X-ray and revealed that the wire breakage is due to large temperature value during machining of titanium. Gupta et al. [11] investigated the effect of pulse on time, pulse off time, voltage and wire feed rate for minimum surface roughness, wire breakage and maximum material removal rate. Okada et al. [12] attempted to correlate the kerf length and nozzle jet flushing with wire deflection and breakage. Habib and Okada [13] revealed that unstable wire behavior and large vibrations of wire electrode has serious effect on wire breakage, reduction in accuracy and low surface finish. Kumar et al. [14] discussed a detail review of researches and their findings about the major problems that frequently encountered in application of WEDM. Das and Joshi [15] presented an approach to estimate the wire safety index based on thermal residual stresses that generate on the wire electrode by using a finite element method based model. Abhilash and Chakrdhar [16] developed an approach to correlate the mean gap voltage variation and wire breakage occurrences during the wire EDM of Inconel material. Earlier researchers also attempted multi-objective optimization of WEDM for minimization of wire breakage and material removal rate using priori approach [17], Taguchi Method [18], Response Surface Methodology [19, 20], Particle swarm optimization [21], Teaching Learning Based Optimization [22, 23], Adaptive Nuro-fuzzy Interface System [24], Neural network [25], Support vector machine [26] etc.

For multi-objective optimization, researchers are mainly employing two approaches - priori approach and posteriori approach. In priori approach, weights are assigned to the different objectives before optimizing. However, if the process engineer does not have compressive knowledge of the process, there is always a chance of selecting inappropriate weights leading to ineffective solution. Hence, for multi-objective optimization, posteriori approach is preferred which provides non-dominated set of optimum solutions. The decision maker is free to choose any solution from this set of optimum solutions. Artificial bee colony algorithm developed by Karaboga and Basturk [27] has been proved to be one of the most powerful and robust algorithms for optimization of several real life applications. In this work an attempt is made to apply multi-objective version of artificial bee colony algorithm proposed by Pawar et al. [28] which is based on the concept of non-dominated sorting [29] as discussed in the next section.

1. Multi-Objective Artificial Bee Colony Algorithm

The artificial bee colony algorithm [27] is inspired by the intelligent behavior of honey bee swarms to search a food source rich in nectar and close to their hive. Just like natural honeybee system, this algorithm models also consist of three groups of bees: onlooker bees, employed bees, and scout bees. Employed bees exploit a source of food and also share the information about this food source to onlooker bees, onlooker bees will use the information shared by employed bees to evaluate quality of food source, scout bees discover all food source positions randomly. To extend the application of ABC algorithm for multi-objective optimization with posteriori approach, concept of non-dominated sorting [29] is incorporated in this work. Once the initial population and fitness function is evaluated, the non-dominated sorting of solutions is carried out to rank the solutions till all the solutions got non-dominated status. Based on the rank of the solution the shared fitness values is calculated. The probability to which the onlooker bee is assigned to employed bee is then calculated based on this shared fitness and not based on actual fitness. The rest of the procedure is same as that of artificial bee colony algorithm.

2. Application Example

An application example considered in this work is a special tool for defense application made of EN19 steel material. The details of experimental set up used for data collection are given below:

- Machine type = ULTIMA 1S/2S (Wire cut WEDM submerged type);
- Pulse Generator = ELPULS 55S SERIES;
- Make= Electronica Machine tools;
- Wire material = Brass diffusion coated;
- Wire diameter = 0.25 mm;
- Wire composition = Cu 65% and Zn 35%;
- Wire strength = 400 N/mm^2;
- Wire tension = 19.63 Newton;
- Dielectric = distilled water (HCl and Carbide soda);
- Range of dielectric temperature = 20°C to 240°C.

Due to chromium, molybdenum and manganese in EN 19 steel, it has high abrasion and impact resistance, high fatigue strength, high toughness and torsional strength. Because of the high hardness and high strength of EN 19 steel it finds greater utility in the defense applications. However, due to these distinct properties of EN 19 material, the conventional machining processes are not suitable for machining of this material. In nontraditional machining processes, the wire electric discharge machining process find suitable for machining of EN 19 material. The wire electric discharge machining is mostly used in applications of making complex and intricate shapes (which are either two or three dimensional) from difficult to machine materials by means of erosion. However, there are certain problems in wire electric

discharge machining of EN 19 material. These include the low material removal rate, high wire electrode wear rate, and poor surface finish. During wire electric discharge machining of EN 19 material, large size craters are produce on the wire electrode. These craters increase the chance of wire breakage and ultimately lead to lowering the surface finish and dimensional accuracy of work-piece. The wire electrode breakage during wire electric discharge machining results in harmful and highly undesirable distortions of surface of machined component as well as it decreases the accuracy of machining. It has been experimentally found that the wire electrode breakage is increases with increase in pulse duration and open circuit voltage and it is decreases with decrease in wire speed. As the higher pulse duration, peak voltage and wire speed etc. are essential for better material removal rate value but these leads to greater wire wear rate. The schematic sketch of WEDM process showing wire feed mechanism is shown in Fig. 1.

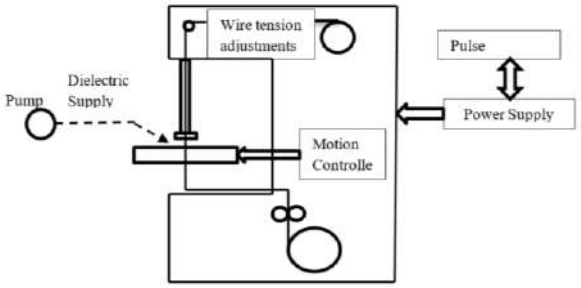

Fig. 1. - Schematic sketch of WEDM process showing wire feed mechanism

Keeping in view the above-mentioned aspects of product manufacturing, the two objectives considered are (i) Minimization of frequency of wire breakage (by ensuring that tension sustained by the used wire, T_{uw} is maximum) (ii) Maximization of material removal rate (R). To minimize the frequency of wire breakage, the parameters should be so selected that the minimum tensile stress should be induced in the wire. For this, the tension sustained by the used wire before breakage is measured. It is obvious that for the parameter setting for which the tension withstand by the used wire is maximum, the risk of the wire breakage is also minimum. The important process variables identified affecting the above mentioned responses are: pulse on time (T_{on}), Pulse off time (T_{off}),Peak voltage (V_p), dielectric fluid pressure (P_w), Wire feed rate (f), Machine speed (V_m), and Cutting speed override (O). Operating ranges of these process variables and their coded levels are presented in Table 1.

Table 1. Process variables and their coded values

Parameters	Coded levels				
	-α	**-1**	**0**	**1**	**α**
T_{on} (μsec)	103	105	107	109	111
T_{off} (μsec)	23	30	37	44	51
V_p (Volts)	10	11	12	13	14
P_w (Kgf/cm^2)	7	11	15	19	23
f (mm/min)	2	3	4	5	6
V_m (RPM)	75	100	125	150	175
O (%)	15	20	25	30	35

A response surface model is obtained by conducting 149 experiments as the number of independent variables are 7. The details of these 149 experiments are provided in Appendix-I. A second-order polynomial response is fitted into the following equation to study the effect of independent variables on dependent variables as given by Eq. (1) and Eq. (2) provided in appendix 1.

To test whether the data are well fitted in model or not, the calculated r^2value of the regression analysis for material removal rate (R) and tension withstand by the used wire (T_{uw}) are obtained as 0.97 and 0.87 respectively. The high r^2 values obtained for both the responses clearly indicate that the regression models developed in this work fit the data well. The next section describes the application of non-dominated sorting based artificial bee colony algorithm for parameter optimization of wire electric discharge machining.

3. Multi-Objective Optimization using Non-Dominated Sorting Based Artificial Bee Colony Algorithm

To demonstrate and validate the proposed approach, following multi-objective optimization model is formulated:

Objective 1: Maximization of material removal rate (R) as given by Eq. (1)

Objective 2: Maximization of tension that the used wire can withstand without breakage (T_{uw}) as given by Eq. (2).

Although the population size is of 50 is considered in this work, only first five solutions are considered for demonstration. The proposed approach is demonstrated through following steps.

Step 1: Parameters selection:

- Number of employed bees (=Number of food sources): 20
- Number of onlooker bees: 50
- Number of scout bees: 1

Step 2: Calculate the nectar amount for each food source

The nectar amount of each food source is obtained by evaluating the objective function values as shown in Table 2.

Table 2. Nectar amount (in terms of R and T_{uw}) for each food source

Solution No.	T_{on} (μsec)	T_{off} (μsec)	V_p (Volts)	P_w (kgf/cm^2)	f (mm/min)	V_m (RPM)	O (%)	R (mm^3/min)	T_{uw} (N)
1	104.6	47.1	11.3	11.8	3.4	80.4	35.0	0.93	3.25
2	110.6	23.0	12.6	14.7	5.2	137.4	19.8	0.87	3.30
3	108.5	46.2	14.0	12.1	3.8	174.9	16.2	1.09	2.65
4	105.9	49.7	11.4	12.0	4.5	162.6	31.1	0.91	3.08
5	110.8	35.1	11.0	11.1	3.1	140.0	16.7	0.87	3.43

Step 3: Non-dominated sorting of solutions

The solutions are ranked based on non-dominated sorting as shown in Table 3.

Table 3. Rank assigned to each solution

Solution No.	R (mm^3/min)	T_{uw} (N)	Rank
1	0.93	3.25	3
2	0.87	3.30	2
3	1.09	2.65	2
4	0.91	3.08	4
5	0.87	3.43	2

Step 4: Determine normalized Euclidean distance of each solution

Table 4 shows normalized Euclidean distance of each solution from every other solution is calculated using Eq. (3).

$$d_{ij} = \sqrt{\sum \left(\frac{x_s^i - x_s^j}{x_s^{max} - x_s^{min}} \right)^2} \quad (3)$$

Table 4. Normalized Euclidean distance of each solution

Solutions	1	2	3	4	5
1	0.00	1.60	1.58	0.91	1.41
2	1.60	0.00	1.10	1.33	0.84
3	1.58	1.10	0.00	1.06	0.98
4	0.91	1.33	1.06	0.00	1.16
5	1.41	0.84	0.98	1.16	0.00

Step 5: Determine niche count of the solution

A niche count (nc_i) provides an estimate of the extent of crowding near a solution and is calculated using the equation:

$$nc_i = \sum sh(d_{ij}) \quad (4)$$

where, Sh(d_{ij}) is the sharing function values of all the first front solutions as given by equation:

$$Sh(d_{ij}) = \begin{cases} 1 - \left(\frac{d_{ij}}{\sigma_{share}} \right)^2 \end{cases} \; if \; d_{ij} < \sigma_{share}$$

$$= 0 \qquad \text{otherwise} \quad (5)$$

where, σ_{share} is the maximum distance allowed between any two solutions to become members of a niche. The σ_{share} value in this equation is to be chosen appropriately. The sharing function values shown in Table 5 are obtained by using Eq. (5).

Table 5. Sharing function values of each solution

Solutions	Sharing function values				
	1	2	3	4	5
1	1.00	0.00	0.00	0.17	0.00
2	0.00	1.00	0.00	0.00	0.29
3	0.00	0.00	1.00	0.00	0.04
4	0.17	0.00	0.00	1.00	0.00
5	0.00	0.29	0.04	0.00	1.00

Niche count for first 5 solutions is then obtained using Eq. (4) as given in Table 6 below.

Table 6. Niche count of each solution

Solution No.	1	2	3	4	5
Niche count (N_c)	2.22	2.62	1.79	2.74	2.20

Step 6: Determine the shared fitness values of the solutions:
Considering the dummy fitness value for rank 1 solutions as 50, the shared fitness values for 5 sample solutions are obtained using Eq. 6) and are presented in Table 7.
Shared fitness (F_i) = Dummy fitness (f) / nc_i (6)

Table 7. Shared fitness values

Solution No.	1	2	3	4	5
Shared Fitness	1.26	5.25	7.66	0.34	6.24

Step 7: Determine the probabilities based on the shared fitness values evaluated in step 6:
The probability (P_i) with which the onlooker bee is assigned to employed bee is obtained based on the shared fitness is obtained using Eq. (7) as shown in Table 8:

$$P_i = \frac{\sum_{k=1}^{R} (1/f_k)^{-1}}{f_i} \quad (7)$$

Table 8. Probabilities of assigning onlooker bees to employed bees

Solution No.	1	2	3	4	5
P_i	0.008	0.032	0.047	0.002	0.038

Step 8: Calculate the number of onlooker bees, which will be sent to food sources
The number of onlooker bees sent to an employed bee (N) shown in Table 10 are obtained using Eq. (8) below:

$N = P_i \times m.$ (8)

Where, 'm' is the total number of onlooker bees.

Table 9. Number of onlooker bees assigned to employed bees

Solution No.	1	2	3	4	5
N	0	2	2	0	2

Step 9: Determine new position of each onlooker bee
Each food source position is updated 'N' times using the Eq. (9):

$$x_i' = x_i \pm (x_j - x_k) \quad (9)$$

Where, x_i' is updated food source position, x_i is current food source position, x_j and x_k are randomly chosen food source position from current population. Each food source is then updated if better position is obtained by onlooker assigned to that food source.

The positions of these onlooker bees are obtained as mentioned in Table 10.

Table 10. Positions of onlooker bees

Solution No.	Position of onlooker bee 1	R (mm^3/min)	T_{uw} (N)	Position of onlooker bee 2	R (mm^3/min)	T_{uw} (N)
2	(110.2, 23.1, 12.4, 13.6, 5.3, 141.7, 21.0)	0.83	3.34	(111.0, 23.7, 12.4, 14.1, 5.3, 137.7, 19.0)	0.89	3.31
3	(108.4, 48.3, 14.0, 11.3, 3.6, 175.0, 17.1)	1.04	2.63	(108.9, 44.8, 14.0, 12.2, 4.2, 175.0, 15.8)	1.11	2.65
5	(110.9, 34.3, 10.7, 12.4, 2.8, 133.8,17.4)	0.81	3.52	(110.8, 35.0, 11.2, 11.7, 3.4, 146.3, 17.4)	0.90	3.32

The positions of onlooker bees for each food source are then compared with the position of the employed bee assigned to that food source. The priori approach is used to for comparing the new solution with the old one, so as to make the decision whether to replace the old solution with new solution or not. For evaluating combined objective function equal weights of both objectives are considered. The combined objective function (to be minimized) is then evaluated as:

$$Z = -\frac{R}{R^*} - \frac{T_{uw}}{T_{uw}^*} \tag{10}$$

where R^* and T_{uw}^* are threshold values of material removal rate and tension sustained by used wire respectively.

The values of combined objective functions for employed and onlooker bees using Eq. (10) are shown in Table 11. In MO-ABC approach, the non-dominated sorting is performed on original population of solutions. Hence, the rank 1 solutions will be given a chance multiple times to generate better solution, as the number of bees assigned to a solution is based on shared fitness value. Thus it is ensured that diversity is maintained for Pareto optimality. However, the priori approach is used just to get a reference value for choosing the best among the newly generated solution. However, anyway the so chosen solutions will have to undergo non-dominated sorting in the next generation. The equal weights for the objectives are used for unbiased selection.

Table 11. Combined objective functions for employed and onlooker bees

Solution No.	'Z' for employed bee	'Z' for onlooker bee 1	'Z' for onlooker bee 2
2	-1.29	-1.27	-1.30
3	-1.29	-1.26	-1.31
5	-1.314	-1.29	-1.31

It is observed from the above Table that combined objective function values of onlooker bee 2 and 3 are better than those of corresponding employed bee, hence the solution 2 and solution 3 are updated. For solution 5, combined objective function value of employed bee is better than both those of both the onlooker bees hence the position of the employed bee is retained. Table 12 shows the new set of first five solutions.

Table 12. Set of updated Solutions

Solution No.	Updated employed bee position	Z
1	(104.6, 47.1, 11.3, 11.8, 3.4, 80.4, 35)	-1.315
2	(111.0, 23.7, 12.4, 14.1, 5.3, 137.7, 19.0)	-1.303
3	(108.9, 44.8, 14, 12.2,4.2, 175.0, 15.8)	-1.309
4	(105.9, 49.7, 11.4, 12.0,4.5,162.6, 31.1)	-1.266
5	(110.8, 35.1,11.0,11.1,3.1,140.0,16.7)	-1.314

This process maintains elitism as best among new solutions is compared with old solution and the one which is superior gets selected.

Step 10: Evaluate the best solution

The global best of the honeybee swarm is (107.1, 32.4, 11.8, 18.9, 5.6, 75, 15) with value of R and T_{uw} as 1.05 mm^3/min and 3.47 N respectively.

Step 11: Update the scout bee

Since number of scout bee is one, a random solution is generated as (104.2, 33.3, 12.6, 23.0, 3.1, 148.7, 22.4) with Z = -1.163. The worst of the updated solution is (106.2, 50.5, 11.7, 12.5, 4.6, 165.8, 30.9) with Z = -1.266. Since, the worst solution is better than the randomly generated (scout) solution, the worst solution will not be replaced by scout solution.

Step 12: Obtain the set of Pareto-optimal solution

The steps 2-11 are iterated for 140 generations to obtain the set of Pareto optimal solution as shown in Table 13. Although 20 initial solutions were considered, the algorithm is able to maintain the diversity in the population resulting into 13 Pareto optimal solutions.

Table 13. Set of Pareto optimal solutions

S. N.	T_{on} (μsec)	T_{off} (μsec)	V_p (Volts)	P_w (kgf/cm^2)	f (mm/min)	V_m (RPM)	O (%)	R (mm^3/min)	T_{uw}(N)
1	111.0	51.0	14.0	22.9	4.6	175.0	35.0	1.34	2.29
2	111.0	51.0	12.0	22.2	5.2	89.8	35.0	1.30	2.58
3	111.0	51.0	11.4	23.0	4.9	125.6	35.0	1.25	2.74
4	110.4	46.9	10.5	18.6	4.9	164.4	15.0	1.10	3.33
5	109.6	50.9	10.7	16.5	5.2	75.0	15.0	1.05	3.62
6	108.7	51.0	10.4	17.4	5.3	75.0	15.0	1.02	3.73
7	110.9	51.0	10.0	18.0	5.2	87.3	15.0	1.00	3.77
8	110.0	51.0	10.3	15.3	5.3	75.0	15.0	1.00	3.81
9	111.0	51.0	10.0	16.2	5.1	75.0	15.0	0.98	3.85
10	111.0	50.9	10.0	15.3	5.3	75.0	15.0	0.97	3.88
11	107.1	51.0	10.4	15.0	5.2	75.0	15.0	0.96	3.90
12	109.3	51.0	10.0	12.9	5.3	75.0	15.0	0.91	4.07
13	106.9	51.0	10.0	13.7	5.5	75.0	15.0	0.88	4.16

This set of Pareto optimal solution can be used as ready reference by the process engineers to select the most appropriate solution as per his/her requirement. The Pareto-front is shown in Fig. 2.

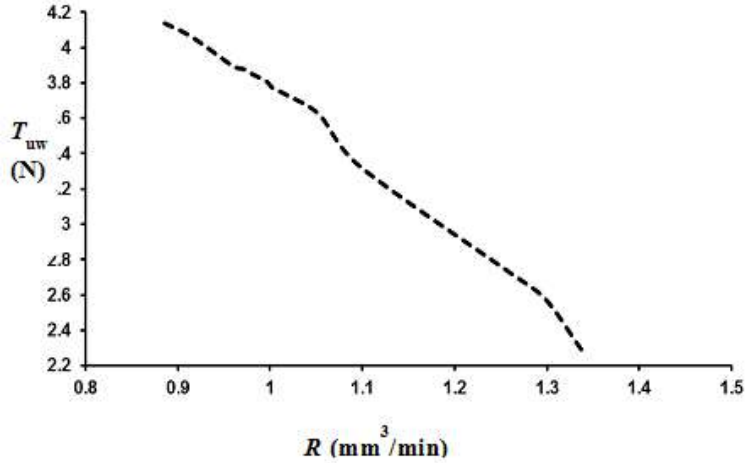

Fig. 2. - Pareto front

The effect of each process variable (while keeping other variables at their optimum level) on material removal rate and frequency of wire breakage is presented through Figures 4 to 10.

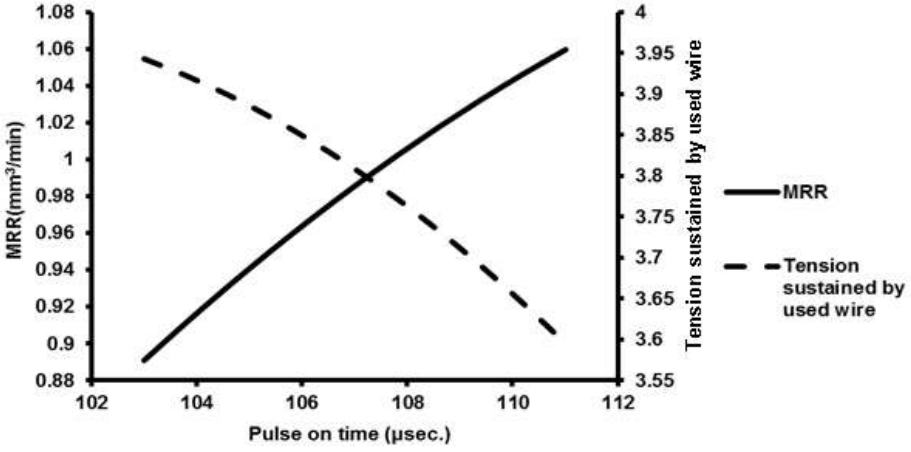

Fig. 3. - Effect of pulse-on time on objective functions

As shown in Fig. 3, material removal rate increases with increase in pulse on time as, with increase in pulse on time electric discharge rate increases. However, increased electric discharge rate also increases chance of wire breakage as indicated by reduction in tension sustained by used wire. Fig. 4 shows that the material removal rate increases with increase in pulse off time as, with increase in pulse off time better flushing of debris take place from the inter-electrode gap, resulting in increase in MRR. However, with increase in pulse off time the tension sustained by used wire decreases.

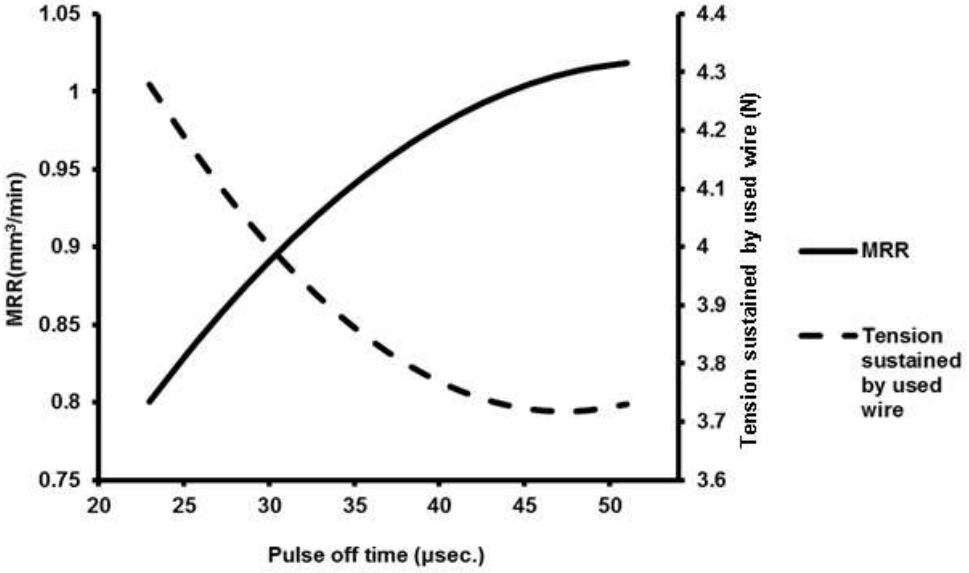

Fig. 4. - Effect of pulse-off time on objective functions

As shown in Fig.5, the peak voltage has significant effect on both the objectives. Material removal rate initially increases with increase in peak voltage up to 13 volts and then start decreasing. Also, at higher peak voltage large amount of heat is generated which results into overheating of wire electrode. Hence with increase in peak voltage the tension sustained by used wire the decreases indicating more chances of wire breakage.

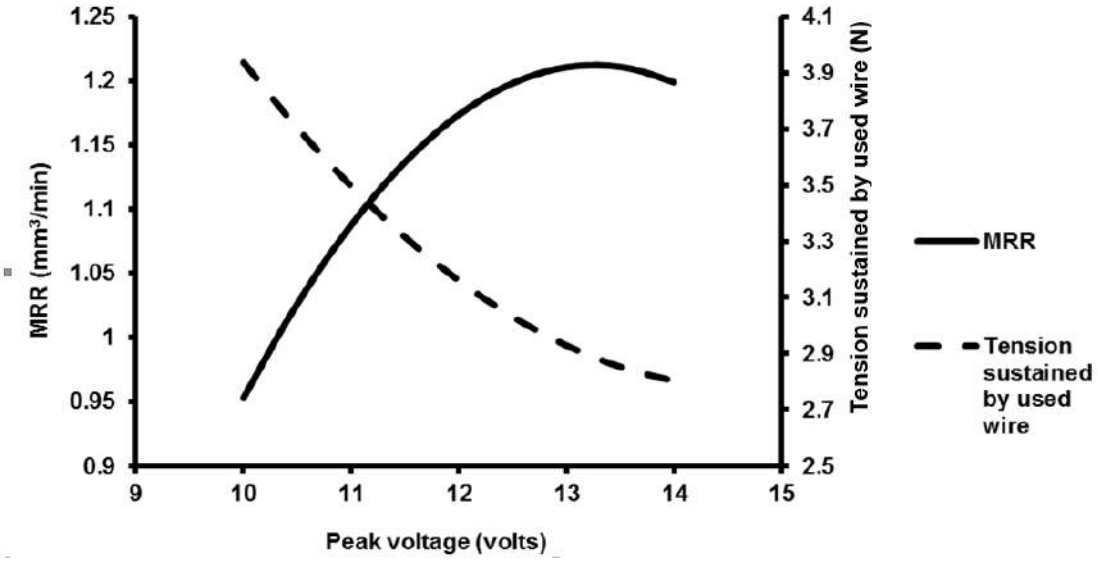

Fig. 5.- Effect of peak voltage on objective functions

The effect of dielectric fluid pressure on material removal rate and tension sustained by used wire is shown in Fig. 7. Increasing dielectric fluid pressure increases flushing rate which results into higher material removal rate. However, higher dielectric fluid pressure causes more force acting on wire electrode which increases chances of wire breakage. The effect of wire feed rate on material removal rate and tension sustained by used wire is shown in Fig. 7. Increasing wire feed rate increases Material removal rate. The tension sustained by used wire also increases initially (up to wire feed rate of 4.5 mm/min) and then decreases with increase in wire feed rate. This is due to the fact that above certain value of feed rate, bowing effect on wire electrode increases critically resulting into higher chances of wire breakage.

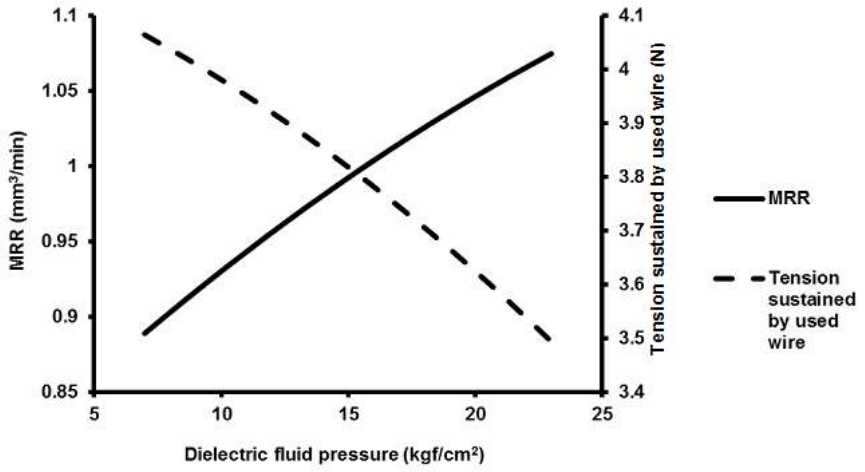

Fig. 6. - Effect of dielectric fluid pressure on objective functions

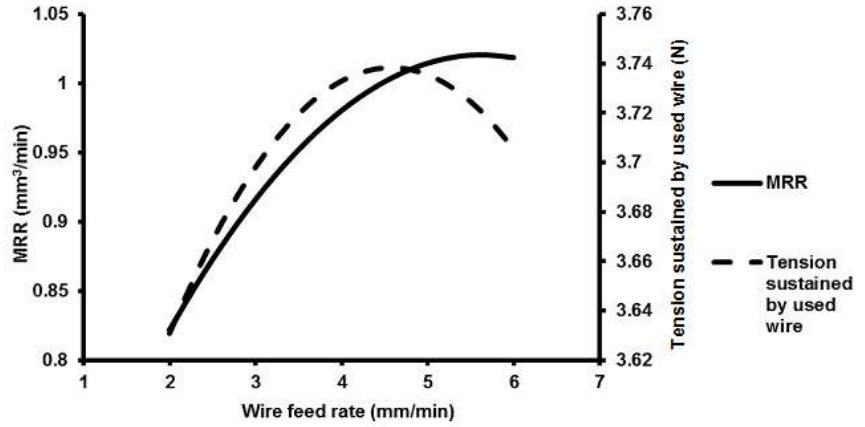

Fig. 7. - Effect of wire feed rate on objective functions

The effect of machine speed on material removal rate and tension sustained by used wire is shown in Fig. 8. The material removal rate increases with increase in machine speed. However, the tension sustaining capacity of used wire decreases with increase in machine speed. The effect of cutting speed override on material removal rate and tension sustained by used wire is shown in Fig. 9. The material removal rate initially decreases with increase in cutting speed override and becomes minimum at 25% override, after that it increases with further increase in cutting speed override. It can also be seen that the tension sustaining capacity of used wire decreases with increase in machine speed.

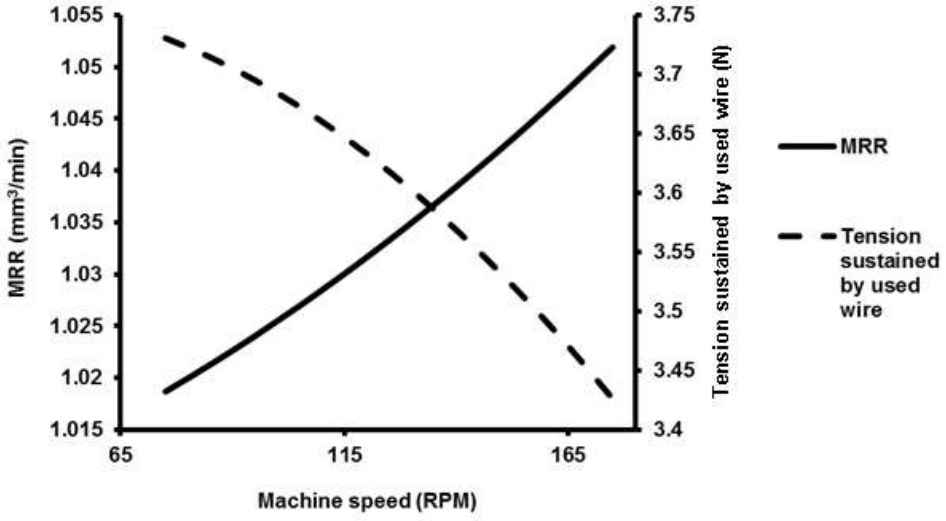

Fig. 8. - Effect of machine speed on objective functions

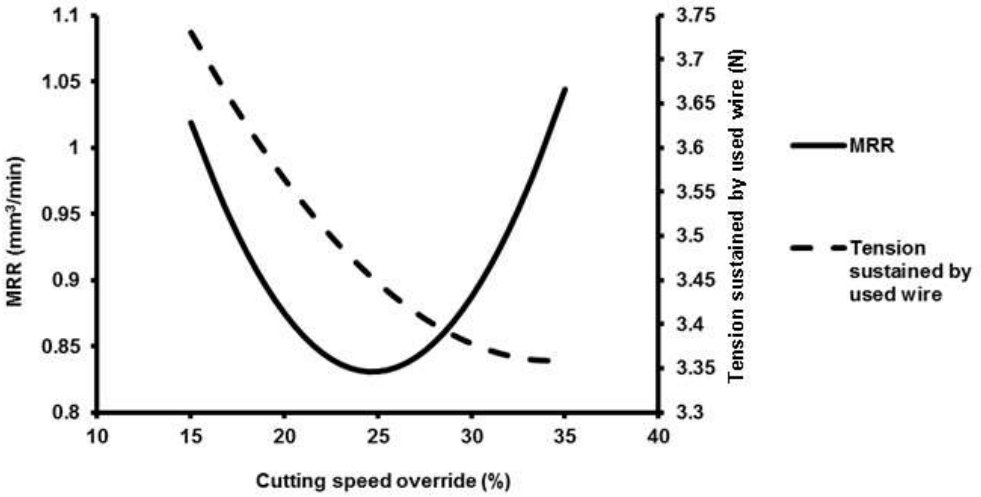

Fig. 9. - Effect of cutting speed override on objective functions

Although the parameters ranges available on machine are very wide, this study reveals that parameter values in some specific ranges only are effective to achieve better process performance of wire electric discharge machining process with respect to material removal rate and frequency of wire breakage. The most effective ranges of process variables to ensure best performance with respect to both objectives considered in this work are provided by value path plot as shown in Fig. 10.

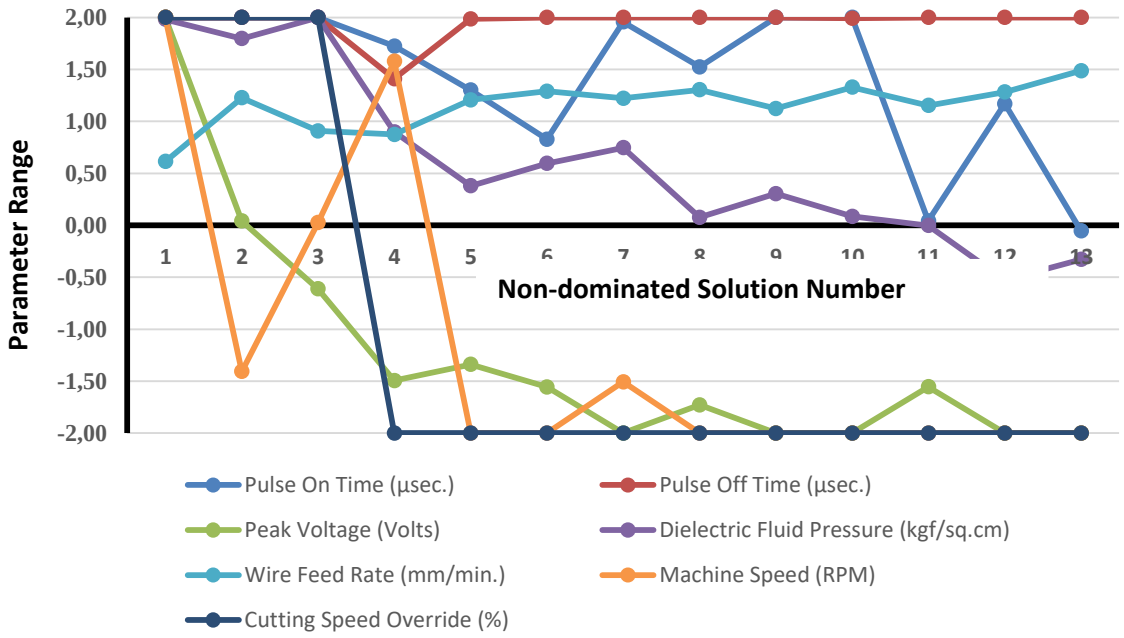

Fig. 10. - Value path plot

Conclusions

Wire breakage and low material removal rate are serious issues in wire electric discharge machining especially for machining of hard to cut materials with complex profiles. In this work, multi-objective version of artificial bee colony algorithm based on the concept of non-dominated sorting is proposed to deal with issues. The two objectives considered are: minimizing frequency of wire breakage and maximization of material removal rate. A concept of maximizing tension sustained by used wire is applied to ensure minimum frequency of wire breakage. A set of 13 non-dominated solutions is obtained using proposed multi-objection optimization approach. This provides ready reference to process engineers to set best operating parameters on machines as per his/her requirements. Value path plot reveals that from wire breakage and MRR point of view most effective ranges of process parameters are: pulse on time: 107-111 µsec, pulse off time: 47-51 µsec, peak voltage: 10-10.8 Volts, dielectric fluid pressure: 13-19 kg/cm^2, wire feed rate: 4.5-5.5 mm/min, machine Speed:

5-175 rpm and cutting speed override: 15-35 %. Combined objective function values for set of non-dominated solutions obtained by using proposed multi-objective ABC algorithm shows an average improvement of about 17.9% over those obtained by initial data set obtained experimentally. This clearly indicate the effectiveness of the proposed approach of maximizing the tension sustained by used wire to minimize the wire breakage in wire electric discharge machining of hard materials like EN19.

Declaration of Competing Interest. The authors declare that they have no known competing of interest.

References

[1] Kinoshita N., Fukui M., Gamo G. Control of wire – EDM preventing electrode from breaking //CIRP Ann Manuf Technol., 1982, Vol. 31, P. 111 – 114.
[2] Rajurkar K. P., Wang W. M., Lindsay R.P. On-line monitor & control for wire breakage in WEDM //CIRP Ann Manuf Technol., 1991, Vol. 40, P. 219 – 222.
[3] Yan M. T., Liao Y. S. Monitoring & self-learning fuzzy control for wire rupture prevention in wire electrical discharge machining //Int. J. Mach. Tools Manuf., 1996, Vol. 36, P. 339 – 353.
[4] Liao Y. S., Chu Y. Y., Yank M. T. Study of wire breaking process & monitoring of WEDM // Int. J. Mach. Tools Manuf., 1997, Vol. 37, P. 555 – 567.
[5] Yan M. T., Liao Y. S. Adaptive control of the WEDM process using the fuzzy control strategy //Journal of Manufacturing Systems, 1998, Vol. 17, P. 263 – 274.
[6] Luo Y. F. Rupture failure & mechanical strength of the electrode wire used in wire EDM //J. Mater. Process. Technol., 1999, Vol. 94, P. 208 – 215.
[7] Guo Z. N., Yue T. M., Lee T. C., Lau W. S. Computer simulation & characteristic analysis of electrode fluctuation in wire electric discharge machining //J. Mater. Process. Technol., 2003, Vol.142, P. 576–581.
[8] Saha S., Pachon M., Ghoshal A., Schulz M. J. Finite element modeling & optimization to prevent wire breakage in electro-discharge machining //Mech. Res. Commun., 2004, Vol. 31, P. 451–463.
[9] Cabanes I., Portillo E., Marcos M., Sanchez J. A. On-line prevention of wire breakage in wire electro - discharge machining //Robot Comput Integr Manuf., 2008, Vol. 24, P. 287–298.
[10] Kumar A., Kumar V., Kumar J. Microstructure analysis & material transformation of pure titanium & tool wear surface after wire electric discharge machining process //Mach. Sci. Technol., 2014, Vol. 18, P. 47–77.
[11] Gupta K., Chaube S. K., Jain N. K. Exploring wire – EDM for manufacturing of high quality meso – gears //Procedia Materials Science, 2014, Vol. 5, P. 1755 – 1760.
[12] Okada A., Konishi T., Okamoto Y., Kurihara H. Wire breakage & deflection caused by nozzle jet flushing in wire EDM //CIRP Ann Manuf Technol., 2015, Vol. 64, P. 233 – 236.
[13] Habib S., Okada A. Study on the movement of wire electrode during fine wire electrical discharge machining process //J. Mater. Process. Technol., 2016, Vol. 227, P.147–152.
[14] Kumar S., Goyal K. K., Kumar R. Research trends in Wire electrical discharge machining (WEDM): A Review // Int. J. Technol. Res. Eng., 2015,Vol. 2, P. 1164 – 1171.
[15] Das S., Joshi S. N. Estimation of wire strength based on residual stresses induced during wire electric discharge machining // J. Manuf. Process., 2020, Vol. 53, P. 406-419.
[16] Abhilash P.M., Chakradhar D. ANFIS modelling of mean gap voltage variation to predict wire breakages during wire EDM of Inconel 718 //CIRP J Manuf Sci Technol., 2000, Vol. 31, P. 153-164.
[17] Ramakrishnan R., Karunamoorthy L. Multi response optimization of wire EDM operations using robust design of experiments //Int. J. Adv. Manuf. Technol., 2006, Vol. 29, P.105–112.
[18] Nourbakhsh F., Rajurkar K. P., Malshe A. P., Cao J. Wire electro-discharge machining of titanium alloy //Procedia CIRP, 2014,Vol. 5, P. 13 – 18.
[19] Mandal A., Dixit A. R., Das A. K., Mandal N. Modeling & optimization of machining Nimonic C-263 super alloy using multi-cut strategy in WEDM //Mater. Manuf. Process., 2015, Vol. 31, P. 860 – 868.
[20] Habib S. Optimization of machining parameters & wire vibration in wire electrical discharge machining process //Mech. Adv. Mater. Struct., 2017, Vol. 3, paper 3.
[21] Nain S. S., Dixit G., Kumar S. Performance evaluation of the WEDM process of aeronautics super alloy //Mater. Manuf. Process., 2018, Vol. 33, P.1793-1808
[22] Devarasiddappa D., Chandrasekaran M. Experimental investigation & optimization of sustainable performance measures during wire-cut EDM of Ti-6Al-4V alloy employing preference-based TLBO algorithm //Mater. Manuf. Process., 2020, Vol. 35, P. 1204-1213.
[23] Shandilya P., Rouniyar A. K., Saikiran D. Multi-objective parametric optimization on machining of Inconel-825 using wire electrical discharge machining //J. Mech. Eng. Sci., 2020, Vol. 234, P. 4056-4068
[24] Phate M., Bendale A., Toney S., Phate V. Prediction & optimization of tool wear rate during electric discharge machining of Al/Cu/Ni alloy using adaptive neuro-fuzzy inference system // Heliyon, 2020, Vol. 6, e5308
[25] Chou P-H, Hwang Y-R, Yan B-H The study of machine learning for wire rupture prediction in WEDM // Int. J. Adv. Manuf. Technol., 2022, Vol. 119, P. 1301-1311.
[26] Goswami K., Samuel G. L. Support vector machine regression for predicting dimensional features of die-sinking electrical discharge machined components //Procedia CIRP, 2021, Vol. 99, P. 508–513.
[27] Karaboga D., Basturk B. On the performance of artificial bee colony (ABC) algorithm // Applied Soft Computing, 2008, Vol. 8, P. 687-697.
[28] Pawar P. J., Vidhate U. S., Khalkar M. Y. Improving the quality characteristics of abrasive water jet machining of marble material using multi-objective artificial bee colony algorithm // J Comput Des Eng., 2018, Vol. 5, P. 319-328.
[29] Deb K. Multi-objective optimization using Evolutionary Algorithms. - Wiley India Pvt. Ltd., India, 2005.

Appendix 1

$$R=0.8486+0.0477.x_1+0.058.x_2+0.066.x_3+0.043.x_4+0.033.x_5+0.0088.x_6+0.0044.x_7-0.0026.x_1^2-0.0119.x_2^2-0.0244.x_3^2-0.0026.x_4^2-0.015.x_5^2+0.0005.x_6^2+0.050.x_7^2-0.0015.x_1.x_2-0.0015.x_1.x_3+0.0015.x_1.x_4-0.00078.x_1.x_5+0.00078.x_1.x_6+0.00156.x_1.x_7-0.00156.x_2.x_3+0.00078.x_2.x_4-0.0015.x_2.x_5+0.x_2.x_6+0.00156.x_2.x_7+0.00156.x_3.x_4-0.00078.x_3.x_5-0.00078.x_3.x_6+0.00078.x_3.x_7+0.x_4.x_5+0.x_4.x_6-0.0015.x_4.x_7-0.0054.x_5.x_6-0.0039.x_5.x_6-0.0023.x_6.x_7 \quad (1)$$

$$T_{uw}=3.079-0.0845.x_1-0.1514.x_2-0.2536.x_3-0.086.x_4+0.0463.x_5-0.04485.x_6-0.0720.x_7-0.0099.x_1^2+0.0463.x_2^2+0.0525.x_3^2-0.0099.x_4^2-0.01617.x_5^2-0.0099.x_6^2+0.0244.x_7^2+0.0093.x_1.x_2-0.00313.x_1.x_3+0.0039.x_1.x_4-0.0101.x_1.x_5+0.0046.x_1.x_6+0.0031.x_1.x_7-0.0031.x_2.x_3-0.0085.x_2.x_4-0.0031.x_2.x_5-0.0054.x_2.x_6+0.x_2.x_7+0.007.x_3.x_4+0.0007.x_3.x_5+0.0046.x_3.x_6+0.0085.x_3.x_7+0.0031.x_4.x_5+0.0093.x_4.x_6+0.0085.x_4.x_7+0.0007.x_5.x_6+0.0062.x_5.x_7+0.0117.x_6.x_7 \quad (2)$$

Information of the authors

Pawar Padmakar., PhD, professor, K. K. Wagh Institute of Engineering Education and Research
e-mail: pjpawar1@rediffmail.com

Amol Dalavi, PhD, assistant professor, Symbiosis Institute of Technology
e-mail: amol.dalavi@sitpune.edu.in

Thorve K. M., K. K. Wagh Institute of Engineering Education and Research